



TECHNISCHE
UNIVERSITÄT
WIEN

DISSERTATION

High-performance silicon micro cavities for quantum science

Ausgeführt zum Zwecke der Erlangung des akademischen Grades
eines Doktors der technischen Wissenschaften unter der Leitung von

Univ. Prof. Dipl. Ing. Dr. Techn. Dr. Hannes-Jörg Schmiedmayer
E141
Atominstitut

eingereicht an der
Technischen Universität Wien
Fakultät für Physik

von

Dipl.-Ing. Georg Wachter
Matrikelnummer 0526111
Stranzenberggasse 5/2/3 1130 Wien

Wien, am



Die approbierte gedruckte Originalversion dieser Dissertation ist an der TU Wien Bibliothek verfügbar.
The approved original version of this doctoral thesis is available in print at TU Wien Bibliothek.

In memoriam my grandfather
Univ. Prof. Dr. Erwin M. Hörl 1929-2018



Die approbierte gedruckte Originalversion dieser Dissertation ist an der TU Wien Bibliothek verfügbar.
The approved original version of this doctoral thesis is available in print at TU Wien Bibliothek.

Kurzfassung

Die Wechselwirkung von Licht und Materie spielt eine zentrale Rolle für unzählige Anwendungen in der Physik und in der Industrie. Mikrocavities können in vielen Bereichen eingesetzt werden und dank ihrer Eigenschaften die Licht-Materie Wechselwirkung erhöhen. Die in dieser Arbeit verwendeten Cavities können aufgrund ihres kleinen Radius das Licht in einem wesentlich kleineren Bereich konzentrieren als große Cavities. Die Konstruktion als „offene“ Cavity ermöglicht es die Partikel am Ort der größten Feldstärke zu platzieren. In dieser Arbeit zeige ich wie konkave Mikrospiegel berechnet, gefertigt, zusammengebaut und gemessen werden. Die Cavitiespiegel haben einen Radius von $100\ \mu\text{m}$ bis $1.3\ \text{mm}$. Aus diesen Mikrosiegeln wird eine offene Infrarotcavity ($1550\ \text{nm}$) gebaut. Dieses besteht aus 2 Siliziumchips mit Spiegeln und einem Spacer Chip in der Mitte. Der Öffnungsdurchmesser der Spiegel liegt im Bereich des Durchmessers eines menschlichen Haares ($200\ \mu\text{m}$ to $60\ \mu\text{m}$). In dieser Arbeit war es uns möglich Spiegel mit einer Finesse von bis zu 5×10^5 herzustellen. Im Design Prozess geht es darum alle kritischen Werte für die geplante Anwendung zu berechnen. Aufgrund dessen werden die Spiegel danach gefertigt. Hierfür haben wir einige neue Verfahren entwickelt sowie bekannte Methoden weiterentwickelt und verfeinert. Hier ging es vor allem darum die Rauheit und die Form der Spiegel zu verbessern. Nach umfangreichen Untersuchungen war es möglich einen Drei-Schritte-Plan zur Spiegelproduktion festzulegen. Im ersten Schritt wird die Spiegelform definiert. Der zweite Schritt dient dazu, die Form bis zum Zielradius zu vergrößern. Zuletzt wird poliert, um auf die notwendige Rauheit zu kommen. Es gelang uns die Rauheit auf unter $0.4\ \text{nm RMS}$ zu senken. Um diese Prozesse besser zu verstehen, wurden eine Reihe von Messungen, Berechnungen und Simulationen durchgeführt. Es wurde unter der Annahme das ein nicht parabel-förmiger Spiegel vorliegt das elektromagnetische Feld im Inneren der Cavity berechnet. Auf diese Weise konnten wir den Einfluss von Abweichungen von der perfekten Form untersuchen und festlegen, ob die von uns gefertigten Mikrospiegel die geforderte Qualität haben. Danach werden die Spiegel von einer externen Firma mit dielektrischen Spiegelschichten ausgestattet. Anschließend wurden Spacer für die Spiegel entwickelt und von uns gefertigt. Diese legen den Abstand und die Ausrichtung zwischen den Spiegeln fest. Durch eine formschlüssige Verbindungsmethode ist es uns hier gelungen, die Spiegel auf weniger als $2\ \mu\text{m}$ genau zueinander auszurichten. Zusammen mit den Spiegeln ergeben diese eine Cavity. Als letzter Schritt erfolgt die Vermessung und Charakterisierung, die wiederum in die Weiterentwicklung besserer Spiegel einfluss. Mit der von uns erzeugten Cavities wurden bereits physikalische Experimente durchgeführt und es konnten damit Nanopartikel detektiert werden. Zudem wurde das Verhalten der Cavities mit einem Dielektrikum untersucht. Als letzten Punkt berichte ich über zukünftige Anwendungen.

Abstract

Light-matter interactions are central to numerous methods in physics and engineering. They enable sensitive detection, cooling and manipulation of particles such as nanospheres, molecules, atoms and defects in semiconductors. Microcavities can strongly enhance these interactions. For the cavities in this thesis, this enhancement is achieved by strong spatial confinement of light using mirrors with small radii of curvature. Open access allows the placement of particles in the strongest portion of the light field.

In this work I describe the design, manufacturing and implementation of high-finesse microcavities in silicon. The design is an open microcavity operating at infrared wavelengths (1550 nm). This cavity is built out of two silicon chips with mirrors on both and a spacer in between. The radii of curvature of these mirrors are in the range of 100 μm to 1300 μm . The sizes of these mirrors range from 200 μm to 60 μm in diameter, comparable to the diameter of a human hair. In this work, we created microcavities with a finesse in excess of 5×10^5 .

The design process is guided by the goals of the application, which determines the characteristics of the cavity such as waist size, linewidth and finesse. These characteristics determine the physical parameters of the microcavity including the mirror reflectivity, radii of curvature and its length.

The next step was to manufacture the mirrors. For this purpose, we developed new techniques and improved existing processes. These improvements led to a reduction in the mirror roughness and a better definition of the shape of the mirrors. The fabrication consists of a three-step process: in the first step the shape is defined, in the second the shape is amplified up to the necessary radius. The last step was a polishing procedure to improve roughness down to 0.4 nm RMS or less.

Finally the mirrors were coated by an external company with a dielectric mirror coating. For these mirrors we developed a spacer. This spacer defines exactly the length of the cavity and has special features to guarantee an alignment with an error below 2 μm . The cavity structure is then assembled. Various characterization measurements are performed on these cavities. These measurements were used to improve the cavity design and manufacturing process.

To gain further insight into the whole fabrication process, a suite of measurements, simulations and calculations were performed. In order to understand how deviations from the desired shape influence the finesse, the electromagnetic field inside a cavity was calculated for a non-parabolic shape. Furthermore, a simplified simulation of the etch process was constructed to determine the point during the etch process which yields the most parabolic profile.

I report on how these cavities were successfully integrated into an experiment to detect nano particles. Additionally, the behavior of the cavities with a dielectric was investigated. Finally an outlook towards applications in quantum photonics is given.



Die approbierte gedruckte Originalversion dieser Dissertation ist an der TU Wien Bibliothek verfügbar.
The approved original version of this doctoral thesis is available in print at TU Wien Bibliothek.



Die approbierte gedruckte Originalversion dieser Dissertation ist an der TU Wien Bibliothek verfügbar.
The approved original version of this doctoral thesis is available in print at TU Wien Bibliothek.

Contents

1	Micro Mirrors and Micro Cavities: An Introduction	1
1.1	Why small?	1
1.1.1	Cooperativity and beam waist	2
1.1.2	Length of a cavity	2
1.1.3	Field gradient inside a cavity	4
1.2	State of the art	5
1.2.1	Macroscopic Fabry-Pérot resonators	5
1.2.2	Whispering gallery mode resonators	6
1.2.3	Cylindrical cavities	7
1.2.4	Pillar cavities	8
1.2.5	Open Fibre Cavities	9
1.2.6	Bottle resonators	11
1.2.7	Photonic crystal resonators	11
1.3	Micro cavities in silicon	12
1.4	Structure of this thesis	15
2	Theoretical background	17
2.1	Paraxial Wave Equation	17
2.2	Gaussian beam	18
2.3	Hermite-Gaussian beam	19
2.4	Laguerre-Gaussian beam	20
2.5	Cavity theory	21
2.5.1	Free spectral Range	21
2.5.2	Resonance linewidth	22
2.5.3	Finesse	22
2.5.4	Quality factor or Q factor	25
2.5.5	Birefringence	25
2.6	Fabry-Perot cavities	26
2.6.1	Beam geometry in a Fabry-Perot cavity	26
2.6.2	Cooperativity and the Purcell factor	27
2.6.3	Radius of curvature measurement	29
2.6.4	Cavity stability	31

3	Numerical Simulations of the EM field in a cavity	37
3.1	Effective Radius of a Polynomial	37
3.2	Calculation method	39
3.3	Numerical Calculation	41
3.4	Example simulations	44
3.4.1	Parabola	44
3.4.2	Gauss	44
3.4.3	Parabola with error	50
3.4.4	Real mirror shapes	55
3.5	Conclusion	59
4	Micro mirror design	61
4.1	Limitations	61
4.2	The three-fstep etch process	62
4.2.1	First step: define the shape	62
4.2.2	Second step: amplification and opening	62
4.2.3	Third step: polishing	63
4.3	Calibration curves for etching	65
4.4	First run	68
4.4.1	Roughness	68
4.4.2	Cavity length	68
4.4.3	Beam radius and mirror diameter	69
4.4.4	Depth	72
4.4.5	Etching times and initial opening	72
4.4.6	Summary for first run	72
4.5	Second run	78
4.5.1	Roughness	78
4.5.2	Cavity length	78
4.5.3	Beam radius and mirror diameter	78
4.5.4	Depth	78
4.5.5	Etching times and mirror diameter	79
4.5.6	Summary for second run	79
5	Manufacturing of a micro mirror	81
5.1	Mask design	82
5.2	Silicon etching	85
5.3	Photoresist removal	87
5.4	Thermal polishing	88
5.5	Mirror coating	90
5.6	Cavity configurations	91

5.7	From wafer to mirror	92
5.7.1	Mirror chip	92
5.7.2	Spacer chip	93
5.8	From chip to cavity	98
5.8.1	Assembly of the monolithic cavities	98
5.8.2	Assembly of the Piezo setup	98
6	Measurements on cavities	101
6.1	Experimental setup	101
6.2	Results of the first run	106
6.2.1	Best finesse	106
6.2.2	Finesse as a function of cavity length	107
6.2.3	Birefringence	108
6.2.4	Spectrum	109
6.2.5	Mirror characterization	112
6.2.6	Conclusion	115
6.3	Results of the second run	117
6.3.1	Measurements in curved-curved configuration	118
6.3.2	Measurements in flat-curved configuration	121
6.3.3	Mirror characterization	127
6.3.4	Conclusion	127
7	Cavity containing a dielectric chip	131
7.1	Losses due to absorption	131
7.2	Losses at the interface	133
7.2.1	Cavity in vacuum	133
7.2.2	Losses at a rough surface inside the cavity	134
7.2.3	Losses due to dielectric effects	135
7.2.4	Effects of anti-reflection coating	136
7.2.5	Conclusions from the theory	138
7.3	Experiment	141
7.3.1	Silicon with anti-reflection coating	142
7.3.2	Thin diamond chip inside a long cavity	143
7.3.3	Thin diamond chip in a short cavity	145
7.4	Improvements for cavity enhanced quantum systems	148
7.5	Conclusion	150
8	Nano particle detection in cavities	153
8.1	Experimental setup	155
8.2	Results, discussion and outlook	157

9 Summary and outlook	161
Bibliography	163
Appendix	173
A Theory of etching mirrors in silicon	173
A.1 Etching simulations	173
A.2 The three regimes of etching	177
B Masks and schematics	181
B.1 piezo mount	181
B.1.1 Mechanical drawings	181
B.1.2 Electrical drawings	188
B.2 mount for monolithic cavities	191
B.3 Coating mount	195
B.4 Mask set for mirrors	198



Die approbierte gedruckte Originalversion dieser Dissertation ist an der TU Wien Bibliothek verfügbar.
The approved original version of this doctoral thesis is available in print at TU Wien Bibliothek.

CHAPTER 1

Micro Mirrors and Micro Cavities: An Introduction

This thesis is about optical micro cavities in silicon. This type of optical cavity consists of 2 mirrors facing each other. Earlier work (2006) on this subject was done in London [1], where many different ways to manufacture micro cavities in silicon were investigated and a finesse (\mathcal{F}) of 6000 was reached, four years later with some improved polishing 64 000 was reached [2]. These approaches build a great foundation for this thesis, where we were able to achieve a finesse of 500 000.

Cavities are typically used to increase the interaction of any object inside the cavity with the light field. The finesse is an important value to determine the quality of a cavity. The finesse is defined in detail in section 2.5.3. There is another figure of merit to describe a cavity: the Q-factor. It is especially useful for cavities where the finesse can not be measured. Details are given in section 2.5.4.

Optical microcavities play a central role in many different applications and experiments, such as cavity-enhanced atomic emission spectroscopy [3, 4], micro lasers [5], as well as sensing applications [6] and cavity quantum electrodynamics experiments [7–9].

1.1 Why small?

The first question when thinking about micro cavities is why micro, why do we need small cavities? There exist many "normal sized" ultra-high finesse cavities (with \mathcal{F} up to $(1.9 \pm 0.1) \times 10^6$ [10]). These cavities use half inch mirrors with a separation of 4 mm and a radius of 173 mm. So, why go small? The idea is that a smaller cavity allows a smaller radius. This small radius is a key point for micro cavities, because it also means that the beam waist w_0 of the Gaussian beam inside the cavity becomes small. This behavior (for a flat-curved configuration) is shown in equation 1.1:

$$w_0 = \sqrt{\frac{\lambda}{\pi} \cdot \sqrt{R_1 \cdot L - L^2}} \quad (1.1)$$

Here, w_0 , R_1 and L are the waist, mirror radius of curvature and cavity length, respectively (see section 2 and figure 2.5 for details). λ is the wavelength of the light. There are three ways to get a small beam waist: Either the length of cavity (1) is minimized, but for geometric reasons this is not practical, or R_1 is increased

to approach L . This leads to difficulties because the beam size on the curved mirror goes towards infinity under this condition. For a realistic case, the length is typically significantly smaller than the radius and the radius is the only relatively free parameter in this formula. So, to get a small waist, the radius has to be made small.

1.1.1 Cooperativity and beam waist

Now, why is a small waist, in the middle of a cavity, desirable for light matter interactions? In many applications a cavity is used to increase the coupling between the object of interest and the light field. The advantage of a cavity is that the light passes the interaction volume more than one time. Now it is possible to define the interaction area of the cavity:

$$\sigma_C = \pi w_0^2, \quad (1.2)$$

which is the area of a circle with w_0 as its radius. This value is typically bigger than the cross section of the quantum object. The cross section of a two level atom on resonance is defined as:

$$\sigma_E = \frac{3\lambda^2}{2\pi} \quad (1.3)$$

Now it is possible to define the cooperativity C :

$$C = \frac{2}{\pi} \frac{\sigma_E}{\sigma_C} \cdot \mathcal{F} \cdot \eta, \quad (1.4)$$

which indicates how much a cavity enhances the light matter interaction. The finesse \mathcal{F} defines how many times the light passes the area. The factor η includes the fact that not all objects inside the cavity have a discrete spectrum. η is 1 for a two-level system, but for example only ≈ 0.02 for nitrogen vacancy centers in diamond, due to the phonon side bands not in resonance with the cavity.

How to improve the cooperativity? The obvious way is to make the mirrors better and the finesse higher or w_0 smaller. Because σ_C depends on w_0 , which in turn only depends on the radius, microcavities are the best choice. So to improve the cooperativity, a small radius and a big finesse are the goals.

1.1.2 Length of a cavity

For all sections before the assumption was that the length of the cavity is constant. But for a real cavity setup also the length counts. In figure 1.1 w_0 and w_M (beam waist) are plotted versus the cavity length. There are two regimes where w_0 is small: for very short cavities and very long cavities, compared to the radius R_1 . Both regimes have their issues; for short ones it is very difficult to place something inside the cavity. For long cavities the spot size on the mirror w_M gets very large. This is

an issue because it is very difficult to produce a good mirror shape with excellent roughness over the whole mirror. If the beam size on the mirror increases, it is more and more likely that imperfections are sampled by the beam and the finesse will decrease.

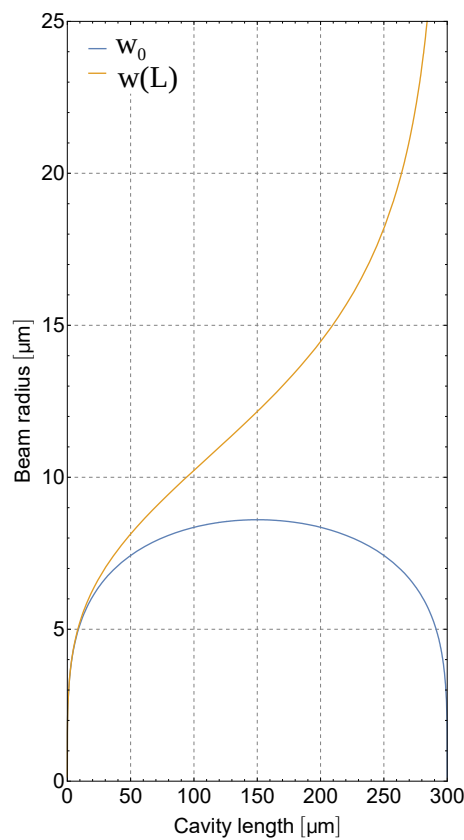


Figure 1.1: w_M (orange) and w_0 (blue) depend on the cavity length for a given radius (300 μm) assuming a wavelength of 1550 nm. This calculation was done for a flat-curved configuration, for curved-curved the x-axis would be scaled a factor of 2.

1.1.3 Field gradient inside a cavity

The next interesting point is the field gradient, which is important for experiments aiming at the trapping and cooling of particles in a cavity. For trapping objects much smaller than the wavelength of the light, two gradients are important. The gradient along the optical axis is given by the alternating field maxima and minima of the standing wave. The radial intensity gradient is defined by the cavity geometry and can be maximized by minimizing the beam waist w_0 . This makes micro cavities well suited for trapping experiments.

For trapping particles much bigger than the wavelength, the relevant field gradient is given by the derivative of the spot size along the cavity axis. Figure 1.2 shows the difference between the fields of a relatively large cavity and a microcavity. It is important to note that these figures use the same scale. This figure shows also very clearly why σ_C for micro cavities is smaller, as discussed in section 1.1.1.

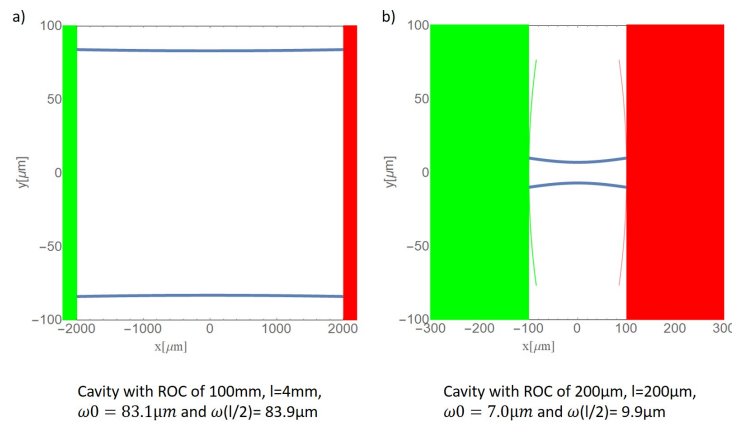


Figure 1.2: The calculated beam width (blue line) for two different cavities. a) shows a normal sized cavity with $L = 4\text{ mm}$ and $R_1 = 170\text{ mm}$ and b) a microcavity with $L = 200\text{ }\mu\text{m}$ and $R_1 = 300\text{ }\mu\text{m}$. The red and green bars are the mirrors. The field gradient is much larger in the microcavity.

1.2 State of the art

There are many different kinds of cavity designs. In this section, I will cover briefly the most common, the most unique and the best cavities regarding their Q-factor. For more comprehensive reviews of optical microcavities the reader is referred to previous work [11, 12]. I will discuss a few important properties for the cavities presented here.

First, whether the cavity is closed or open, depending whether the location of the highest field amplitude is inside a solid body or not. This is important if something has to be placed inside the cavity.

Second, the Q-factor. This is the figure of merit of the optical quality of the cavity.

Third, the scalability is also an interesting property. It basically determines how many cavities can be produced at once. This is especially relevant for industrial applications.

Another way to think about scalability is how monolithic a cavity design is. A cavity out of one piece is far more scalable than a design out of many pieces. A fully monolithic design requires no cavity alignment.

Another question is how to get the light into and out of the cavity in a controlled way. Normally this is done with free-space optics such as a microscope objective or other lens systems. For many applications it is desirable however to have fibre optics for in- and outcoupling, or even integrated waveguides.

1.2.1 Macroscopic Fabry-Pérot resonators

The Fabry-Pérot resonator is the earliest design of an optical cavity or optical resonator. It consists, as shown in 1.3, of two mirrors facing each other. This design is open and it is easy to place something between the mirrors. The typical application is the laser [13, 14]. The resonators are built in most cases using macroscopic mirrors with diameters in the mm range. The best cavities of this type ever built had a finesse of 2×10^6 and a corresponding Q of 1.8×10^{10} [10].

These resonators are not scalable because they consist of two mirrors, two mirror mounts and a lens to couple the light into the resonator. The manufacturing is easier than the other approaches, because modern production methods achieve the best possible mirror quality and surface roughness. This has been optimized for decades by the optics industry to produce curved mirrors for many different applications. Advanced dielectric mirror coatings make it possible to reach incredibly high finesse and Q-factors. Fabry-Pérot cavities are used for many applications: in lasers, in spectrometers, as a frequency reference and also in many kinds of scientific experiments. The only real disadvantage of macroscopic Fabry-Pérot cavities is that they have larger mode waists, and therefore small cooperativities.

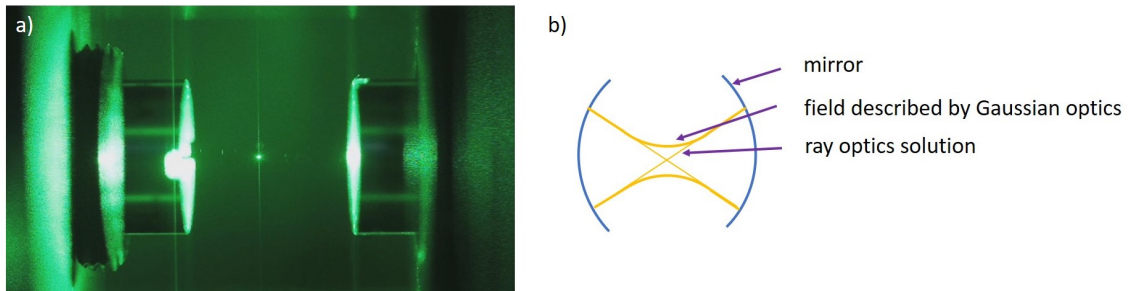


Figure 1.3: a) shows a Fabry-Pérot resonator with a nano particle^b. b) General setup of a Fabry-Pérot resonator, consisting of two mirrors (blue) facing each other.

^b James Millen (UCL Physics & Astronomy) <https://www.flickr.com/photos/uclmaps/16841346482/>

1.2.2 Whispering gallery mode resonators

Whispering gallery modes are well known from acoustics, but also exist in optics. In a cylindrical structure the light can be totally reflected by the surface of a transparent object as shown in figure 1.4. This kind of mirror has the big advantage that there is no need for an expensive dielectric mirror coating, the limiting factor is only how clean and smooth the surface for the total reflection can be made. Most of these resonators are closed. The very first optical whispering gallery resonators were made using a small glass sphere [15]. More modern designs create a silica toroid on top of a micro tower [16]. This design is monolithic and quite scalable, it can be manufactured by microfabrication in large quantities. Usually the light is coupled in with a fibre. The Q-factors are very high, reaching 4×10^8 and a corresponding finesse of 2.6×10^6 [17]. The toroids are produced by melting amorphous silica with a laser, this results in an ultra smooth surface. This design has been used to demonstrate a micro laser [18] by implanting erbium atoms in the material.

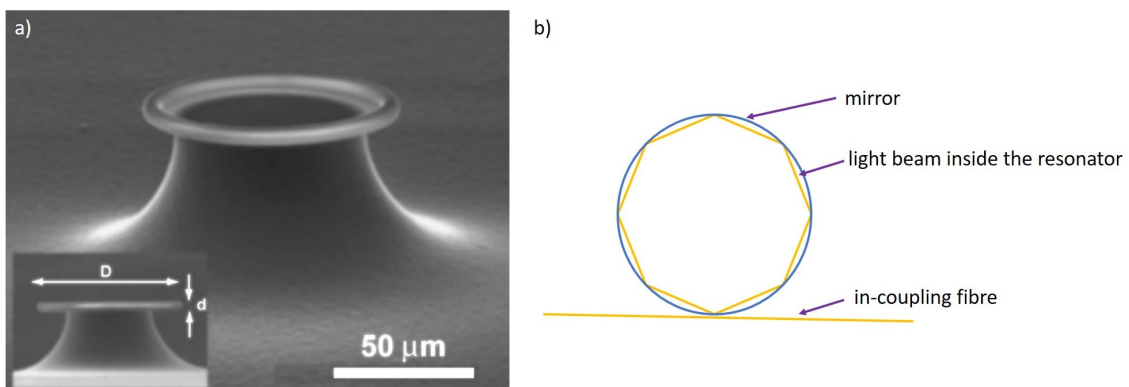


Figure 1.4: a) Scanning electron microscopy (SEM) picture of a whispering gallery mode resonator, taken from [17]. b) illustrates the internal total reflection and the fibre used to couple light into the resonator.

1.2.3 Cylindrical cavities

For many scientific and industrial applications, an open, scalable and chip-integrated cavity design is desirable. One candidate for that are cylindrical micro cavities. Instead of the usual multilayer dielectric mirrors with alternating materials, the mirrors for these cavities consist of gaps between air and material, which creates the necessary step in the refractive index. In principle this design has many advantages, it is scalable, open and can easily be integrated in on-chip optics, also they can be fabricated in a single manufacturing process [19].

The production of these resonators relies on a highly anisotropic Bosch etch process, which results in significant surface roughness. As it is so far not possible to produce mirrors which are curved in both directions [20], these cavities use cylindrical mirrors as shown in figure 1.5. Cavities with cylindrical mirrors are only stable in one axis. To refocus the light, an additional lens is necessary, which can be achieved for example by placing a fibre inside the cavity.

This design is a hybrid between an open and a closed cavity. It is open but unstable without lens or stable with a fibre in the middle of the cavity. If a hollow fibre is used the medium of interest can be pumped through the fibre, never contaminating the mirror surface.

Because of the big jump in the index of refraction between silicon and air, good mirrors can be fabricated with relatively few mirror layers, the use of a single material also makes them rather cheap. The Q-factor is in a middle range (around 1000) [19], mainly due to the surface roughness introduced by the Bosch etch.

The approach is scalable, many of these cavities can fit on a chip. The only issue is that the fibre has to be placed at the right position and the fibre thickness has to be tuned to the cavity to get the best possible performance. If mirror and fibre are not well matched, the resonance will be split due to birefringence into two peaks because there are two effective radii inside the cavity. This design is almost completely monolithic because the mirrors are aligned during the manufacturing and only the fibre has to be placed inside the cavity.

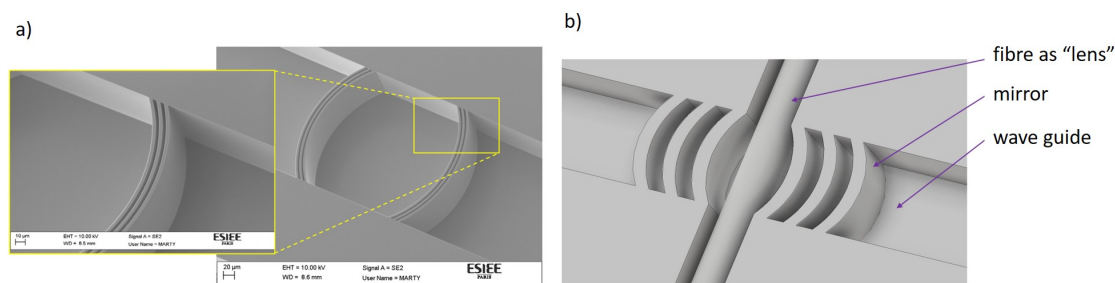


Figure 1.5: a) SEM picture of a cylindrical cavity from [19]. b) is a 3D CAD rendering of the cylindrical cavity design with a fibre as lens.

1.2.4 Pillar cavities

The best mirrors for optical wavelengths are dielectric mirrors. They consist of alternating layers of materials with different indices of refraction, where each layer has an optical path length of $\lambda/4$. The idea is to manufacture the "inside" of the cavity on top of the bottom mirror, simply by making a $n \cdot \lambda/2$ layer out of one of the mirror materials. The cavity is closed with a second dielectric mirror on top. Such a cavity can be produced in a single fabrication process. For lateral confinement of the light, micropillars are etched out of the multilayer structure. In [21] a pillar design with a diameter of only $2 \mu\text{m}$ and a Q-factor of around 2×10^5 is presented. The pillar design is extremely scalable and as monolithic as possible. They form the smallest cavities covered in this summary.

Light can be coupled to the pillar cavities using regular microscope objectives. A more scalable approach is to use optical fibres for coupling in and out of the cavities [22]. More advanced ideas are shown in [23], where optical bond wires are fabricated, which can be used to connect cavities to each other or to the output connection.

A disadvantage of this design is that it is hard to make long cavities, as this would require very thick layers. The biggest drawback however is that it is a closed cavity design. To place an object in the cavity, the fabrication process has to be interrupted while growing the middle layer, the object has to be placed and then the fabrication can continue. Often these cavities are used in combination with semiconductor quantum dots. It is very hard to define the exact properties of the emitters. To make sure the emitter sits in the middle of a micro pillar, it has to be located before etching. As the spectra of the quantum dots vary, while the cavity resonance cannot be precisely controlled, only a few quantum dots will be resonant with the cavity. This poses a limit on the scalability. More controllable defects such as the nitrogen vacancy center in diamond or SiC centers could help to overcome this issue.

The Vertical Cavity Surface Emitting Laser (VCSEL) [24] is an industrial application of this micro cavity setup. Micro pillar cavities are also used for single photon emitters with a high repetition rate [25].

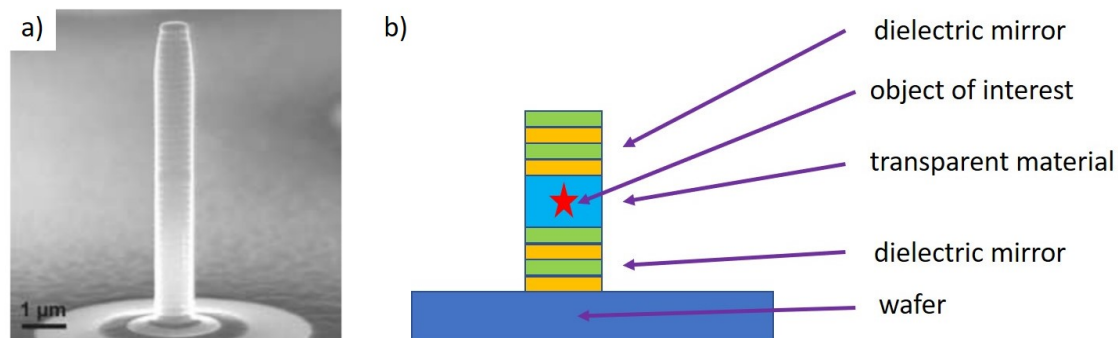


Figure 1.6: The micro pillar design. a) is a SEM picture from [7] with an impressive aspect ratio. The dielectric mirror layers as well as the cavity layer are faintly visible. b) illustrates the principle of a pillar cavity.

1.2.5 Open Fibre Cavities

A very common, flexible and elegant solution for a microcavity is the fibre cavity. The idea of the open fibre cavity [26] is to shape the end of a fibre as a curved mirror, mirror-coat it and place it opposite a flat mirror or another curved fibre end. A sketch of this is shown in figure 1.7. There are plenty of applications, for example high temperature sensing [27], optomechanical applications [28] and many more.

To shape the fibre end, a high-power laser is used [29]. Because these lasers have a Gaussian beam shape, also the mirror shape becomes Gaussian and not parabolic. The next issue is that the laser beams are not perfectly round, which causes significant birefringence. This can be reduced by advanced manufacturing techniques [30] or compensated by using matched fibre mirrors. The birefringence can also be turned into a feature to create cavities with two fundamental modes [31].

This design is open and not monolithic. The highest finesse achieved so far is around $>1.9 \times 10^5$ [32]. The mechanical setup is very difficult because a fibre end has to be placed and aligned over a mirror with three degrees of freedom or opposite another fibre with six degrees of freedom plus rotation [33]. The big advantage of this design is its high flexibility. The object of interest can be placed or manufactured directly on the flat mirror and, apart from the alignment, different measurements can be performed rapidly. This design is more scalable than a macroscopic cavity. It might be possible to build arrays out of these fibres and align them all together.

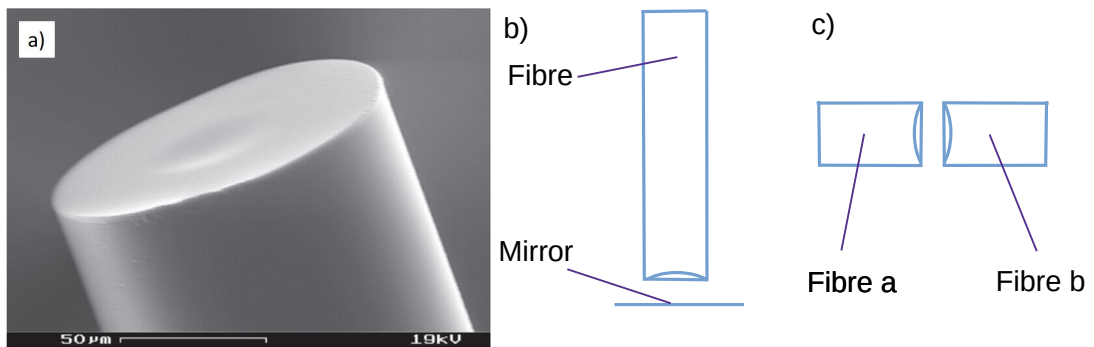


Figure 1.7: a) SEM picture of a mirror formed on a fibre tip, taken from [32]. b) shows a fibre cavity in a flat curved configuration and c) a curved-curved configuration with two fibers.

1.2.6 Bottle resonators

The bottle resonator is a closed, monolithic, fully fibre-based variant of an optical cavity [34]. In figure 1.8 the concept is shown. The idea is to use a very small area of the fibre. To the left and the right of this area, the fibre is thinned down to create an effective mirror. Similar to the open fibre cavities, only a small amount of additional optics are needed. The monolithic design makes them very scalable, Q-factors of around 3.6×10^8 can be reached.

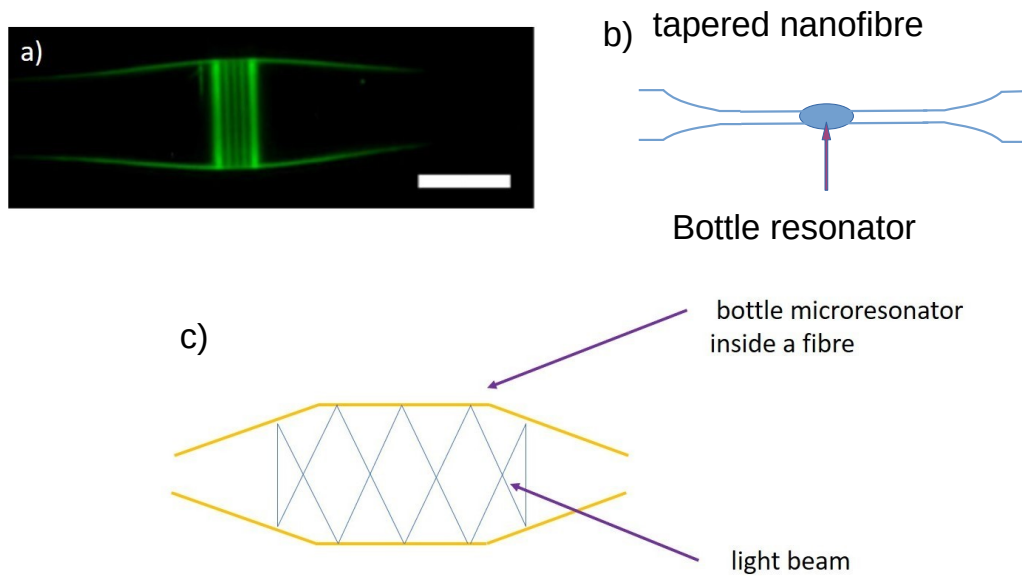


Figure 1.8: A microscope picture of the bottle resonator during an experiment from [34], the scale bar is $30 \mu\text{m}$. b) illustrates a fibre bottle resonator. The fibre is thinned on both sides of the resonator, light will be back reflected from this taper, as indicated by the blue ray.

1.2.7 Photonic crystal resonators

All cavities discussed before use dielectric mirrors or internal total reflection to store the light inside the cavity. But there is also another approach where the dielectric constant of the material is manipulated. The typical way to do this is to etch very precise holes inside a transparent material, or any other periodic structure [35]. As the holes are smaller than the wavelength of the light, the light sees only a change in the index of refraction. With this effect a photonic crystal resonator can be built [36]. This method is challenging from the manufacturing point of view, as it is very difficult to precisely etch holes with a tolerance in the range of nm. This makes it very difficult to scale up their number, even though it is theoretically possible. This design is monolithic and closed, the Q-factors are in the range of 1×10^6 [37]. There are also ideas to combine a photonic crystal mirror with a fibre [38]. The photonic

crystal can also be inverted, using pillars instead of holes. With this design open resonators can be built [39], making this system more flexible compared to the hole design.

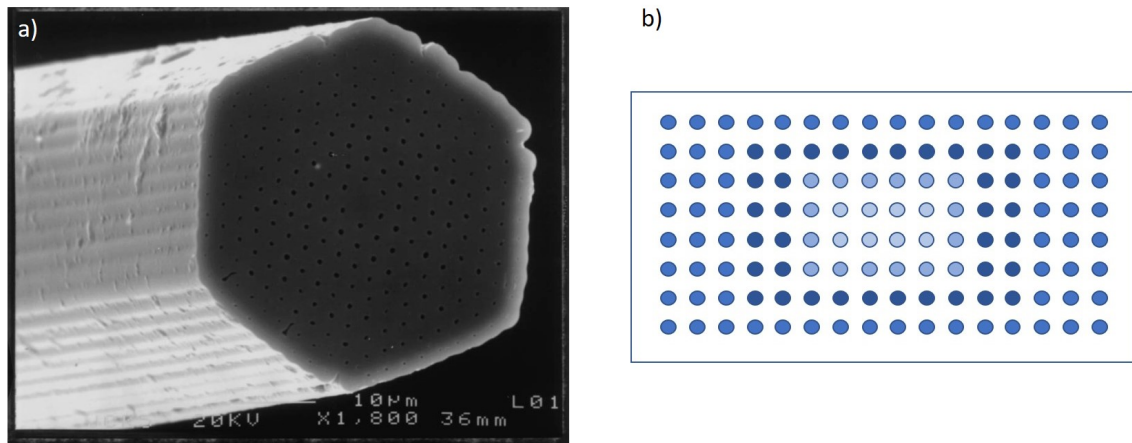


Figure 1.9: a) SEM image of a photonic crystal fibre [40]. This hollow core fibre can be used to concentrate the light inside the fibre (50 μm in diameter, holes between 1 μm and 1.2 μm). b) Symbolic picture of a photonic crystal. The different blue circles represent holes with different diameters.

1.3 Micro cavities in silicon

Table 1.1 summarizes the key properties of the cavity designs discussed above. The best Q-factors are found in closed cavities like the whispering gallery design or the bottle resonators. The big problem of all closed cavities is how to implant the object. The open cavities are all based on the Fabry-Pérot resonator. Although the object of interest can easily be placed inside these cavities, they are typically not scalable and they are hard to align.

The idea behind our design (shown in 1.10) is to combine the monolithic and open cavity approaches without their drawbacks. To achieve this, our cavities are not built out of one solid block, but we try to get as close as possible to this ideal situation. Our cavities are built out of three parts: two mirror chips and a spacer between them. We make holes in the mirror chips and corresponding posts on the spacers. In that way a form-fit alignment is guaranteed. This method makes it possible that the alignment only depends on the lithographic process. All cavity dimensions are set during the production similar to the other monolithic designs, but with the advantage that objects can be placed inside the cavity and changes to the cavity length can be made by replacing the spacer. Our design is also very scalable: We can manufacture thousands of mirrors on a single chip as shown in figure 1.11. The cavities are usually addressed using standard optics one at a time, but it is possible to use fibre blocks for interfacing many simultaneously [41].

Table 1.1: Summary of the different cavity designs. Code: Y=Yes, N=No, o=open, c=closed

Design	Q-Factor	Finesse	closed/open	monolithic Y/N	scalable Y/N	integrated in-coupling optics Y/N	Applications	Ref.
Normal sized Fabry-Pérot resonators	1.8×10^{10}	1.9×10^6	o	N	N	N	[42]	[10]
Whispering gallery mode resonators	4×10^8	2×10^5	c	Y	Y	N	[18]	[17]
Cylindrical cavities	1×10^3	3.6	o/c	Y	Y	Y		[19]
Pillar cavities	2.5×10^5	NaN ¹	c	Y	Y	N	[7]	[21]
Open fibre cavities	2.5×10^5	1.3×10^5	o	N	N	Y	[43]	[32]
Bottle resonators	3.6×10^8	NaN ¹	c	Y	Y	N	[44]	[34]
Micro cavities in silicon	9.6×10^6	5×10^5	o	Y	Y	Y	[45]	[1]

Cavities are used to increase the coupling between light and matter. As shown before, microcavities also bring the advantage of a high cooperativity. Many applications can profit from our microcavity design due to its scalability, the high finesse and the strong field gradient.

A typical application for the open microcavity design presented in this thesis would be the sensing of molecules in a gas or fluid [46, 47]. The cavities can also be used

¹ These cavities are designed only for one wavelength and the FSR is not measured. This makes it difficult to find a corresponding finesse.

for the detection of bigger objects like dust particles [48], pollen or biological samples including living cells [49].

Optical cavities are crucial parts of lasers. The high scalability of our micro cavities offers a way to create a multi laser array, optical gain could for example be provided by a fluid [50] or nanocrystals [51]. If one could individually control the cavity length and the vertical position of each cavity, the wavelength and the phase of each laser can be adjusted, allowing full control over the emitted waveform. In fact, arrays of independently tunable microcavities have been shown before using electrical deflection of cantilevers [41].

Cavities change the boundary conditions in a way that a single photon emitter preferentially emit the photon into a cavity mode, which means a that stream of single photons can be generated. A triggered single photon source becomes possible, which would be extremely useful in quantum optics and quantum technology.

The detection and cooling of nano particles [52] is the first real-world application of our microcavity design, this work is presented in chapter 8 and in [53]. The idea here is to use the cavity field to reduce the kinetic energy of the particle. In the future we want to perform matter wave interference experiments with these low-energy nano particles.

In conclusion, we are confident that our microcavity design is a versatile platform which can become useful for many applications in applied and fundamental science.

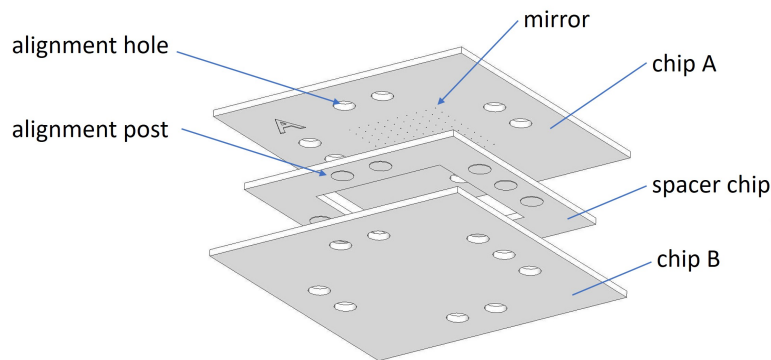


Figure 1.10: Drawing of the design of our silicon microcavities. The mirrors are located on the top (A) and the bottom chip (B). Each chip has an array of 100 mirrors etched into the silicon. The spacer chip separates the mirror chips. The alignment holes on the mirror chips fit precisely to the posts on the spacer chip. This guarantees the best possible alignment.

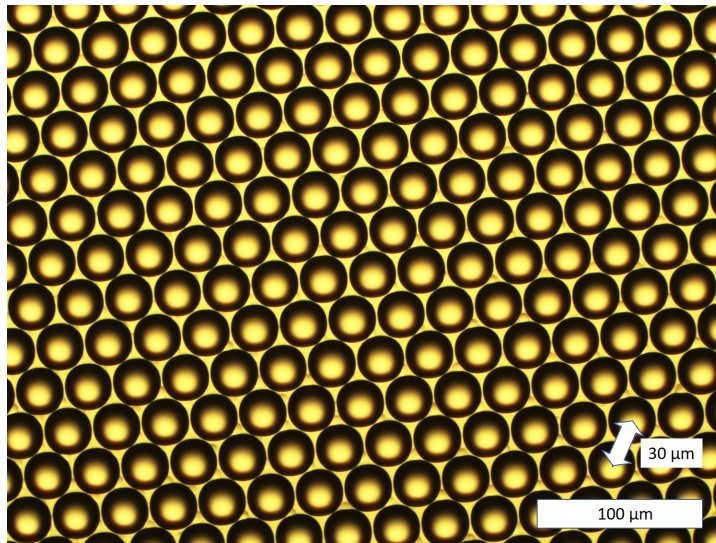


Figure 1.11: Microscope image of densely packed cavity mirrors. The spacing between the mirrors is $30\ \mu\text{m}$. In this arrangement, we have tested how dense we can make the cavity arrangement before our manufacturing process fails. As can be seen from the image, the mirrors can be packed tightly and the number of mirrors is only limited by the chip size.

1.4 Structure of this thesis

This thesis is structured as follows: I will start with a discussion of Gaussian optics and the general properties of cavities in chapter 2. Chapter 3 presents numerical simulations of different mirror shapes. Chapter 4 takes the reader through the complete design process of the microcavity chips. In chapter 5, the manufacturing process is covered. The measurements on the completed microcavities are presented in chapter 6. In chapter 7 cavity experiments with a dielectric layer are discussed as a first step towards more advanced cavity experiments. The detection of nano particles as a first application is shown in chapter 8. All results are summarized in 9, where I also give an outlook on future experiments and developments.



Die approbierte gedruckte Originalversion dieser Dissertation ist an der TU Wien Bibliothek verfügbar.
The approved original version of this doctoral thesis is available in print at TU Wien Bibliothek.

CHAPTER 2

Theoretical background

This chapter summarizes the theoretical background required to understand the electromagnetic field in optical microcavities. We start with a discussion of the paraxial wave equation (sec. 2.1), which guides us to Gaussian optics in section 2.2 as a model for a laser beam. Subsequently the Hermite-Gaussian beam (section 2.3) and the Laguerre-Gaussian beam (section 2.4). In section 2.5, we discuss the properties of optical cavities, most importantly the linewidth, the finesse, the Q-factor and the free spectral range.

The theory presented in this chapter is covered by many text books We closely follow [54] in our derivations. A comprehensive understanding of the field inside a cavity is required to correctly interpret the results from the experiment. We also use the theory covered here to get exact solutions for the field equations to simulate the finesse of non-parabolic mirrors in chapter 3.

2.1 Paraxial Wave Equation

Ray optics are a greatly simplified way to describe optical beams. A more realistic description is the paraxial wave approximation. The idea is to describe the light in the form of a wave function. This equation is fit into the wave equation and with the slowly varying envelope approximation the paraxial wave equation can be derived. For this purpose, the electric field component $E^{(+)}(r)$ of the light is described as a wave by:

$$E^{(+)}(r) = \Psi(r)e^{ikz} \quad (2.1)$$

Ψ is the envelope and e^{ikz} the carrier wave. Equation 2.1 is now plugged into the wave equation:

$$(\nabla^2 + k^2) E^{(+)} = 0, \quad (2.2)$$

which brings us to the following form:

$$\left(\nabla_r^2 + i2k \frac{\partial}{\partial z} + \frac{\partial^2}{\partial z^2} \right) E^{(+)} = 0, \quad (2.3)$$

where

$$\nabla_r^2 = \frac{\partial^2}{\partial x^2} + \frac{\partial^2}{\partial y^2} \quad (2.4)$$

is the transverse Laplacian. If Ψ changes negligibly on length scales of λ , the wavelength of the light, we can make the following simplification:

$$\frac{\partial \Psi}{\partial z} \ll \frac{\Psi}{\lambda} \quad (2.5)$$

which can be rewritten as

$$\frac{\partial \Psi}{\partial z} \ll k\Psi. \quad (2.6)$$

Now the second derivative becomes:

$$\frac{\partial^2 \Psi}{\partial z^2} \ll k \frac{\partial \Psi}{\partial z} \quad (2.7)$$

These simplifications and assumptions are called the slowly varying envelope approximation. The result is the paraxial wave equation:

$$\left(\nabla_r^2 + i2k \frac{\partial}{\partial z} \right) \Psi = 0 \quad (2.8)$$

A simple solution of this equation is the plane wave in the form of $\cos(kx - \omega t)$. Our optical cavities however impose curved boundaries. This is the reason why we introduce the Gaussian beam as a solution of equation 2.8 at this point. The Hermite-Gaussian beam and Laguerre-Gaussian beam discussed further down are more sophisticated solutions for this equation.

2.2 Gaussian beam

The typical way to think about a laser beam is to use Gaussian optics, where the laser beam is described as a transversal wave with a Gaussian amplitude dependence in transversal direction. The Gaussian beam is the simplest model of a directed beam that satisfies Maxwell's equations in the form of the paraxial wave equation 2.8. It is also the simplest case of a "Transversal Electromagnetic Mode" (TEM) wave, where both the electric and the magnetic field are perpendicular to the direction of the beam. The electric field for a beam traveling in the $+z$ direction can be written as:

$$E^{(+)}(r) = E_0^{(+)} \frac{w_0}{w(z)} \exp \left[-\frac{r^2}{w^2(z)} \right] \exp \left[ikz - i \cdot \tan^{-1} \left(\frac{z}{z_0} \right) \right] \exp \left[ik \frac{r^2}{2R_1(z)} \right] \quad (2.9)$$

This equation uses polar coordinates ($r = \sqrt{x^2 + y^2}$). $E_0^{(+)}$ is the overall field-amplitude. z_0 is a constant called the Rayleigh length, the distance from the beam waist where the peak amplitude has dropped by $1/\sqrt{2}$. The assumptions here are symmetry around the beam axis and a transverse field distribution that can be described with a single Gaussian shape. An other assumption is that the wave front has the shape of a sphere and can be described by $R_1(z)$. These assumptions are met by most laser beams.

2.3 Hermite-Gaussian beam

A general solution of the paraxial wave equation (eq. 2.8) can be written as a sum over all different modes of the form:

$$E_{l,m}^{(+)}(r,z) = E_0^{(+)} \frac{w_0}{w(z)} \sqrt{\frac{1}{2^{l+m} l! m!}} H_l \left[\frac{\sqrt{2}x}{w(z)} \right] H_m \left[\frac{\sqrt{2}y}{w(z)} \right] \cdot \exp \left[-\frac{r^2}{w^2(z)} \right] \exp \left[ikz - i(1+l+m) \tan^{-1} \left(\frac{z}{z_0} \right) \right] \exp \left[ik \frac{r^2}{2R(z)} \right] \quad (2.10)$$

H_l and H_m are the Hermite polynomials, l and m are positive integers. Some interference patterns of these polynomials can be found in figure 2.1. All the other variables are the same as for the Gaussian beam, which is the special case $l = 0$ and $m = 0$ of this general solution. This solution appears for rotationally symmetric problems with only one maximum in the center which can be described by a Gaussian shape. For this case all the other modes are zero and only the $TEM_{0,0}$ survives. For a more complex situation, the field is described as a sum over all modes which are non-zero. For a general solution the number of necessary modes can be incredibly large. So it is important to choose the coordinate system carefully and use all possible symmetries in the problem. For this purpose the field can be also described in polar coordinates, as discussed in the following section.

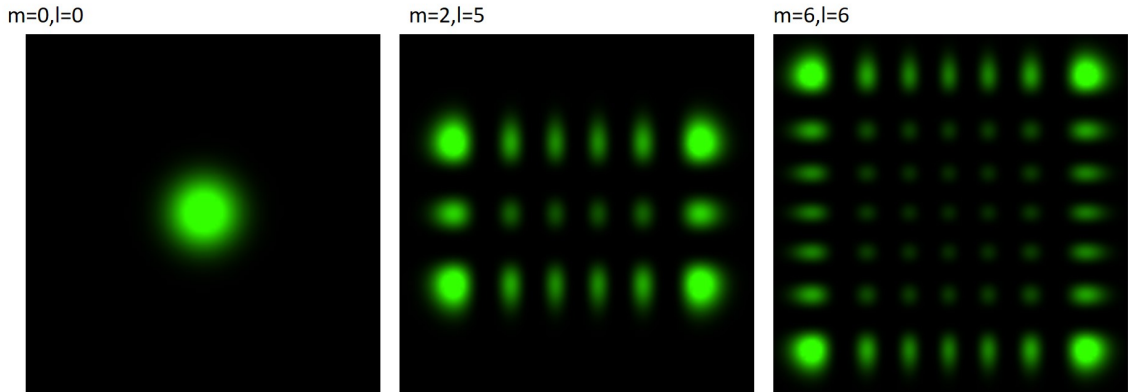


Figure 2.1: Product of Hermite polynomials $H_l \cdot H_m$.

2.4 Laguerre-Gaussian beam

The Laguerre-Gaussian beam is a general solution of the paraxial wave equation in cylindrical coordinates. Because laser beams and also the cavities in this thesis are approximately rotationally symmetric, Laguerre-Gaussian beams are used for the numerical simulations in chapter 3. They are defined as

$$E_{l,m}^{(+)}(r,z,\phi) = E_0^{(+)} \sqrt{\frac{2l!}{\pi(l+|m|!)}} \left(\frac{\sqrt{2}r}{w(z)}\right)^{|m|} L_l^{|m|} \left[\frac{2r^2}{w^2(z)}\right] \cdot \exp\left[-i(2l+|m|)\tan^{-1}\left(\frac{z}{z_0}\right)\right] e^{im\phi}. \quad (2.11)$$

In contrast to the Hermite-Gaussian modes, l and m have to follow:

$$l \geq 0 \quad (2.12)$$

and

$$|m| \leq l \quad (2.13)$$

L_l^m are the associated Laguerre polynomials, an interference pattern can be found in figure 2.2. The size difference between the interference pattern $m=0, l=0$ and $m=0, l=1$ is huge, a factor of 2 in radius (or 4 in area). This is the reason why scattering into higher modes has to be avoided as we will see later in the numerical simulations.

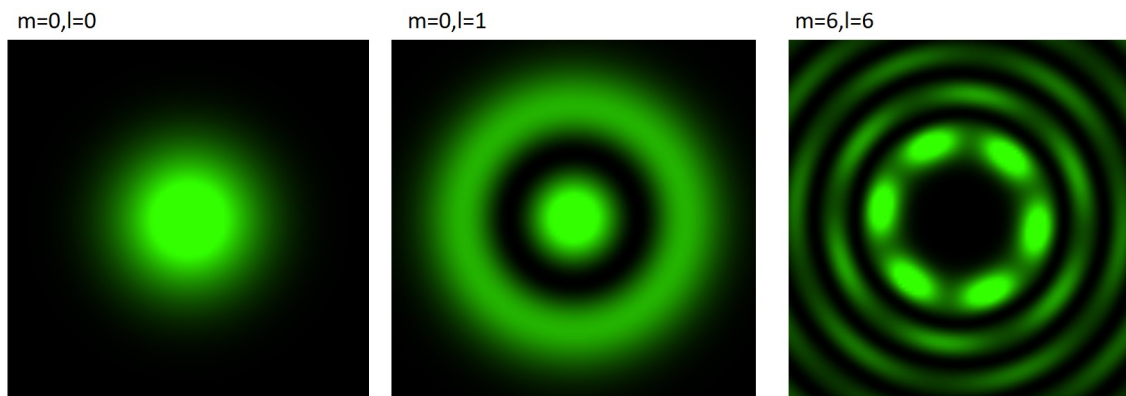


Figure 2.2: Intensity distribution for a selection of Laguerre polynomials.

2.5 Cavity theory

In this section we discuss the different values which we can calculate for an optical cavity setup. A cavity is a system of mirrors facing each other. When the electromagnetic waves in such a system interfere constructively, a resonance occurs. This condition is fulfilled for plane two mirrors if the cavity length L is:

$$L = m \frac{\lambda}{2} \text{ with } m = 1, 2, 3 \dots \quad (2.14)$$

Most experiments work with this resonance peak of a cavity. Only when on resonance, light can enter the cavity efficiently.

2.5.1 Free spectral Range

The free spectral range (FSR) is the frequency difference $\Delta\nu_{FSR}$ between two resonances of the same mode (typically the fundamental (00) mode):

$$\Delta\nu_{FSR} = \frac{c}{2L} \quad (2.15)$$

It depends only the cavity length L , c is the speed of light. From the FSR, the length of a cavity can be calculated:

$$L = \frac{c}{2\Delta\nu_{FSR}} \quad (2.16)$$

For the cavities designed in this thesis, the FSR can easily be measured. It is used to calculate the length and finesse. In table 2.1, typical values for different cavity lengths are shown and this dependence is plotted in 2.3.

Table 2.1: FSR for typical microcavity lengths in air.

Length of the cavity	$\Delta\nu_{FSR}$
600 μm	0.249 THz
300 μm	0.499 THz
150 μm	0.99 THz
30 μm	4.99 THz
15 μm	9.99 THz

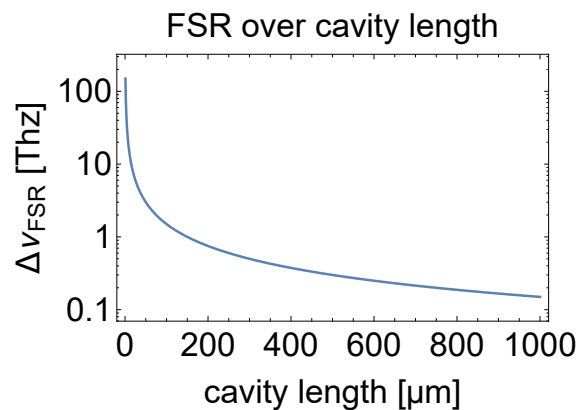
2.5.2 Resonance linewidth

The next important value is the resonance linewidth $\Delta\nu$. This is the spectral width (FWHM) of the peak during a scan over the resonance. This peak width appears because of losses inside the cavity or in other words, because of the finite lifetime of the photon inside a cavity.

There are several loss channels: roughness, alignment, shape causing scattering into higher transverse modes and the output channel. If roughness, alignment and shape are perfect, the only loss channel is the output channel. It is necessary for any functional cavity to have some light going into the cavity and, because this path can be used in both directions, this is also a loss channel.

2.5.3 Finesse

In the last section we argued that the peak width is a good indicator for the quality of a cavity because if the peak width gets small, the loss factors are also small. However, the width also scales with the length of the cavity and this makes it difficult

**Figure 2.3:** FSR versus cavity length.

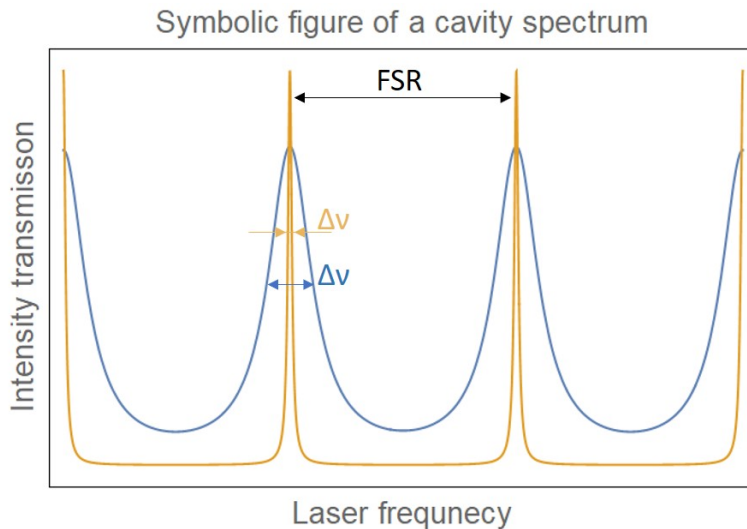


Figure 2.4: Transmission spectra of two cavities. Both cavities have the same length and for that reason the same FSR. The cavity with higher reflectivity (orange) exhibits narrower resonance peaks, due to a longer photon lifetime inside the cavity.

to compare two different cavities. Here the finesse \mathcal{F} comes into play. It is defined in the following way:

$$\mathcal{F} = \frac{\Delta\nu_{FSR}}{\Delta\nu}. \quad (2.17)$$

The idea of the finesse is to multiply the inverse peak width with some factor to compensate for the dependence of the peak width on the cavity length. Because it is very difficult to measure the length directly, the FSR is used instead. The FSR depends only on the length and is easily measured. The finesse is only dependent on the losses inside the cavity. It is the ideal parameter to compare different cavities or cavity concepts.

Another definition of the finesse is:

$$\mathcal{F} = \frac{\pi\sqrt{\mathcal{R}}}{1-\mathcal{R}}, \quad (2.18)$$

In this formula, \mathcal{R} is the effective round trip reflectivity of the electric field, accounting for all loss channels.

The lifetime of a photon can be calculated in the following way:

$$P(n) = P_s^{n-1}(1 - P_s), \quad (2.19)$$

where $P(n)$ is the probability of surviving n round trips and P_s the survival probability for one round trip. Now it is possible to show that:

$$\langle n \rangle = \sum_{n=1}^{\infty} nP(n) = \frac{1}{1 - P_s} \quad (2.20)$$

Where $\langle n \rangle$ is the average number of round trips that a photon survives. The time for one round trip is $\tau_{rt} = 2d/c$ or more generally:

$$\tau_{rt} = \frac{1}{\Delta\nu_{FSR}} \quad (2.21)$$

Now the average life time is calculated as product of one round trip time and the average number of trips:

$$\tau_p = \tau_{rt} \langle n \rangle = \frac{1}{\Delta\nu_{FSR}(1 - P_s)} \quad (2.22)$$

Because we are interested in "good" cavities, we calculate the limit $P_s \rightarrow 1$. The survival probability is equal to the squared field reflection coefficient, $P_s = \mathcal{R}^2$. The finesse \mathcal{F} can now be written in terms of the survival probability:

$$\mathcal{F} = \frac{\pi P_s^{1/4}}{1 - \sqrt{P_s}} \quad (2.23)$$

For $P_s \rightarrow 1$, we can use the following approximations:

$$P_s^{1/4} \approx 1 \quad (2.24)$$

and

$$(1 - P_s) = (1 - \sqrt{P_s})(1 + \underbrace{\sqrt{P_s}}_{\approx 1}) \approx 2(1 - \sqrt{P_s}) \quad (2.25)$$

Now we can write the finesse as:

$$\mathcal{F} \approx \frac{\pi}{1 - \sqrt{P_s}} \approx \frac{2\pi}{(1 - P_s)} \quad (2.26)$$

By using this expression in equation 2.22 for the survival time brings us to:

$$\tau_p \approx \frac{1}{2(\Delta\nu_{FSR})(1 - \sqrt{P_s})} = \frac{\mathcal{F}}{2\pi\Delta\nu_{FSR}} \quad (2.27)$$

Thus we arrive at an "uncertainty relation"

$$\tau_p \Delta\nu = \frac{1}{2\pi} \quad (2.28)$$

for optical cavities. This formula shows that for high finesse cavities the line width of the resonance peak is directly proportional to the inverse lifetime.

The other insight here is that the line width must change with the length of the cavity. This can be understood in the following way: if the cavity is longer, the photon moves along a longer path between the mirrors and therefore has a longer lifetime in the cavity. This results in a smaller peak width. We assume here that there are no losses due to scattering from objects inside the cavity. In figure 2.4, the resonance linewidths for two cavities with the same length but different reflectivity are shown.

2.5.4 Quality factor or Q factor

The Q factor is also a very common way to investigate the quality of a cavity. This factor is usually used in microwave cavities, or other designs where the FSR cannot be measured. There are several reasons for such a situation, for example if the cavity is designed for only one resonance, or the FSR is so high that it is impossible to reach the next peak. For the Q factor, the peak width is compared to the central frequency:

$$Q = \frac{\nu_{res}}{\Delta\nu} \quad (2.29)$$

This is usually possible because the laser frequency is well-known, and the peak width can be measured. For optical cavities, this factor can have incredibly high values. Another issue is that the Q factor depends on the length of the cavity. For our cavity design the Q factor is not a good figure of merit because of the wide variation of different cavity lengths.

2.5.5 Birefringence

In a real high-finesse cavity it is common to find birefringence. Birefringence is well known from crystals, where each polarization axis of the light behaves differently. Something similar can be found in a cavity. Due to misalignment, stress in the mirror coating or an un-symmetric shape, two radii can appear inside a cavity. Light polarized along x and y experience different boundary conditions, which results in a frequency shift between resonance frequencies for the two polarizations. Theoretically this situation can be described as two different radii R_1 and R_2 inside the cavity [33]. In

$$\Delta\nu_B = \delta\nu_1 - \delta\nu_2 = \frac{\nu_{FSR}}{2\pi k} \frac{R_1 - R_2}{R_1 R_2}, \quad (2.30)$$

the birefringence is defined in absolute terms, typical units are MHz. $\delta\nu_1$ and $\delta\nu_2$ are the frequencies of the different peaks. $\Delta\nu_B$ changes with the length of the cavity, which makes it difficult to compare different cavities to each other. Similarly to the finesse this can be solved by dividing the birefringence by the FSR.

$$\delta\phi_{rt} = \frac{2\pi\Delta\nu_B}{\Delta\nu_{FSR}} \quad (2.31)$$

In that way the birefringence of a cavity is defined as the phase shift difference per round trip. This definition gives us the ability to compare the birefringence for cavities with different lengths.

2.6 Fabry-Perot cavities

Until now, all parameters like Q factor, resonance linewidth, finesse and FSR can be found in all types of resonators. In this section we will discuss an ideal optical Fabry-Perot cavity in detail. Figure 2.5 shows two typical configurations which we use in this thesis, the flat-curved and the curved-curved configuration. We will not investigate curved-curved configurations with different R_1 on both ends, as this would go beyond the scope of this chapter.

2.6.1 Beam geometry in a Fabry-Perot cavity

For the following discussion, we assume a Gaussian beam inside the cavity, which makes it possible to calculate the beam waist for different cavity forms. The origin of z is set to the position of the smallest beam radius. This so-called "beam waist" is defined as the radius where the intensity of the field falls to $1/e^2$ of the maximum intensity. The corresponding Rayleigh length z_0 is given as:

$$z_0 = \frac{\pi w_0^2}{\lambda} \quad (2.32)$$

Because it has the smallest beam radius, the beam waist is also the position with the highest field intensity. For a cavity, this is the ideal place for an object to interact with the field. To maximize the coupling, the beam waist has to be as small as possible. The beam radius varies along the optical axis and can be written as:

$$w(z) = w_0 \sqrt{1 + \left(\frac{z}{z_0}\right)^2} \quad (2.33)$$

The radius of curvature (R_1) of the wave-front is given by:

$$R_1(z) = z \left[1 + \left(\frac{z_0}{z}\right)^2 \right] \quad (2.34)$$

To describe an ideal cavity, the radius of curvature of the wavefront has to match the radius of curvature of the mirror. Only in that case, the Gaussian beam describes the field inside the cavity correctly, otherwise more complex field distributions, as discussed in chapter 3, occur. Figure 2.6 a) shows a sketch of a Gaussian beam with all quantities discussed above. In b) the field intensity given by equation 2.9 is

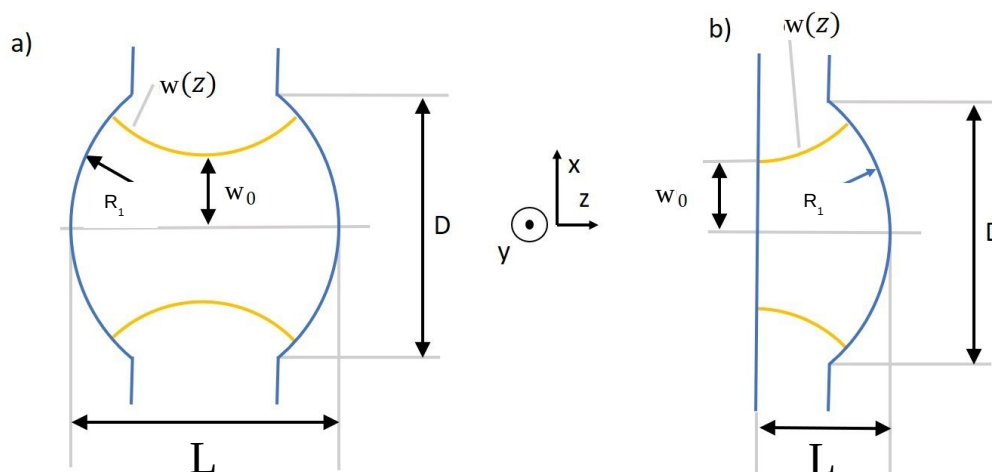


Figure 2.5: In this thesis two different cavity configurations are used. The curved-curved configuration shown in a) and a flat curved configuration shown in b). The blue lines are the mirrors. R_1 is the radius of curvature of the mirror surface. The yellow lines show the width $w(z)$ of the Gaussian beam. w_0 is the beam waist inside the cavity. D is the diameter of the cavity mirror. L is the length between the mirrors. The origin of the coordinate system used throughout this thesis is centered at the beam waist. The axis along the cavity is the z axis and the other two are x and y . A typical radius of our micro mirrors is $100\ \mu\text{m}$ to $1000\ \mu\text{m}$. The length is in the range of $15\ \mu\text{m}$ to $280\ \mu\text{m}$.

shown.

If equation 2.32 is substituted into equation 2.34, it is possible to write w_0 in terms of R_1 and L . z can be identified as L for a flat-curved configuration):

$$w_0(L, R_1) = \sqrt[4]{\left(\frac{R_1}{L} - 1\right) \frac{L^2 \lambda^2}{\pi^2}} \quad (2.35)$$

From this, w_0 and $w(z)$ can be found.

2.6.2 Cooperativity and the Purcell factor

As we have seen in the introduction (1.1.1), the Cooperativity C gives us the ability to understand how much a small cavity can increase the coupling between an object inside the cavity and the cavity field. It is defined as

$$C = \frac{2 \sigma_E}{\pi \sigma_C} \cdot \mathcal{F} \cdot \eta, \quad (2.36)$$

the quantities in this equation are discussed in section 1.1.1.

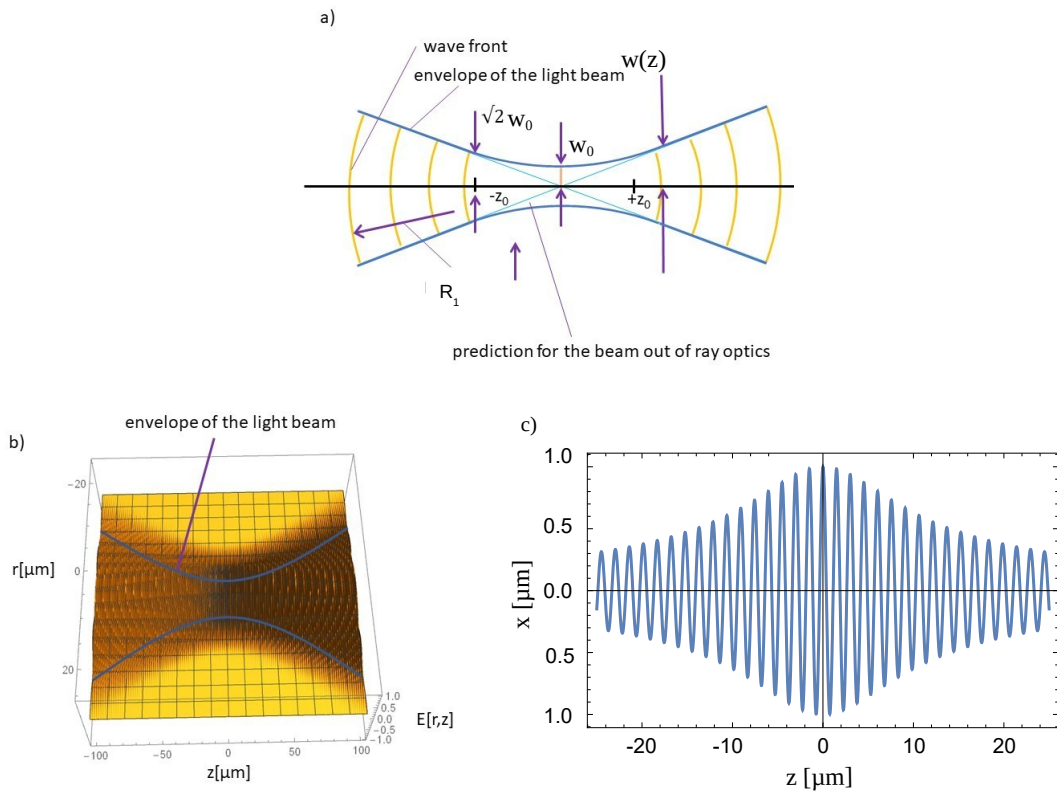


Figure 2.6: a) The quantities of a Gaussian beam between two curved mirrors with radius $R_1(z)$. b) is a 3D-plot of equation 2.9. c) is the field distribution along the z -axis.

The Purcell factor [55] is the enhancement of the spontaneous emission rate of a quantum system due to a cavity. It is defined as:

$$F_P = \frac{3}{4\pi^2} \frac{Q}{V} \left(\frac{\lambda}{n} \right)^3 \quad (2.37)$$

In this equation, Q is the Quality factor and n the refractive index. V is the mode volume of the resonator [56]. It is a measure of the volume the field is concentrated in and important to compare different cavity designs.

The Cooperativity and the Purcell factor are closely related, as both quantities describe the same physical fact: the enhancement of the light-matter interaction due to the presence of a cavity. This can be shown by rewriting the Purcell factor in terms of the cooperativity and by substituting Q and V in the formula. For simplicity we set n to one.

$$F_P = \frac{3}{4\pi^2} \underbrace{\nu_{res}}_Q \underbrace{\frac{1}{\pi w_0^2 L/4}}_{1/V} \lambda^3 \quad (2.38)$$

By identifying $\mathcal{F} = \frac{c}{2L\Delta\nu}$, $\sigma_E = \frac{3\lambda^3}{2\pi}$, $\sigma_L = \pi w_0^2$ and $\nu_{res} = \frac{c}{\lambda}$ the equation changes to:

$$F_p = 2 \frac{\sigma_E}{\pi \sigma_L} \mathcal{F} = 2C \quad (2.39)$$

Which shows that the Purcell factor is two times the Cooperativity for the case that η is one.

2.6.3 Radius of curvature measurement

As we will see later, the R_1 of a micro mirror can not be measured easily. However, from the spectrum of the cavity we can deduce the effective R_1 of its mirror. It can be calculated from the frequency difference between the $TEM_{0,0}$ and a higher $TEM_{l,m}$ mode. This is possible for an ideal case where the result is the same as in equation 2.34 and also for a non-ideal shape which results in an effective radius. The first step is to extract the phase term from the Hermite-Gaussian beam (equation 2.10):

$$\phi_{m,l}(r,z) = kz - (1+l+m)\tan^{-1}\left(\frac{z}{z_0}\right) + k\frac{r^2}{2R(z)} \quad (2.40)$$

Because we are only interested in the on-axis phase, r is set to 0 which gives us:

$$\phi_{m,l}(0,z) = kz - (1+l+m)\tan^{-1}\left(\frac{z}{z_0}\right) \quad (2.41)$$

Now the round trip phase between mirrors located at z_1 and z_2 is defined as:

$$\Delta\phi_{rt} = 2[\phi(0,z_2) - \phi(0,z_1)] = 2k(z_2 - z_1) - (1+l+m) \left[\tan^{-1}\left(\frac{z_2}{z_0}\right) - \tan^{-1}\left(\frac{z_1}{z_0}\right) \right] \quad (2.42)$$

For constructive interference, the phase change must be $\Delta\phi_{rt} = 2\pi q$ for some integer q . Solving for k and using $z_2 - z_1 = L$ transforms the equation into:

$$k_{l,m,q} = \frac{\pi}{L}q + \frac{1}{L}(1+l+m) \left[\tan^{-1}\left(\frac{z_2}{z_0}\right) - \tan^{-1}\left(\frac{z_1}{z_0}\right) \right] \quad (2.43)$$

with $k = 2\pi\nu/c$ and $\Delta\nu_{FSR} = c/2L$, the equation changes to:

$$\nu_{l,m,q} = \Delta\nu_{FSR} \left(q + \frac{1}{\pi}(1+l+m) \left[\tan^{-1} \left(\frac{z_2}{z_0} \right) - \tan^{-1} \left(\frac{z_1}{z_0} \right) \right] \right) \quad (2.44)$$

With a little algebraic digression it is possible to show that:

$$\cos \left[\tan^{-1} \left(\frac{z_2}{z_0} \right) - \tan^{-1} \left(\frac{z_1}{z_0} \right) \right] = \sqrt{(1-L/R_a)(1-L/R_b)} \quad (2.45)$$

In this equation, R_a and R_b are the radii of curvature of the cavity mirrors. This allows to rewrite the frequency as:

$$\nu_{l,m,q} = \Delta\nu_{FSR} \left(q + \frac{1}{\pi}(1+l+m) \cos^{-1} \left(\sqrt{(1-L/R_a)(1-L/R_b)} \right) \right) \quad (2.46)$$

The difference between the lowest mode and a higher mode (with the same q) can be written as:

$$\Delta\nu_{00 \leftrightarrow lm} = \nu_{0,0,q} - \nu_{l,m,q} = \frac{\Delta\nu_{FSR}}{\pi} (l+m) \cos^{-1} \left(\sqrt{(1-L/R_a)(1-L/R_b)} \right) \quad (2.47)$$

One can now invert this equation to get the radius of curvature. In this thesis, we work with two different cavity configurations. For a curved-curved configuration with $R_a = R_b = R_{1|}$ we get:

$$R_{1|} = \frac{L}{\left(1 - \cos \left(\frac{1}{(l+m)} \Delta\nu_{00 \leftrightarrow lm} \frac{2L\pi}{c} \right) \right)} \quad (2.48)$$

and for the flat-curved configuration where $R_a = \infty$ and $R_b = R_{1|}$

$$R_{1|} = \frac{L}{1 - \left(\cos \left(\frac{1}{(l+m)} \Delta\nu_{00 \leftrightarrow lm} \frac{2L\pi}{c} \right) \right)^2} \quad (2.49)$$

To recapitulate this section, the spectrum of the cavity contains a wealth of information about the cavity. The length can be calculated from the FSR, the losses can be quantified by the resonance linewidth. The finesse gives us a figure of merit for the quality of the cavity and from the frequency difference between two transverse modes it is possible to determine the radius of curvature.

2.6.4 Cavity stability

In this section, the theoretical stability limit of a cavity is discussed. The calculations are valid for perfect mirror shape and infinitely sized mirrors. In reality, both conditions are not fulfilled. Reaching even 80% of the stability limit is an excellent result for a real cavity.

The idea of the calculation is to use the ray optics [57, 58] in combination with the matrix method to search for the stability limits. One round trip can be described as:

$$\mathbb{M} = \begin{bmatrix} A & B \\ C & D \end{bmatrix} = \underbrace{\begin{bmatrix} 1 & 0 \\ -\frac{1}{f_a} & 1 \end{bmatrix}}_{\text{mirror } a} \underbrace{\begin{bmatrix} 1 & L \\ 0 & 1 \end{bmatrix}}_{\text{distance } L} \underbrace{\begin{bmatrix} 1 & 0 \\ -\frac{1}{f_b} & 1 \end{bmatrix}}_{\text{mirror } b} \underbrace{\begin{bmatrix} 1 & L \\ 0 & 1 \end{bmatrix}}_{\text{distance } L} \quad (2.50)$$

with the result:

$$\mathbb{M} = \begin{bmatrix} A & B \\ C & D \end{bmatrix} = \begin{bmatrix} 1 - \frac{L}{f_b} & L \left(2 - \frac{L}{f_b}\right) \\ -\frac{1}{f_a} - \frac{1}{f_b} + \frac{L}{f_a f_b} & \left(1 - \frac{L}{f_a}\right) \left(1 - \frac{L}{f_b}\right) - \frac{L}{f_a} \end{bmatrix} \quad (2.51)$$

\mathbb{M} is the description of one round trip through an optical cavity. The light beam starts at mirror 1, travels the distance L to the other mirror, is reflected there and goes back. $f_{1,2}$ are the focal lengths of mirror one and two. After the n^{th} round trip the equation looks like:

$$\begin{bmatrix} y_n \\ y'_n \end{bmatrix} = \begin{bmatrix} A & B \\ C & D \end{bmatrix}^n \begin{bmatrix} y_0 \\ y'_0 \end{bmatrix}, \quad (2.52)$$

$[y_0, y'_0]^T$ is the input vector of the light and $[y_n, y'_n]^T$ the vector after the last round trip.

The first step to solve this problem, is to analyze one round trip and then generalize the solution to the n^{th} step. The characteristic polynomial of

$$\begin{bmatrix} y_1 \\ y'_1 \end{bmatrix} = \mathbb{M} \begin{bmatrix} y_0 \\ y'_0 \end{bmatrix} \quad (2.53)$$

is

$$\lambda^2 - \text{Tr}(\mathbb{M})\lambda + \det(\mathbb{M}) = 0. \quad (2.54)$$

From equation 2.51 we calculate that $\det(\mathbb{M}) = 1$. Then the equation is solved for λ :

$$\lambda_{\pm} = \beta \pm \sqrt{\beta^2 - 1} \quad (2.55)$$

with $\beta = \text{Tr}(\mathbb{M})/2 = (A + D)/2$. Let's keep this result in mind and decompose $[y_0, y'_0]^T$ into its eigenvector $[y_{\pm}, y'_{\pm}]^T$ with some constant α_{\pm} :

$$\begin{bmatrix} y_0 \\ y'_0 \end{bmatrix} = \alpha_+ \begin{bmatrix} y_+ \\ y'_+ \end{bmatrix} + \alpha_- \begin{bmatrix} y_- \\ y'_- \end{bmatrix} \quad (2.56)$$

This makes it possible to write the eigenvalue equation as:

$$\mathbb{M} \begin{bmatrix} y_{\pm} \\ y'_{\pm} \end{bmatrix} = \lambda_{\pm} \begin{bmatrix} y_{\pm} \\ y'_{\pm} \end{bmatrix} \quad (2.57)$$

After one round trip we get:

$$\mathbb{M} \begin{bmatrix} y_0 \\ y'_0 \end{bmatrix} = \alpha_+ \lambda_+ \begin{bmatrix} y_+ \\ y'_+ \end{bmatrix} + \alpha_- \lambda_- \begin{bmatrix} y_- \\ y'_- \end{bmatrix} \quad (2.58)$$

and after n passes,

$$\begin{bmatrix} y_n \\ y'_n \end{bmatrix} = \mathbb{M}^n \begin{bmatrix} y_0 \\ y'_0 \end{bmatrix} = \alpha_+ \lambda_+^n \begin{bmatrix} y_+ \\ y'_+ \end{bmatrix} + \alpha_- \lambda_-^n \begin{bmatrix} y_- \\ y'_- \end{bmatrix} \quad (2.59)$$

To simplify the following considerations we write the next equation only for y_n . y'_n is calculated in the exact same fashion.

$$y_n = (\alpha_+ y_+) \lambda_+^n + (\alpha_- y_-) \lambda_-^n = \gamma_+ \lambda_+^n + \gamma_- \lambda_-^n \quad (2.60)$$

The constants are summarized into $\gamma_{\pm} = \alpha_{\pm} y_{\pm}$. Now we have all components to answer the question about the stability. Out of equation 2.55, we know that there are two kinds of eigenvalues, real and imaginary. First the real eigenvalues are covered, which means that $\beta^2 - 1 > 0$ which gets us $|\beta| > 1$. If these two results are set into equation 2.55 it is found that $|\lambda_+| > 1$ and $|\lambda_-| < 1$. Which brings us to $|\lambda_+| > |\lambda_-|$ and $|\lambda_+|^n > |\lambda_-|^n$. Let us now reexamine the solution:

$$y_n = \gamma_+ \lambda_+^n + \gamma_- \lambda_-^n \quad (2.61)$$

From the above considerations, we can see that for $n \rightarrow \infty$ the y_n diverge. That means for real eigenvalues the unstable case is found. For the case of $\beta^2 - 1 < 0$ we get $|\beta| \leq 1$ we can rewrite:

$$\lambda_{\pm} = \beta \pm i\sqrt{1 - \beta^2} \quad (2.62)$$

Now it is possible to calculate the unit modulus:

$$|\lambda|^2 = \lambda_{\pm} \lambda_{\pm}^* = \left(\beta \pm i\sqrt{1 - \beta^2} \right) \left(\beta \mp i\sqrt{1 - \beta^2} \right) = \beta^2 + (1 - \beta^2) = 1 \quad (2.63)$$

Which means that $|\lambda_{\pm}| = 1$ and also $|\lambda_{\pm}^n| = 1$. Now it is possible to define $\phi = \cos^{-1}\beta$ which make it possible to write:

$$\beta = \cos\phi \quad (2.64)$$

and this bring us to

$$\sqrt{1 - \beta^2} = \sin\phi. \quad (2.65)$$

The eigenvalues can be represented as

$$\lambda_{\pm} = \beta \pm i\sqrt{1 - \beta^2} = \cos\beta \pm i\sin\beta = \exp(\pm i\phi) \quad (2.66)$$

and out of this equation $\lambda_{\pm}^n = \exp(\pm in\phi)$. Now we can write the solution as:

$$y_n = \gamma_+ e^{-in\phi} + \gamma_- e^{in\phi} = y_{max} \sin(n\phi + \phi_0) \quad (2.67)$$

where y_{max} and ϕ_0 are constants. This last equation is obviously not divergent, so these are the stable solutions.

The condition for stable solutions is $|\beta| \leq 1$. From this and the definition of $\beta = \text{Tr}(\mathbb{M}) = (A + D)/2$, it follows that

$$|\text{Tr}(\mathbb{M})| \leq 2 \quad (2.68)$$

or

$$|A + D| \leq 2. \quad (2.69)$$

This last inequality is now used to calculate the stability limits in terms of radius and cavity length:

$$-2 \leq A + D \leq 2 \Rightarrow 0 \leq A + D + 2 \leq 4 \Rightarrow 0 \leq \frac{A + D + 2}{4} \leq 1 \quad (2.70)$$

With the definition of A and D we found:

$$\frac{A + D + 2}{4} = \left(1 - \frac{L}{f_b}\right) + \left(1 - \frac{L}{f_a}\right) \left(1 - \frac{L}{f_b}\right) - \frac{L}{f_a} = \left(1 - \frac{L}{2f_a}\right) \left(1 - \frac{L}{2f_b}\right) \quad (2.71)$$

Now is it possible to define the stability parameters:

$$g_{1,2} = \left(1 - \frac{L}{2f_{a,b}}\right) = \left(1 + \frac{L}{R_{1(a,b)}}\right) \quad (2.72)$$

Which yields the stability conditions in the form of

$$0 \leq g_1 \cdot g_2 \leq 1 \quad (2.73)$$

Figure 2.7 shows the stable region of a cavity. The geometries interesting for this thesis are: First the symmetric concentric case, here the stability limit is reached at $L = 2 \cdot R_{1(0)}$. Second the concave-planar setup where the stability limit is $L = R_{1(0)}$. That means if the cavity length is over this limit the cavity becomes unstable.

There is also a much simpler and more intuitive way to understand the stability limit for big cavity. This situation is depicted in figure 2.8. With the flat mirror in the focal point of the curved mirror, the border ray is reflected back to the opposite border of the mirror. With the flat mirror any further away, the border rays are lost from the cavity. We introduce this method because we also want to investigate cavities with a dielectric slab inside. By introducing a medium with $n > 1$ in the cavity, the focal point of the curved mirror is shifted further away, as indicated in the figure. Therefore, a cavity with a medium can be longer than an air cavity. For examples refer to chapter 7. This geometric optics picture is a simplification and can only be used for a basic understanding of the stability limit, it does not describe the beam waist inside a cavity as shown in figure 2.8.

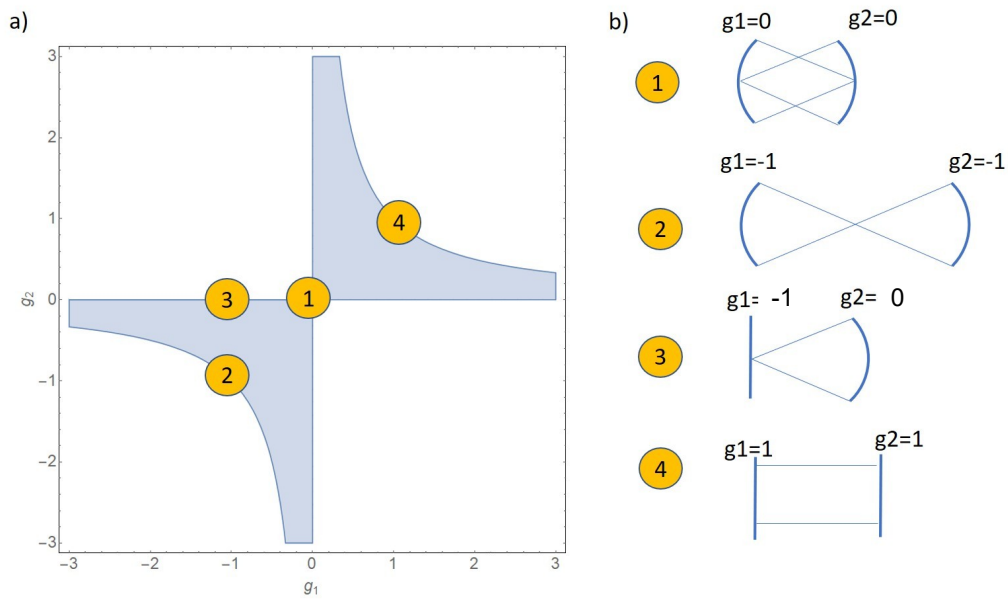


Figure 2.7: Stability plot of an optical cavity. a) The blue shaded area marks the stable region of a cavity. In b) the four special points labeled in a) are sketched. 1 is the confocal resonator with $g_{1,2} = 0$ and $R_{a,b} = -L$. 2 is the spherical resonator or symmetrical concentric resonator. It has the parameters $g_{1,2} = -1$ with $R_{a,b} = -L/2$. 3 is the Confocal planar resonator with $g_1 = 0, g_2 = 1, R_a = -L$ and $R_b = \infty$. 4 is the planar resonator.

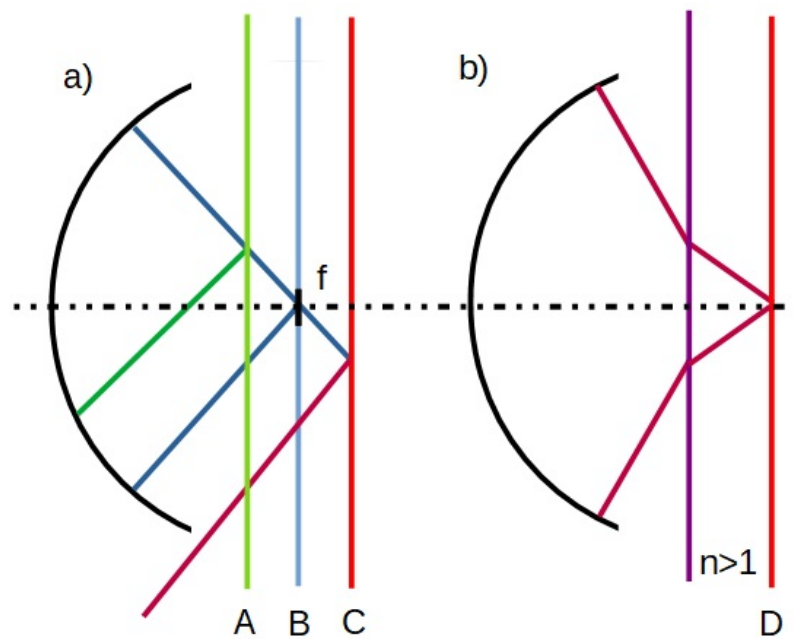


Figure 2.8: a) shows three different configurations of a flat-curved cavity. The flat mirror at position A (green) is a stable configuration, all rays are reflected back onto the curved mirror. Position B (blue) is the edge case where the border ray reflects into itself. With the flat mirror at position C (red), the cavity is unstable as light leaves the cavity. b) shows the case where a dielectric is placed inside the cavity. The plane C and D have the same distance to the mirror, but for D a stable configuration exists.

CHAPTER 3

Numerical Simulations of the EM field in a cavity

In this chapter, the well known optical modes of an ideal cavity are used to find new modes for arbitrary mirror shapes. For this calculation, Gaussian optics [59] are suitable. The new modes are used to calculate the scattering from the lowest-order mode to higher transverse modes. This loss channel predicts the maximal achievable finesse and therefore gives a figure of merit for the different mirror shapes. The algorithm is discussed in [60] and successfully used in [61] to calculate the finesse from the shape of a fibre cavity. The goal of this section is to find some tolerance criteria to distinguish between "good" and "bad" mirrors.

In the first section of this chapter, we define the effective radius of a polynomial. In the second section, the idea of the numerical algorithm is presented. Section 3.3 explains the numerical details.

In the end of this chapter, different mirror shapes are simulated: First a parabola to represent the ideal case, second a Gaussian shape because this appears in many different settings such as fibre cavities. Then the effect of an error introduced to a parabolic shape is studied. Finally, real shapes are discussed. For this purpose, a sixth-order polynomial is fitted to the atomic force microscope (AFM) measurement of a real mirror and the finesse is calculated for different cavity lengths.

3.1 Effective Radius of a Polynomial

First we need a mathematical model for the mirror shape. A spherical shape is a bad choice because the radius is the only degree of freedom. Conversely, the spherical shape is the only shape for which the radius is well defined at all positions. To get more free parameters a polynomial can be used. This can be adjusted easily to fit a real mirror shape. For this reason, it is necessary to define an effective radius for a polynomial. To find this value a half circle is defined, then developed into a Taylor series to get the corresponding polynomial. This Taylor series is compared with the original polynomial to find the effective radius.

In a half circle, the radius R is well defined:

$$C_{ir}(x,R) = R - \sqrt{R^2 - x^2} \text{ with } x \in \{-R,R\} \quad (3.1)$$

The half circle is defined in a way that the minimum is at the origin as shown in figure 3.1. The polynomial is defined as:

$$Poly(x, \vec{a}) = a_0 + a_1x + a_2x^2 + \dots + a_nx^n \quad (3.2)$$

Such a polynomial can fit easily inside a mirror shape. The difference between a circle and a second order polynomial is shown in figure 3.1. To find the effective radius of the polynomial, $Cir(x, R)$ is developed into a Taylor series around $x = 0$ up to the n^{th} order:

$$Taylor [Cir(x, R)] = \sum_{n'=1}^{n'=\frac{n}{2}} x^{2n'} \frac{\prod_{n''=0}^{n''=n'-1} (1 + n'')}{-\prod_{n'''=0}^{n'''=n'-1} (-\frac{1}{2} + n''')} \frac{1}{R^{2n'-1}} + O(n+1) \quad (3.3)$$

The explicit result is compared to a polynomial of similar form:

$$\frac{x^2}{2R_2} + \frac{x^4}{8R_4^3} + \frac{x^6}{16R_6^5} + \frac{5x^8}{128R_8^7} + \dots = a_2x^2 + a_4x^4 + a_6x^6 + a_8x^8 + \dots \quad (3.4)$$

It is visible that the coefficients R_n can be identified as the effective radius of the polynomial fit. For a perfect circle, R_2, R_4, \dots, R_n are all the same, but for a real mirror shape each value of R_n can be different. However, the theoretical description of a cavity requires a single radius of curvature to be assigned to each mirror. In the experiment, the shapes of the mirrors are either measured with an AFM or deduced from the cavity spectrum (details in section 2.6.3). For the AFM measurements, we need a way to define an effective R_1 from a polynomial fit. For this purpose, we use a parabolic fit and neglect higher orders of the polynomial, such that the radius is well defined. In fact, the paraxial approximation implies a parabolic wavefront for the Gaussian beam.

The final result is that a parabola can be defined with an effective radius of the form:

$$parabola(x, R) = \frac{x^2}{2R} \quad (3.5)$$

This form is used whenever a radius of curvature is measured.

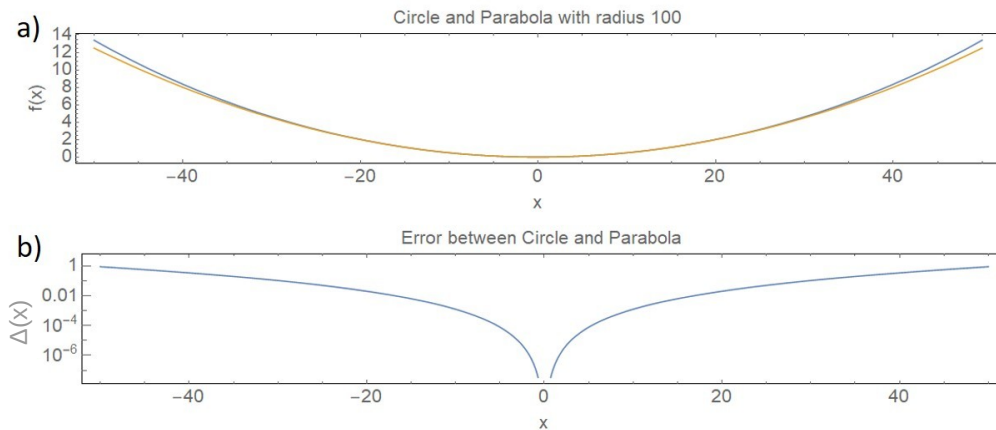


Figure 3.1: a) A circle segment (blue) and a parabola (orange). Both curves overlap very well around the origin, the difference becomes larger towards the edges. b) shows the absolute difference between the two curves.

3.2 Calculation method

This section discusses how to calculate the electromagnetic field inside a cavity for an arbitrary mirror shape [60]. For this purpose, a basis transformation is used. The idea is to use a known problem, in our case the Laguerre-Gaussian beam, and describe the new basis vectors in this old basis. After this transformation, we analyze how much light stays in the new fundamental mode. If all the light is stored in the new mode, the cavity is perfect. Any scattering into higher modes is a loss channel which reduces the lifetime of the photon inside the cavity.

The first step is to define the field $|\psi\rangle$ inside a cavity as:

$$|\psi\rangle = \sum_s C_s |\psi_s\rangle, \quad (3.6)$$

where the $|\psi_s\rangle$ are the eigenvectors and the C_s the corresponding coefficients. We are interested in the eigenvalues γ_i of the system:

$$\gamma_i |\psi_i\rangle = \mathbb{M} |\psi_i\rangle \quad (3.7)$$

The matrix \mathbb{M} is called the "mode-mixing operator"

$$\mathbb{M} = \exp(2ikl)\mathbb{A} \cdot \mathbb{B}, \quad (3.8)$$

which defines the geometry of the cavity. $\exp(2ikl)$ is the phase shift due to the cavity length, \mathbb{A} and \mathbb{B} describe the mirror geometry. These terms are discussed in more detail later. From the eigenvalues, the power loss per round trip of each mode is calculated:

$$\delta_i = 1 - |\gamma_i|^2 \quad (3.9)$$

The loss δ_i can be rewritten as an effective reflectivity, which determines the finesse \mathcal{F} given by equation 2.18 under the assumption of perfectly reflecting mirrors:

$$\mathcal{F} = 2\pi/\delta_i \quad (3.10)$$

This is the simple idea of the calculation. The only necessary ingredient is \mathbb{M} . Figure 3.2 shows the cavity which we want to calculate. \mathbb{A} represents a curved mirror with a radius of r_A or a more complex shape described by $\Delta_a(\rho, \Phi)$. The origin of the coordinate system is set in a way that the phase shift from the mirror shape is always positive. \mathbb{B} describes a flat mirror which means that $\mathbb{B} = \mathbb{1}$.

The matrix $\mathbb{A}_{s,t}(z)$ describes the scattering from mode $s = (n, m)$ to mode $t = (n', m')$ under the presence of a mirror, or vice versa [60]. Its matrix elements are given by the overlap integral of the in- and outgoing beams Ψ_t^{-*} and Ψ_s^+ over the mirror size:

$$\mathbb{A}_{s,t} = \int_0^{\rho_a} \int_0^{2\pi} \rho \, d\rho \, d\Phi \, \Psi_s^+ \, \Psi_t^{-*} \, e^{-2i\Delta_a(\rho, \Phi)} \Big|_{\zeta = \frac{z_a}{z_0}}, \quad (3.11)$$

$\rho = \frac{r}{w(\zeta)}$ is the dimensionless representation of the radius and $\zeta = \frac{z}{z_0}$ is the dimensionless representation of the coordinate along the axis. $z_0 = kw_0^2/2$ is the Rayleigh length. $w(\zeta) = w_0\sqrt{1 + \zeta^2}$ is the mode radius. The integration limit ρ_a is given by the mirror size. The beam is defined as in equation 2.11. With the above substitutions for r and z , the mode is described as:

$$\Psi_{n,m}^{\pm}(\rho, \zeta, \varphi) = N \rho^{|m|} L_n^{|m|}(2\rho^2) e^{-\rho^2 \pm i\theta(\rho, \zeta) + im\varphi}, \quad (3.12)$$

with the phase part as:

$$\theta(\rho, \zeta) = -\zeta\rho^2 + (2n + |m| + 1) \tan^{-1}\zeta. \quad (3.13)$$

$$N = \sqrt{\frac{2^{|m|+1}n!}{\pi(n + |m|)!}} \quad (3.14)$$

is the normalization constant to ensure that $\iint \rho \, d\rho \, d\varphi \, |\Psi(\zeta)|^2 = 1$.

Now all functions are defined and it is time to think under which conditions these integrals can be solved. There are two simple situations where \mathbb{A} can be calculated analytically: first, if $\Delta_a = 0$, which represents a flat mirror. For such a situation \mathbb{A} becomes $\mathbb{1}$ and all eigenvalues are 1, which means that the new and the old basis are the same. This is not a very useful test case for our numerics.

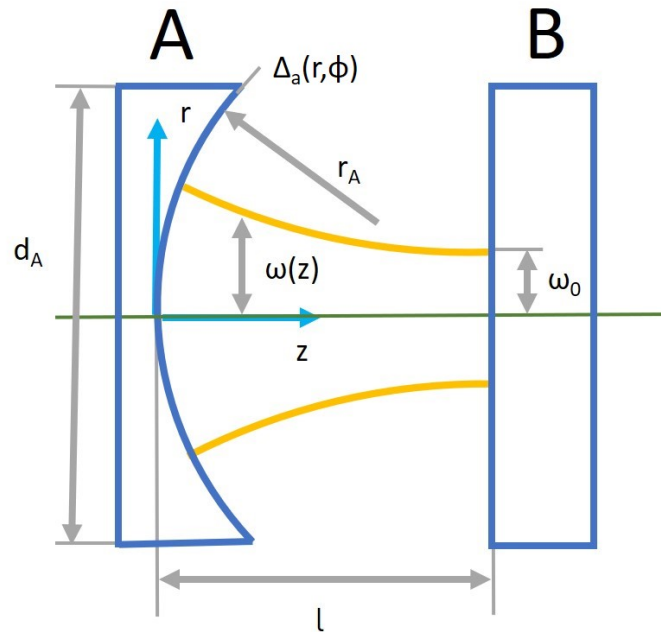


Figure 3.2: In blue the mirrors are shown. Here, a flat-curved configuration is used. The origin is at the center of mirror A. The yellow line shows the beam radius of the light field $w(z)$. w_0 is the waist of the beam. l is the length of the cavity and d_A is the diameter of the mirrors. In numerical simulations, we can work with finite size mirrors, compared to the analytical approach which always requires an integration over the radius from 0 to ∞ .

Second, the case where $\Delta_a = \frac{r^2}{2R_1}$ and $\rho_a = \infty$, which represents a parabolic mirror with infinite size. This is an interesting test case because its eigenvalues are not trivial and it can be simulated easily. This case is discussed in section 3.4.1.

3.3 Numerical Calculation

Equation 3.11 can be solved analytically in some cases, for example when the integral takes the form

$$\int_0^b \text{Poly}(x) \cdot 1 dx \quad (3.15)$$

describing a flat mirror or

$$\int_0^b \text{Poly}(x) \cdot \text{Gauss}(x) dx \quad (3.16)$$

for a parabolic mirror. The more interesting case of a more complex mirror shape

yields for example an integral like

$$\int_0^b \text{Poly}_1(x) \cdot \exp(i \cdot \text{Poly}_2(x)) dx, \quad (3.17)$$

which has to our knowledge no closed analytical solution [62]. For this purpose a numerical algorithm is used to calculate the finesse for different cavity lengths. In figure 3.3 the flowchart of the algorithm is shown.

The first step is to define all the functions and variables. As shown in the previous section all variables are known except for w_0 .

Therefore we need to search for the beam waist w_0 . For this purpose, the golden-section search [63] is used to maximize $|\mathbb{M}_{00,00}|$. This element of \mathbb{M} gives the probability that the light in mode 00 stays in 00. If the maximum of this matrix element is found, the corresponding w_0 fits the w_0 in the real world very well.

The idea here is that for an ideal cavity the scattering from the 00 to the 00 mode is one and $|\mathbb{M}_{00,00}|$ has a maximum. The same behavior is also found in the new basis.

Now we can calculate the mixing matrix $\mathbb{M} = \exp(2ikL)\mathbb{A} \cdot \mathbb{B}$. The first term defines the cavity length, the second can be calculated and the third term is $\mathbb{1}$ because we assume that this mirror is flat. The integral \mathbb{A} from equation 3.11 sums over the radius and the angle for different combinations of modes. Not every mode has an overlap with any other mode due to symmetry arguments. We are interested in the properties of a cylindrically symmetric shape which is perfectly aligned and has a finite size. Because of the cylindrical symmetry of the problem, the integration over the angle becomes:

$$\int_0^{2\pi} e^{i\varphi(m-m')} d\varphi = \begin{cases} 2\pi & \text{for } m = m' \\ 0 & \text{for } m \neq m' \end{cases} \quad (3.18)$$

This gives us the first rule: $m = m'$. Second, there is no preferred direction, scattering from s to t and from t to s have the same probability, which means only the upper half and the diagonal elements of the matrix have to be calculated. The third rule comes from the definition of the Laguerre-Gaussian beam, where the helicity is defined as ($|m| \leq n$). These three rules reduce the effort of the calculation significantly.

The next step in the calculation of \mathbb{M} is to discuss how many mode combinations have to be calculated. In principle, the mixing matrix \mathbb{M} acts on an infinitely-dimensional mode space and its eigenmodes are exact solutions. The Laguerre-Gaussian modes are similar to the expected modes of our microcavities, hence the overlap with higher order modes is expected to be small. Therefore it is enough to calculate only the first eight mode numbers in most cases to reach sufficient precision.

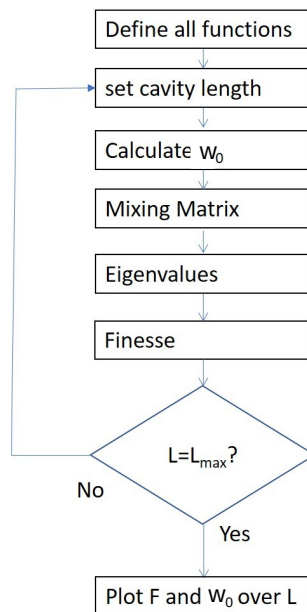


Figure 3.3: This is a simple flow sheet of the algorithm.

To solve the integral numerically, a Romberg integration [64] is used. This method has the big advantage that it allows to calculate an upper limit for the error of the integral. This is necessary because for a finesse of 1×10^6 the error in the integral has to be at most 1×10^{-7} , to be on the safe side we accept only errors below 1×10^{-8} . The high precision requires the use of 64 bit floating point variables for the real and the imaginary part of all numbers inside the integral. A 32 bit floating point is only precise up to 6 digits behind the decimal point and because of rounding this last digit is typically corrupted.

The last step is to calculate the eigenvalues and the finesse from the mixing matrix, then the entire procedure is repeated for different cavity lengths.

The main results of the calculation are three plots: w_0 , the finesse and the matrix element (00) for different cavity lengths. From the finesse plot, we get an upper limit on the cavity length, below which the cavity performs best. The matrix element tells us how much light stays inside the 00 mode and how much is scattered into higher modes.

All this information can be used to analyze the shape and to find out which divergence from the perfect shape is acceptable. This algorithm is very powerful because in general it allows to calculate the finesse of realistic cavities, including different mirror shapes, mirror sizes, alignment, roughness and all other geometrical properties which might be of interest. In this work we use this algorithm only for

cylindrically symmetric problems, but it is easily possible to investigate more complex geometries.

3.4 Example simulations

We use the simulation algorithm developed above to analyze optical cavities in a flat-curved configuration as depicted in figure 3.2. The nominal radius of curvature for these simulations is 200 μm . The first test shape is the parabola. For an infinitely sized parabola, the integrals can be solved analytically. In this example we use the results of the analytic solution to test the performance of the numerical algorithm. The second shape is a Gaussian, which appears typically for fibre cavities. For this calculation we introduce the sweep parameter s to show how a parabola performs against a Gaussian shape. The third test shape is a polynomial with quartic error. This function can easily be matched to an AFM measurement. We try here to give a limit for the quartic error for a given length. The last example treats real shapes we measured with the AFM. To simulate these shapes, a sixth order polynomial is fit to the measurements. The results of this last simulation are used in the experimental section (figure 6.7) where we compare them to real world cavities.

3.4.1 Parabola

The parabola is the perfect shape for a mirror and \mathbb{A} and w_0 can be calculated analytically. This means the parabola is the ideal test case for the algorithm. Equation 2.35 describes the expected form of w_0 for this geometry, this formula is compared to the results of the simulation in figure 3.4. The red dots from the simulation fit very well to the theoretical curve in blue, indicating that the first step of the algorithm, where w_0 is calculated, works as expected. So for a perfect shape $w_0(L)$ looks like a dome-shaped function. For other, more realistic shapes, this will change.

For a perfect shape with perfect reflectivity, the finesse is infinite over the full stable range. Because any realistic finesse is under 10×10^7 we set a limit for the finesse in the algorithm at 6.5×10^8 . This also protects us from dividing by 0 in equation 3.10 if δ_i becomes 0. In figure 3.5 the finesse of a parabola shape is shown. This step function is expected for a perfect mirror shape. The matrix element $M_{00,00}$ is one for cavity lengths below the stability limit and then quickly falls to zero.

3.4.2 Gauss

Mirrors with a Gaussian shape appear in many fibre cavities. To simulate this, we have to define an effective radius for the Gaussian. This can be done in the same way as for the parabola shape. We define the Gaussian shape with a sweeping parameter s :

$$Gauss(x,r,s) = s - s \cdot e^{-\frac{x^2}{2rs}} \quad (3.19)$$

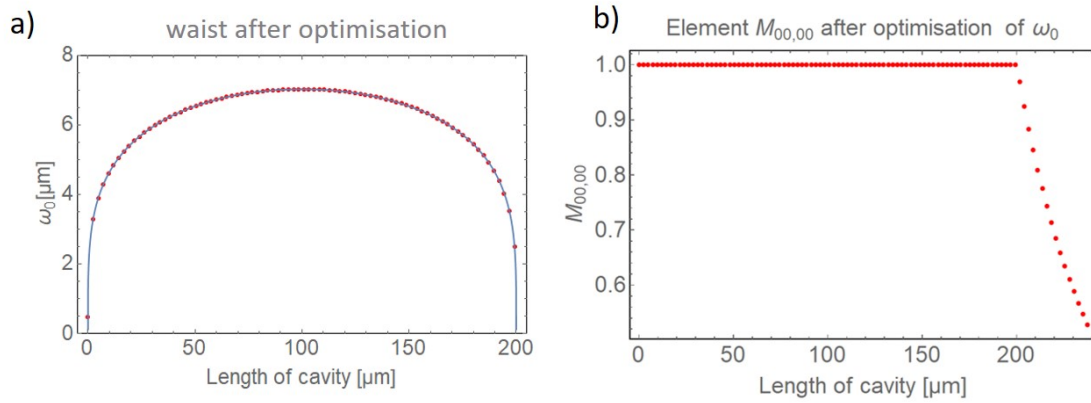


Figure 3.4: a) w_0 for different cavity lengths. The shapes used for this calculation are a parabola with a radius of curvature $200\ \mu\text{m}$ for mirror A and a flat mirror for B. To optimize the numerical results, the opening diameters are set to 6 times w_0 . The red dots are from the numerical calculation and the blue line is a plot of equation 2.35. b) shows $M_{00,00}$ versus cavity length. These plots show how well the simulation of the ideal case agrees with the theoretical results of chapter 2.

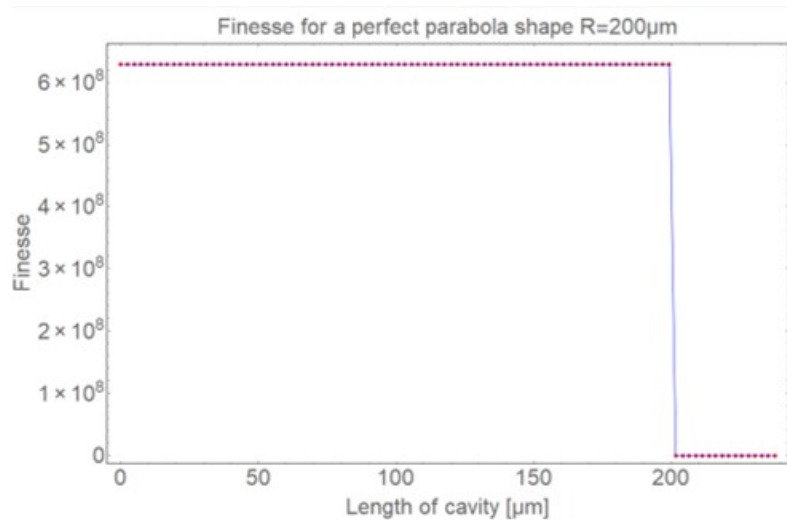


Figure 3.5: The finesse versus cavity length for a parabola shape with a radius of $200\ \mu\text{m}$. The finesse is limited at 6.5×10^8 . The red dots are from the numerical simulation, the blue line from theory.

This curve is shifted by s and flipped around such that the origin is in the middle of the mirror and the arrangement is similar to the previous example. To investigate the dependence on s we expand equation 3.19 into a Taylor series around 0 up to the fourth order:

$$\text{Taylor}(\text{Gauss}(x,r,s)) = \frac{x^2}{2r} + \frac{x^4}{8(r^2s)} + O(6) \quad (3.20)$$

For $s \rightarrow \infty$ this equation goes to $\frac{x^2}{2r}$, which is a parabola with the effective radius r . Higher order terms are proportional to $1/s^2$ or higher. The parameter s gives us the possibility to add some error at the edges of the mirror. This reflects a realistic situation where the middle part of the mirror is good and the edges are weakly distorted. If the shape in the middle of the mirror is deformed, it is impossible to produce a functioning cavity, so we do not discuss this case here. The influence of the sweeping parameter s on the Gaussian shape is shown in figure 3.6.

For the opening we choose 6 times w_0 which is a reasonable size for a mirror. For smaller openings, the influence of the opening shows up in the simulation. If parts of the modes are not reflected back on the mirror this becomes a major loss channel. For our simulation we want to investigate a non-perfect shape and a not too small mirror. In section 4.1, the limits for the opening are discussed in detail.

The next step is to simulate these different shapes. Figure 3.7 shows the results of the simulation of w_0 for different cavity lengths. w_0 follows the behavior of a perfect mirror for short cavity lengths very well. For longer cavities, w_0 deviates from the

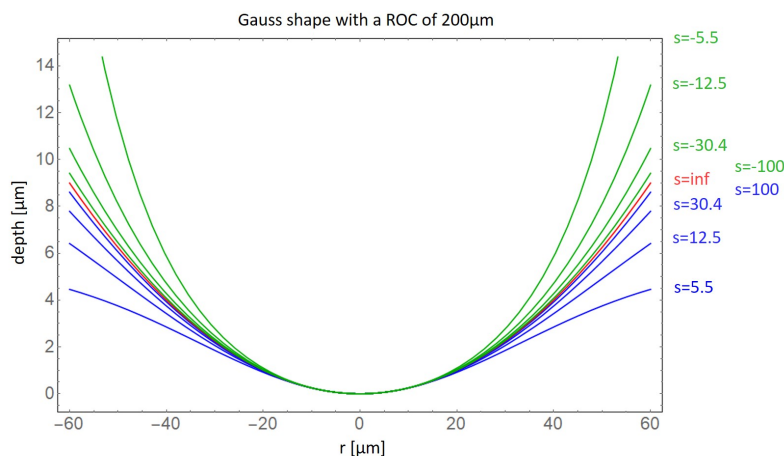


Figure 3.6: In this figure the Gaussian shapes which are used in the simulation are shown. For each function, the sweep parameter is placed on the right side. The red curve represents $s = \infty$, which means this function fits the parabola best. The blue functions are for $s > 0$ and the green for $s < 0$.

dome shape shown in figure 3.4 and at a particular point it changes its behavior completely. These results are not unexpected. For short cavities, the modes cover only a small area in the middle and cannot see the edge of the mirror. For longer cavities the deviation near the edge becomes an issue.

In figure 3.8, the matrix element $M_{00,00}$ is shown for different cavity lengths. For a perfect shape (red) this element is 1 and falls to zero if the cavity length reaches the stability limit. In this figure a massive difference between the green and the blue curves appears. The blue ones stay at 1 with a small divergence at the end. The green curves fall to a low value much earlier.

The last step in the simulation is to calculate the finesse for the different cavity shapes. These results are shown in figure 3.9. The raw data shown in a) is a bit confusing and difficult to interpret. The contour plot in b) shows the same data in a more intuitive way. The order of the s parameter on the left side of b) follows naturally from figure 3.6, the vertical distance between the horizontal lines is fixed.

The contour plot is generated by using a spline fit between the curves. Be aware that only the points along the colored lines (red, green, blue) are from the simulation and the points in between are from the fit. However, in this form the plots are easier to discuss. The red line is the parabola with a finite size. This curve is placed in the middle of b). The green lines are the shapes where the R_1 falls towards to the edge,

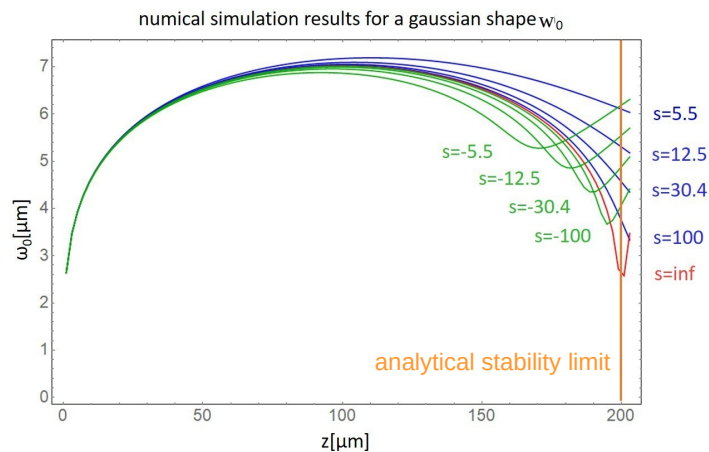


Figure 3.7: The behavior of w_0 for different cavity lengths. The red line represents a perfect, finite sized mirror. The last two points are off because of the finite size. The blue functions are for the case that the effective R_1 rises towards the edges of the mirror and the green ones are for the opposite case. The orange line represents the position where the theoretical stability limit of infinitely sized mirror would be.

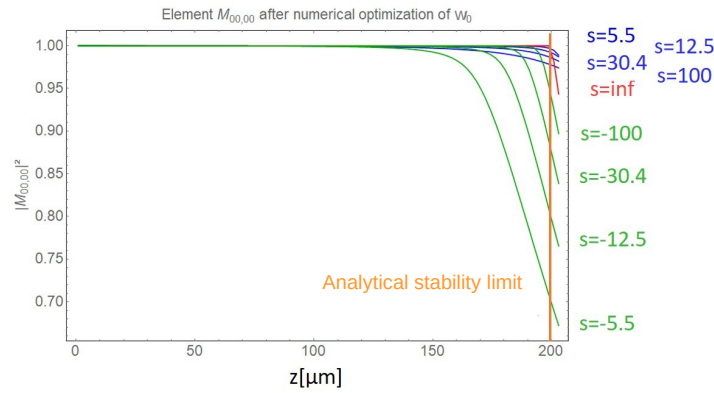


Figure 3.8: The matrix element which describes the scattering of the lowest-order mode back to itself. If this element is 1, the light stays in the lowest-order mode and exhibits no losses.

the blue lines represent shapes where the R_1 increases at the edge.

As expected, for short cavities the finesse is high. The finesse of the blue shapes drops at around 50% of the stability limit. The reason is that at this point the lowest-order mode and the next higher mode are very likely to overlap, causing a drop in the finesse. The curve with $s = 100$ allows a stable mode even beyond the stability limit. The reason for this behavior is that this non perfect shape changes the effective R_1 to a higher value which shifts this limit. This is also the reason for the asymmetry between the blue and the green curves, since the green ones shift the effective radius to smaller values and the blue curves behave in the opposite way.

For a flat-curved mirror pair with an effective R_1 of $200\ \mu\text{m}$, the shape is no issue if the length of the cavity is below 25% of the R_1 . For a higher ratio of L/R_1 , the shape begins to be an issue, as summarized in figure 3.9 b). As long as the mirror stays in the yellow area the shape is no issue, but a very fast drop appears if the shape begins to scatter the light to higher modes.

The main results of this investigation is that short cavities are less affected if the shape diverges from the ideal shape.

The Gaussian mirror shape can be found in fibre cavities (see sec. 1.2.5) because these cavities are typically manufactured by a high power laser beam. This laser beam has a Gaussian shape which melts the glass fiber end. An example can be found in [30]. These shapes have typically $s > 0$, meaning that the radius rises with the opening radius. In our etching approach we expected to find shapes with $s < 0$ because of the way the shape appears during etching. Details discussed in chapter 2.

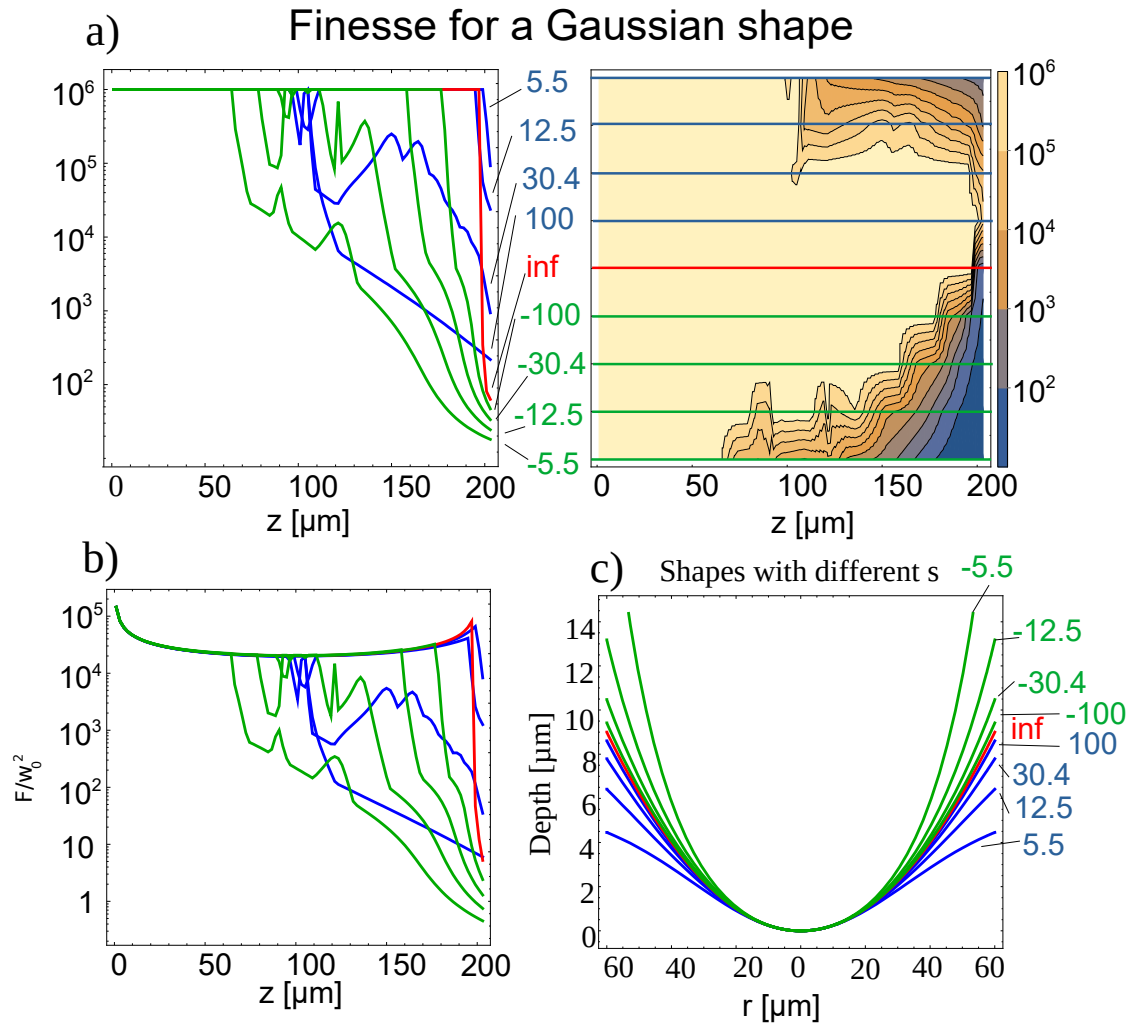


Figure 3.9: a) shows the simulated finesse for different cavity lengths of Gaussian shaped mirrors. In b) the finesse is divided by w_0^2 , which is the cavity dependent parameter in the Cooperativity (see sec. 1.1.1). Over a large range of intermediate cavity lengths, where the beam waist is almost constant, the cooperativity depends mostly on the Finesse. c) shows the different shapes used in this figure, more details are given in the text.

The Gaussian shape is an elegant solution to think about cavities, the problem is that it does not fit very well to real mirror shapes and it would be interesting to have a model where higher order correction terms can easily be implemented. For this reason a polynomial is used in the next section.

3.4.3 Parabola with error

Using a polynomial function to describe the mirror shape has two big advantages: First it is very easy to add higher order terms. Second, it can be fit easily to a real mirror shape.

In our measurements we see that it is possible to fit the mirror very well if a small positive ($s > 0$) quartic term is added to the function.

This model is the perfect choice for our mirror simulations. We simulate here a parabola with an error introduced in the quartic part. The radius of curvature is again set to 200 μm . The quartic term is diminished by a factor of 1×10^{-6} , reflecting the expected order of magnitude of the error. The shape function then looks like:

$$\text{Shape}(r; s) = r^2 \frac{1}{2 \cdot 200} + r^4 \cdot 10^{-6} s, \quad (3.21)$$

where r is the radial coordinate and s is the sweep parameter. The goal of the simulation is to draw a map for the "good" and "bad" mirrors. As shown in the last section, the boundary between these two areas is very sharp. To get this map, s is varied over a wide range. Because the polynomial inverts for $s \ll 0$, we can not go far in this direction. For $s > 0$ we can go to relatively high values to answer the question of how bad is a really bad shape. In figure 3.10 the shapes for the simulations are shown. As before, the red curve is the parabola without any aberration ($s=0$), the green shapes have an effective R_1 which is rising and the blue ones behave in the opposite way.

Again, we start with the simulation of w_0 . Figure 3.11 shows w_0 for different cavity lengths. The red curve is w_0 for a perfect parabola, like before the last point is off due to the finite size of the mirror. The green curves are shifted to slightly higher beam waists, the reason for this behavior is that their effective radius is bigger. For the blue curves we find the opposite behavior.

In figure 3.12 the matrix element $M_{00,00}$ is shown for different cavity lengths and sweep parameters. For a high finesse cavity, this matrix element has to be as close as possible to 1. For a big sweep parameter, the point where this value falls is shifted to smaller cavity lengths. This is expected because a bigger error has more effect on the shape. However, the conclusion of this figure is that the matrix element always starts at 1, which means that even for the worst case a good cavity performance can be achieved when the cavity is short.

The results of the finesse simulation are summarized in figure 3.13. We chose a

wide variation of the sweep parameter to analyze "bad" shapes. For a big error like $s=10$, a cavity still works well if it is short enough. The area of "good" mirrors is roughly given by the border of the light-yellow area in figure 3.13. It be approximated with an exponential function with s in the exponent, at least for for big values of s (approximately $s > 2$). For this range of the sweep parameter we find:

$$\mathcal{B}(s) = a \cdot e^{-s^2/b^2} \quad (3.22)$$

This line is shown in the inset to figure 3.13.

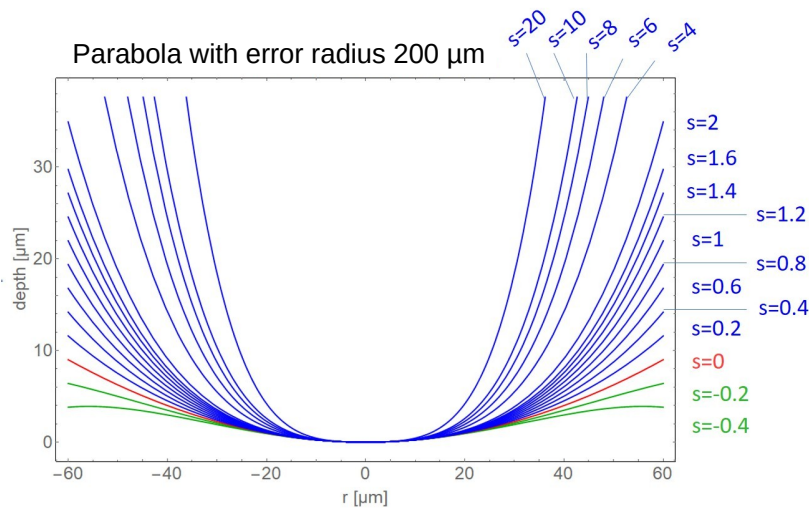


Figure 3.10: The parabolic shapes with an aberration depending on the sweep parameter s . In this and all following figures of this section, the red lines represent $s = 0$, the green $s < 0$ and the blue $s > 0$.

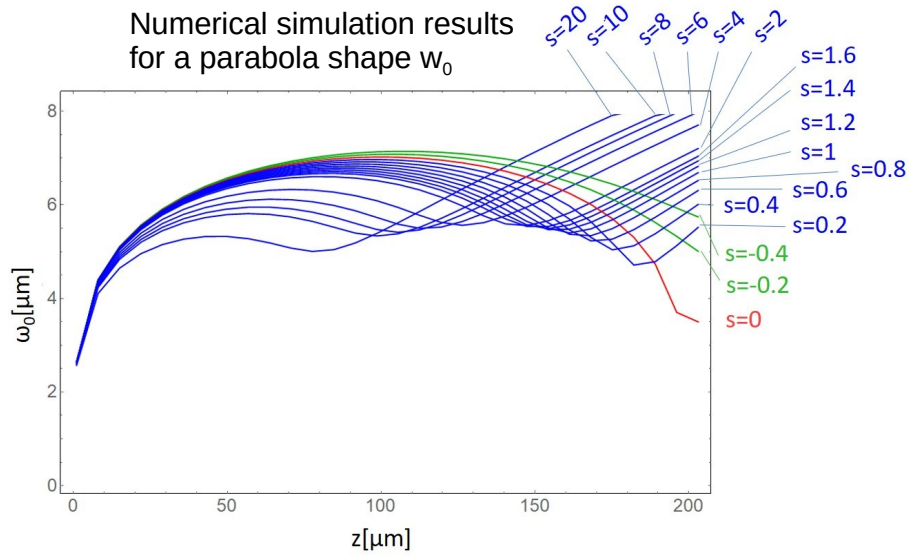


Figure 3.11: w_0 for different cavity lengths for a parabolic mirror with quadratic distortion.

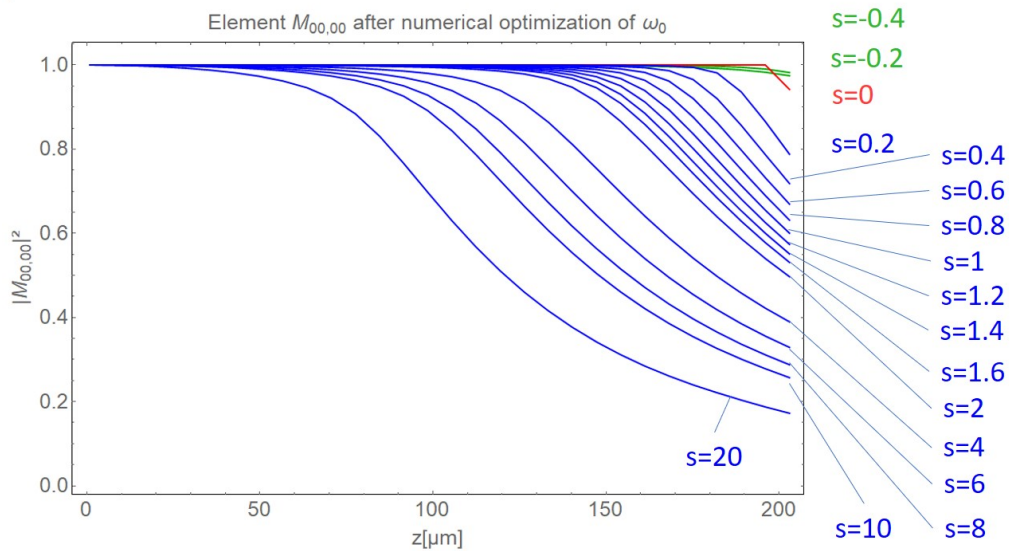


Figure 3.12: The matrix element $M_{00,00}$ for a parabola with a quadratic error. Details are given in the text.

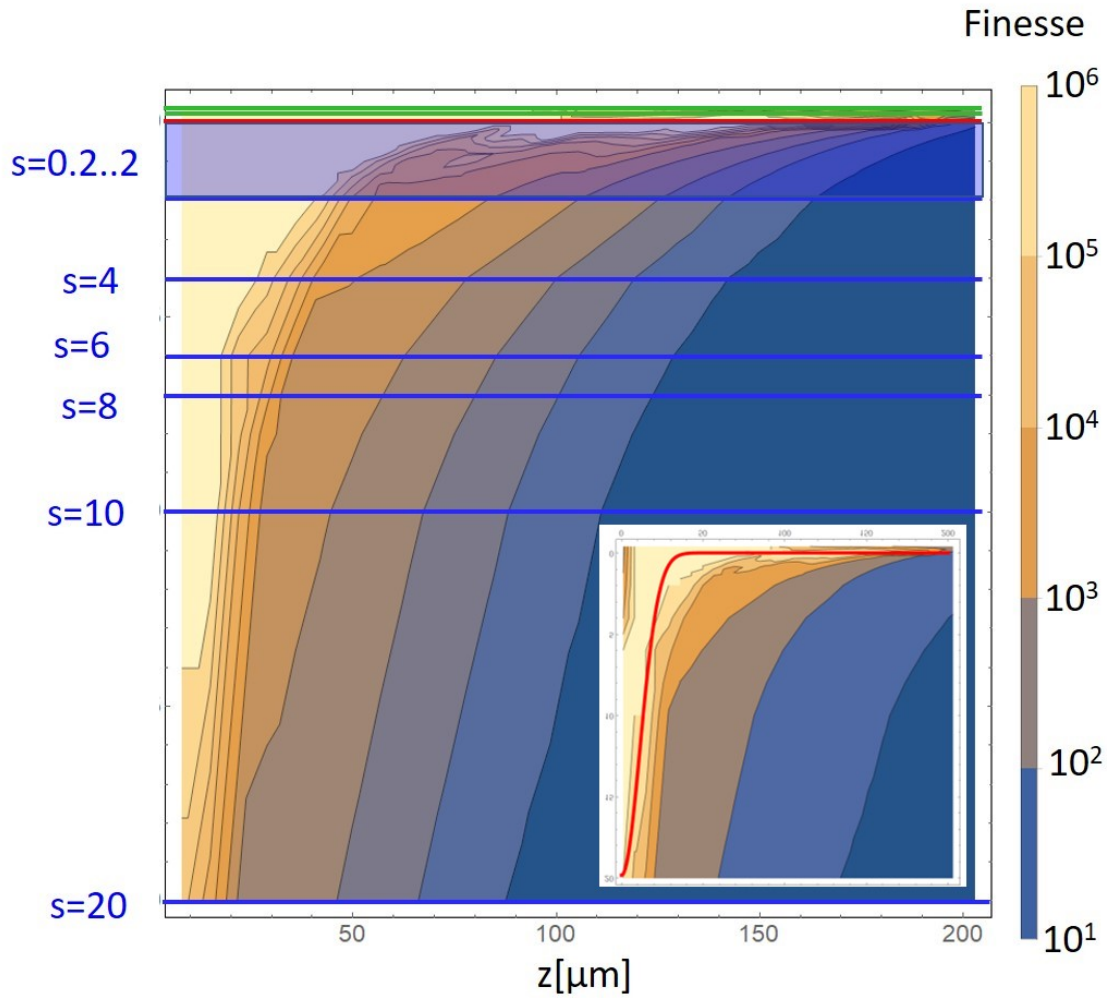


Figure 3.13: The finesse over length with a variation of the sweep parameter s . The horizontal lines indicate the simulated s values. The points between the lines are obtained using a spline fit. The color scale is the finesse in logarithmic units. The shortest simulated cavity is $5\ \mu\text{m}$ long for numerical reasons. Inset: The boundary \mathcal{B} (red line) of the region with high finesse can be approximated (for short cavities) with equation 3.22, we get $a = 19$ and $b = 16$ from a conservative fit.

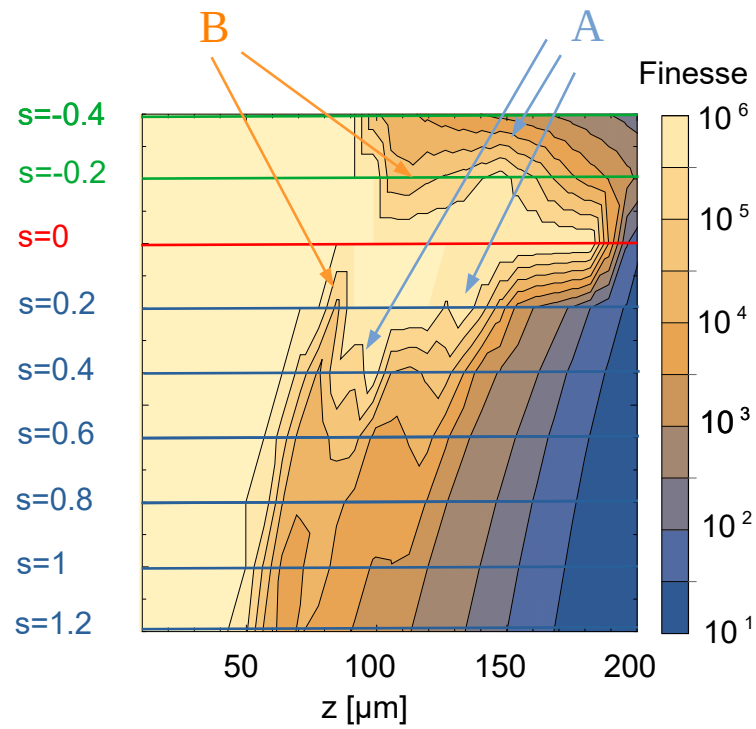


Figure 3.14: Detail of figure 3.13. The lines are the calculated curves. As discussed in detail in the text, the yellow region is the area in which the shape distortion can be neglected. A shows areas with a low coupling to higher modes and B a high coupling.

3.4.4 Real mirror shapes

In this section I present the simulation of real mirror shapes. For this purpose we fit a sixth-order polynomial to the AFM measurements of the real mirrors. Figure 3.15 shows three different mirror shapes. The simulated area is cut to $\pm 20 \mu\text{m}$ around the center of the mirror. In this area a sixth-order polynomial fits very well. These mirrors are from the first fabrication run, details can be found in chapter 6.

For the simulation, again a flat-curved cavity arrangement is used. The color code is the same in all figures. Blue is the biggest shape with a R_1 of $1660 \mu\text{m}$, the orange shape represents a medium sized curve with a R_1 of $672 \mu\text{m}$ and the green one is a small mirror with a R_1 of $114 \mu\text{m}$. These mirrors are also used in chapter 4 for the etch time calculations.

As the R_1 for these three mirrors varies over more than one order of magnitude, we introduce the relative cavity length L/R_1 as a new parameter, allowing us to compare the results. The R_1 is found from the quadratic part of the polynomial as explained in 3.1.

Similar to the previous examples, we now plot the beam waist (figure 3.16), the matrix element (figure 3.17) and the finesse (figure 3.18) for the three real shapes. In sub-figures a) to c) the results are displayed individually and in d) the simulated quantities are plotted versus the relative cavity length to make them comparable. As expected, we see that the green shape which is closest to the perfect shape is the best one and the blue one, with the largest deviation, the worst.

For a perfect shape we expect the stability limit at $L/R_1 = 1$ (see section 2.6.4). Even for the best real mirror shape (green) we reach only 50% of this value, as even small deviations from a parabolic shape cause scattering to higher modes.

The three shapes investigated here are obviously not perfect, but the data shows that it should be possible to build cavities out of them. From the finesse measurements, we can see that for the orange curve a spacer thickness (=cavity length - 2 mirror depth) of around $80 \mu\text{m}$ is needed, while the green and the blue curve require $50 \mu\text{m}$ and $20 \mu\text{m}$ respectively. For a real cavity arrangement a spacer thickness of more than $100 \mu\text{m}$ is necessary for experimental reasons. Luckily, as a rule of thumb, the high-finesse cavity length can be doubled for a curved-curved configuration.

A single chip contains 100 mirrors with varying sizes, the three shapes here are the smallest (green), one from the medium size range (orange) and the largest mirror (blue). From the simulation, we expect several working cavities with a $100 \mu\text{m}$ spacer.

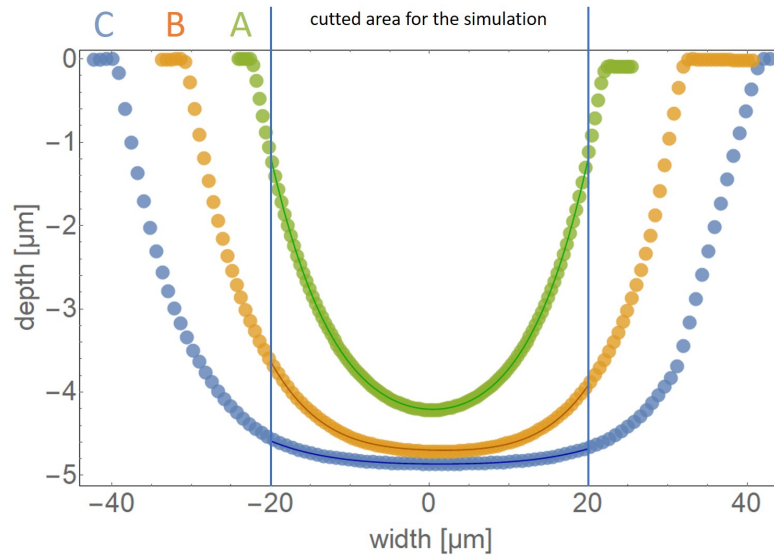


Figure 3.15: The three different mirrors used in this section. The curves are measured with an AFM. The inner portions between $\pm 20 \mu\text{m}$ are used to fit a polynomial, which is used as input for the simulation. That means for the simulation an opening diameter of $40 \mu\text{m}$ is used.

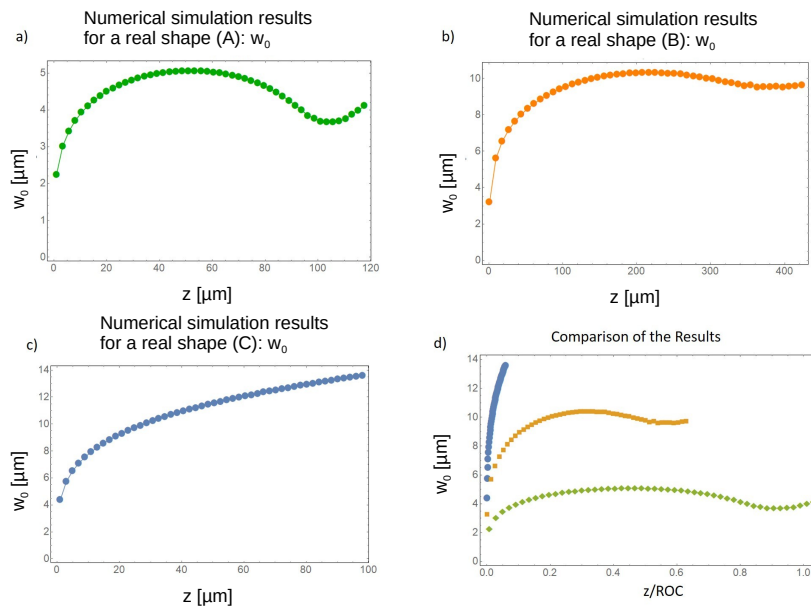


Figure 3.16: Beam waist over cavity length. a) Below $L=80 \mu\text{m}$ the curve in looks like a perfect shape, as we have seen in section 3.4.1. Above this value some divergence can be spotted. In b) and c) this point is even earlier. The comparison in d) shows the quality difference of the three mirrors.

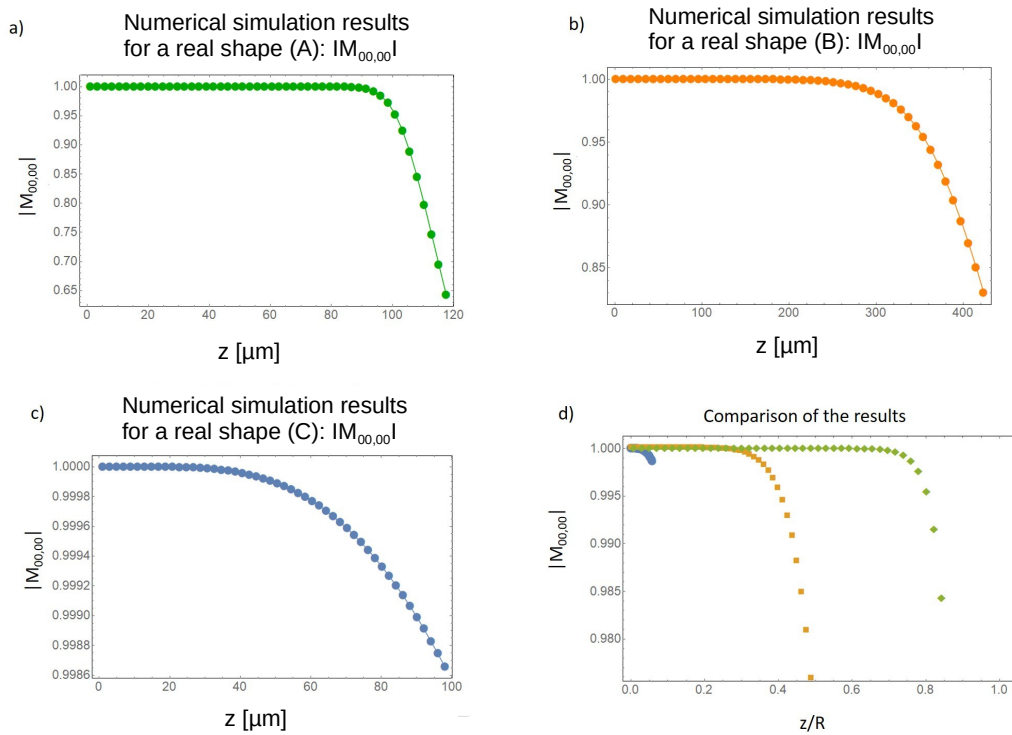


Figure 3.17: Matrix elements $M_{00,00}$ for the three shapes. Again, we see that the green curve shows the highest stability limit.

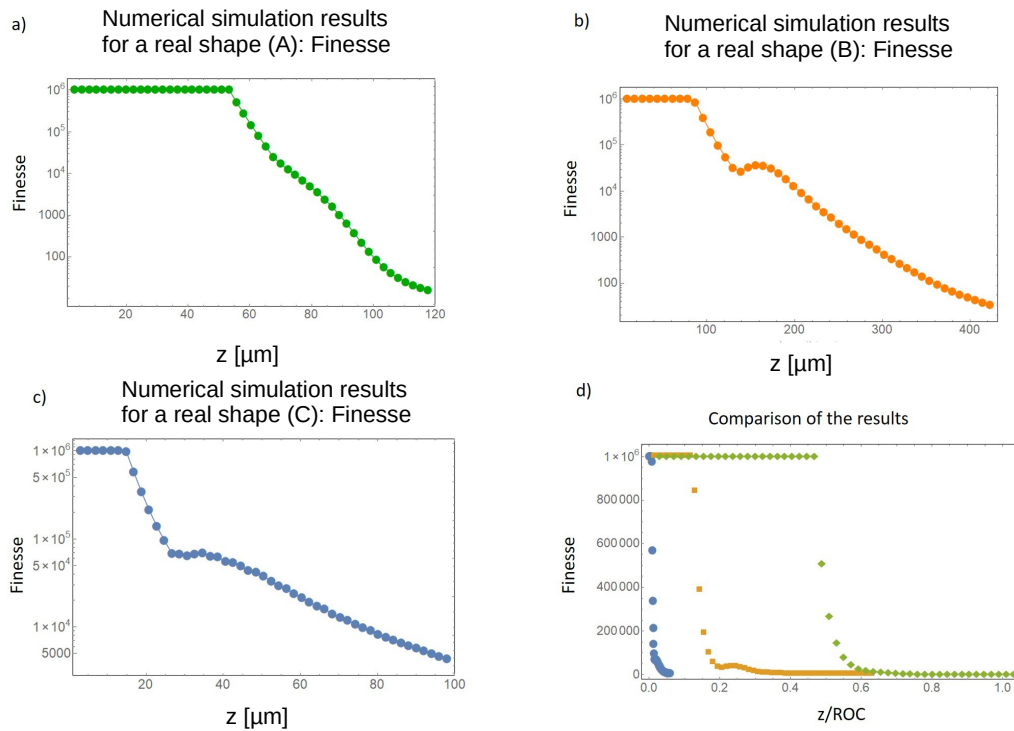


Figure 3.18: a)-c): Logarithmic plots of the simulated finesse. The finesse is limited to 1×10^6 , as a higher value would be unrealistic due to the surface roughness. This figure illustrates how quickly the finesse drops when scattering to higher modes occurs. This behavior is also observed in real cavity measurements. d) compares the different cavities.

3.5 Conclusion

Scattering of light to higher-order modes is a limiting factor in cavity performance. The numerical algorithm presented in this chapter is a powerful tool to analyze this behavior. To get the simulation running, it is necessary to measure the shape and find a suitable fitting function. This is not an easy task because for the simulation the shape in middle of the mirror influences the results drastically while the edge is less important. Typical fitting algorithms however try to fit the curve to all points as well as possible. To circumvent this problem, only the middle part of the curve is used for the fit. This makes it possible to get to the results presented in the last section.

Many improvements can be made to this algorithm. The obvious one is to solve the equation with the angular part, instead of assuming rotational symmetry. This makes it possible to analyze misalignment, which is very interesting because a tolerance for production can be given. This improvement increases the number of matrix elements which have to be calculated. The next point is to calculate two mirrors instead of just one, which doubles the calculation time. To get good results in reasonable time, it would be very beneficial to run the integration and function evaluation on a graphics card. Modern graphics cards are excellent in solving parallel tasks and the Romberg integration can be very easily parallelized. These improvements should make it possible analyze the shape of a great number of mirrors directly after they are etched. This would also require a high-throughput system to measure the cavity shapes, such as a white light interferometer.



Die approbierte gedruckte Originalversion dieser Dissertation ist an der TU Wien Bibliothek verfügbar.
The approved original version of this doctoral thesis is available in print at TU Wien Bibliothek.

CHAPTER 4

Micro mirror design

The design parameters of a micro mirror are the radius of curvature, depth of the mirror and the opening diameter. For a perfect parabolic shape, only two of these values are independent. The relevant fabrication parameters are the opening of the mask, the first and the second etch time. In this section, we will first discuss the limiting factors for our optical microcavities, then show how the etching rates are calibrated and finally go through an exemplary calculation of two micro mirrors.

4.1 Limitations

What is the maximal achievable finesse? The best ever reported cavity has a finesse of around 2×10^6 [10]. Other limiting factors are the absorption in the mirror coating and the substrate (see section 7.1). There are two ways to get good cavities:

The first approach is to shorten the cavity as much as possible. In that way the spot size of the laser on the mirror gets small. If there are imperfections in the shape of the mirror, the light will most probably not be affected by them. The alignment is also improved because of the small beam size, which fits easily on a big mirror. A drawback of these cavities is that the FSR increases to high values, which can be an issue for the mirror coating and the sweep range of the laser. The other disadvantage of these very short cavities is that usually some object should be placed in the cavity or shot through it to interact with the light. For this reason, it is necessary to have some space in the cavity of around $100 \mu\text{m}$ or more. A short cavity makes this significantly harder to achieve.

The second approach is to get a perfect shape. This is more difficult, as we must etch longer. The etching time must be long enough to come into the third regime (see appendix A for details), after reaching the minimum radius. Long etching has the drawback that the surface roughness rises. These cavities are designed for a relative cavity length L/R_1 of 0.6 to 0.9 (in curved-curved configuration). Under these conditions, the beam diameter on the mirror increases, which means that the roughness of the mirrors and their shape must be perfect over a large range. These mirrors are best suited for quantum optics applications, because in this design a smaller R_1 in combination with a smaller beam waist is achievable.

4.2 The three-fstep etch process

The whole etch process is split into three sub processes with different purposes. The first step defines the shape of the mirror, it can be simulated numerically. In the second step, the structures get enlarged to their desired size. For this part of the process some estimations can be made. In the third and last processing step, the mirror surfaces are polished to reduce scattering losses and a calculation of the required surface quality is presented. How these processes are performed in reality will be discussed in chapter 5.

4.2.1 First step: define the shape

For the first etch step, the silicon wafer is covered with photoresist. This resist is lithographically structured with 100 round holes with diameters between $12.4\ \mu\text{m}$ and $52\ \mu\text{m}$. To ensure the resist survives all the etch steps, three layers with $3\ \mu\text{m}$ each are applied. More details can be found in the chapter 5, which covers the production. The fact that there is a resist layer on most of the wafer influences the amount of available reactive atoms in the etch gas and also causes shadowing effects. The first etch step can be well described with the simulations with a certain anisotropy. The resulting shapes are onion-like, as predicted in figure A.2 a)-c) and observed in [66].

We want to fabricate parabolic mirrors with a small radius of curvature (ROC). From the simulations, we know that there is an etch time resulting in a minimal ROC. This radius and the mirror depth are defined in the first etch step.

4.2.2 Second step: amplification and opening

After defining the shape of the mirrors in the first fabrication step, we want to "amplify", i. e. enlarge the mirrors to their final size. This amplification is achieved by a second, long and isotropic etch process. For this purpose, the resist is removed from the entire wafer. This makes the etch rate more isotropic, as there is no more shadowing. The shape of the mirrors changes from onion-like as in figure A.2 b) (because of under-etching) to a more parabolic shape. During this process, the radii of the mirrors increase, as displayed in figure A.3 b).

In that way, we can reach a wide range of ROCs. The minimum radius is defined in the first step, but these surfaces are not "parabolic" enough. The maximum radius on the other side is more interesting. Theoretically, the maximum radius is limited by the thickness of the silicon wafer. In reality, the limiting factor is how clean the etch process is. A long etching time produces a lot of waste gas. This gas must be sucked out by the vacuum pump. But sometimes waste gas residue covers the wafer surface, which produces roughness on the mirror. In our longest amplification runs, we had issues with this behavior. The maximum achievable radius is given by the acceptable roughness or how good the additional polishing process is.

The first etching step defines the depth of the structure. The second step widens the diameter of the mirror and removes overhanging material left by under-etching,

if present. This step does not change the depth. For a given depth and ROC, only one opening diameter exists which fits the parabola perfectly (see figure 4.3). The optimal etch time for the amplification step can be estimated from these parameters. In chapter 4, the fabrication parameters for an example mirror are calculated.

4.2.3 Third step: polishing

As we discussed in the last section, the long amplification etching induces additional surface roughness. But how bad is roughness for the final cavities?

Scattering of light on a rough surface is physically equivalent to the scattering of radar waves from the rough surface of the sea. This problem is discussed in detail in [93]. The goal is to calculate the scattering losses of a plane wave reflected from a surface with a given RMS roughness. This is calculated by assuming a reflective grid with white noise on the grid size. In the next step, the reflected light is integrated over all directions and over all noise frequencies. This lengthy derivation results in a very elegant solution for the scattering loss l_s :

$$l_s = e^{-(4\pi\frac{\sigma}{\lambda})^2}. \quad (4.1)$$

The losses depend on the RMS roughness amplitude σ and the wavelength of the radiation λ . This result can now be used to determine the influence of the surface roughness on the achievable cavity finesse. As a reminder, it is given by:

$$\mathcal{F} = \frac{\pi\sqrt{\mathcal{R}}}{1-\mathcal{R}}, \quad (4.2)$$

where \mathcal{R} is the reflectivity of the mirror surface. By neglecting all losses other than surface scattering, we can set $\mathcal{R} = 1 - l_s$ and get a connection between the finesse and the roughness:

$$\mathcal{F} = \frac{\pi\sqrt{l_s}}{1-l_s} \simeq \frac{\pi}{(4\pi\frac{\sigma}{\lambda})^2} \quad (4.3)$$

As we neglected other loss factors such as non-ideal mirrors shape, the finesse calculated in this equation is the upper limit and will not be reached in reality. This relationship between roughness and finesse is also plotted in figure 4.1.

A roughness of below 1 nm can not be achieved without additional polishing. The process used in the course of this thesis routinely reaches a surface roughness below 0.7 nm. It is discussed in detail in section 5.4.

The lower limit in the roughness is given by the individual silicon atoms. Their covalent radius is 0.111 nm. By comparing this with figure 4.1, we see that for a

finesse on the order of 1×10^6 , the mirrors need to be smooth on the atomic scale over the full mirror size.

All the above assumptions are very conservative. Recent work [94] suggests that micro roughness on a scale smaller than the wavelength has no detrimental effect on the cavity finesse. This fits our observations from the second production run.

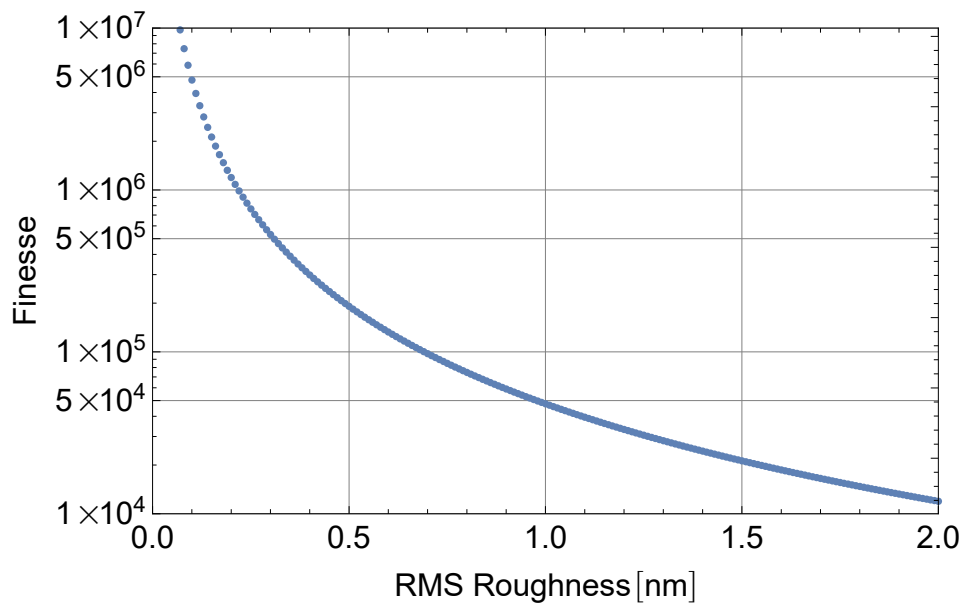


Figure 4.1: The highest possible finesse of a cavity only limited by surface roughness, assuming a wavelength of 1550 nm.

4.3 Calibration curves for etching

Calculating the correct etching times requires some measurements of the expected etching rates (η_z, η_x). It is very challenging to measure these, because they vary during the etching process and interfere with each other. After the first etch, the mirror shape looks onion-like. During the second step, the mirror is opened and the sharp edge (see for example second column in figure A.2) is etched with a high η_x . This rate slows down afterwards, when the shape becomes smoother. This situation also influences η_z , because it changes the exposed area of the mirror. After a while, when the structures are smooth and big enough, η_x and η_z should become constant.

However, to predict the mirror shape, it is necessary to approximate the etch rates. To get an idea of η_x and η_z we measure η_{za} , which is the average etch rate in z direction after the whole process. We define it as:

$$\eta_{za} = z/t_1. \quad (4.4)$$

t_1 is the first etching time and z the mirror depth. For approximating η_x we use the average opening rate, defined by:

$$\eta_{xo} = \frac{d_f - d_i}{2t_2}. \quad (4.5)$$

d_f is the final opening diameter, d_i the original opening and t_2 the second etch time. For long t_2 , η_{xo} should be a good approximation. For a full isotropic process, we expect that η_x and η_z are the same. This behavior should be also found for η_{za} and η_{xo} . However our measurements show that this is not the case, so we have to work with some anisotropy.

To get the etch rates, several wafers are etched. The first and the second etching time are varied over a wide range, using the same mask as for mirror production. The wafers are subsequently analyzed with an AFM for depth and roughness measurement and a light microscope to measure the mirror diameter. The range of the AFM we used is limited to 100 μm in x-y direction and 6 μm in vertical direction. This limits our ability to measure the depth of the mirrors, so that only the mirrors with small diameter could be fully characterized. The second etch step is expected to be very close to isotropic. Therefore the mirror depth should ideally remain unchanged. The isotropy of this process widens the mirror to its final size.

The results of the calibration runs are shown in table 4.1 and in figure 4.2. The red wafers (M1..M6) are all done in the same production run and the results are very similar. The green wafers (S1..S2) are from a later production. S1 and S2 are fabricated using a mask which has smaller openings for the first etching. Details

about the two masks used are given in section 5.1. In these small mirrors a variation in the etch rate can be observed. As an example, the etching rate η_{xo} of S1 is four times higher than for M1. In theory the etch rate should be constant over time, however reality shows that it can vary significantly. For good results a proper calibration should be done before each fabrication.

Table 4.1: Summary of the etching calibration. The depth could only be measured for the smallest mirrors¹. The etch rate η_{xo} for the M series is rather constant, as the diameters are large leading to a more isotropic etching with less shadow effects.

Wafer	T1 [s]	T2 [min]	η_{xo} nm/s	η_{za} nm/s
M1	160	16	24.6	30
M2	320	16	31.5	NaN ¹
M3	320	32	22.2	NaN ¹
M4	320	48	18.6	NaN ¹
M5	480	32	25.4	NaN ¹
M6	480	48	21.6	NaN ¹
S1	80	1.33 min or 80 s	99.2	67.6
S2	160	2.66 min or 160 s	59.2	42.9

Figure 4.3 illustrates an ideal parabolic mirror. First the required depth $t_1 = h/\eta_{za}$ must be reached. This is only true if η_{za} is measured for this opening (d_i) and the new etch time is not too far off the calibration time. If there is no calibration for t_1 available, the etch time has to be estimated assuming a low value for η_{za} .

The second etch time is calculated in a similar way: $t_2 = (d_f - d_i)/(2\eta_{xo})$. To get the mirrors into the third regime, it is necessary that the second etch time is much longer than the first etch time.

To find the right t_2 it is necessary to choose the initial diameter d_i for the lithographic mask. If it is too big, the second etch step does not have enough time to make the shape parabolic and the result is a mirror from the first or second regime. If the initial opening diameter is too small, the first etch step cannot reach the required depth. This issue is solved by manufacturing a great variation of different initial diameters. In that way at least one working mirror should be on one sample chip. This chip can then work as a reference point to find the best etch times and initial diameters for subsequent production runs. An example for this optimization

¹ We cannot measure these values at this time because the mirrors were deeper than the AFM range in z .

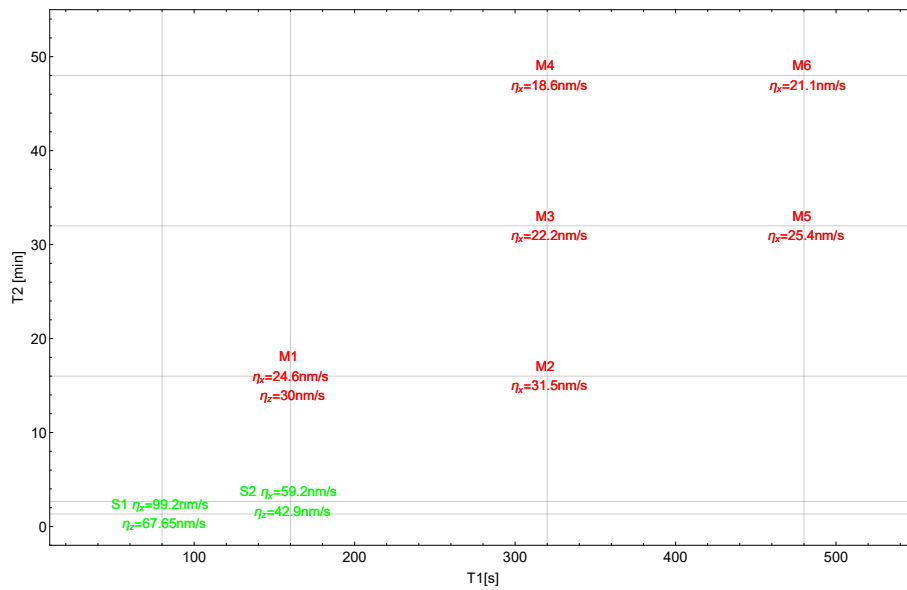


Figure 4.2: M1-M6 (red) and S1-S2 (green) are wafers processed with different etch times. On all wafers, the final diameter is measured. The depth could only be measured for the smallest mirrors. The S and the M series are processed with the same etch recipe, but with different mask sets. The opening for the mirrors in the mask are smaller and denser for S1 and S2.

of the opening diameter is shown in figure 4.7, where the AFM measurements on three mirrors with different initial diameters are compared.

At this point, two examples of a mirror design are discussed. Both examples were manufactured for this thesis and all etching rates are from real world calibrations.

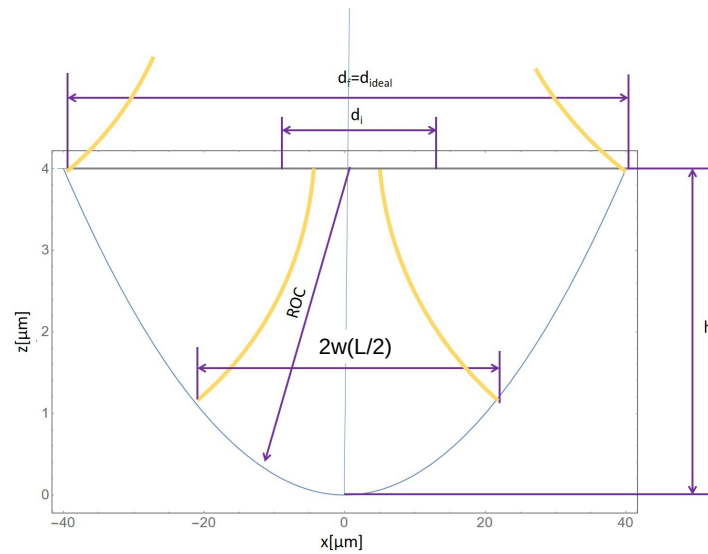


Figure 4.3: A parabola with a radius of curvature of 200 μm . The equation $R_1 = \frac{x^2}{2h}$ connects the radius of curvature, the depth h and the diameter d for an ideal micro mirror. The yellow lines represent the beam diameters $w(L/2)$ and $3w(L/2)$ respectively.

4.4 First run

4.4.1 Roughness

From the finesse, the tolerable maximum roughness is calculated, as discussed in section 4.2.3. The result of this calculation is that a roughness below 0.5 nm RMS is necessary.

4.4.2 Cavity length

In figure 4.4, the beam radius of the cavity is shown as a function of the cavity length. It is important to note that for long cavities the beam diameter on the mirrors becomes big, which is an issue because a roughness below 0.5 nm and a perfect shape is needed over the full area covered by the beam.

The value of the cavity length is chosen depending on the application, as this dictates the required beam waist and spacer length. A good length for a cavity is between 0.1 and 0.8 L/R_1 for a curved-curved configuration and 0.1 to 0.4 L/R_1 for a curved-flat configuration. For L/R_1 of 0.8, the spot size on the mirrors is only 1.3 times bigger than the beam waist in the middle of the cavity. For longer cavities this value increases significantly, cf. figure 4.4 b. A ratio $L/R_1 = 1$ is not recommended (see figure 3.14 for details) because at this point the lowest-order mode scatters very easily into higher modes due to imperfections in the mirror shape, as discussed in detail in section 3.3. A ratio $L/R_1 > 1$ is difficult because the big beam diameter on

the mirror results in a higher average roughness and causes scattering losses. We therefore choose $L = 100 \mu\text{m}$ (with $L/R_1 = 1/2$).

4.4.3 Beam radius and mirror diameter

Now it is possible to calculate all interesting numbers. We start with the beam waist at the center of the cavity, as derived in section 3.3:

$$w_0 = \sqrt[4]{\left(\frac{R_1}{L} - 1\right) \left(\frac{\lambda L}{\pi}\right)^2} \quad (4.6)$$

It is also possible to calculate the beam radius at every point inside the cavity. We want to know how big the mirror has to be such that the mode fits. The beam radius $w(z)$, where the light intensity drops to $1/e^2$ of its central intensity, is given by

$$w(z) = w_0 \sqrt{1 + \left(\frac{z}{z_0}\right)^2}, \quad (4.7)$$

where $z_0 = \frac{\pi w_0^2}{\lambda}$ is the Rayleigh length. Gaussian optics are discussed in great detail in section 2.2. Figure 4.4 shows the relationships defined in equations 4.6 and 4.7. Now we want to calculate the area in which the mirror has to be "good" in terms of roughness and shape. The ideal diameter can be defined as:

$$d_{ideal} = w(L/2) \cdot 2 \cdot 3 \quad (4.8)$$

w is multiplied by 2 to get the diameter and as shown in figure 4.5 b, we want to cover at least 3σ of the beam such that the finesse will not be limited by the mirror size. If the mirror is smaller than d_{ideal} , the mirror opening cuts the Gaussian shape and limits the achievable finesse.

To calculate this behavior the reflectivity is defined as:

$$\mathcal{R} = 1 - \frac{\sqrt{2/\pi}}{\sigma} \int_0^{2\pi} \int_0^{n \cdot \sigma} Gauss(r, \sigma) \cdot r \, dr \, d\phi \quad (4.9)$$

The norm of this formula is given in a way that $1 = \frac{1}{Norm} \int_0^{2\pi} \int_0^\infty Gauss(r, \sigma) \cdot r \, dr \, d\phi$ is fulfilled.

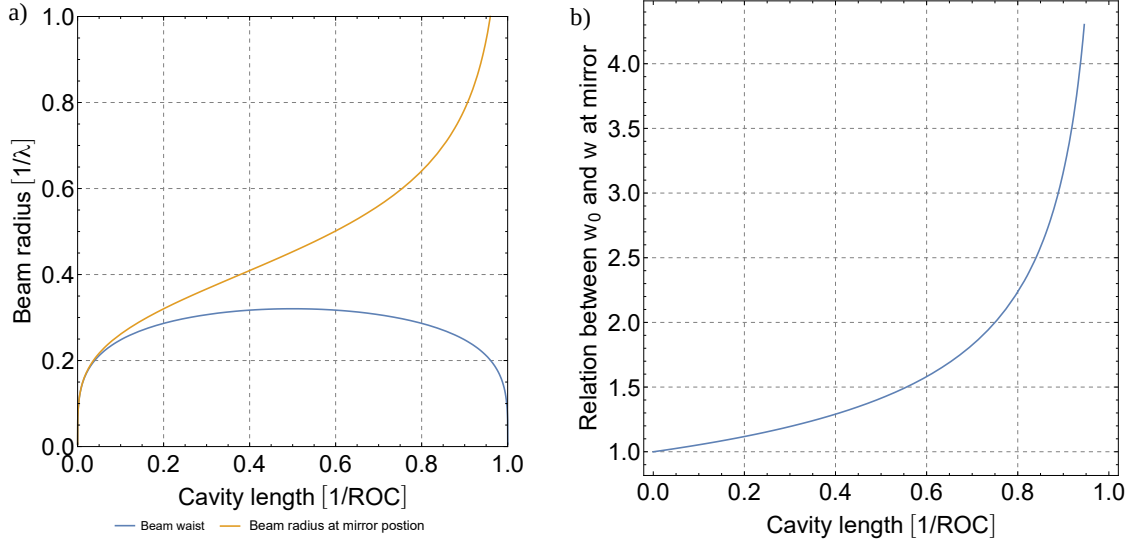


Figure 4.4: For a given L/R_1 of the mirrors in curved-flat configuration, the length of the microcavity determines the beam waist as well as the size of the beam on the mirror surfaces. a) The beam waist (blue) stays rather constant over a wide range of cavity lengths, while the beam radius on the mirrors (orange) increases continuously. At a length larger $1/L/R_1$, the cavity becomes unstable. b) shows the ratio $w(0)/w(L)$ of these two values.

This assumes, in analogy to equation 4.3, that the only loss is the part of the beam that gets cut. The function Gauss is defined here as

$$Gauss(r,\sigma) = \frac{2}{\sigma\sqrt{2\pi}} e^{-\frac{2r^2}{\sigma^2}} = I(0)e^{-\frac{2r^2}{\sigma^2}} \quad (4.10)$$

The integral over this function is one and σ is the value where the function drops to $I(0)/e^2$. The reflectivity \mathcal{R} from equation 4.9 is now used to calculate the finesse limitation by the mirror opening, using again the well-known relationship

$$\mathcal{F} = \frac{\pi\sqrt{\mathcal{R}}}{1-\mathcal{R}}. \quad (4.11)$$

Figure 4.5 shows the limitation of the finesse due to the mirror diameter. It is easy to overcome this issue by manufacturing big enough mirrors. This adds a new important value to the mirror design, the final opening (d_f), which in this first example is:

$$d_f = d_{ideal} \quad (4.12)$$

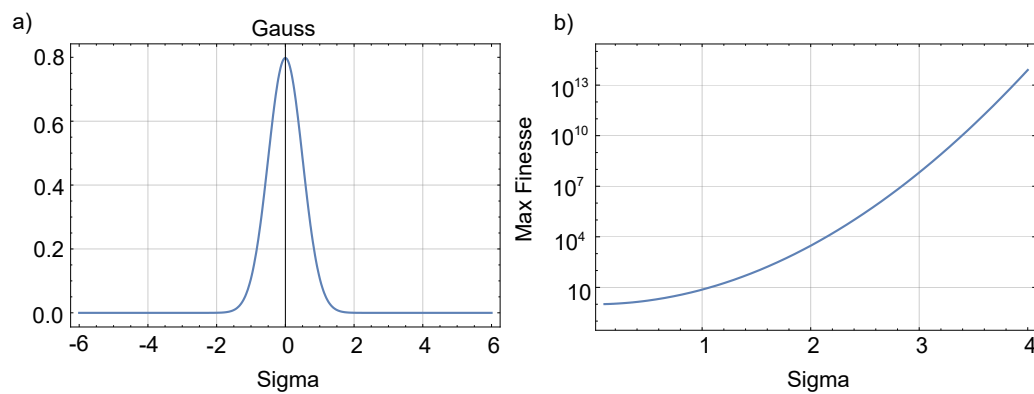


Figure 4.5: In (a), a Gaussian function describing the transverse beam intensity is shown. It is defined in a way that the integral over the function is one and σ is the value where it drops to $I(0)/e^2$. From this Gaussian distribution, a limitation on the finesse can be calculated, as is discussed in the text. The limitation of the finesse is calculate for different values of σ . At $3 \cdot \sigma$, the finesse limitation is far beyond 1×10^7 , but for $2 \cdot \sigma$ the finesse is limited to 1×10^5 . Typically, we want to cover $3 \cdot \sigma$ with the mirrors to overcome clipping issues.

4.4.4 Depth

The next point is to calculate the depth h of the mirror to define the full mirror shape. For a perfect parabolic shape (see figure 4.3), a given L/R_1 and an opening diameter d_f of $45\ \mu\text{m}$, h becomes:

$$h = \frac{(d_f/2)^2}{2R_1} = 5\ \mu\text{m}. \quad (4.13)$$

4.4.5 Etching times and initial opening

With the knowledge of the desired mirror shape and the etch rates η_{xo} and η_{za} from the calibration runs, the two etch times can be calculated. The first etch time is given by:

$$t_1 = h\eta_{za} = 160\ \text{s} \quad (4.14)$$

where we used $\eta_{za} = 32\ \text{nm/s}$. The second etch time is

$$t_2 = (d_f - d_i)/(2 \cdot \eta_{xo}) = 791\ \text{s or } 13\ \text{min}, \quad (4.15)$$

for $\eta_{xo} = 30\ \text{nm/s}$. This time depends also on d_i , the initial diameter in the mask. For the calculation we set $d_i = 25\ \mu\text{m}$.

We want to open the mirror and increase the usable middle area of the shape. This means that the second etch time should be long and the initial opening must therefore be rather small. In the first fabrication run, we vary d_i over a wide range from $12.4\ \mu\text{m}$ up to $52\ \mu\text{m}$. This results in a wide variation of the ROCs in the mirrors. Having a large number of different final shapes helps to correct for errors in the etch rates and to optimize the fabrication parameters.

4.4.6 Summary for first run

To summarize the considerations taken: we start with design goals for the finesse, the radius of curvature L/R_1 and the length of the cavity L . These values can be chosen - with some constraints - relatively freely. The desired finesse dictates the allowed roughness. The geometric parameters d_f and h of the mirrors follow directly from L/R_1 and L . The real production of the micro mirrors is essentially governed by three parameters: the mask opening d_i and the two etch times t_1 and t_2 . The etch times can be calculated from the calibration, only the ideal value of d_i has to be found experimentally. The results of the first mirror design is shown in table 4.2.

Table 4.2: Design considerations for the first micro mirror production.

Finesse goal (\mathcal{F})	100 000
Radius goal (ROC)	200 μm
distance mirrors (L)	100 μm
allowed roughness	0.6 nm
waist in center	6.5 μm
beam radius at mirror 1 σ	7.5 μm
beam radius at mirror 3 σ	22.5 μm
d_{ideal}	45 μm
d_f	45 μm
depth of the mirror (h)	5 μm
first etch time t_1	160 s
second etch time t_2	13 min
initial opening d_i	12.4 μm to 50 μm

The next step in the manufacturing process is the production of a mask. We design a mask with 10×10 mirrors on it, where the opening d_i is varied in 100 steps between 12.4 μm and 52 μm . A drawing of this mask is shown in figure 4.6. The first etch step defines the mirror depth ($t_1=160$ s). Then the resist is removed and the second etch ($t_2=16$ min) step amplifies and forms the shape. This is discussed in detail in chapter 5. Now the mirror has its final shape. At this point, AFM measurements are performed to determine the quality of the mirror shape before the expensive dielectric coating is deposited on the mirror. The results are shown in figure 4.6. In addition to the AFM characterization, the final opening d_f is measured with an optical microscope.

We use these measurements to find out how well the calculations match the real results. The three mirrors picked for AFM inspection are highlighted in figure 4.6, the results are compared in figure 4.7. There is a significant mismatch between the measurements and the calculations, as expected for the first production run. For very small d_i , the shape is a good parabola, but L/R_1 is small. For medium and large d_i , the profiles of the mirrors are very flat in the center with steep edges, far from the ideal parabolic shape.

Figure 4.8 shows the result of 100 white-light interferometer measurements¹. The white-light interferometer was bought 3 years after the AFM measurements. As shown in the figure the new advanced measurement method agrees well with the old measurements.

We can compare the outcome of these measurements with the simulation results from appendix A. The green curve is clearly in the third regime and shows a nice parabolic shape. The orange curve is in the second regime and has an odd shape. The blue curve with the largest d_i is between the first and the second regime. It is very flat in the middle, with steep edges. As is discussed in section A.2, the third regime is best for our mirrors. The conclusion is therefore to make the first etch step longer to ensure that all mirrors enter the third regime. A longer second etch time will furthermore modify the central, parabolic portion of the mirror, leading to further improvement.

1 filmetrics Profil3D

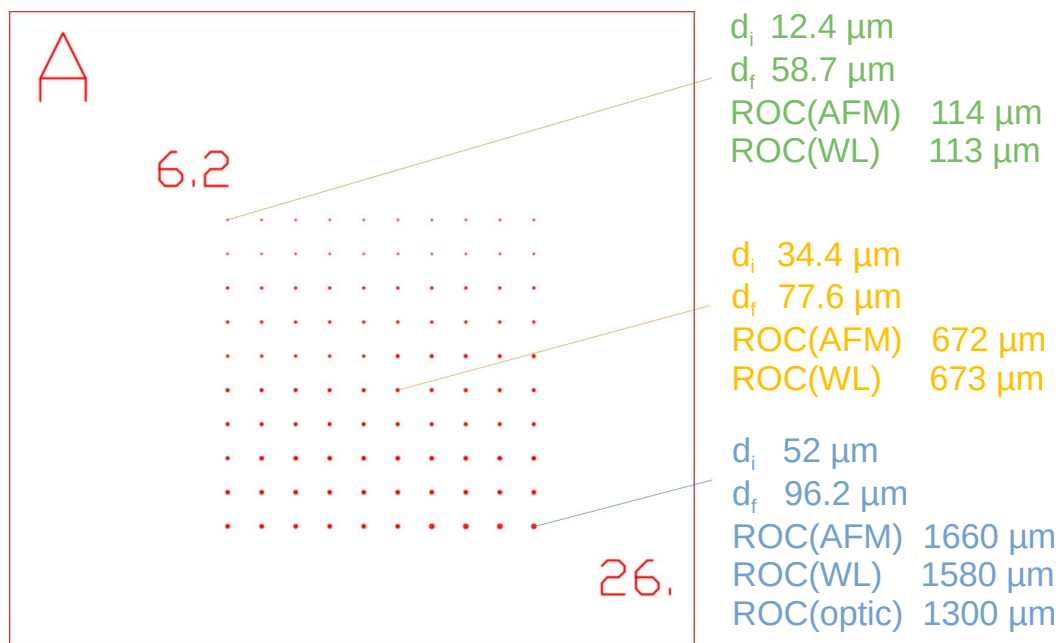


Figure 4.6: Drawing of the mask for mirror production with 100 different opening diameters. We picked three mirrors to perform AFM measurements of the final opening d_f and L/R_1 . For the largest mirror (blue arrow), we also derived L/R_1 from optical cavity measurements (see chapter 6). ROC(AFM) is measured with the AFM, ROC(WL) with the white light interferometer and ROC(optic) is extracted from the cavity experiment.

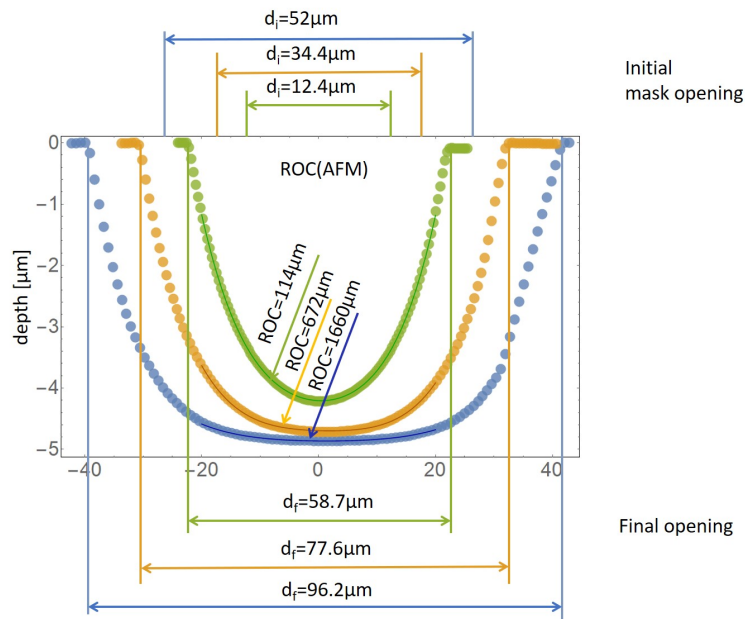


Figure 4.7: This plot shows the AFM profiles of three mirrors with different mask openings d_i . These mirrors are from the first run, which has the same etching times as M1 (see section 4.3, $t_1=160$ s $t_2=16$ min). The solid curves are parabolic fits through the data points from which the ROC is extracted. The green curve has a nice parabolic shape, but the ROC is almost off by a factor of 2 from the desired value of $200 \mu\text{m}$. The depth of this mirror is $1 \mu\text{m}$ less than the others. We attribute this to the very small initial opening of this mirror, leading to strong shadowing effects during the first etch. d_f is close to the expected value of $45 \mu\text{m}$. The shape of the other two mirrors is far from parabolic, as can be seen from the solid lines. The ROC's are calculated from the central region of the mirrors, where the profiles are very flat, resulting in very large ROCs.

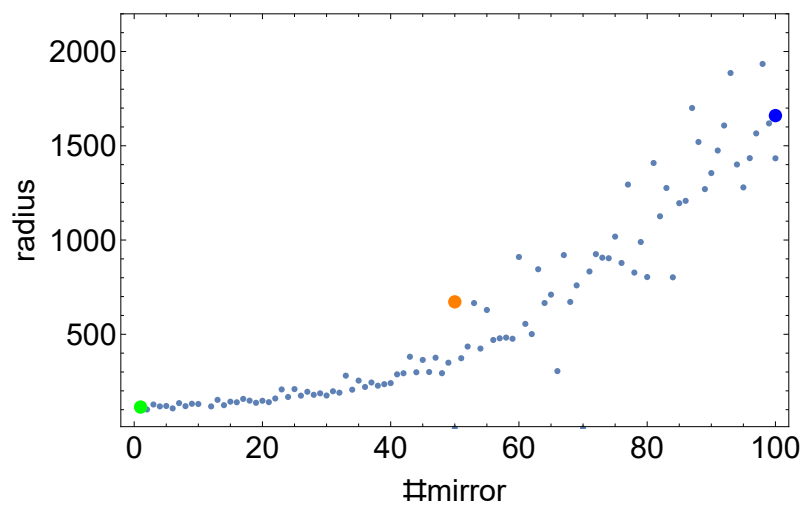


Figure 4.8: This measurement was performed three year after the AFM pictures. With a highly advanced white-light interferometer it was possible it measure all 100 mirrors in a reasonable time. As shown the new measurement agrees with the old one, and also gives some idea about how good the fits are. The noise is smaller for the small mirrors because the shape fits better. The green, orange and blue dots are the same mirrors as in figure 4.7. The x axis represent the different mirror beginning with the largest.

4.5 Second run

From the first production round it became evident that both etch times have to be increased. By increasing the first etch time we ensure that we reach the third etching regime for all mirrors. Increasing the duration of the second etch step opens the mirrors more and results in a larger mirror area.

It should be noted that both etch times have to be adjusted simultaneously. Increasing the second etch time would lead to larger final opening diameters d_f and in order to fit parabolas with the same L/R_1 to these new openings, the mirror depth has to be increased. Therefore also the first etch time has to be extended. The results obtained with these cavities are presented in section 6.3.

4.5.1 Roughness

We use the advanced polishing method discussed in section 4.2.3. This method typically rounds the edges and destroys the shape in this area, which is irrelevant when d_f is much larger than d_{ideal} . The achieved roughness is certainly below 0.3 nm, therefore the finesse goal for the second run was increased to 500 000.

4.5.2 Cavity length

For the second production run the same cavity length of 100 μm is used.

4.5.3 Beam radius and mirror diameter

In the first run, we chose t_2 such that the final opening diameter is equal to the ideal opening diameter, as calculated in equation 4.8.

As it turned out, the side walls of the mirrors do not follow the ideal shape. For the second run we therefore want to have a much bigger final opening diameter: instead of $d_f = d_{ideal}$ (equation 4.12), we now use

$$d_f = d_{ideal} \cdot \alpha. \quad (4.16)$$

with a correction factor α .

For the second production run, we chose $\alpha = 3$. This leads to $d_f = 135 \mu\text{m}$ which should increase the good area in the middle of the mirror. In that way we can be sure that the mode has enough space.

4.5.4 Depth

At this point we calculate the depth h of the mirror. As L/R_1 stays the same, but d_f is increased by a factor of α , the new depth becomes:

$$h = \frac{(d_f/2)^2}{2R_1} = 11.25 \mu\text{m}. \quad (4.17)$$

4.5.5 Etching times and mirror diameter

We use the same vertical etch speed η_{za} . With the new depth the first etch time becomes

$$t_1 = h/\eta_{za} = 320 \text{ s.} \quad (4.18)$$

Similarly, the second etch time is calculated with the same $\eta_{xo} = 18.6 \text{ nm s}^{-1}$ and again a medium sized initial diameter of $d_i = 25 \text{ }\mu\text{m}$:

$$t_2 = (d_f - d_i)/(2 \cdot \eta_{xo}) = 45 \text{ min.} \quad (4.19)$$

For the second production run, the same mask was used, with openings between $12.4 \text{ }\mu\text{m}$ and $52 \text{ }\mu\text{m}$.

4.5.6 Summary for second run

As we have seen in the last section it is not easy to calculate the right fabrication parameters for the perfect mirror shape. The conclusion in the last section was to increase the second etch time to get a better shape. So here we chose the parameters in a way that the second etch time is increased. An improved polishing method is used to decrease the roughness. Table 4.3 shows the design considerations for the second production. The green marked numbers are those which differ from the first mirror production. There are two main differences: first the improved roughness makes it possible to increase the finesse to 500 000. Second, because the second etch time is increased, also the final diameter d_f and the depth are changed.

Figure 4.9 shows a microscope image of the smallest and the biggest mirror. The goal for d_f is $135 \text{ }\mu\text{m}$. In the second production run we reach a d_f between $105.2 \text{ }\mu\text{m}$ and $163.4 \text{ }\mu\text{m}$, which shows how well these design considerations fit. The mirrors are too deep and too wide to perform AFM measurements as in figure 4.7. The ROC and other properties of these mirrors are determined by analyzing the resulting cavity spectra. Details about these measurements and the results for the second fabrication run can be found in section 6.3.

In conclusion, we can say that the results for the first production run were correct, but the short second etching time reduced the quality of the shape. We overcame this issue with a bigger geometry, which results from a longer second etch time. This calculation shows also how important a good calibration is for an exact calculation.

Table 4.3: Design considerations for the second micro mirror production. The green boxed numbers are different from the first production.

Finesse goal \mathcal{F}	500 000
Radius goal (ROC)	200 μm
distance mirrors (L)	100 μm
allowed roughness	0.28 nm
waist in center	6.5 μm
beam radius at mirror 1 σ	7.5 μm
beam radius at mirror 3 σ	22.5 μm
d_{ideal}	45 μm
α	3
d_f	135 μm
depth of the mirror (h)	11.25 μm
first etch time t_1	320 s
second etch time t_2	45 min
initial opening d_i	12.5 μm to 52 μm

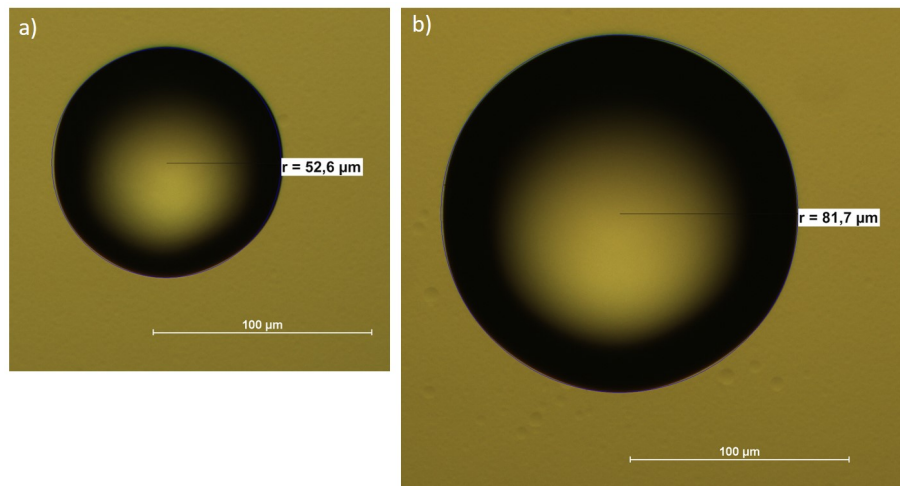


Figure 4.9: Two microscopic pictures of the smallest a) and the biggest mirror b) from the second fabrication. These pictures were taken before the polishing step.

CHAPTER 5

Manufacturing of a micro mirror

In this chapter we will have a look at the microfabrication of the mirrors. The mask design, the cleaning steps, the polishing and the full recipe for cavity production are explained in detail.

The final cavities consist of 3 chips, two mirror chips and a spacer chip. These three chips are plugged together and glued, forming monolithic cavities. To ensure a good alignment, the mirror chips and the spacer chip feature form-fit structures. Alternatively, a mirror chip and a flat mirror can be mounted individually, without a spacer chip, to test mirror quality in the flat-curved configuration. This has the advantage of a very small alignment sensitivity.

The mirrors are produced by a two-step etch process as described in chapter 4. The first step is done with a mask and defines the depth of the mirror, while the second etch step amplifies the shapes. For the second step, the entire wafer surface is exposed to the etch gas to get the most isotropic etch result. Polishing is performed after the second etch step, this procedure is explained in section 5.4. In a third etch step, the form-fit structures are manufactured. These are just 9 holes arranged around the mirrors. The same etch step is also used to separate the individual chips, thus avoiding wafer dicing. To create actual mirrors from the fabricated structures, the front side is coated with a dielectric mirror and the back side with an anti-reflection coating.

The spacer chips are basically rectangular frames for the mirrors, featuring pillars on both sides where the mirror chips have holes. A well-defined etch step on each side of the wafer determines the final thickness of the spacer chip, a third etch step then separates the chips and creates the rectangular holes for the mirrors.

Perfect alignment is a key issue for high-performance cavities. This is provided by the form-fit structures on the mirror- and spacer chips. The structures are designed in an asymmetric fashion to make sure only one orientation is possible. Also the masks used during the fabrication have to be aligned with utmost precision. For this purpose we use highly optimized alignment marks, allowing sub- μm accuracy. Most micro fabrication processes are only performed on one side of the wafer. In our case we etch both sides and therefore need double-sided alignment.

I want to emphasize the significance of this accurate alignment procedure, as it

allows simultaneous alignment of all cavities at once. This is key to the scalability of the presented microcavity system.

5.1 Mask design

A mask set for a lithographic process contains three kinds of features: first the structures which should be produced on the wafer, second the marks for alignment and third annotations on the mask. All these features can be found in figure 5.1. The masks are made out of chrome coated glass, the chrome is structured by a lift-off process. The mask were done by an external company¹.

The mask design is done in Mathematica². This has the advantage that by definition no open polygons exist³, which is a very common problem for masks drawn in Autocad⁴. Drawing the mask in Mathematica also allows to vary very complex structures over any parameter space. The drawback is that this method needs a very high level of abstraction because the designer has to think in mathematical terms and not in figures. The Mathematica files are translated into a script which is then executed in Autocad to create the actual DXF file used by the company.

A typical mask set consist⁵ of the alignment mask which creates the alignment marks on the wafer and several masks containing the structures. The alignment marks themselves are designed in a very careful way such that they are mirror symmetrical and have all necessary features.

The marks are shown in figure 5.2. For double-sided alignment as we use it here, the marks have to fulfill some conditions. First the marks have to be symmetrical with respect to their vertical axis because the mask for the backside has to be mirrored. This now mirrored mask has to be aligned to the un-mirrored alignment marks on the wafer. So the symmetry of the marks is absolutely necessary. The next condition is that the backside mask aligner needs marks with well defined edges. These are necessary because our backside alignment device uses virtual crosses and the best way to set these crosses is to align them to a straight edge. Our marks fulfill all of these conditions. A microscope picture of the alignment marks defined by the golden layer in figure 5.1 is shown in figure 5.3. The full mask set is found in appendix B.4.

1 Rose Fotomasken, Bergisch Gladbach, Germany

2 [Mathematica](#) is a modern technical computing system spanning all areas of technical computing.

3 The laser writer can only handle closed polygons to differentiate between areas that should be exposed or not.

4 [Autocad](#) is a commercial computer-aided design (CAD) and drafting software application.

5 The marks are designed by the group of Univ.Prof. Dr. Ulrich Schmid at the Institut für Sensor- und Aktuatorssysteme, TU Wien

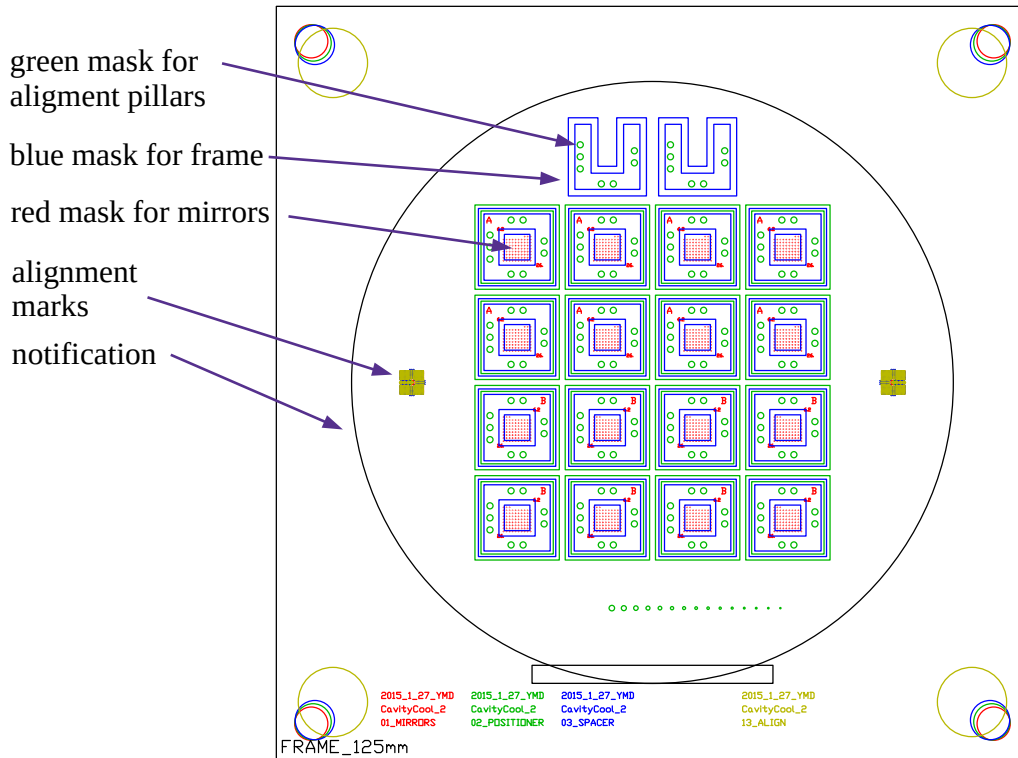


Figure 5.1: A typical mask set design. Four layers of the masks are shown: Red is the layer with the openings for the mirrors. Green is the layer for chip separation and the form-fit structures. The blue layer is for the spacer chips and the gold one defines the alignment marks on the silicon. The black layer of the design file is for documentation and alignment on the glass mask and is not written on a mask. Each mask must contain alignment marks.

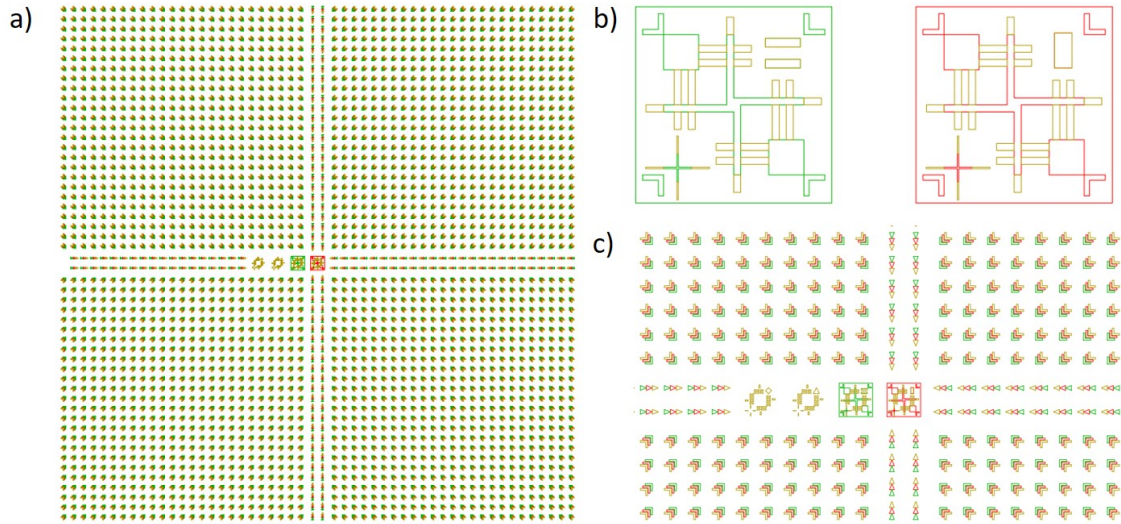


Figure 5.2: The alignment marks. The left marks are shown here, the right ones are mirrored. a) shows the full marks including the arrow field. During the mask alignment, the arrows guide towards the mark. In b) the mark itself is shown. The golden lines are the mark of the alignment mask, written in the first process step. This mask contains an individual mark^a for every mask. Each subsequent mask (green and red in this example) must be aligned with respect to its designated mark. The symbol in the top right corner is unique, a standing rectangle for the red mask and two lying rectangles for the green mask in this figure. Coarse alignment is achieved using the big cross in the middle, fine alignment is done with the small cross in the lower left corner of each mark. The mark itself has a lot of important details. The cross is designed in such a way that the edges of the cross build a new cross which is placed exactly in the middle of a mark. This is important when using the backside mask alignment tool. The small precision alignment cross allows a sub- μm precision. The L-shaped parts around the marks are for investigation in case of under- or over exposure. The squares are for the case that something goes terribly wrong and all smaller features are gone.

^a The marks are designed by the group of Univ.Prof. Dr. Ulrich Schmid at the Institut für Sensor- und Aktuatorssysteme, TU Wien

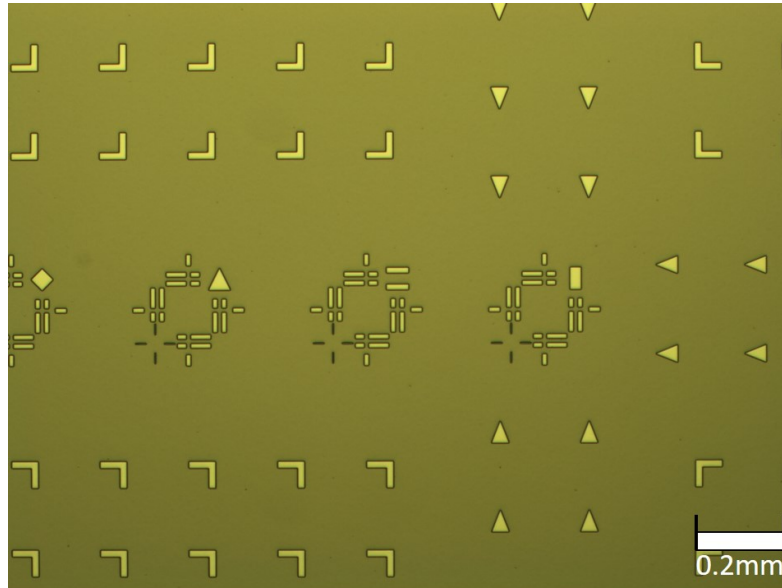


Figure 5.3: Developed photoresist with alignment marks. Note the different symbols in the upper right corner of each mark.

5.2 Silicon etching

Wet etching is the traditional way of etching silicon, using KOH, HF + HNO₃ or other corrosive liquids. For high precision micro- and nanofabrication, it has been almost completely replaced by dry etching methods, where ionized gas particles ablate the surface. Dry etching has many advantages over wet etching, it is much cleaner and controllable and allows for anisotropic etching.

In this work, we exclusively employ inductively-coupled plasma (ICP) reactive-ion etching (RIE) using SF₆ gas¹. The plasma is generated by a radio-frequency (RF) coil operated at around 20 MHz and a power of up to 2 kW. The plasma ignites as soon as the gas pressure exceeds a certain threshold.

The etch process relies on two effects: first, the chemical reaction between the free fluorine atoms and the Si surface, creating gaseous SiF₄ molecules. The second effect is physical surface ablation due to the bombardment with ions.

For simple isotropic etching the desired SF₆ pressure is supplied to the chamber and the plasma is ignited. Details can be found in [65]. Here the chemical etching is the main effect. The relevant parameters are the gas flow, the vacuum valve position and the wafer temperature. The valve is set to 90° (full open) to get the used gas quickly out of the chamber. The temperature of the wafer is set to 24 °C because we want the chemical etch rate to remain high. SF₆ gas with a gas flow rate of 100 sccm

¹ PlasmalabSystem100, Oxford Instruments

is used¹ and all anisotropic systems like electric fields are disabled.

The alignment structures and the chip separation require high aspect ratio etching and very steep walls. This is realized with the two-step Bosch etch process ([66]). First, SF_6 gas is filled into the chamber and the plasma is ignited. In this plasma, free radicals hit the silicon surface and etch it away. Then, the SF_6 valve is closed and C_4F_8 is supplied to the chamber. This gas deposits a chemically inert layer on the substrate. Afterwards SF_6 is used again, but now the physical etch effect removes only material from surfaces parallel to the wafer surface, while the walls remain protected. Once the passivation layer is removed, chemical etching also occurs at these surfaces. This process is repeated many times. In this way it is possible to etch straight into the silicon. As an example for a structure created by Bosch etching, a 1 mm hole through a $350\ \mu\text{m}$ thick wafer is shown in figure 5.4.

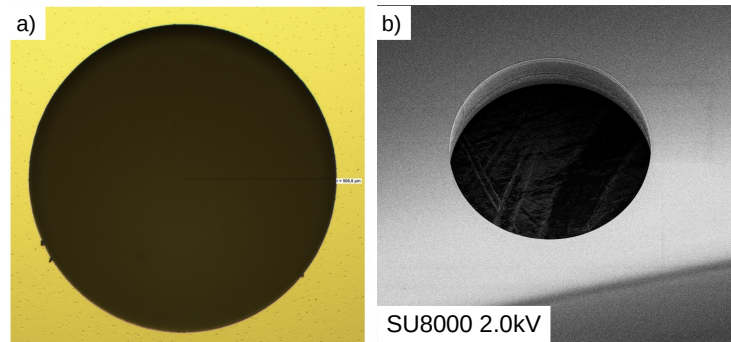


Figure 5.4: One of the alignment holes after ICP-RIE. a) shows the hole under an optical microscope and b) shows the same hole under a tilted electron microscope. The hole has a diameter of 1 mm and a depth of $350\ \mu\text{m}$, penetrating the wafer fully. The SEM picture illustrates clearly how steep the side walls are, made possible by the highly anisotropic Bosch etch process.

¹ sccm stands for standard cubic centimeters per minute. A example for a gas volume under standard condition is at temperature at 0°C and 1.01 bar. Note that for any temperature a pressure can be found so that the standard condition is fulfilled.

5.3 Photoresist removal

One of the big problems in mirror production is surface roughness (as discussed theoretically in section 4.2.3). We have to think which steps in our recipe produce surface damage. One of these steps is the removal of the photoresist¹ after the first etch step. This is typically done with an oxygen plasma in a so-called asher. In our case this oxygen plasma damages or reacts with the silicon surface in a way that any further isotropic etch step produces a lot of roughness (cf. fig. 5.5 a). We replaced this step by another method of cleaning, where the resist is removed with acetone in an ultrasonic bath. This method has the drawback that if the resist is too degenerated, it cannot be removed anymore. Degeneration can occur because of thermal damage during plasma etching. It is therefore necessary to increase the thickness of the photoresist such that only the surface degenerates, while a good (i. e. dissolvable) layer of resist remains. To ensure protection, we apply three layers of resist, each 3 μm thick. The results for the two different cleaning methods are shown in figure 5.5. The pictures were made after the second etch step following the resist removal. This second etch step amplifies the otherwise invisible surface damage.

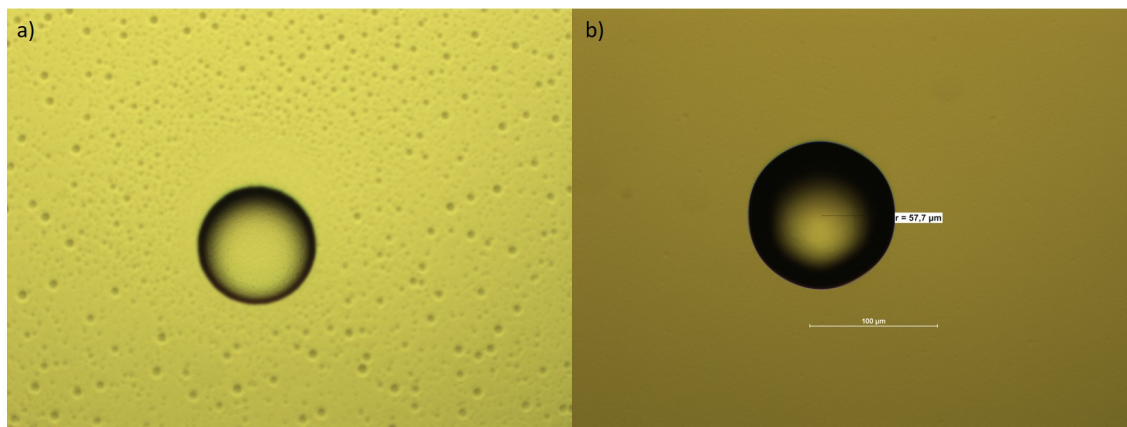


Figure 5.5: Microscope pictures to compare the two methods of photoresist removal. In a) the resist is removed with an oxygen plasma, while in b) acetone in combination with ultrasound is used. After the resist removal, both mirror shapes are amplified by a second etch step. Only then does the dramatic difference becomes visible.

1 Type of photoresist AZ2450

5.4 Thermal polishing

With the methods discussed in section 5.3 and with improvement of the etching methods, we were able to reach a roughness level of around (1.0 ± 0.3) nm which is good, but not good enough. The goal here is to bring the roughness down to a few Å. The way we achieve this is very simple, the idea is described in [2]. A layer of silicon oxide (around $2\ \mu\text{m}$ to $3\ \mu\text{m}$) is grown on the wafer and removed afterwards. This is a very clean process because the oxidation works by diffusion into the silicon, there is no waste gas which could cover the surface and reduce its uniformity in this process. The removal of the silicon oxide is done by a dry hydrogen fluoride (HF) etch process which is also as clean as possible.¹

This process is repeated up to two times, during which a smoothing and leveling takes place. The principle of this method is illustrated in figure 5.6. The oxidation has also the side effect that it cleans the wafer. Any dirt or contamination is removed during this process. The result is a very smooth and clean surface which is an ideal substrate for dielectric mirror coating afterwards. Microscope pictures of a mirror before and after the polishing are shown in figure 5.7. In figure 5.8, an AFM scan of a polished mirror is shown. The roughness on these scans is below the resolution of the AFM. This polishing method is a key point for achieving a finesse over 100 000. It reduces the scattering losses to a level at which they can be neglected.

It is important to note that the ideal oxide layer thickness for the polishing process depends on the initial roughness of the sample and its spectrum. In-house tests with $5 \times 200\ \text{nm}$ only reduced the high frequency roughness and had no effect on the bigger imperfections. $2 \times 2\ \mu\text{m}$ work best for us, because both the high- and the low frequency roughness are reduced. For even thicker oxides layers, we expect a substantial change of the mirror shape.

¹ The entire process is done by 5microns GmbH, Ilmenau, Germany.

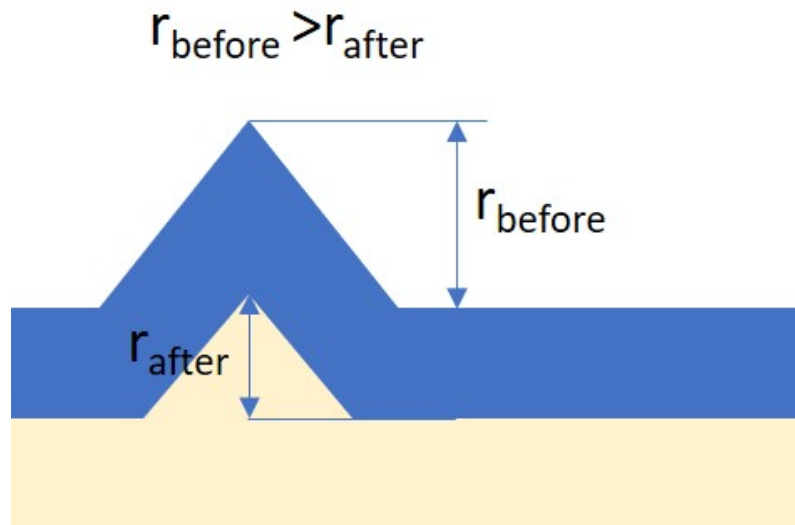
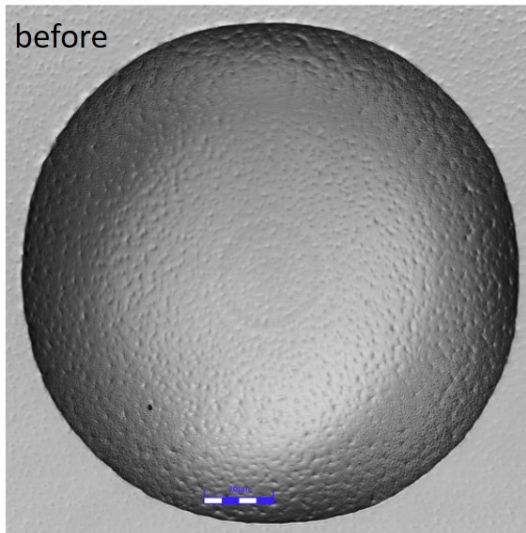


Figure 5.6: This sketch shows how thermal polishing works. Typically, the initial roughness is in the range of 1 nm to 2 nm and the oxide layer produced is 3 μm to 5 μm thick. The oxide layer levels out all spikes and waves in the surface, by removing it the wafer is effectively polished.

w166_2 größte Struktur B



w166_2 größte Struktur A

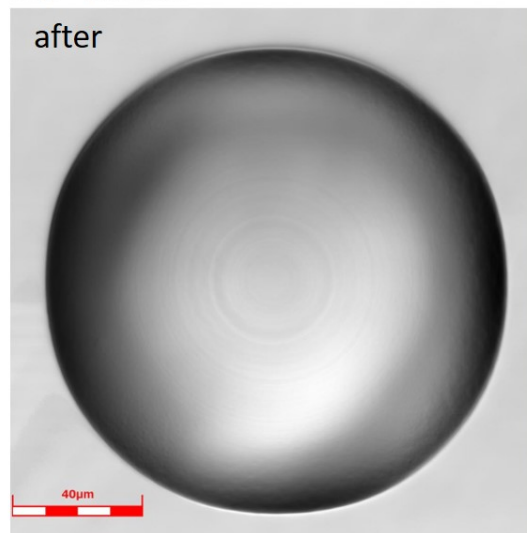


Figure 5.7: Two microscope pictures before and after the polishing. An extreme example of roughness is shown, to point out the capability of this process. The typical initial roughness is lower. These pictures are taken at the PTB Braunschweig, by the group of Ludger Koenders.

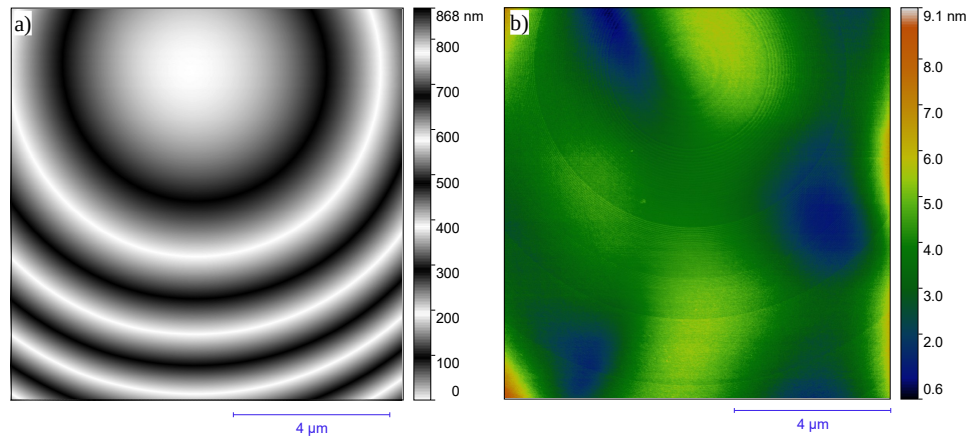


Figure 5.8: a) Raw data of an AFM scan of a thermal polished mirror. The mirror is completely clean and no dirt or defects are visible. b) is the same data after removing a polynomial background up to second order and applying the Gwyddion^a align rows function.

^a *Gwyddion* is a modular program for Scanning probe microscopy (SPM) data visualization and analysis.

5.5 Mirror coating

The operational wavelength of the cavities designed in this work is 1550 nm, where silicon is highly transparent. Highly reflective dielectric mirrors are fabricated on the chips². The mirrors consist of alternating layers of tantalum pentoxide and silicon dioxide, the reflectivity is determined by the number of layers and other parameters optimized by the company, the best mirrors have a transmission of only 1 ppm to 2 ppm. We simply order a mirror coating by specifying the desired reflectivity.

For a perfect surface, the reflectivity only depends on the mirror coating. For a real surface with imperfections scattering losses appear, which we try to minimize as discussed before. The finesse of a cavity is given by equation 2.18 using an effective reflectivity, this contains both the scattering losses due to surface roughness and the finite transmission of the mirror layer. The fundamental difference between a cavity limited by roughness and a cavity limited by mirror transmission is that in the first case the scattered light is lost, while in the latter it can be used for a measurement.

To maximize the finesse while having a measurable signal, it is important that the loss due to the roughness is not the dominating factor. The mirror reflectivity has to be balanced with the effective reflectivity due to the roughness as defined in 4.3.

² The mirror coating is performed by FiveNine Optics, Boulder, USA

5.6 Cavity configurations

Two different cavity designs are used in this work. The design where the length between the mirrors is fixed is called the "Monolithic setup". For this setup it is necessary to produce the mirror chips (section 5.7.1) and a spacer chip (section 5.7.2). The cavities in this setup have a curved-curved configuration. Proper alignment of this configuration is possible because of the well-designed spacer chip. The beam waist in this configuration is in between the mirror chips, allowing to introduce objects into the cavity to interact with the field. A first example highlighting the usefulness of this approach is presented in chapter 8. Because of the simplicity of this assembly, it is very easy to make it compatible with ultra-high vacuum (UHV) applications. The disadvantage of the monolithic curved-curved cavities is their lack of flexibility, as the cavity length is fixed through the spacer chip.

The other setup has a variable length between the mirrors which can be set by a piezo. It is thus called "Piezo setup". For this configuration two different kinds of mirrors are used, ones flat and ones curved, because for a flat surface no lateral alignment is necessary. The beam waist in the flat-curved configuration is on the flat mirror. This can be useful for experiments with crystal defects in solids. The flat-curved configuration with adjustable length is a very practical setup to investigate the quality of the mirrors. In contrast to the monolithic setup, this assembly is not UHV compatible because of the wide range of materials used in the mounting and also much more sensitive to vibrations and thermal drifts.

Figure 5.9 shows a sketch of the two configurations. Construction drawings of the mount of the piezo setup can be found in section B.

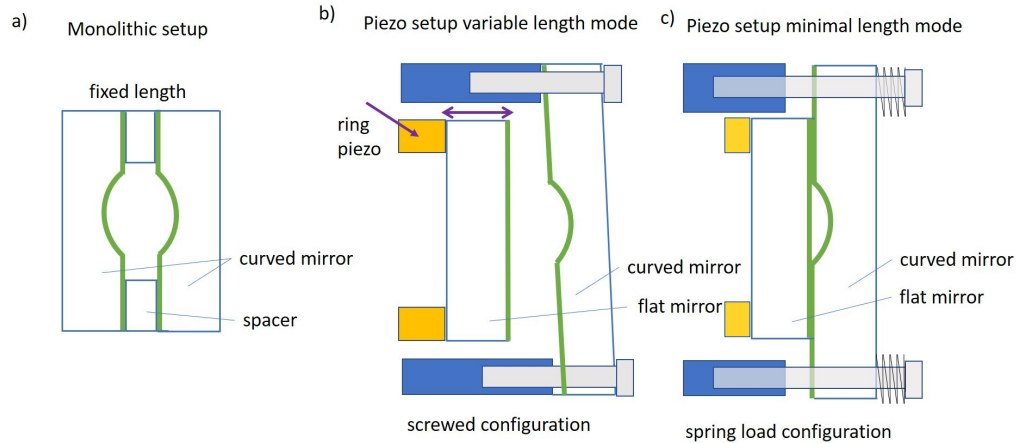


Figure 5.9: The monolithic- and the piezo setup. In the monolithic setup (a), the spacer is used to align the chips with respect to each other, forming a curved-curved configuration. In the Piezo setup (b) one has the ability to set the distance between the mirrors with a piezo crystal. The Piezo setup can also be used in a minimal length configuration (c) where the flat mirror is pressed with springs on the curved mirror to minimize alignment errors.

5.7 From wafer to mirror

We now walk through the entire fabrication process, from the bare silicon wafer to the finished mirror- and spacer chips. As we want to make optical measurements, we start with wafers that are polished on both sides.

5.7.1 Mirror chip

In this section the production of the mirror chip is explained step by step. A summary of the entire process is shown in figure 5.10. The first step is always to create the alignment marks on the wafer. There are two possible ways to place them, either on the front or on the back side. The easy way is to use marks on the front side. The risk here is that if something goes wrong and the marks are damaged the wafer is lost. The other option is to place the marks on the backside, with the advantage that they are protected against all processes on the front side. The drawback is that you need a backside alignment device for the marks, which is more effort. We choose here backside alignment marks because we want to etch the complete front side. The marks are etched into the silicon with a short Bosch etch.

In the next step, the mirror mask is used to define the mirror openings. Then the first etching takes place. SF_6 plasma etches isotropically into the wafer, defining the depth of the mirror. Afterwards the photo resist is removed, as explained in section

5.3 this is done with acetone in an ultrasonic bath to prevent any surface damage. The next step is to amplify the shape with an additional long etching step. Here no mask is required, meaning that the whole wafer is etched, which results in the most isotropic etch possible. This method of etching has a very low etch rate. After the second etch, the mirrors are measured with the AFM for characterization. The interesting questions are: is the mirror shape good enough for further processing, and how much polishing is necessary?

Then the wafers are sent for thermal polishing. Two repetitions are applied. Again an AFM measurement is performed to determine the final roughness and shape. The next step is to separate the wafer into chips and to create the alignment holes. This is done with a highly anisotropic Bosch process, see section 5.2.

Afterwards the chips are placed in an aluminum mount (see section B.3) and sent to the mirror coating facility. The final result is shown in figure 5.11.

5.7.2 Spacer chip

The monolithic cavity setup requires a spacer chip to define the cavity length and to ensure proper alignment of the mirrors. There are two versions of the spacer chip: one is a full frame around the mirror field, the other one is L-shaped, allowing access to the optical cavities. The first point is to choose the right silicon wafer. The wafer has to be polished on both sides and the wafer thickness must be well defined. It is given by:

$$h_{wafer} = l_{Cavity} - 2z_{Mirror} + 2h_{pillar} - \rho_h \quad (5.1)$$

h_{wafer} is the initial thickness of the wafer and l_{cavity} is the target length of the cavity. From this length, the mirror depth has to be subtracted. The pillar height is

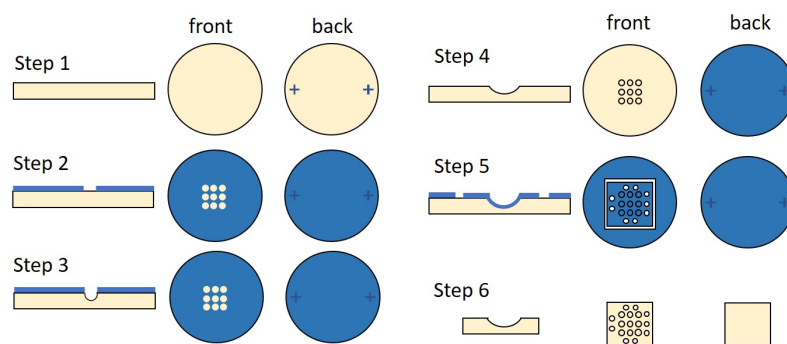


Figure 5.10: The production steps of a mirror chip. Step 1: place mark on backside. Step 2: define mirror opening with mask. Step 3: First isotropic etch, subsequent photoresist removal is not shown. Step 4: Second etch to amplify the features. Step 5: define alignment structures and chip boundaries. Step 6: Bosch etch through the whole wafer.

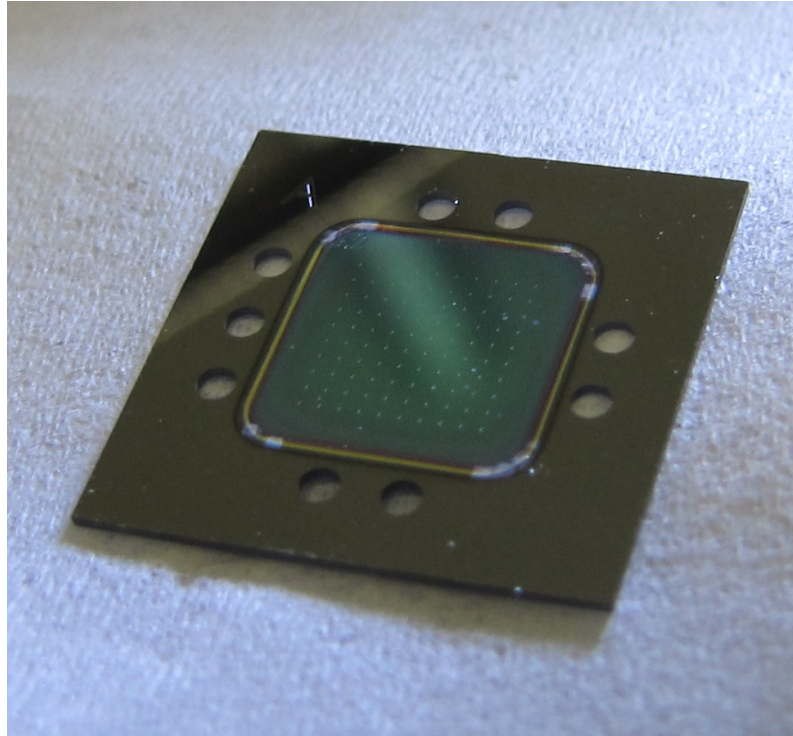


Figure 5.11: Picture of a complete mirror chip. The green area is the mirror coating, the small white dots are the mirrors. The frame is black because it is covered by the aluminum mount during mirror coating. In the top left corner, the letter "A" is written, barely visible in this picture. This allows a distinction between the mirror chips.

added to the thickness as this is the amount etched away later. ρ_h is subtracted to made the spacer a little thinner so that there is some tolerance for the case that the holes or pillar have a slightly cone-like shape. Using typical values for the mirrors, the pillars and ρ_h , the wafer thickness for a cavity length of $200\ \mu\text{m}$ has to be:

$$h_{wafer} = 200\ \mu\text{m} - 2 \cdot 5\ \mu\text{m} + 2 \cdot 15\ \mu\text{m} - 10\ \mu\text{m} = 210\ \mu\text{m} \quad (5.2)$$

An important limitation is that a chip thinner than $100\ \mu\text{m}$ is extremely brittle and becomes impossible to handle. After selecting the initial wafer, we start the fabrication by etching the marks into the silicon, this time on the front side.

On the spacer chip, we want pillars where the mirror chips have holes. This guarantees the best possible alignment. The only gap between the pillars and the holes comes from the under- and over etching during the Bosch etch process. We expect this gap to be smaller than $0.5\ \mu\text{m}$. To achieve this, we create an inverted version of the mask used for the holes on the mirror chips. Only the surface of the pillars (and the back side of the wafer) is covered in photoresist during the first Bosch etch, creating raised structures with almost perfectly vertical walls. The same

process is performed on the other side.

To separate the chips and to create the frame for the mirrors, another Bosch process with the appropriate mask is used. At this point we apply some (1 min to 2 min) isotropic etching from both sides. This reduces the thickness of the wafer a little bit and makes the pillar shape smoother, which helps a lot during the assembly process. After this last step the thickness of the chip and the pillars are measured and checked. If the chip is a little bit too thick it is possible to improve this with some more isotropic etching.

The entire production of the spacer is summarized figure 5.12 and a microscope picture of a finished spacer chip is shown in figure 5.13. The mask set used can be found in section B.4.

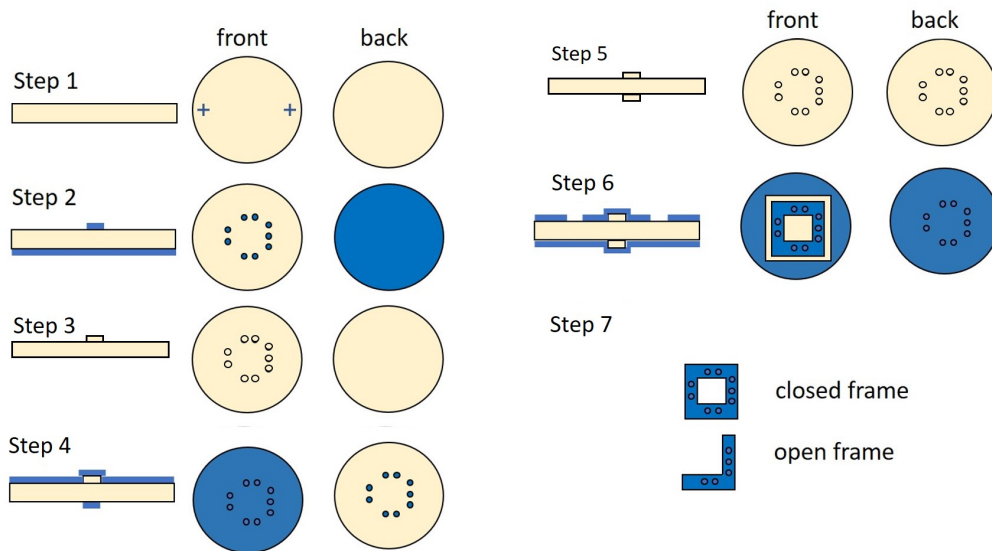


Figure 5.12: Production of the spacer chip. Step 1: fabrication of the alignment marks on the front side. Step 2: The back side is covered completely with photo resist. On the front side, the inverted mask for the alignment holes (green layer of figure 5.1) is used. Step 3: Bosch etch to create the alignment pillars on the front side. Step 4: Cover the front side with photo resist and apply the inverted mask to the backside. Step 5: Bosch etch on the back side for the alignment pillars. Step 6: Mask for the mirror frame and chip separation. Step 7: Final Bosch etch and finished spacer chips.

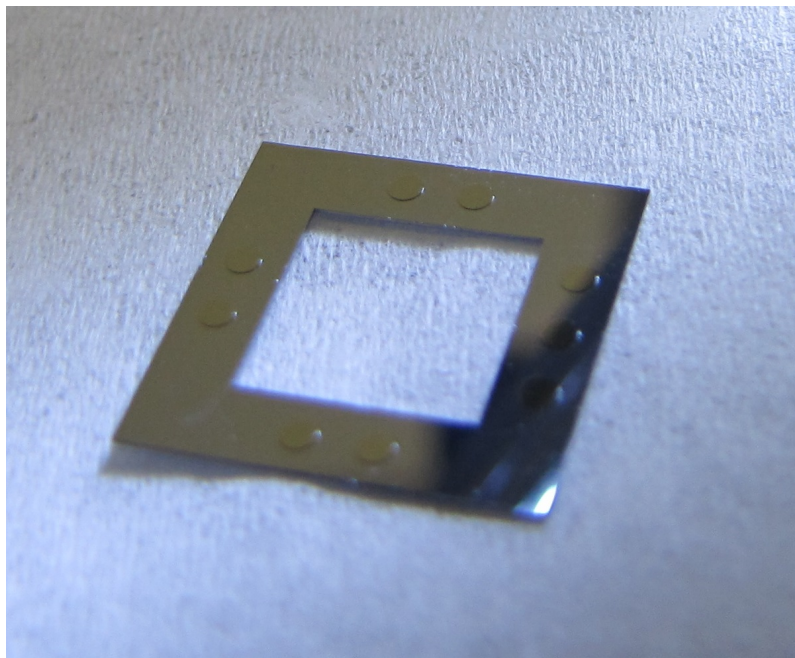


Figure 5.13: Spacer chip ready for cavity assembly. The alignment pillars are $35\ \mu\text{m}$ high with a diameter of $1\ \text{mm}$.

5.8 From chip to cavity

Once the mirror chips are finished we can build cavities. As explained in section 5.6, we have two mounting options.

5.8.1 Assembly of the monolithic cavities

The first step for assembly is to glue the first mirror to an aluminum mount. In this way a solid base is established. The next step is to place the spacer on the mirror chip. At this point, the spacer is moved around in small circles, until it snaps in. Then the next mirror is placed on top and also snapped to the spacer. Afterwards the whole stack is clamped together with a second mount. A drawing of the full monolithic cavity assembly is shown in figure 5.14. To check if everything is well aligned, we use a light source from the side. If the light can be seen from the other side there is a gap between the mirror and the spacer, which means you have to start over. The alignment can also be checked with a microscope from the top and bottom. If everything is well aligned the pillars and the holes show perfect form-fit.

5.8.2 Assembly of the Piezo setup

The flat-curved configuration is used for many cavity measurements because it is more flexible than the monolithic one. This setup consists of a movable part where the flat mirror is mounted and a fixed part with the curved mirror chip. The mirror chip is glued to an aluminum mounting plate, which in turn is screwed onto a massive aluminum mount. This mount is attached to the fixed part of a standard optical translation stage¹. The flat mirror is glued to a piezo ring². The piezo ring is then

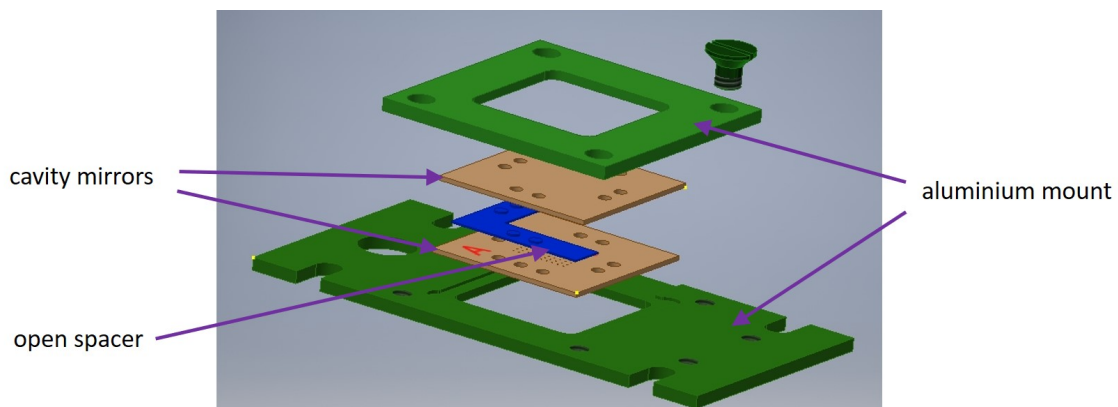


Figure 5.14: Explosion drawing of the monolithic cavity assembly with an open spacer. Here the mirror chips (brown) are aligned with the spacer (blue). The aluminum mount (green) holds everything together.

1 newport M-UMR3.5

2 noliac NAC2121-A02

glued to a brass pillar, with a layer of Kapton tape for electrical isolation in between. The pillar is screwed into the moving part of the translation stage. The complete assembly is placed on an optical table for alignment with the in- and outcoupling optics. The piezo setup is shown in figures 5.15 and 5.16.

The key advantage of this setup is the adjustable cavity length and, because one mirror is flat, that the lateral alignment is not critical. The coarse adjustment is done with the translation stage, and can then be fine-tuned with the piezo crystal. This cavity configuration is used to find the optimal length for the monolithic cavities, for mirror characterization and for comparison with the numerical simulations from chapter 3.

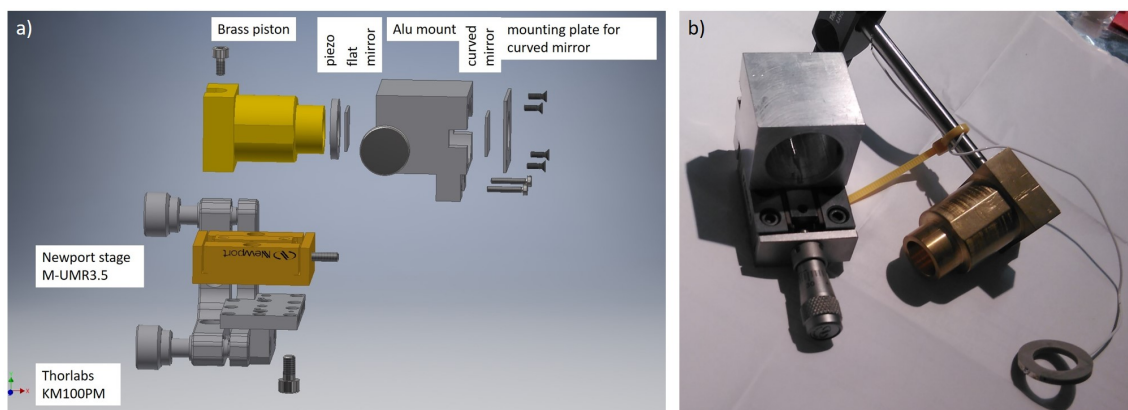


Figure 5.15: a) is an explosion figure of the piezo setup. All schematics can be found B.1. In b) a photo of the of the piezo setup before assembly is shown.

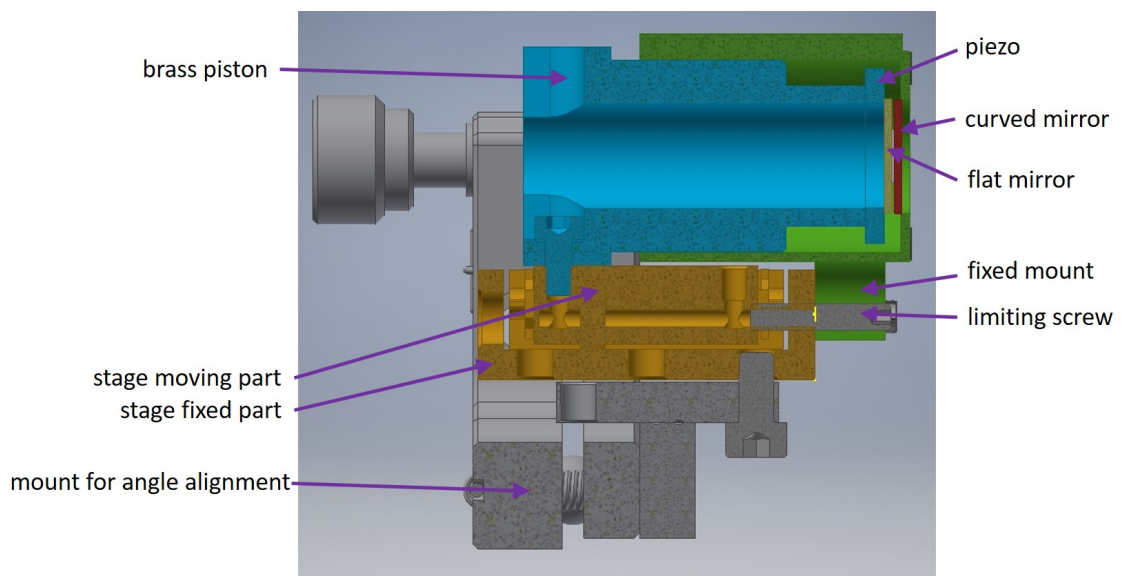


Figure 5.16: The piezo mount in a half section view. The green parts are fixed and screwed to the frame of the stage. The 22 mm brass pillar (turquoise) is guided by the aluminum mount (green). At the tip of the pillar, the piezo is placed for fine alignment. The flat mirror is glued to the piezo and the curved mirror to the fixed aluminum mount.

CHAPTER 6

Measurements on cavities

So far we have discussed the theoretical aspects of optical cavities, calculated the losses due to non-ideal shapes and discussed the entire fabrication process from silicon etching to cavity assembly. This chapter will first present the experimental setup for measurements of the optical properties of the cavities. I then show the results obtained for the cavities. Throughout this thesis, two complete fabrication cycles have been performed. The first one was done right in the beginning of this project, where many of the steps still had to be optimized. Two years later, after all the problems have been identified and solved, the second fabrication run was done. The results of the second run show a dramatic improvement of all relevant parameters and constitutes the main results of this thesis.

All measurements for the first run were performed using the flat-curved configuration with the piezo. This is ideal for testing various parameters of the mirrors. The curved-curved configuration was only used to detect nano particles (see chapter 8). The zero-length flat-curved configuration was not available for the first measurements. The mirrors from the second run were tested in all configurations, the curved-curved cavities are used to improve the nano particle detection at the time of writing.

6.1 Experimental setup

As shown in section 2.5, the finesse is a key value of interest for a cavity. After design and fabrication it is now necessary to measure this value to find out how good these cavities are. The typical values for the FSR for our cavity lengths are in the range of 0.5 THz to 3 THz, therefore a laser which can hop and sweep in this range is necessary. As we want to design and characterize high-finesse cavities with \mathcal{F} up to 500 000, the linewidth of the laser should be below 100 kHz.

For this purpose we use the PPCL300 laser module¹. This module gives us a high level of flexibility in our measurements because we can hop the laser frequency, as well as sweep the frequency in a range of up to 5 THz. With this laser, we can jump to the first frequency, scan over 100 GHz, then jump 100 GHz up and scan again and so on. In that way it is possible to search for cavity resonances simply by changing

¹ A low noise integrable tunable laser assembly (ITLA) from Pure Photonics PPCL300.

the laser frequency. Sidebands can be modulated onto this laser by means of an Electro-optical modulator (EOM)¹.

For the latest cavity measurements we use a new laser², which can sweep the frequency faster, is more stable than all our other lasers and has the ability to sweep over 13.3 THz. This wide sweep range is necessary for very short cavities which are measured in the second run.

The first step is to align the laser to the cavity. Because the mirrors are highly reflective and very small, this is a challenge. A imperfectly aligned cavity has basically zero transmission at the design wavelength. Only the resonances in the aligned cavities lead to a measurable signal. To make our life easier we use a 1392 nm laser³. As the mirror coating is not optimized for this wavelength we get significantly more transmission during the alignment.

A scheme of the experimental setup is shown in figure 6.1. The modulated laser light is passed through a fiber optical circulator. After the outcoupler, the polarization is defined and an objective lens couples the laser into the cavity. A collection fiber brings the transmitted light to a photodiode, the reflection is measured from port 3 of the circulator. A photo of the compact optical setup is shown in figure 6.2. The alignment procedure starts by aligning the pickup fiber with respect to the laser. Then the 1392 nm laser is rastered across the mirror chip using the translation stage. In between the mirrors, a weak transmission is observed. As soon as the laser beam hits the edge of a mirror, transmission changes because the light is efficiently scattered. The laser frequency is swept continuously over a range of 1 THz to 2 THz with a frequency of around 60 Hz to make sure the resonance frequency is found. When the beam hits the center of the mirror, the transmission rises drastically at the resonance frequency. Now the geometric alignment can be fine-tuned to maximize the transmission signal. Then we switch to the 1550 nm laser and try to find the corresponding resonance frequency by sweeping the laser. Once the signal is found, the geometry is optimized again.

The wide sweep range of the 1550 nm laser allows to easily measure the FSR by sweeping the laser from the first found resonance to the next one. To calculate the finesse, the linewidth of the resonance is needed. The issue here is that if the laser is scanned slowly across a resonance to measure its width, the drift of the cavity is too fast and the measurement is corrupted. The solution is to measure the resonance linewidth much faster than any thermal drift. This can be done with sideband modulation of the laser using an EOM. Now the laser has a main frequency and two sidebands with a well-defined frequency separation. If such a laser now sweeps over

1 Electro optical modulator Optilab 10Gb/s Modulator SN:D031037

2 Continuously Tunable Laser Toptica CTL-1550

3 A fiber coupled laser diode, EP1392-5-BM-B01-FM from Frankfurt Laser Company.

a resonance, three peaks appear on the detector. Because the separation between these three peaks is well defined, it is possible to measure the linewidth of the cavity resonance. Alternatively, instead of sweeping the laser frequency, the cavity length can be changed using the piezo crystal.

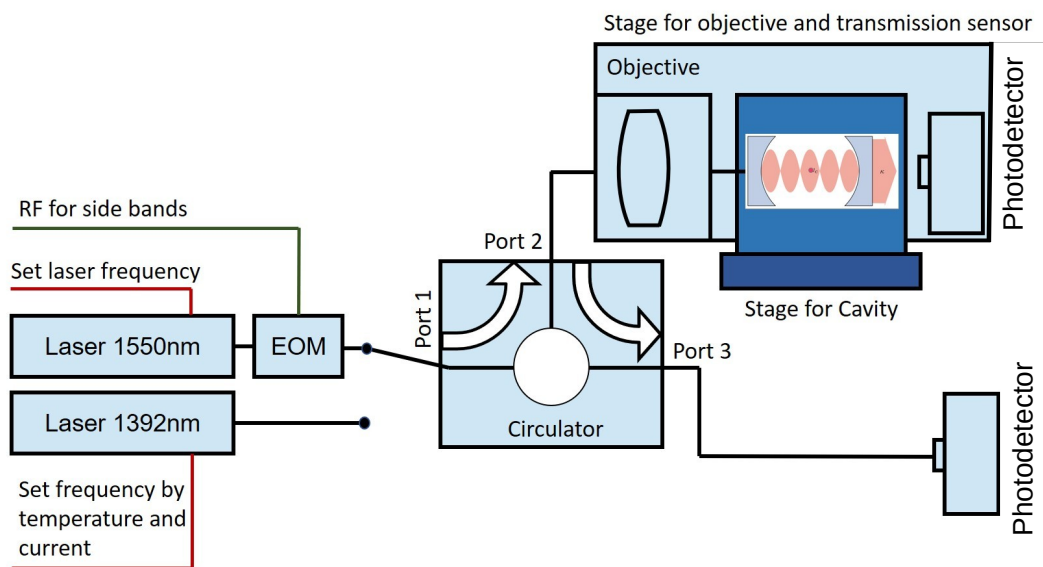


Figure 6.1: Schematic of the optical setup. We can switch between the 1550 nm and the 1392 nm laser. The red lines are digital or analog communication lines to control the lasers. The green line is the signal from the radio frequency generator for the EOM. The black lines are fibres, all optical paths are in fibres except for the path through the cavity. The transmitted light is picked up by a plastic fibre and guided to a detector.

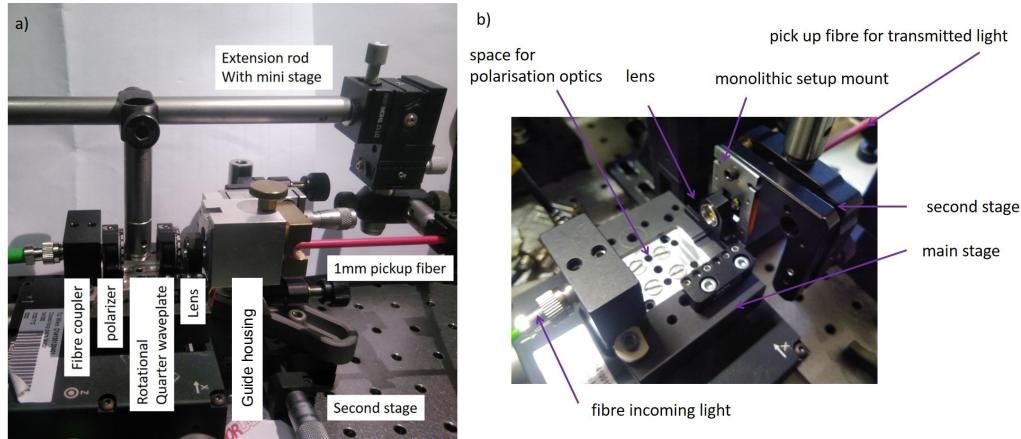


Figure 6.2: a) is a photograph of the real setup. The piezo assembly is contained inside the guiding housing. b) is a similar setup without polarization optics and the monolithic setup as main experiment. The main stage is necessary to move the laser beam with respect to the mirror chip. The polarization optics, consisting of a polarizer and a half-wave plate, are needed to investigate the birefringence. The lens focuses the beam onto the mirror. The experimental space is placed on the second stage. The mini stage on the extension rod is necessary to change the position of the plastic collection fibre. This fibre has to be in line with the incoming beam to pick up the transmitted light.

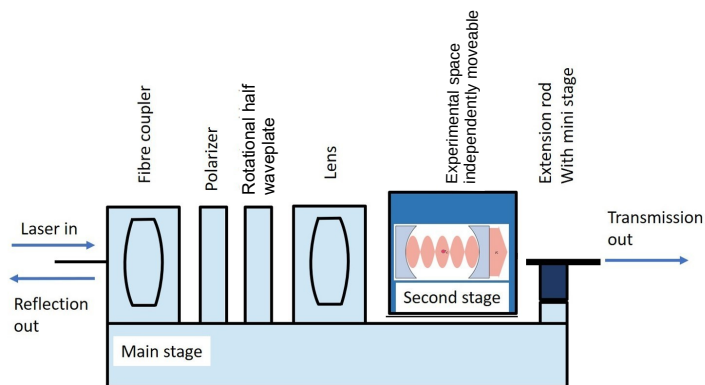


Figure 6.3: A schematic of the main stage. The main stage holds the fiber coupler, the polarization optics, the objective lens and the collection fiber on the other side. The cavity itself is mounted on an independent second stage such that the laser beam can be directed to different mirrors.

6.2 Results of the first run

The first production run was done in the early stages of this project. The design process is outlined in section 4.4. The shape of the mirrors is still far from perfect and the polishing is not optimized. The mirror coating has a transmission of 15 ppm, which means a reflectivity of 99.9985% without additional losses. The etch times are 160 s for the first etch and 16 min for the second etch. The biggest opening before etching is 52 μm in diameter and the smallest is 12.4 μm , as defined by the mask. The mask can be found in appendix B.4. All measurements presented in this section were performed on second biggest mirror, figure 6.4 indicates its position. This is the only mirror on that chip with a finesse above 100 000. All the others are around 20 000 or worse, due to shape deviations and surface roughness. The first chip served as a testbed for the different fabrication processes and allowed to identify problems.

6.2.1 Best finesse

The idea of this measurement is to draw a baseline so that we have a point form where we can improve the mirror. This measurement is done with a flat-curved configuration in a piezo tuned setup. The best finesse was measured at a very short cavity length of 40.5 μm . The ROC of this mirror is 900 μm . Details of how this number is calculated follow in section 6.2.4. In that regime the cavity is robust to alignment and shape imperfections, as we discussed in section 3.4.3. The insensitivity of very short cavities to shape imperfections is also shown in figure 3.14.

The measurements of the peak width were done with sidebands at ± 300 MHz. Instead of sweeping the laser, the cavity length was modulated using the piezo crystal. The measured signal is the transmitted light intensity.

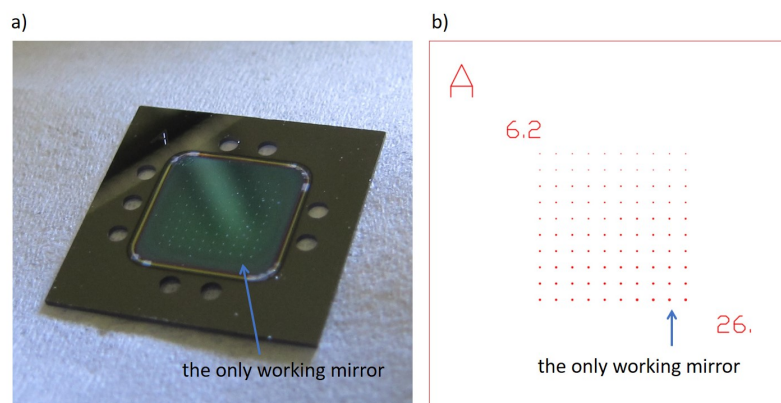


Figure 6.4: a) is a photo of the mirror chip and b) is a schematic of the mirror mask. Only one mirror works as intended. For the others, the finesse is very small or the signal is so weak that it is impossible to make a measurement. We assume that a combination of bad shape and large roughness led to poor cavity performance.

The piezo is set to a certain (high) voltage, this voltage is modulated¹ with a ca. 1 V signal at 500 Hz, causing a periodic change in the resonance frequency of ± 34 GHz. The oscilloscope is triggered every time the cavity is resonant. The raw measured data is shown in figure 6.5 a. Three Lorentzian peaks are fit to the data. The known frequency difference of the sidebands is now used to calibrate the frequency axis. To acquire good statistics, we repeat this measurement 100 times, fit each set of data and average over the results, summarized in figure 6.5. As this method measures the cavity resonance very quickly, it is insensitive to slow drifts of the cavity or the laser.

The theoretical maximum for a roughness of zero and a transmission of 15 ppm is around 3×10^5 . The measured finesse of $(1.4 \pm 0.2) \times 10^5$ means that some light is scattered due to the roughness. The measured roughness under the AFM of this chip is (0.6 ± 0.2) nm, results in a maximum finesse of 1.32×10^5 .

6.2.2 Finesse as a function of cavity length

We measure the cavity finesse as a function of the cavity length to find a good working point for the spacer thickness. The right spacer thickness is a critical point for a working curved-curved cavity. The spacer is used to define the distance between two mirror chips. In theory the finesse should high until the critical length is reached, as we discussed at length in section 2.6.4. For a flat-curved configuration the critical length is equal to the ROC and for a curved-curved configuration equal to 2 times the ROC. However, if the cavity gets longer the beam width on the mirror becomes also larger. Now the beam covers a bigger area on the mirror, which means that a shape aberration can have a large effect. Also the roughness has to be perfect over the full spot size on the mirror. This changes the finesse as a function of cavity length for real mirrors, as shown in figure 6.6.

In the measurements, three regimes can be identified: First, for very short cavity lengths, the finesse fluctuates up to very high levels. This is followed by a constant part. In the last part the finesse falls rapidly.

It is likely that the fluctuations for short cavities come from imperfections in the surface. There are some areas which are smoother than others. The focal point on the mirrors is moving due to drifts, we correspondingly see variations in the finesse. If this is true, reducing the roughness should be improve the fluctuations drastically.

In the second regime the beam diameter on the mirror gets bigger, averaging over the spatially varying roughness, therefore no fluctuations appear. As expected, the finesse in this regime is constant and limited by the roughness.

In the third regime the finesse decreases rapidly. Here shape imperfections are the limiting factors and lead to a decrease in finesse long before the theoretical limit of

¹ The modulator is homemade, schematics can be found in appendix B.1.2 and at <https://circuitmaker.com/Projects/Details/Georg-Wachter/Piezo-AC-with-Biase>

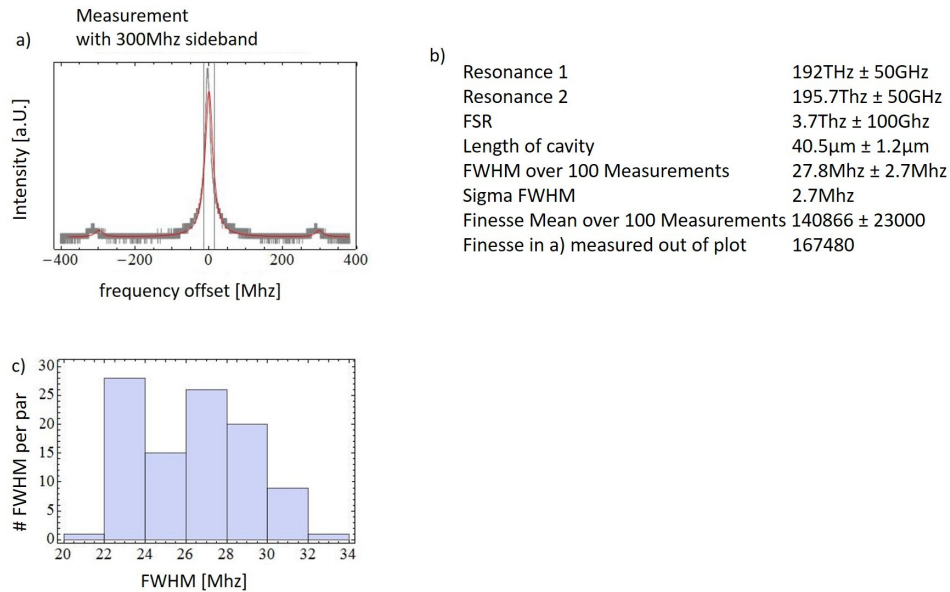


Figure 6.5: The results of a cavity measurement. a) shows a typical cavity transmission trace, the cavity resonance and the two sidebands are clearly visible. The x-axis has already been rescaled to frequency. A sum of three Lorentz functions (red line) is used to fit each peak. For every measurement, the resonance linewidth is determined, this is repeated 100 times. b) summarizes the results. The distribution of the FWHM linewidth is shown in the histogram in c).

around 1000 µm cavity length is reached. This means that the mirrors on this wafer have some roughness issues limiting the finesse, but the biggest problem is the shape which reduces the usable length.

We now explore how well these experimental results match the theory described in chapter 3, where the losses due to a imperfect shape are calculated. Figure 6.7 shows the outcome of the numerical simulation for three AFM measurements. The fits used to approximate the shapes and other details such as the finite radius for these simulations are presented in section 3.4.4.

6.2.3 Birefringence

Birefringence (cf. section 2.5.5) is an important indicator of how symmetric a cavity is. Birefringence is well known from optical materials, where each crystal direction has its own refractive index, which means that light with different polarizations behaves differently. Something similar can be observed in a cavity because of imperfections in the symmetry of the mirror pair. This leads to a situation where there are two different ROCs in the cavity [33]. The result is a splitting of the resonance peak as shown in figure 6.8, for the measurement we vary the input polarization with the

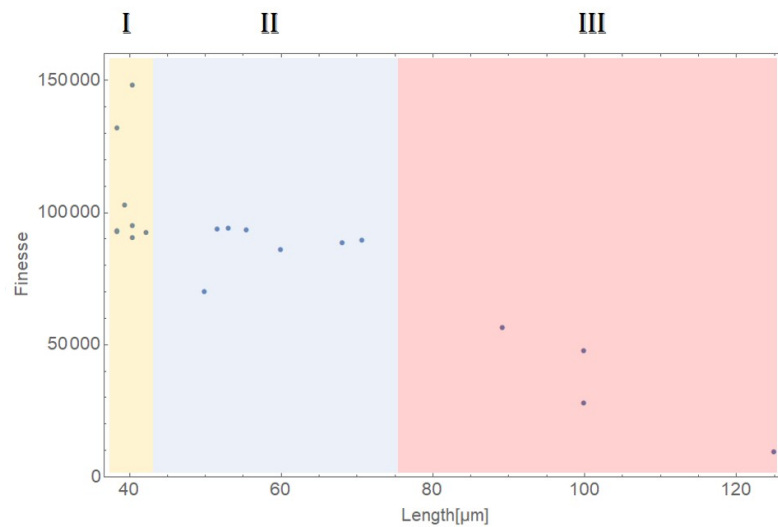


Figure 6.6: Dependence of the finesse on the cavity length. It is possible to identify 3 different regimes. For short length (yellow) the finesse is fluctuating. For a cavity length up to 75 μm the finesse has a rather constant value (blue) and for longer cavities the finesse drops rapidly.

half-wave plate in front of the objective lens (c.f. fig. 6.3).

Cavity birefringence can be observed due to a variety of reasons; first, different etch rates due to the crystal structure, for silicon this is unlikely because of the symmetric crystal structure. Second, because of misalignment, and third, stress inside the mirror coating can also lead to birefringence [67]. However, our measurements show that the birefringence is on the order of the peak width.

6.2.4 Spectrum

To measure or at least estimate the aberration of the ROC from the ideal form, we investigate the higher transverse modes. How the ROC can be determined from the frequency shift between the transverse modes is explained in section 2.6.3.

We measure the cavity spectrum over a full FSR. This measurement is again performed on the second biggest mirror in flat-curved configuration with variable length. The setup is optimized to get maximal light into the fundamental transversal mode (TEM_{00}). The cavity length is changed by a piezo driver over a FSR. This is equivalent to sweeping the laser frequency. During optimization of the spatial mode, also the input polarization is changed in a way to minimize the effect of the cavity birefringence. This reduces the intensity of all spectral components where the other polarization direction is needed.

The spectrum is recorded for two different cavity lengths, in figure 6.9 the measurement of a cavity with a length of 42 μm is shown and in figure 6.10 with 68 μm .

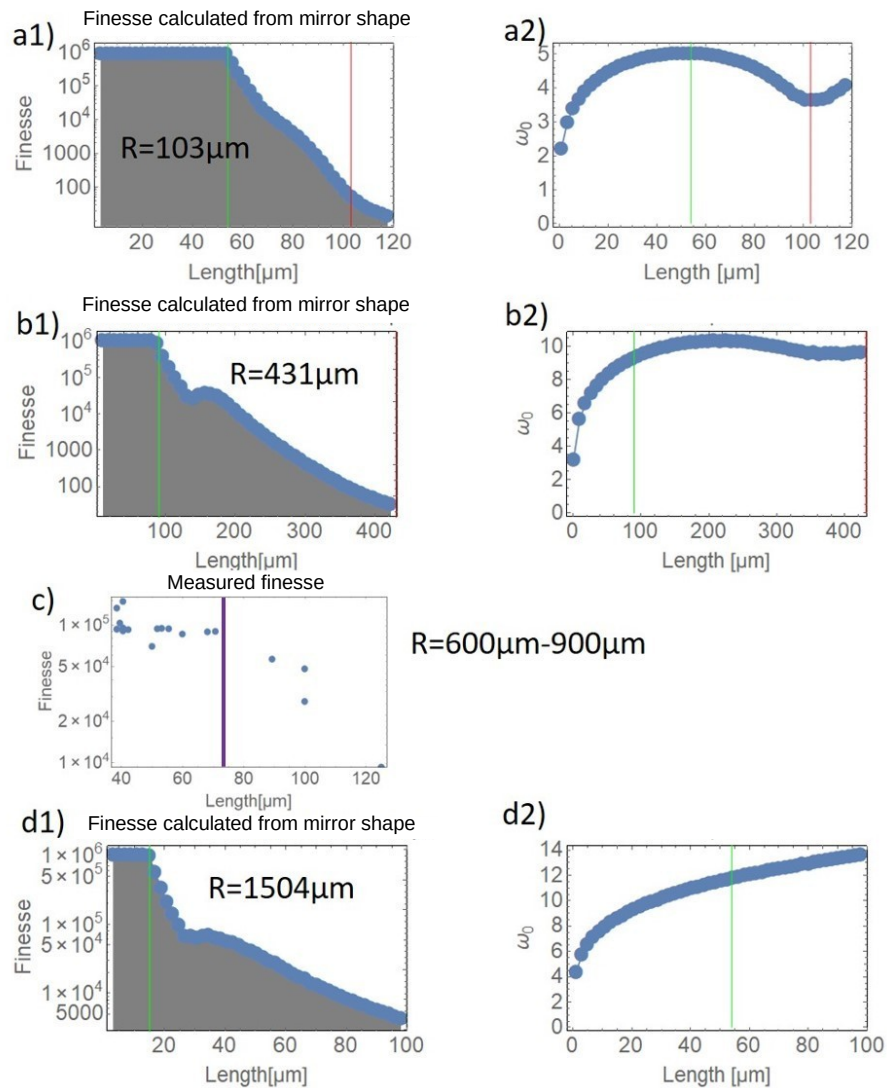


Figure 6.7: Results of the numerical simulation of three AFM-measured mirror shapes. The finesse vs. length is shown in a1), b1), d1), the beam waist vs. length in a2)-d2). The green lines are the positions at which the finesse reaches a value of more than 1×10^6 . We limit the finesse to this value in the simulation. This limit is chosen arbitrarily, for our mirrors 1×10^5 would be enough, however the qualitative result remains the same. The red line marks the radius of the mirror. This is the theoretical maximum where the finesse should drop for a perfect shape. In figure c), the length over finesse measurement from before is reproduced. Unfortunately, no AFM measurements are available for the only working cavity of the first run. The ROC of the cavity in c) is calculated for each cavity length from the frequency difference between the first and the second transverse mode. As discussed in section 6.2.4, it varies between 900 μm to 600 μm . The violet line in c) is approximately the position where $L/\text{ROC} = 0.1$. As the simulations do not include roughness, we can not show the measured fluctuations. The overall shape of the simulations and the measurement agree, the finesse stays constant over a range of cavity lengths and then drops sharply. In the measurement, the finesse stays high up until 80 μm , which is between the value observed in b) and d).

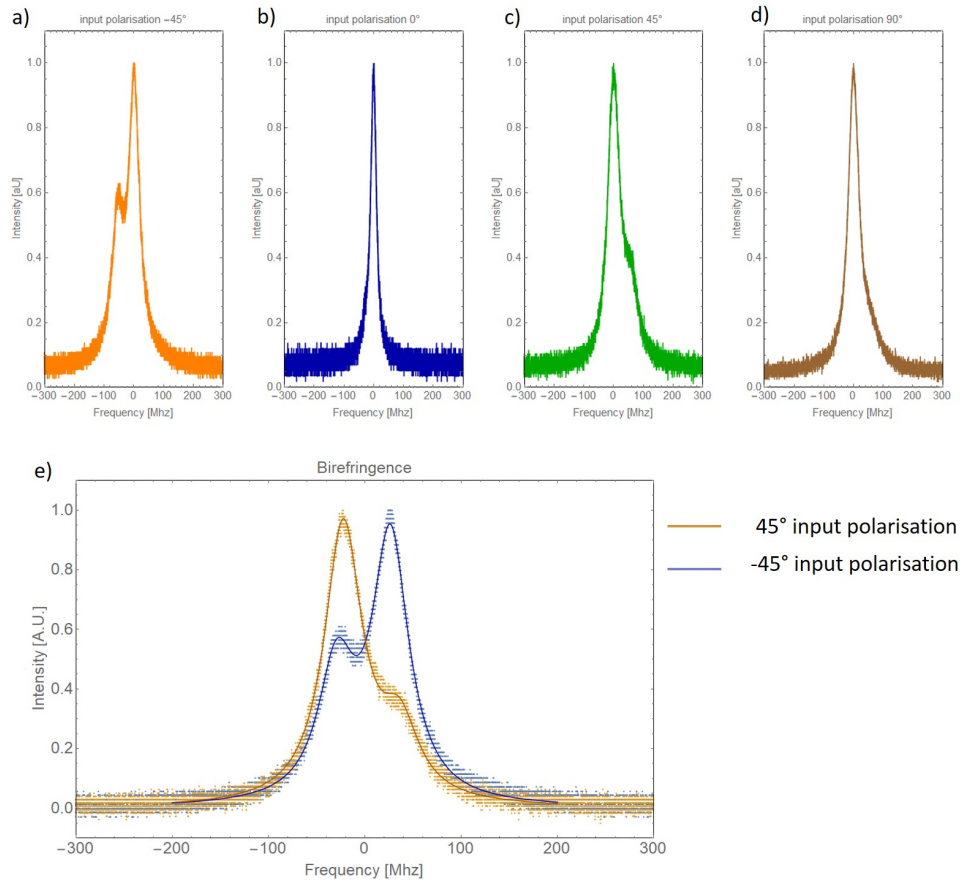


Figure 6.8: Birefringence measurement. a)-d) shows the cavity resonance peak for four different input polarizations. In e), the curves a) and c) are plotted together to highlight the birefringence. In b) and d), the two orthogonal polarizations are aligned to the "crystal axes" of the cavity. The peaks are shifted by (57 ± 10) MHz, which is slightly more than the full width at half maximum (FWHM) linewidth of (43 ± 5) MHz. The birefringence can also be expressed by the phase shift per round trip, as defined in equation 2.31, of $96.8 \mu\text{rad}$. These measurements use a flat-curved configuration at a finesse of $84\,000 \pm 1000$ and an FSR of 3.7 THz.

The goal of the measurements is to get information how constant the ROC is across the mirror. For a constant ROC the frequency spacing between the transverse modes should be constant. This is not the case here. Furthermore, the frequency of modes with $(1 + l + m) = \text{const}$ (equation 2.40), should have the same frequency. For real mirrors a small separation is found.

However, it is possible to calculate an effective radius of curvature from the frequency spacing between the modes. Equation 2.46 is used to calculate the effective radius from the frequency difference between the first and the second, the second and the third mode and so on. Because these modes have a different size on the mirror, this can be used to get information how constant the ROC over the mirror size is. In h) and i) and in f) and g) of figures 6.9 and 6.10 respectively, this variation of the ROC is shown, proving that the mirror shape deviates significantly.

6.2.5 Mirror characterization

At the end of the third year of my PhD, we had the great opportunity to purchase an advanced white light interferometer¹. This device allows a contactless surface characterization with a vertical precision of down to 0.1 nm. For more information, the reader is referred to the manual of this device and for example [68, 69]. The following subsection summarizes all data about the mirrors from the first production run that we acquired with the white light interferometer. I would like to point out that all other experiments in this thesis were performed done prior to the purchase of the white light interferometer.

The data from the white light interferometer shows good agreement with the AFM measurements from in the first and second year. Due to the very long acquisition time, only three mirrors were characterized by AFM. With the new white light interferometer it is now possible to measure all 100 mirrors in 5 h, which gives us the ability to analyze the mirrors in more detail.

In figure 6.11, cuts through all mirrors are shown. For this purpose, I developed a Python code to analyze the surface data. This code uses a pattern search function² to find the mirror in the data. With this information the data is cut into two slices. These slices are then leveled and shifted to make all different mirrors comparable. The gap between the surface and the mirror center appears because no light comes back from the walls of the mirror. As discussed before in chapter 4, the mirrors of the first run are not perfectly shaped and look more like bowls with a flat bottom, as we can clearly see from the cuts.

1 Filmetrics Profilim 3D

2 This function can found in the library opencv-python 4.0.0.21

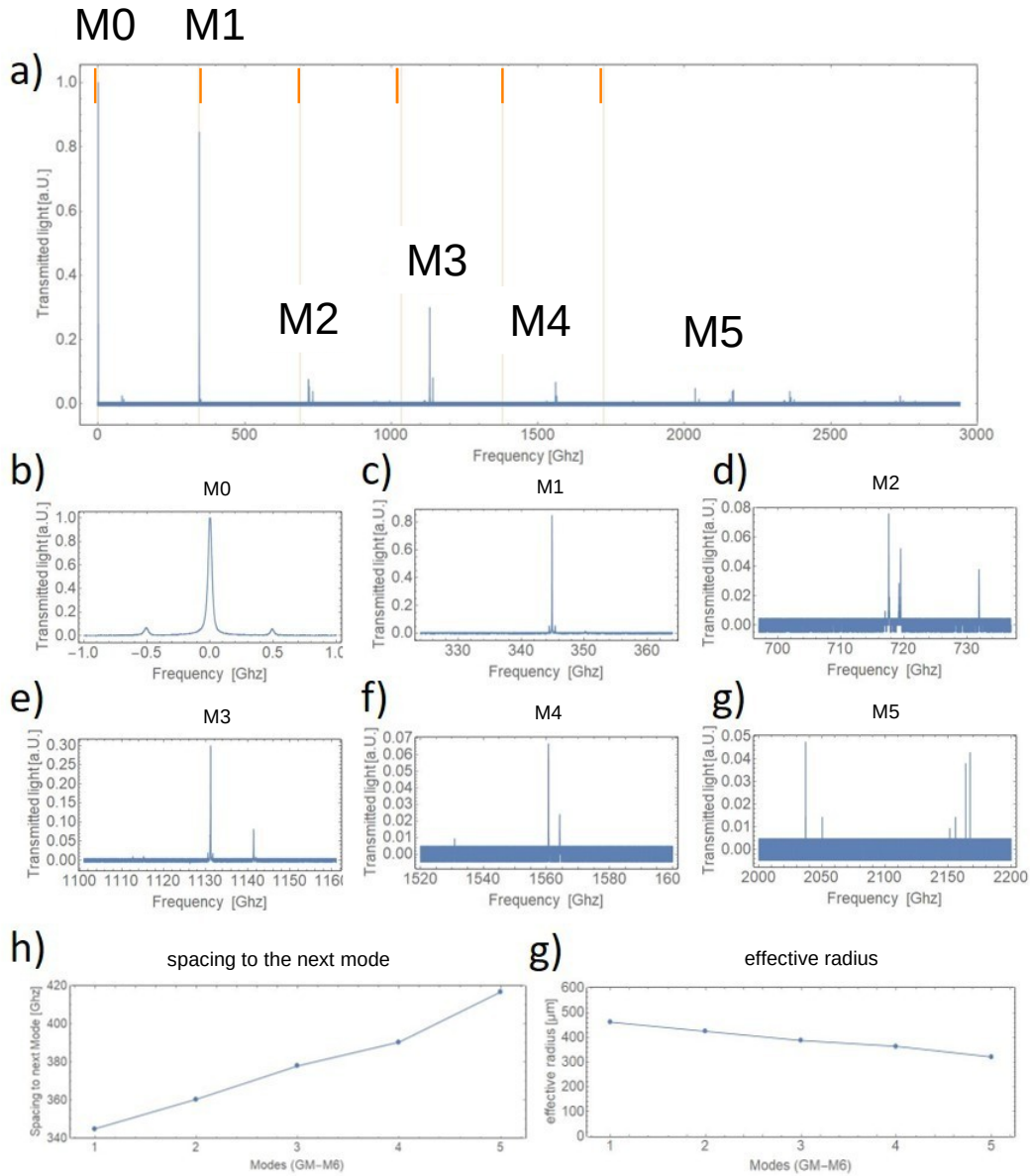


Figure 6.9: In a) the measured spectrum for a flat-curved mirror pair with a length of $42 \mu\text{m}$ and a finesse of 69 700 is shown. The orange lines mark the frequency spacing between the first and the second mode. It is clear that the spacing increases between higher order modes. b), c), d), e), f), g) are zoomed versions of the different modes. The fundamental mode in b) shows the two sidebands from the EOM. c) in the second mode two peaks are expected because of the broken symmetry of 01 and 10 the right one is suppressed due to the choice of polarization. d) is the third mode and three peaks can be found (02,20,11). h) is the frequency spacing between the modes and i) is the effective radius calculated out of this information.

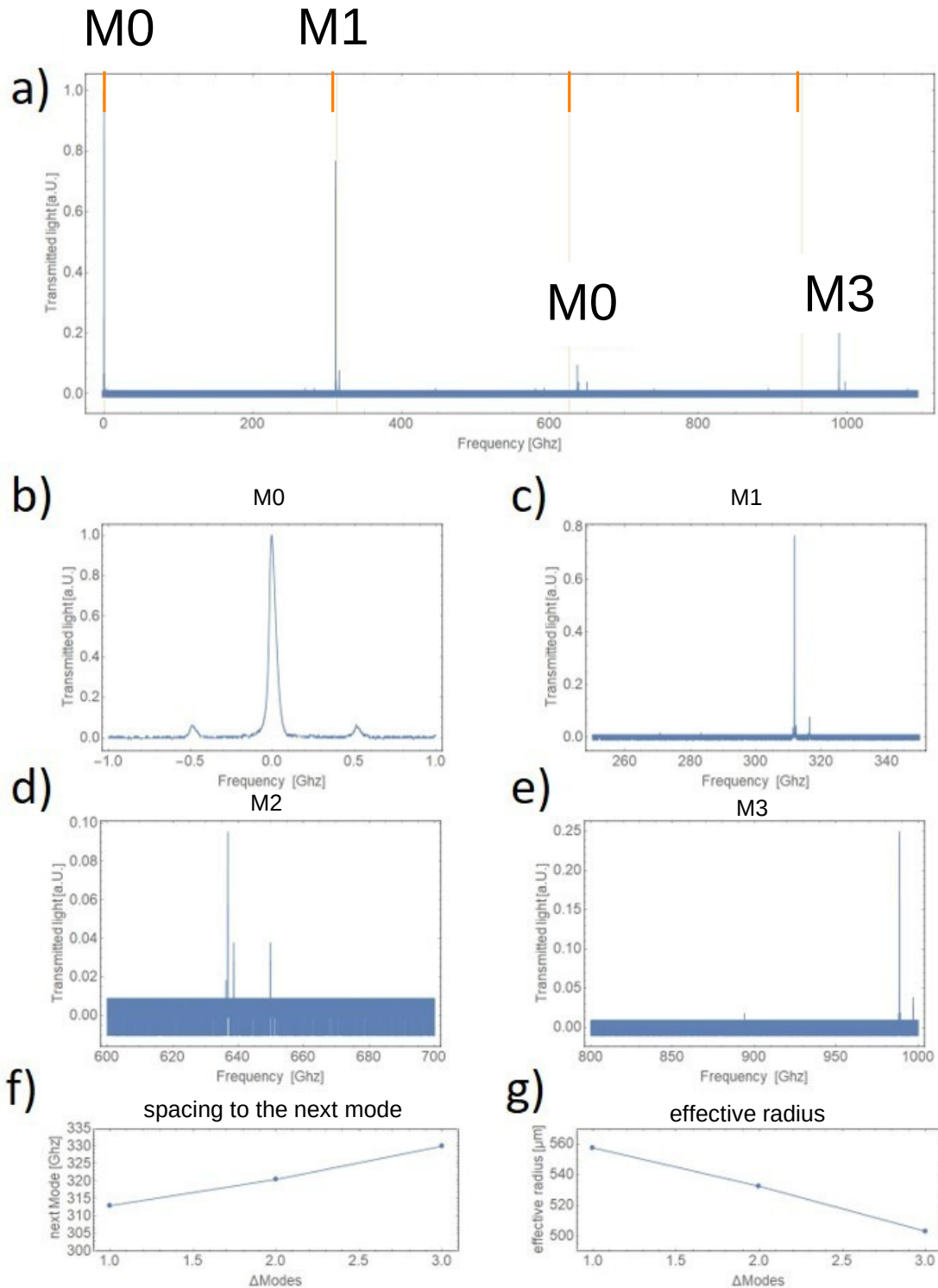


Figure 6.10: This is the same mirror pair as in figure 6.9 but with a longer cavity length of 68 μm and a finesse of 88 400. It was only possible to find the first four modes b), c), b), e) compared to six in the shorter cavity. Also, the radius calculations in g) give slightly different results.

In figure 6.12 the data of each cross section is analyzed by fitting a parabola through the center of the mirror. In that way the radius and the depth of the mirror is determined. This data agrees very well with the AFM data. The mirrors measured also by AFM are highlighted. The original AFM data is shown in figure 4.7.

The white light interferometer is also used to investigate the roughness of the mirrors. An example is shown in figure 6.13. Also for this type of measurement, the white light interferometer outperforms the AFM by far. There, the acquisition time for a single mirror as shown in figure 5.8 is on the order of hours.

6.2.6 Conclusion

We see from the finesse measurements that the roughness has to be improved. The variation of the finesse over length and the fact that the cavity spectrum contains many higher order modes with different frequency spacings indicates that the shape is far from ideal and has to be optimized. The rather small birefringence shows that we can safely assume our mirrors to be rotationally symmetric. The lessons learned from this first production run are important for the optimization of our fabrication techniques.

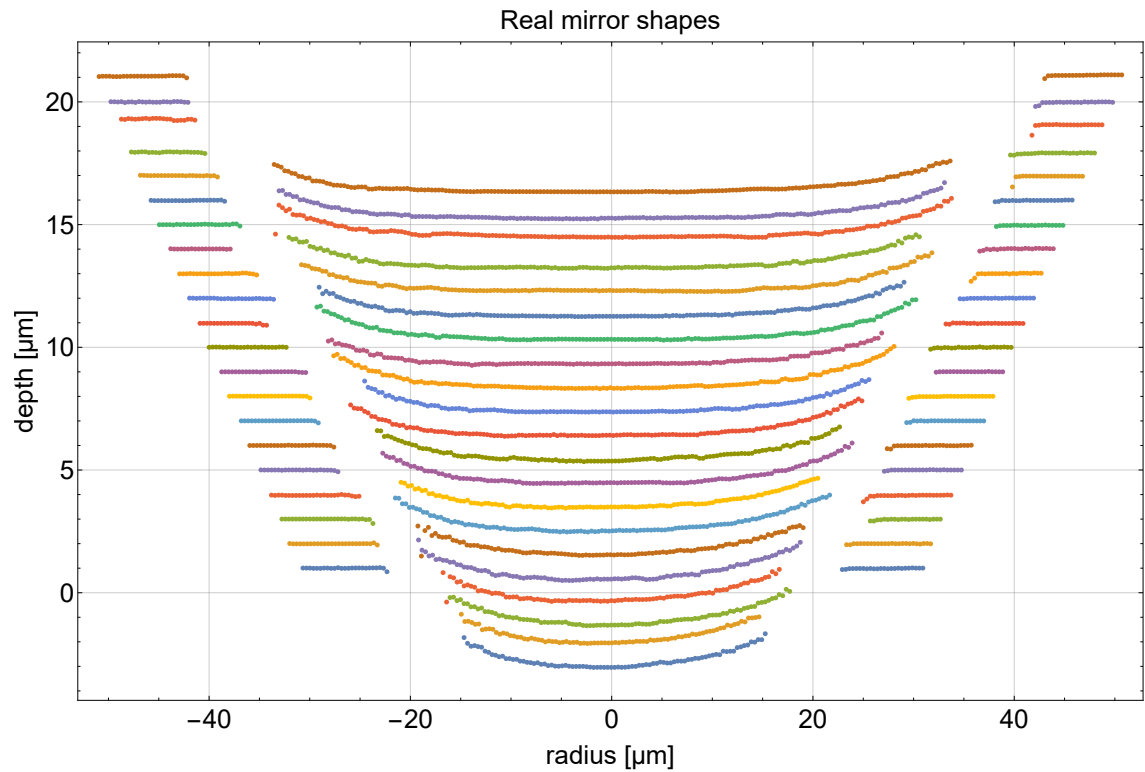


Figure 6.11: These lines show the shapes of each fifth mirror from the first run. Details are given in the text.

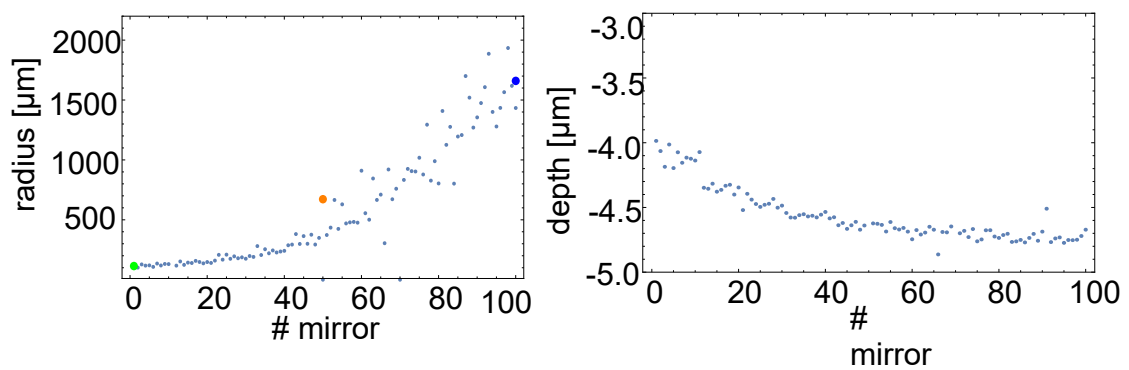


Figure 6.12: This is a summary of the results of the fits of the mirrors. a) shows the radius the colored points are the AFM measurements which are discussed in figure 4.7 in detail. b) shows the depth of the mirrors.

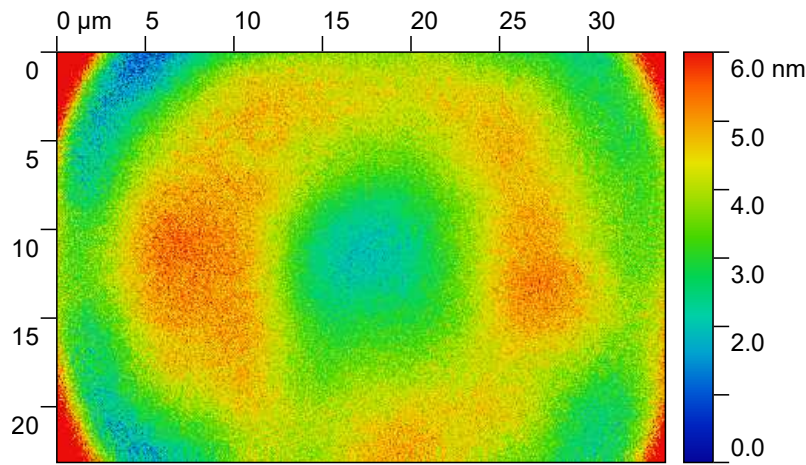


Figure 6.13: Roughness measurement taken with an optical profilometer. If the roughness of an area of $15\ \mu\text{m} \times 15\ \mu\text{m}$ is analyzed an RMS roughness (S_q) of 0.8 nm is found. For an area of $5\ \mu\text{m} \times 5\ \mu\text{m}$ we found an RMS roughness of 0.4 nm.

6.3 Results of the second run

The cavities produced in the second run represent the main result of this thesis. To the best of our knowledge, they hold the world record for the finesse of open, microscopic Fabry-Perot cavities.

The years in between the production runs were spent on optimizing the different steps of the fabrication, from a deeper understanding of the theoretical aspects, better etch recipes to improved polishing methods and higher mirror reflectivity. All this results in a much better yield: for the second run 88 % of the cavities work in the flat-curved configuration, compared to 1 % before.

In the curved-curved configuration, still $\sim 70\%$ of the cavities work, using a $100\ \mu\text{m}$ spacer chip and a cavity length of $160\ \mu\text{m}$. Only the smallest mirrors perform badly because the length to ROC ratio is too large.

In this section I will present a detailed investigation of all aspects of the mirrors from the second run. First, an overview of the results of the curved-curved configuration is given, then a comprehensive characterization of the cavities is performed to get information about birefringence and the ROC. These measurements are needed in preparation to the nano-particle experiment which will be discussed in chapter 8. However, the best performance of the cavities is expected for a flat-curved configuration. This gives us a figure of merit for the mirror quality from the second run.

The mirror coating for the wafer is designed for a transmission of just 5 ppm. This corresponds to $\mathcal{F}=620\,000$ when neglecting all other losses. The etch times for this wafer are 320 s for the first and 45 min for the second etch time, as compared to 160 s and 15 min in the first run. The much longer etch times result in a huge improvement

of the mirror shape. Figure 6.14 shows an overview of the chip.

All measurements on the mirrors from the second run were performed by Stefan Kuhn using their Toptica CTL-1550 laser. This new and fast laser allows to fully characterize a chip with 100 mirrors within two weeks. His measurements help us to get a full picture of the mirrors of the second run in a very short amount of time.

6.3.1 Measurements in curved-curved configuration

The new chips allow cavity measurements in the monolithic curved-curved configuration, with 70 % of all cavities showing reasonable transmission. Figure 6.14 summarizes a part of the measurements. We see that the ROCs, again calculated from the spacing between the transverse modes, are much smaller than before. This indicates that the shape at the center is much more parabolic, since the longer etching times brought us into the third etch regime (cf. sec. A.2). The drastic improvement in the shape is also apparent from the highest achievable ratio L/ROC , which used to be below 0.1 in the first run. Now we even find working cavities at $L/\text{ROC} = 1$. The best cavity has a finesse of 388 000 at $L/\text{ROC} = 0.5$.

In figure 6.15 the measurement of the birefringence is shown. The birefringence depends on the size of the mode on the mirror. Because the shape is not perfect, a larger beam diameter will sample more of the imperfections, this behavior increases the birefringence. For a smaller ROC the beam size on the mirror is bigger (at a given cavity length) compared to a mirror with bigger radius. This effect is shown beautifully in figure 6.15. For big ROCs, a slight increase of birefringence shows up. This appears because the shapes of the big mirrors are slightly worse than the small and middle-sized mirrors. A birefringence in the range of 50 μrad to 300 μrad per round trip is a wonderful result. In modern high finesse fibre cavities [33], a very similar birefringence of 49 μrad to 250 μrad and a similar frequency shift of around 20 Mhz can be observed.

Next, we are interested in the ROC of the mirrors. As before it is calculated from the spacing of the transverse modes. From the radius we can calculate important information like the waist of the cavity, the cooperativity (equation 2.36) and also the beam diameter for different positions inside the cavity. Furthermore, the radius also determines the theoretical stability limit.

Another question is how close to the stability limit the cavities can operate. For a curved-curved pair this limit is $L/\text{ROC} = 2$, where the beam diameter on the mirror goes to infinity. A small beam diameter on the mirror is generally preferred because shape imperfections are avoided. However in our measurements we see mirrors working even at $L/\text{ROC} = 0.95$, where the beam diameter on the mirror is 1.4 times bigger than w_0 while still achieving a finesse of around 94 000. In figure 6.16 this behavior is shown. This indicates a very good mirror shape. It also allows to use a thicker spacer chip, which means a bigger gap to place objects in the cavity as well as a longer photon lifetime and dramatically improved performance for nanoparticle

cooling (see chapter 8).

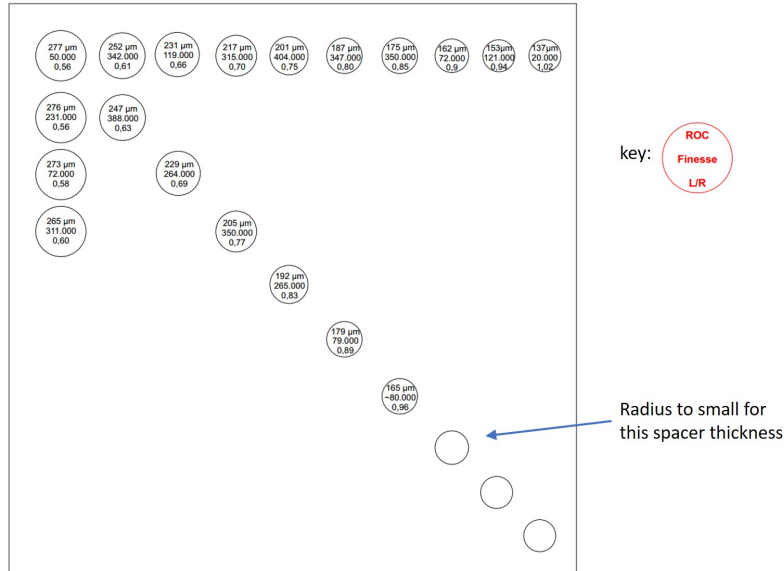


Figure 6.14: The mirror chip from the second production run. Each circle represents a measured mirror. The first number is the ROC, the second the finesse and the third the length to radius ratio for the curved-curved configuration with the spacer chip. For these measurements, a fixed spacer thickness of 160 μm in a curved-curved configuration was used.

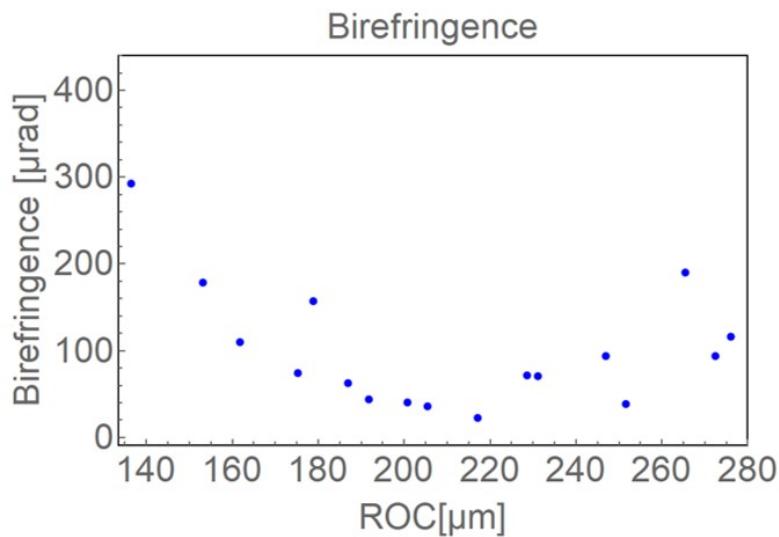


Figure 6.15: Birefringence of 19 different cavities expressed as the round-trip phase shift. Details are given in the text.

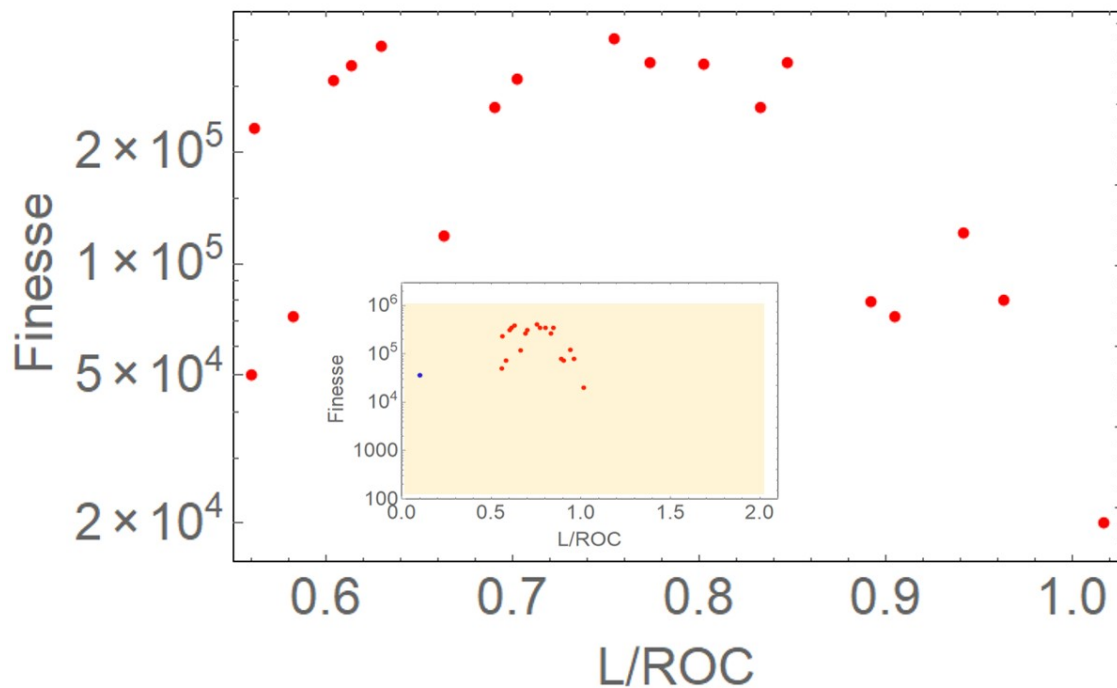


Figure 6.16: Finesse versus relative cavity length for symmetric cavities with a $160\ \mu\text{m}$ spacer. All middle sized mirrors of the second run have a finesse over 100 000. Only the biggest and smallest ones are under this value. The best ones reached a value of 404 000 at a radius of $201\ \mu\text{m}$ and L/ROC of 0.75. The inset shows the same data, but also including the cavity from the first production run in curved-curved configuration (blue dot), this cavity was also used for the experiments presented in chapter 8. The yellow area indicates the stability region.

6.3.2 Measurements in flat-curved configuration

To get the highest finesse we use the flat-curved configuration with the smallest possible length, the so called zero-length method, where mirrors are not screwed to the base but springs are used instead (see figure 5.9). This method guarantees self alignment between the curved and the flat mirror. For the measurement, we sweep the laser frequency instead of varying the cavity length with a piezo driver. This technique enable higher mechanical stability and a lower noise floor.

Because the reflectivity of the mirror coating is well known, it is possible to calculate the additional losses from the finesse. The zero length setup should have an almost perfect alignment and due to the short cavity length, the shape imperfections become irrelevant. This means the losses in this setup are dominated by surface roughness.

In figure 6.17 a representative finesse measurement is shown. As before, we calibrate the frequency axis by sideband modulation. The FSR is determined by sweeping the laser. The FSR is 8.136 THz which corresponds to a cavity length of 18.7 μm . With a peak width of around 15 MHz, we measure a finesse of $496\,650 \pm 9600$. This indicates that our polishing process works as we are at 80 % of the theoretical limit of 620 000 neglecting all losses. This result also fits to the AFM measurements shown in section 5.4, where the roughness values are in the range of 0.4 nm.

We fully characterize all 100 cavities of one chip published in [70]. 88 of them work well enough for a finesse- and ROC measurement. Figure 6.18 gives an overview of the full mirror field. There are no particular areas with very high or very low finesse. Only the very small mirrors in the first column have lower finesse and for some of them no finesse can be measured at all. There are three possible reasons for this behavior: First, it could be that the manufacturing parameters for these mirror sizes are not ideal. Second, the cavity is so short that it was impossible to measure the FSR or to see a resonance at all with the laser. Third, the finesse can go down because the mirror coating is not optimized any more if the resonance is more that ~ 9 THz away from the design wavelength.

We can now perform a statistical analysis of the finesse measurements. The idea of the cumulative probability shown in figure 6.19 is to calculate how many of the mirrors reach a given goal. The graph shows that all of the 88 working mirrors reach a finesse above 150 000 and 59 % reach a finesse of 400 000 or more. For two of them a finesse of more than 500 000 is found. This result shows how repeatable our process of mirror production is.

From the AFM measurements of the first run we know that the depth is roughly the same for big and middle sized mirrors. But in the summary plots in 6.21, we see that the mirror with the biggest ROC is not the cavity with the longest length. A tilt of the flat mirror is the best explanation for this behavior. The cavity length is plotted without and with tilt correction in figure 6.22. We found a tilt of 1 nm per

μm in x -direction (the same direction as the rows) and $0.44\text{ nm per } \mu\text{m}$ in the other direction. The most likely explanations for this tilt are either dust particles in the μm size on the chip or a non-planar mirror layer.

In 6.22, the ROCs of all cavity mirrors are shown. The effective ROCs calculated from the second harmonic of the cavity mode follow a smooth curve, which makes it possible to calculate the ROC for given process parameters and opening diameters. This can be used as calibration in the design process as discussed in chapter 4.

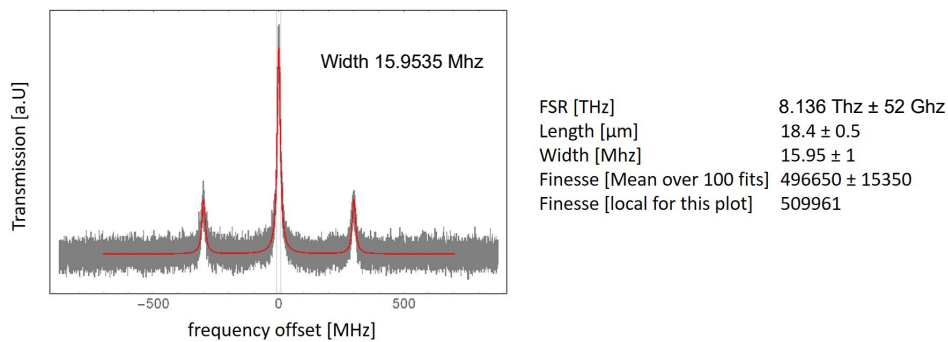


Figure 6.17: Typical finesse measurement of the second production run in a flat-curved configuration.

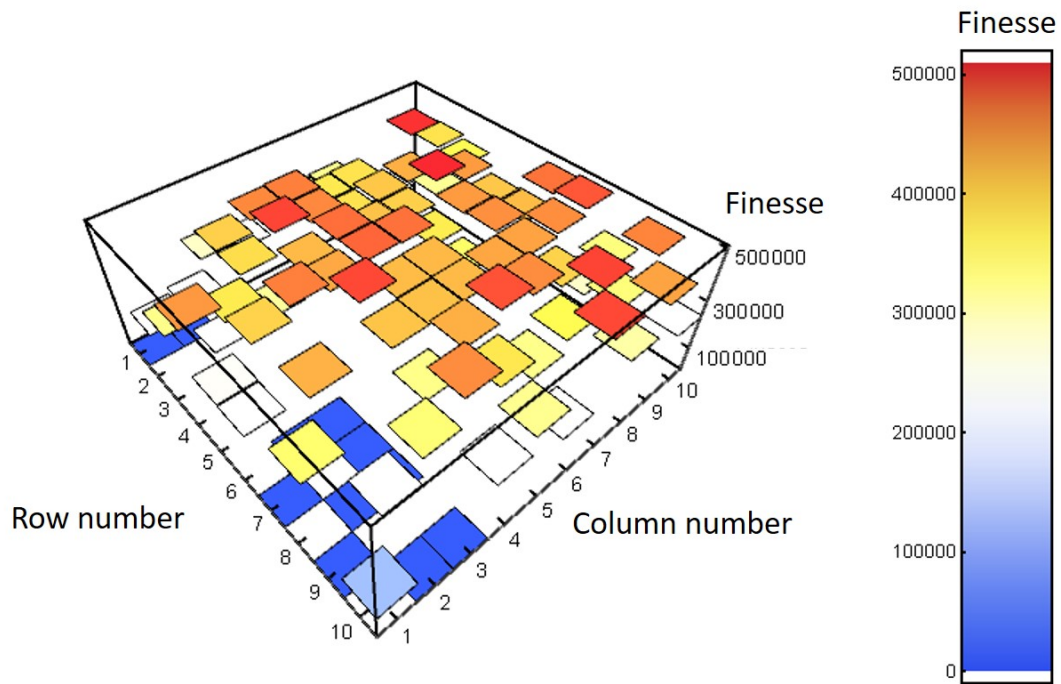


Figure 6.18: The measured finesse for all 100 mirrors. Distribution of the finesse over the whole chip is reasonably even. Only for the smallest mirrors in column 1 is generally low.

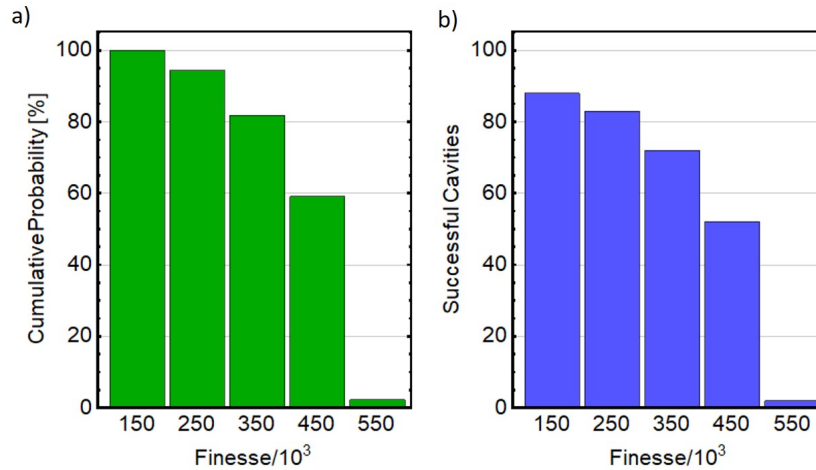


Figure 6.19: Cumulative probability for the cavity finesse, in both absolute (blue) and relative numbers (green). The first bar shows that 88 cavities are measured and all of them (100%) are above 100 000 and the last bar means that only two reached a finesse of more than 500 000. It is remarkable that 50% of the mirrors have a finesse over 400 000

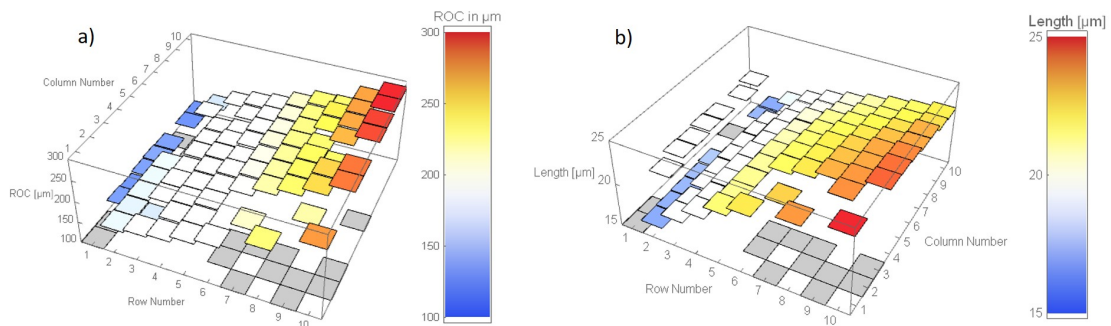


Figure 6.20: The results of the ROC measurements in a) and the cavity length measurements in b). It is visible that the biggest ROC (row 10, column 10) does not correspond to the longest cavity, which indicates that there is a small tilt in the chip assembly.

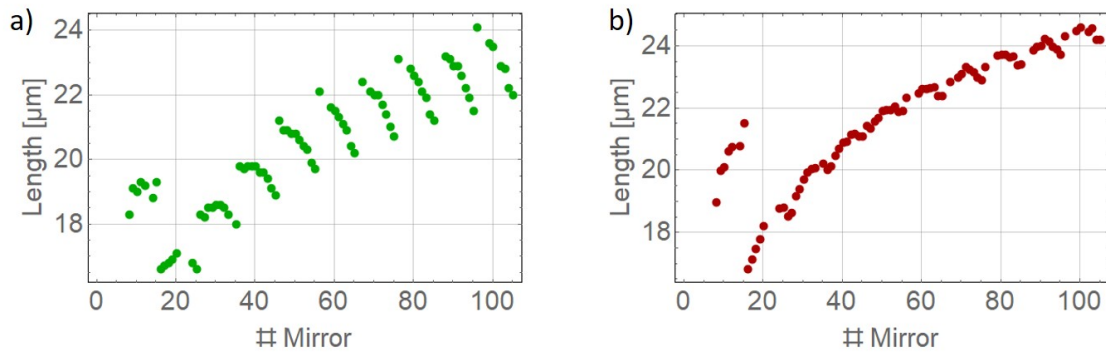


Figure 6.21: a) shows the cavity length data without tilt correction. b) shows the same data with tilt correction. The jump in the first 15 points appears because these points were measured one day after the other 85 mirrors. Due to thermal drifts the first points are offset by $6\ \mu\text{m}$.

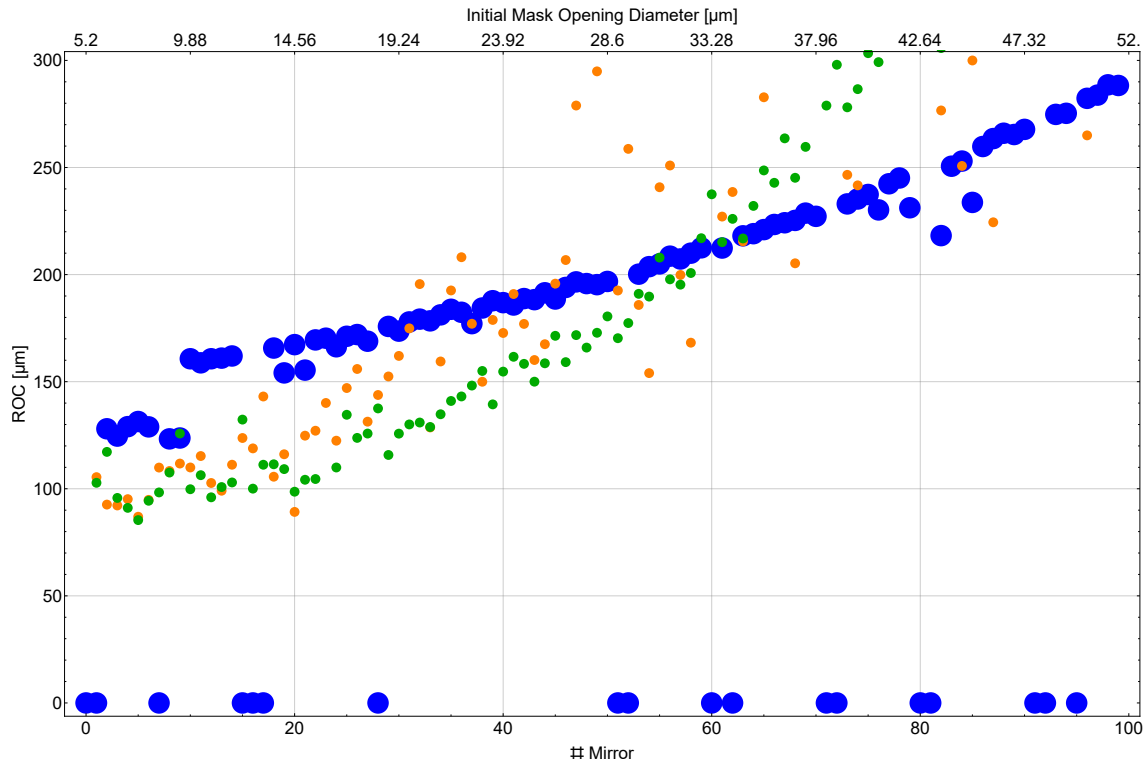


Figure 6.22: ROC measurements for all mirrors. The blue points are the ROCs calculated from the transverse mode spectrum. If it was not possible to measure the ROC, the value is set to 0. The points follow a smooth curve, a bigger initial opening diameter results in a larger ROC. This measurement gives the effective ROC as seen by the light in the cavity. Another way of determining the ROC is using the white light interferometer to measure the shape of a mirror and fit a parabola to its center. The results of these measurements are shown for a fit region of $10\ \mu\text{m} \times 10\ \mu\text{m}$ (green) and $20\ \mu\text{m} \times 20\ \mu\text{m}$ (orange points). Obviously the interferometer data is noisy and depends strongly on the chosen fit region. This data is only shown for reference, to get reliable information about the ROCs from the white light interferometer, a more sophisticated analysis algorithm has to be developed in the future. This should account for the growing mirror size, use a round instead of a quadratic window and weigh the data appropriately. Once this algorithm exists (and works reliably), the advantage would be a speedy ROC analysis without the need to construct a cavity.

6.3.3 Mirror characterization

We performed the same white-light interferometer measurements on the mirrors of the second production run. In figure 6.23, cross-sections of some mirrors are shown. The analyzing method is the same as before (see section 6.2.5). The mirrors are deeper than before, from 4.4 μm in average in the first run to around 9.5 μm in the second. This leads to a better, more parabolic shape.

All shapes in figure 6.23 have a gap in the data. Around the edges of the mirrors, the angle of the surface is too big, which means that no light can be reflected back to the optics. To solve this issue, a tilted measurement is performed. This is not the usual way to make a measurement on a white light interferometer. In contrast, for a normal measurement, it is important to get the measured surface as parallel as possible to the focal plane. If not, the algorithm of the device fails to reconstruct the surface. In our white light interferometer some more advanced reconstruction algorithms are built in, which are typically used to measure rough surfaces. They are more forgiving if noisy or missing data occurs during the measurement. With the help of these algorithms, it is possible to perform a tilted measurement. The result of this is shown in 6.24.

Figure 6.25 shows a roughness measurement of the mirrors of the second run. The roughness is better than from the first production run (compare with figure 6.13). The improvement of 0.2 nm seems small, but as the losses are exponentially dependent on the surface roughness, this is the difference between a finesse of 100 000 and 500 000 as discussed in 4.2.3.

6.3.4 Conclusion

We have learned enough from the first run to make the second run significantly better. The results of this effort are shown in the last section. We have improved the mirror production in a way that it is now possible for us to reliably produce mirrors of high quality. We are now able to design novel experiments for the fascinating world of quantum optics.

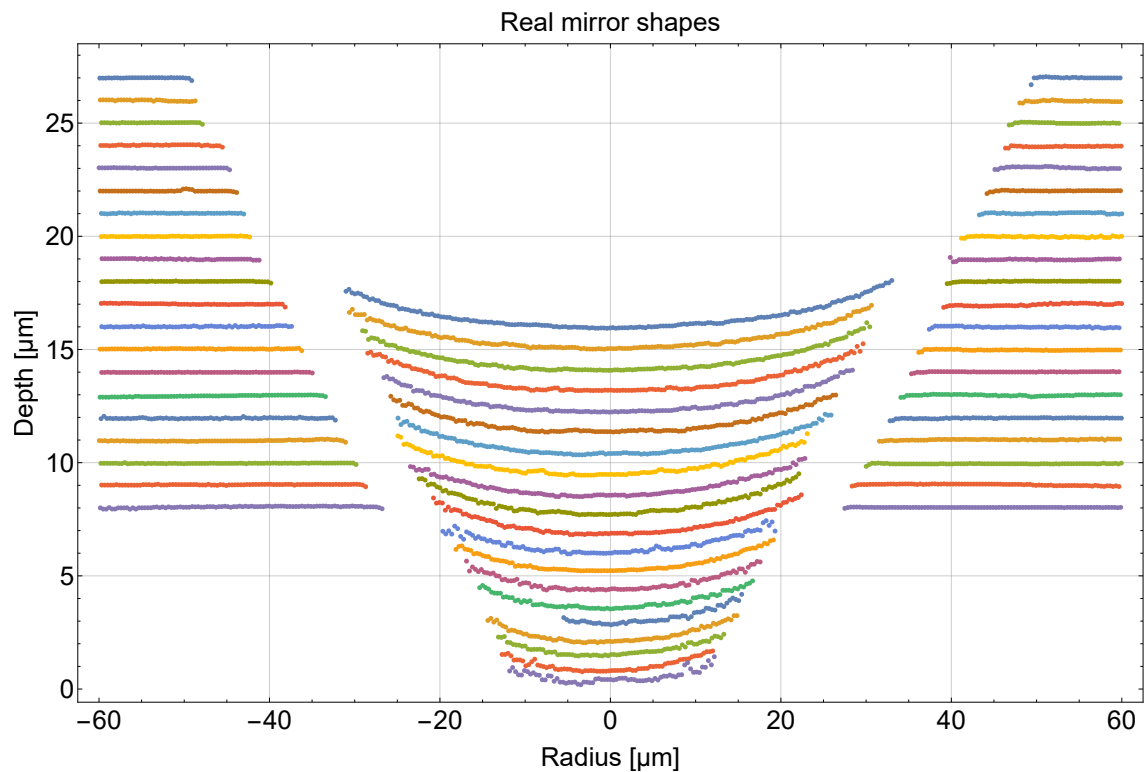


Figure 6.23: The shape of 1/5 of all 100 mirrors from the second run. Details in the text.

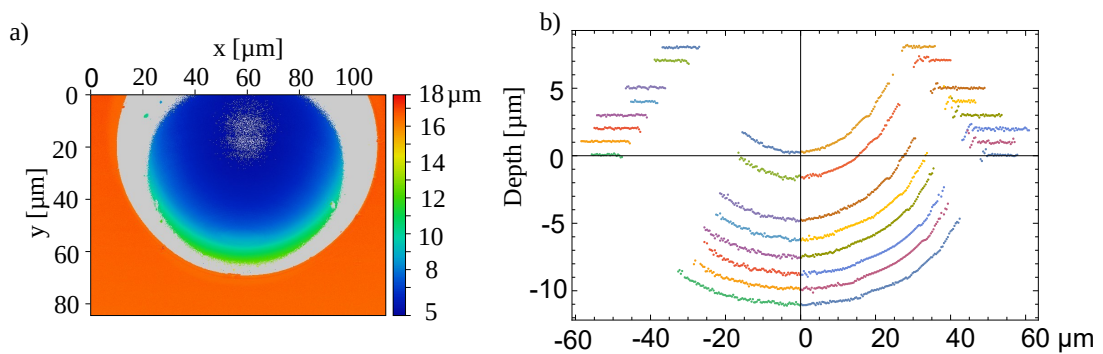


Figure 6.24: Tilted measurement of the mirror shapes. a) shows a typical measurement result, the grey area corresponds to the "missing" data points. b) shows the shape of 9 mirrors from the tilted measurement. The left half is the cut in x -direction without tilt, still showing a large gap. The right half is the cut in y -direction, the gap is almost gone.

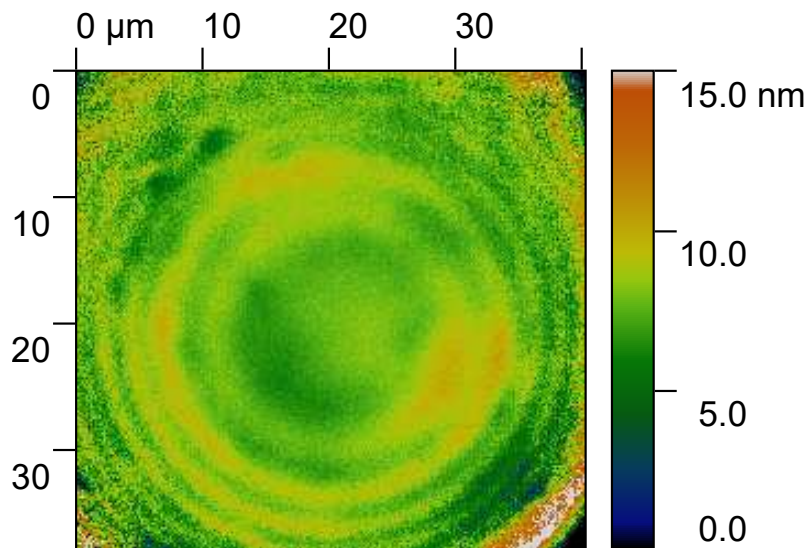


Figure 6.25: The roughness inside a mirror. The RMS roughness (S_q) over an area of $15\ \mu\text{m} \times 15\ \mu\text{m}$ is $0.64\ \text{nm}$ which is an improvement of $0.2\ \text{nm}$ from the last run. For an area of $5\ \mu\text{m} \times 5\ \mu\text{m}$ a roughness RMS of $0.27\ \text{nm}$ is found.



Die approbierte gedruckte Originalversion dieser Dissertation ist an der TU Wien Bibliothek verfügbar.
The approved original version of this doctoral thesis is available in print at TU Wien Bibliothek.

CHAPTER 7

Cavity containing a dielectric chip

In this chapter cavities, containing a dielectric chip are discussed. In the first sections the theoretical background is presented after which I show the experimental results for two different dielectric materials, silicon and diamond.

Experimentally, silicon is the simplest material to implement because only the flat mirror has to be flipped to perform the experiment. Also the losses in the cavity should be small due to the anti-reflection coating and high purity of the silicon. Absorption inside the silicon is well understood [71] which make this material the perfect choice to begin with.

Because diamond can contain nitrogen vacancies (NV) [72], a thin diamond chip is a very interesting object inside a cavity. The diamond is not anti-reflection coated so we can expect a more complicated spectrum. The wavelength of the laser used for the measurements is still at 1550 nm, which is not resonant with any NV transition.

The long-term goal of these experiments is to couple a quantum emitter to the cavity. For such a system, the losses are crucial. The losses for an empty cavity are discussed in chapter 4. The losses introduced by different dielectric materials are discussed here.

The next section is split in two parts: first I discuss the losses due to absorption. In the second part, losses at the interface due to the change in the index of refraction and surface roughness are investigated.

7.1 Losses due to absorption

The absorption inside the dielectric material is higher than in air, where the absorption coefficient is obviously near zero, depending on the gas composition, water droplets and dust. Here absorption is discussed using silicon, as the effect is well understood and measured to a high precision there. The absorption in silicon is very small at the relevant wavelength, but a high-finesse cavity can still be affected by it. The reason for this behavior is that the light passes the dielectric material many times, which turns this small effect into a major loss channel.

The losses inside an ultra pure silicon crystal are dominated by free carrier absorption coefficient (FAC) [73], where the photons are absorbed by electrons in

the conduction band. This effect depends on how the energy bands look like in the semiconductor. Any impurity or doping changes the bands and also the absorption of photons. This can be described by the simple equation:

$$\alpha = \text{FAC} \cdot \rho_n, \quad (7.1)$$

where α is the absorption coefficient which depends of the FAC and ρ_n describes the density of impurities.

For n-type silicon at 1550 nm, the FAC is found to be $(7.7 \pm 1.7) \times 10^{-18} \text{ 1/cm}^2$ [71]. For the silicon wafers used in this work, the density of phosphorous atoms is below 10^{-14} cm^{-3} , which means the absorption is $10^{-7} \text{ }\mu\text{m}^{-1}$. With equation 4.2, a limit on the finesse can be calculated depending on the thickness of the silicon. Figure 7.1 shows a parametric plot of the finesse limit, depending on the impurity density and the thickness of the dielectric. For a full round trip (two times the thickness of one silicon chip) of around $400 \text{ }\mu\text{m}$ we found a limit of 72 000 for the finesse. For a real cavity, losses due roughness, the shape and other loss channels will further reduce to this limit.

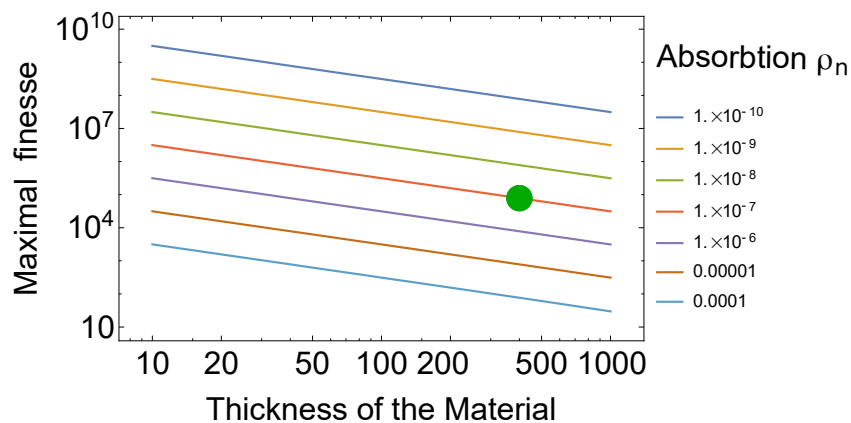


Figure 7.1: Best possible finesse, assuming the absorption inside the dielectric layer is the only limiting factor. The cavity used in this work is represented by the green dot. The color code is the absorption inside the medium per μm .

7.2 Losses at the interface

The spectrum of a cavity containing a dielectric layer can be calculated with a matrix method [74, 75], which is usually used to describe optical multilayer structures. The idea of the matrix method is to describe each surface and each distance in the cavity by a matrix. The matrix \mathbb{L}_i describes the propagation through the layer i with a thickness d_i :

$$\mathbb{L}_i = \begin{bmatrix} e^{-i\xi_i d_i} & 0 \\ 0 & e^{i\xi_i d_i} \end{bmatrix} \quad (7.2)$$

ξ is defined as $\xi_i = (2\pi\lambda)\bar{n}$, where λ is the wavelength of the light and \bar{n} is the complex refractive index defined as: $\bar{n}_j = n_j + i \cdot \kappa_j$. The imaginary part κ_j of the refractive index describes the absorption in the material. We can write the electric field in the following way:

$$E(z,t) = \left[E_0 \cdot e^{i\left(\frac{2\pi}{\lambda}\bar{n}z - \omega t\right)} \right] = e^{-\frac{2\pi}{\lambda_0}\kappa z} \left[E_0 \cdot e^{i(kz - \omega t)} \right] \quad (7.3)$$

If we assume that $\frac{2\pi}{\lambda_0}\kappa z$ is small, we can make the simplification:

$$e^{-\frac{2\pi}{\lambda_0}\kappa z} \approx 1 - \left(\frac{2\pi}{\lambda_0}\kappa z\right) = 1 - \rho \quad (7.4)$$

Here ρ is the total absorption coefficient of a layer. The imaginary part κ of the complex refractive index \bar{n} can now be written as:

$$\kappa = \frac{\lambda_0}{2\pi} \cdot \rho \cdot 1/z \quad (7.5)$$

Interface losses, for example due to roughness, have to be modeled by adding a thin layer of absorbing material. To describe reflection and transmission at the interface between layer i and j we introduce another matrix:

$$\mathbb{I}_{ij} = \begin{bmatrix} 1 & r_{ij} \\ t_{ij} & t_{ij} \\ r_{ij} & 1 \\ t_{ij} & t_{ij} \end{bmatrix} \quad (7.6)$$

The transmission is described by $t_{ij} = 2\bar{n}_j/(\bar{n}_j + \bar{n}_i)$ and the reflection by $r_{ij} = (\bar{n}_j - \bar{n}_i)/(\bar{n}_j + \bar{n}_i)$. Note that this matrix does not include any losses. For our cavity mirrors we use r and t directly.

7.2.1 Cavity in vacuum

We start with the simple case of an empty cavity to demonstrate the matrix method. In figure 7.2 a sketch of the situation is shown. For the first interface we assume a transmission of 10 ppm and a reflection of: $1 - 10 \text{ ppm} = 0.99999$ which gives us the first matrix \mathbb{I}_{IA} (input to A). The next matrix \mathbb{L}_A describes the propagation through

the first dielectric zone. The matrix \mathbb{I}_{AB} describes the middle surface. Because the cavity is empty, this matrix is the unit matrix, followed by the second propagation matrix \mathbb{L}_B and the last surface \mathbb{I}_{BO} (B to output). In mathematical terms, the system matrix \mathbb{S} can be written as:

$$\mathbb{S} = \mathbb{I}_{IA} \cdot \mathbb{L}_A \cdot \mathbb{I}_{AB} \cdot \mathbb{L}_B \cdot \mathbb{I}_{BO} = \begin{bmatrix} S_{11} & S_{12} \\ S_{21} & S_{22} \end{bmatrix} \quad (7.7)$$

The reflection- and transmission coefficients S_R and S_T of the whole system are now defined as $S_R = S_{21}/S_{11}$ and $S_T = 1/S_{11}$. The spectrum of a cavity can now be calculated as $S_T(\lambda)$. In figure 7.3 the spectrum of an air cavity is calculated using the presented matrix method. As shown in the figure, the peaks are evenly spaced and have the same width, which leads to the same intensity.

7.2.2 Losses at a rough surface inside the cavity

In this section, a surface roughness at the interface \mathbb{I}_{AB} is introduced. For the purpose of this calculation, it makes no difference if the light is absorbed or scattered out of the cavity, because thermal effects are not included. This calculation again assumes an empty cavity, to see only the effect of the losses at the surface and no additional effects from a change of the dielectric constant.

In figure 7.4, the spectrum of a lossless cavity with a length of 125 μm and a mirror transmission of 100 ppm is shown. As expected for a cavity with no loss and only one dielectric, the reflection goes to zero at the position of a resonance and the resonances are evenly spaced. 7.5 shows a zoomed version of the resonances

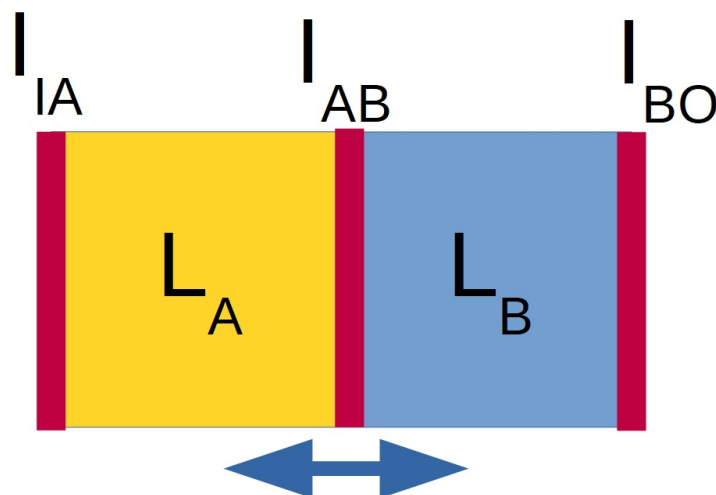


Figure 7.2: A simplified picture of a cavity. The 3 interfaces are red, the two dielectrics are yellow (A) and blue (B).

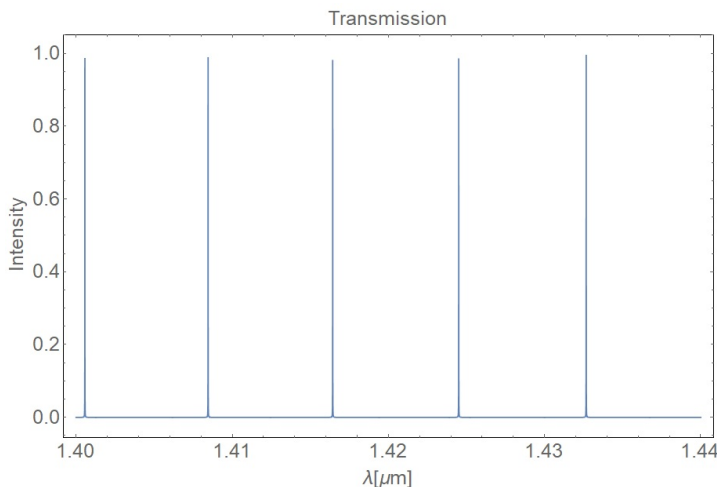


Figure 7.3: Calculated transmission spectrum of an air cavity. Note that the peaks are evenly spaced and also have the same intensity. For the purpose of clarity, the losses are increased to 0.001. When using the real value of 10 ppm, the peaks become a lot thinner than one pixel.

with different losses. An infinitely thin absorbing layer is introduced by adding a complex refractive index to the interface \mathbb{I}_{AB} . The interface is placed at a position of 100 μm after the first mirror and 25 μm before the second mirror. The effect of this additional loss is different for each resonance. The resonances B,D,F,H (labels from figure 7.4) are weakly affected by this absorption, while the others (A,C,E,G) are fully suppressed when the absorption is in the same range as the transmission of the mirrors.

In the particular case of a loss of 100 ppm at the interface, only half of the resonances are visible. The reason for this behavior is that if the field at the interface has a node, there is zero absorption, while an anti-node at the interface experiences maximum absorption.

The approximation that the layer of absorption is infinitely thin is applicable if the roughness is a lot smaller than wavelength of the light. This is true for our case, where the wavelength is around 1.55 μm and the measured surface roughness is in the range of 1 nm.

To summarize we can say that scattering or absorption from an infinitely thin layer inside a cavity change the intensity profiles of the resonances and can also suppress some resonances completely.

7.2.3 Losses due to dielectric effects

Now we introduce a dielectric material in the cavity and perform the same calculation as above. We use diamond as a first example. The width of zone A is set to 100 μm and zone B with the diamond to 25 μm to 27 μm . Figure 7.6 c) shows the calculated

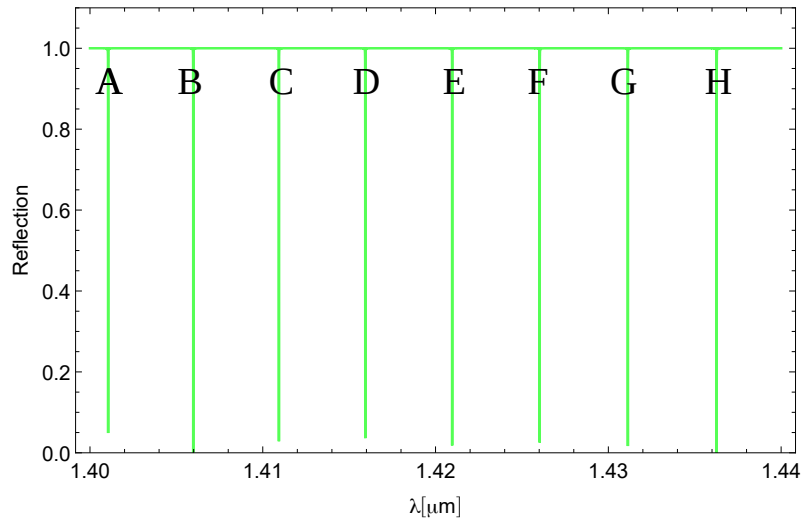


Figure 7.4: The reflection spectrum of a lossless air cavity with a length of $125\ \mu\text{m}$ and a mirror transmission of $100\ \text{ppm}$. Note that the resonances all have the same depth, the differences in the plot arise from plotting extremely narrow features. A detailed view on the resonances is given in figure 7.5

reflection spectrum of such a cavity. The rather complex spectrum can be explained by avoided crossings between the resonances in the air- and the diamond part of the cavity.

A vertical cut through 7.6 c) at $25\ \mu\text{m}$ diamond is shown in figure 7.7. The calculation does not include losses at the interface, yet the resonance dips do not have the same depth any more and are no longer evenly spaced.

In figure 7.8, detailed plots of the first eight resonances from figure 7.7 are shown, with varying amount of interface loss. As in 7.5, some resonances are hardly affected at all by the loss.

The expected spectrum quickly became very complex. We did not include any higher modes in this calculation, which means the real spectrum in the experiment will look even more interesting.

7.2.4 Effects of anti-reflection coating

Now we discuss the case where an anti-reflection coating is applied on the surface between the two dielectric materials. For an ideal anti-reflection coating, the matrix takes the form

$$\mathbb{I}_{AB} = \begin{bmatrix} 1 & 0 \\ 0 & 1 \end{bmatrix}. \quad (7.8)$$

This changes the results as shown in figure 7.9. The spectrum is spaced evenly

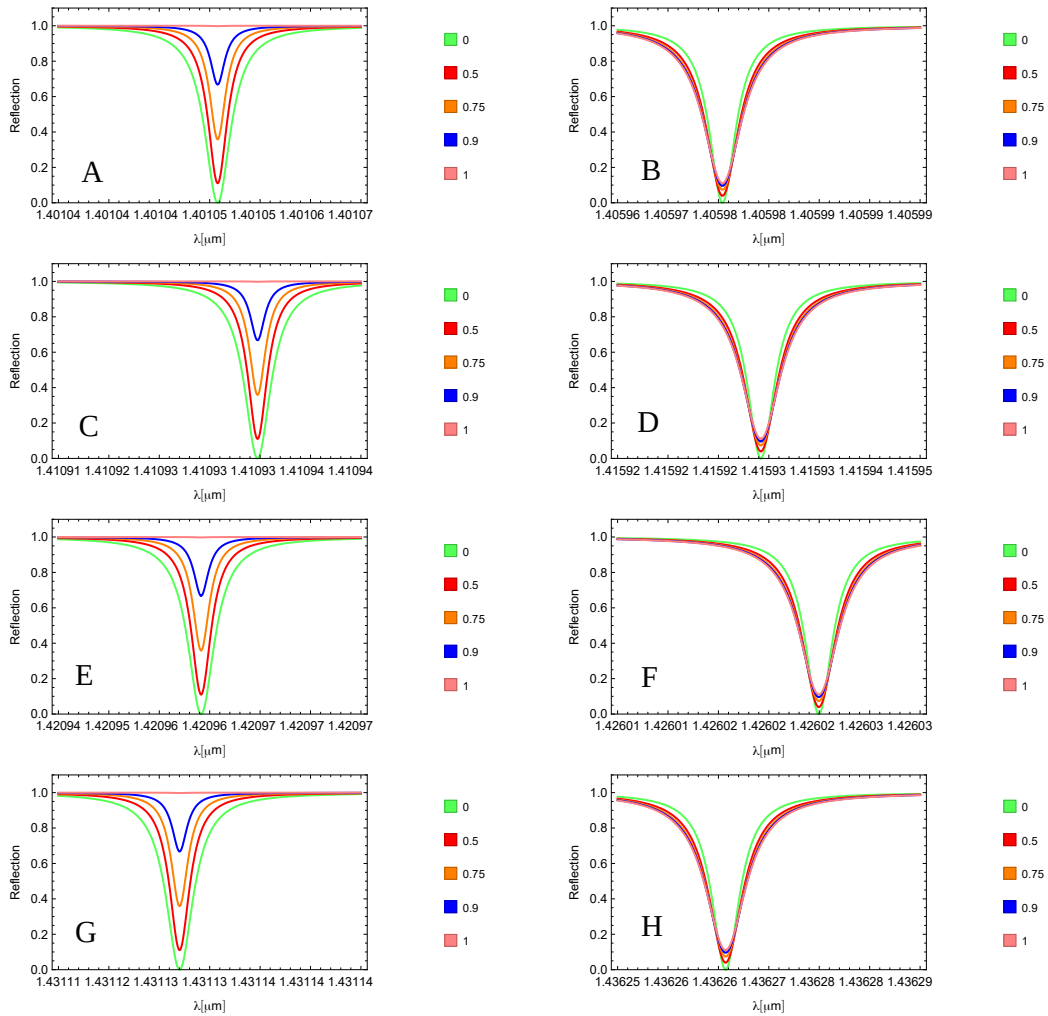


Figure 7.5: Detail of the different peaks from the previous figure. The color code shows the losses in units of the mirror transmission. This means the green curves are without any losses and for the pink curve, the absorption is equal to the mirror transmission.

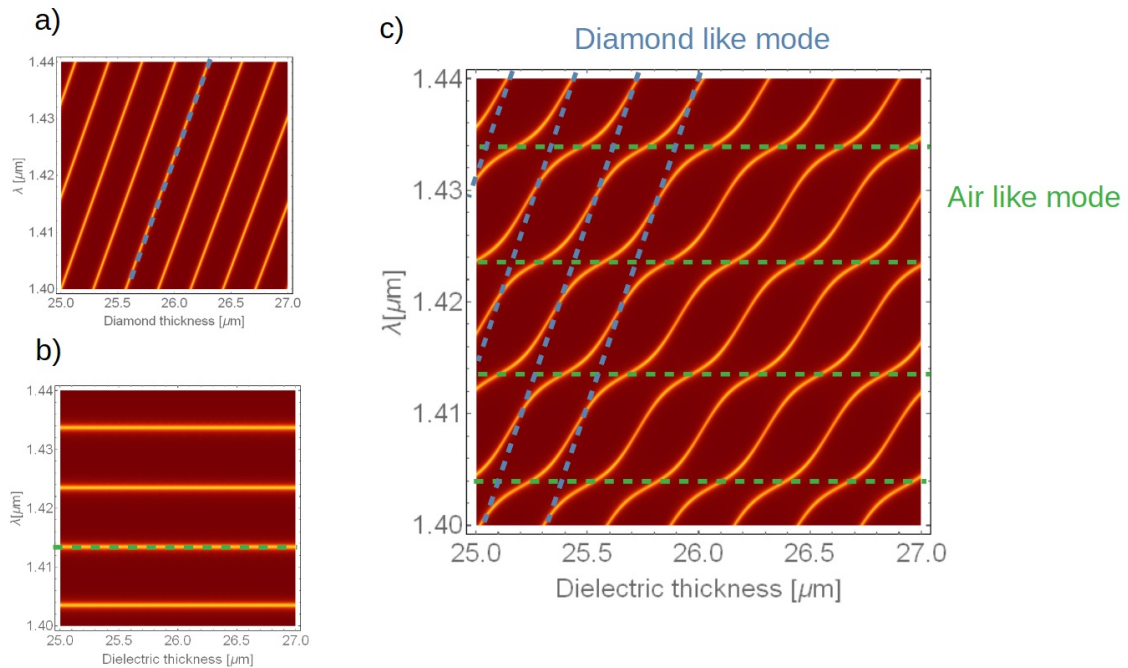


Figure 7.6: Three different reflection spectra. Dark red represents 100 % reflection and yellow is 0 % reflection. Spectrum a) is a diamond cavity with a length of 25 μm to 27 μm . b) shows a spectrum for an air cavity with a constant length of 100 μm . For consistency the same x-axis as before is used, but has no meaning in this case. c) shows a combination of a 100 μm air and a 25 μm to 27 μm thick diamond chip. As guide to the eye some of the diamond modes (blue, from a) and the air like modes (green, from b) are drawn in c). The coupled system out of a) and b) shows avoided crossings where both systems are at resonance.

again and also the resonances have the same intensity. This case is very similar to a cavity with only one dielectric. The anti-reflection coating mixes the two dielectric constants in a way that the whole system sees only an effective refractive index. This allows to describe such a system in a very simple way.

7.2.5 Conclusions from the theory

There are several factors affecting the resonances in a cavity containing a dielectric layer: the absorption in the material, the jump in the refractive index at the interface and the loss due to surface roughness at the interface.

The absorption can be minimized by using very pure and thin materials. The loss due to interface scattering depends on the amplitude of the electromagnetic field at the interface. If the wave has a node at the interface this loss become very small. In the case of an anti-node these effects can be the main loss factor and even suppress

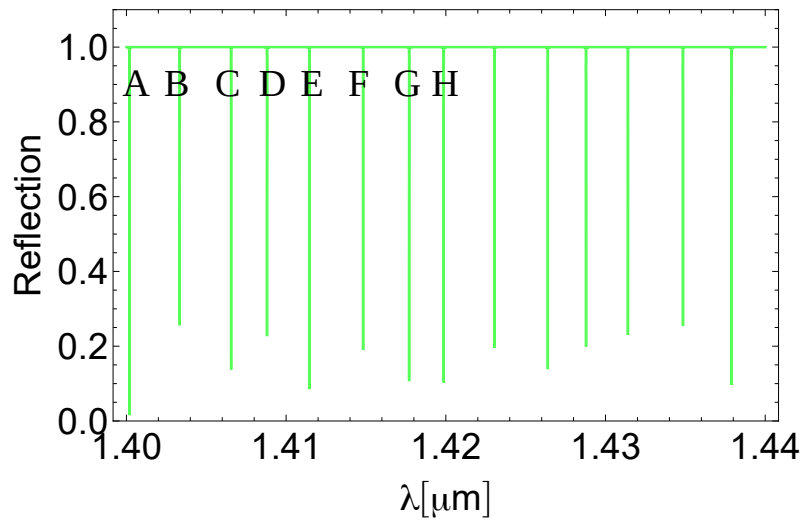


Figure 7.7: Shows the reflection spectrum for a cavity with roughness loss and dielectric loss. The different depth of the resonance peaks is no artifact here, but reflects the effects described in the text.

a resonance completely, if the losses become larger than the transmission of the mirror.

To reduce the losses due to the dielectric jump an anti-reflection coating is useful. The losses due to roughness can be reduced by polishing the interface to a very high level or use only resonances having nodes at the interface.

For the measurements without anti-reflection coating, we expect a very complex spectrum where not all lowest-order modes might be visible. For a silicon layer with an anti-reflection coating we expect a spectrum very similar to an air cavity.

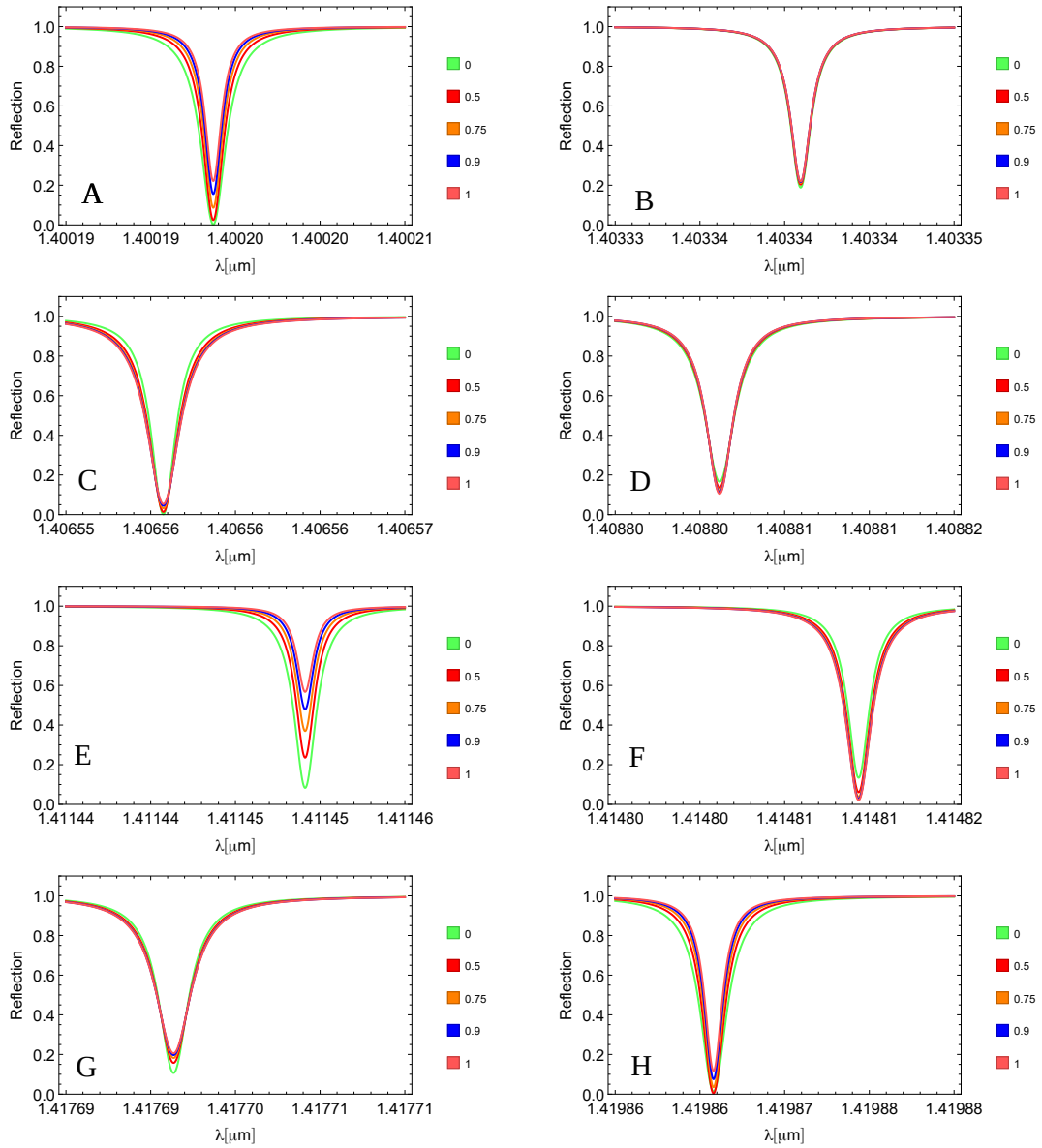


Figure 7.8: Zoom into each resonance from the previous figure. Interface loss of varying strength is added, the color scale is in units of the mirror transmission. Each resonance is affected differently by the loss.

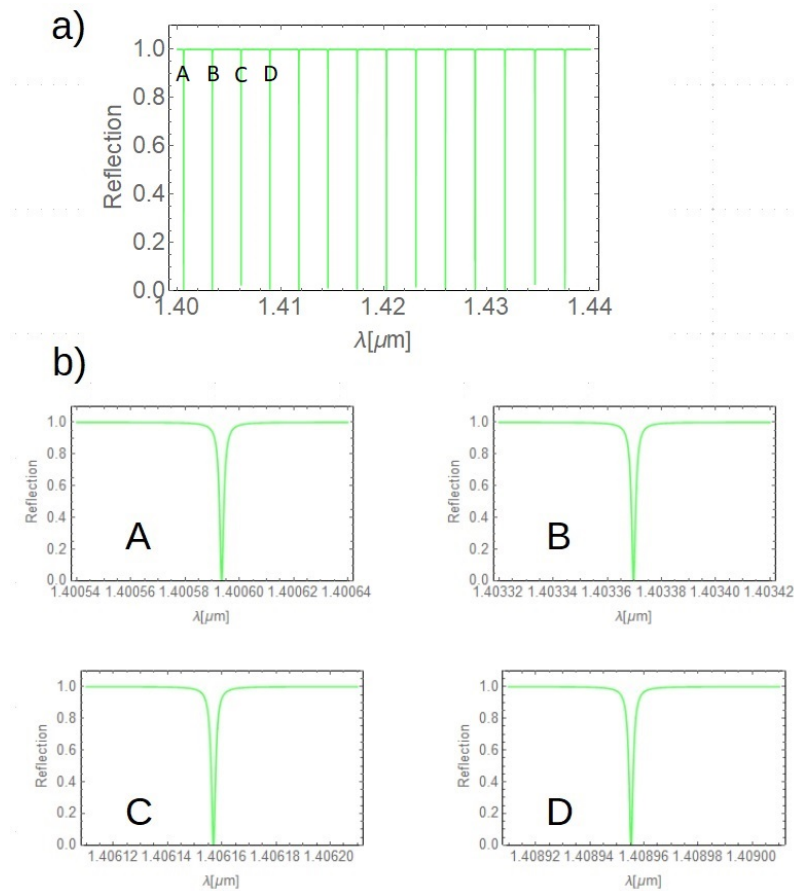


Figure 7.9: The reflection spectrum of a cavity with 25 μm diamond and 100 μm air. The interface between air and diamond is introduced as a perfect anti-reflection coating. The resonances in a) are evenly spaced and as shown in b), all resonances have the same contrast.

7.3 Experiment

For the experiments two different samples are used. For measurements with silicon as the dielectric material in the cavity, we simply flip the flat cavity mirror. Now the reflection coating is on the outside and the anti-reflection coating is on the inside. This is a good example for a long cavity with 340 μm silicon and 25 μm air.

The second sample is a thin diamond chip without anti-reflection coating. This sample should have a small absorption and also small losses at the surface because the polishing is as good as possible. We expect to see a complex spectrum from this sample. Figure 7.10 shows both cases.

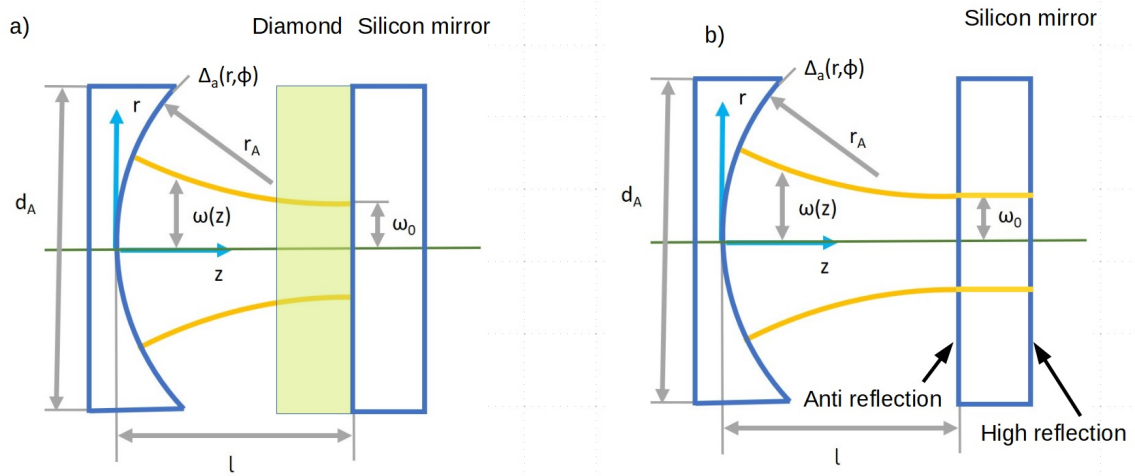


Figure 7.10: The two test objects. a) is a cavity with a diamond chip inside, shown as the greenish area. In b) the flat mirror is simply flipped, such that the anti-reflection coating is on the inside. Note that the thickness is not to scale here, the flat silicon mirror is $340\ \mu\text{m}$, while the air part is only $25\ \mu\text{m}$.

7.3.1 Silicon with anti-reflection coating

This is our first experiment with a dielectric inside a cavity. The mirror has a transmission of 10 ppm, which corresponds to a theoretical maximum finesse of 315 000 without any additional losses. In difference to all experiments before, the flat mirror is flipped such that the residues mostly inside the silicon. The anti-reflection coating on the layer between air and silicon should result in a nice spectrum. The losses in the silicon can be estimated as discussed in section 7.1.

For this experiment, we perform ring-down measurements on 10 mirrors along a diagonal of our chip. For the ring down measurement, the laser is swept across frequency. If a resonance is found, the laser light is switched off within $< 1\ \text{ns}$ by an EOM very quickly. Over time the light is transmitted out of the cavity. The lifetime of the photons inside the cavity is dictated by the finesse. This method is used because absorption of light inside the silicon changes the temperature of the cavity, making the cavity unstable due to thermal drifts. The ring-down measurement is much faster than the sideband modulation used in previous chapters and is therefore preferred in a regime where absorption is an issue.

The results are shown in figure 7.11. A resonance is found for all ten cavities. The FSR is very similar for all cases. We see some fluctuations in the finesse, but on average the cavities have a finesse of around 25 000, showing that a cavity with anti-reflection coating in silicon at 1550 nm works well. The lower finesse compared

to the ideal case (314 000) is due to the absorption in the thick silicon and the increased cavity length.

7.3.2 Thin diamond chip inside a long cavity

In this experiment a diamond is placed in the cavity and SiC (Silicon Carbide) chips are used as spacer. The SiC is around 100 μm thick which should give us a cavity length of around 125 μm with 25 μm diamond and 100 μm air. Because of the lack of an anti-reflection coating we expect more interesting features. In figure 7.12 an example of such a spectrum is given. The spectrum itself became very difficult to read compared to the spectrum in figure 6.9, which is very clear and simple.

For any resonance, a Q-factor can be calculated because the Q-factor is defined as (detailed discussion in section 2.5.4):

$$Q = \frac{\nu_{res}}{\Delta\nu} \quad (7.9)$$

For the finesse however, the FSR needs to be determined. As discussed in section 7.2.3, the FSR varies between the peaks because they are shifted due to avoiding crossings. In section 2.5.1, the finesse is defined as the resonance width divided by the FSR. The finesse can be seen as a figure of merit to compare different cavities independent of their length. To get the same result here, we use the nominal FSR, which is well-defined according to equation 2.15. Because the optical path inside the cavity has a well defined length, we can calculate a nominal FSR using the nominal thickness values of the spacer and the depth of the mirror. For an air cavity the FSR and the nominal FSR are the same.

In figure 7.13 a typical measurement is shown. The measurements are done with sideband modulation as discussed in detail in section 6.1. In table 7.1, a summary of the results for different cavities is given. In figure 7.14 the position of all measured cavities on the mirror chip are shown.

For these long cavities with diamond, we find an average finesse of 16 200 and an average finesse of 66 800 for an air cavity. These values are surprisingly low in comparison to a theoretical finesse of 314 000 without any loss. The conclusion here is that the cavities are too long which causes additional loss due to shape or misalignment. The next step is to reduce the cavity length to a minimum which is discussed in the next section.

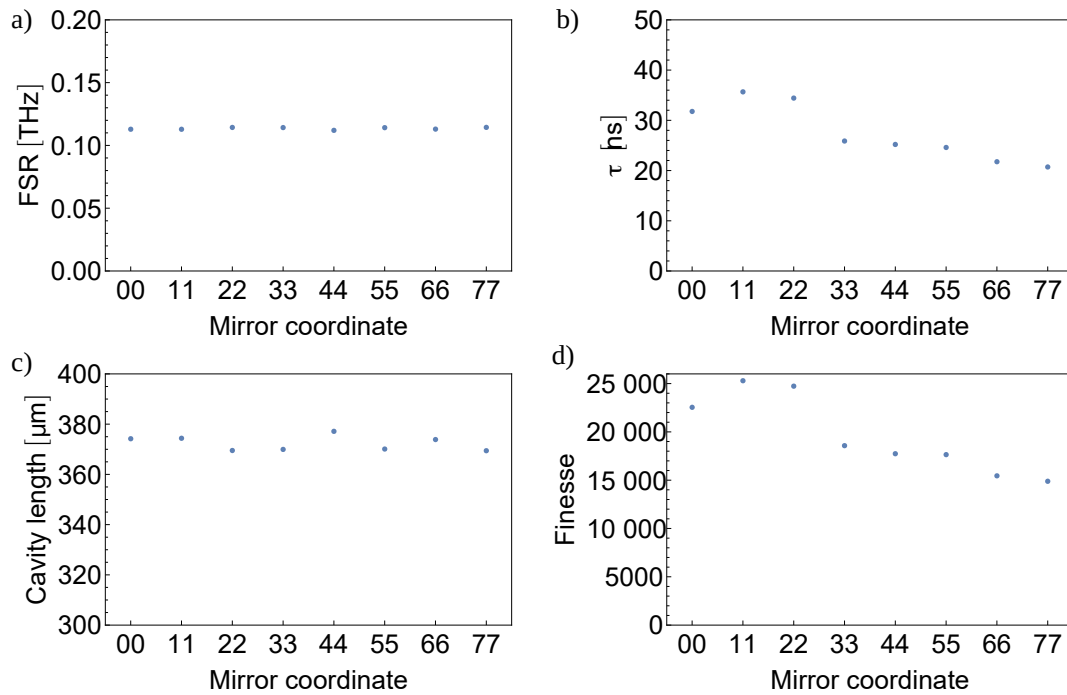


Figure 7.11: Summary of the results for the silicon cavities. Each point represents one cavity. The numbers on the x -axis are the coordinates on the chip. a) is the FSR in THz and b) the lifetime inside the cavity. From these two measurements the cavity length in c) and the finesse in d) are calculated. Further discussion of the results in the main text.

Table 7.1: Finesse and Q-factor for cavities with a total length of 125 μm with a 25 μm diamond chip and without. Row and Column describe the position of the mirror on the chip.

type	Row	Column	Finesse	Q-factor
diamond	0	5	10 500	2.5×10^6
diamond	0	4	11 460	2.7×10^6
diamond	0	3	19 600	4.7×10^6
diamond	4	5	16 800	4.1×10^6
diamond	5	5	23 000	5.5×10^6
air	9	5	69 800	11.0×10^6
air	8	5	61 200	9.8×10^6
air	7	5	71 600	11.2×10^6
air	6	5	64 600	10.1×10^6

7.3.3 Thin diamond chip in a short cavity

We now investigate shorter cavities, where we expect smaller loss due to shape imperfections and roughness. The cavities have a total length of 50 μm , some have a 25 μm diamond layer inside. For a cavity containing a dielectric we use a modified equation for the FSR, the nominal $\Delta\nu_{FSRN}$:

$$\Delta\nu_{FSRN} = \frac{c}{2(l_{air} + n_{dia} \cdot l_{dia})} \quad (7.10)$$

This results in a value of 3 THz for the empty cavity and 1.7 THz for the cavity with diamond. An air cavity with just $l_{air} = 25 \mu\text{m}$ would have an FSR of 6 THz.

The transmission spectrum of a short cavity with diamond is shown in figure 7.15. The spectrum is cleaner than for the long cavities, but not as regular. The two biggest resonances are around 6 THz apart, much more than the expected 1.7 THz. This indicates that some fundamental resonances of this cavity are suppressed. Additionally, we see that the pattern is irregular. The theoretical considerations above provide a rough explanation for the observed spectrum. As depicted in figure 7.6, the air- and diamond like resonances exhibit avoided crossings, resulting in irregular spacings. Interface loss changes the intensity of a resonance, depending on its field strength at the internal interface (see 7.2).

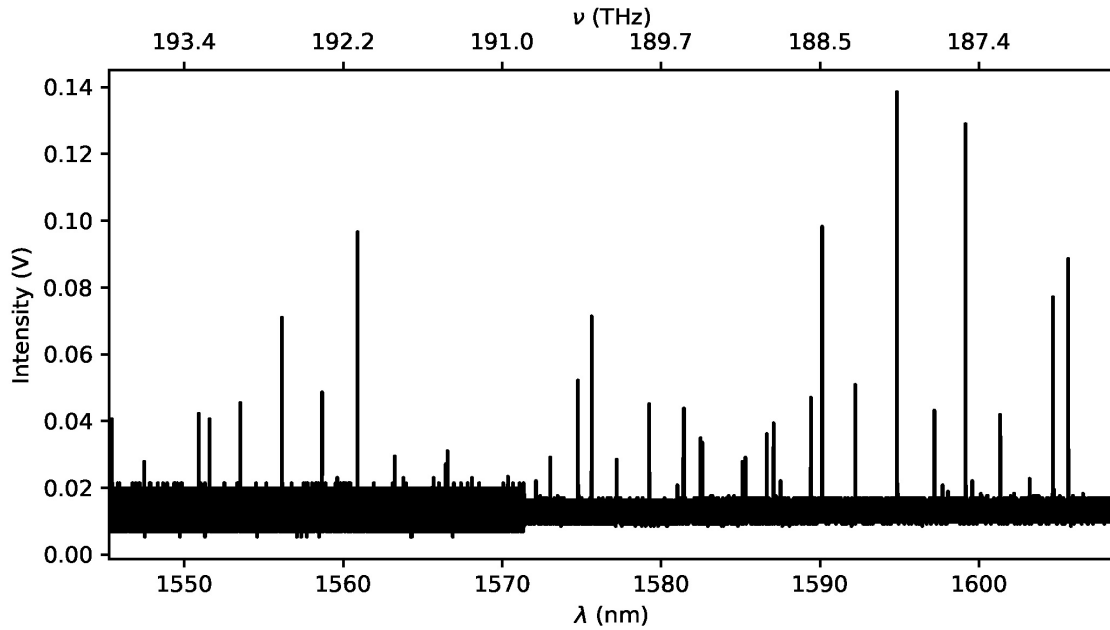


Figure 7.12: This is the transmission spectrum of the long diamond cavity. The coordinate of this mirror is row 0 column 4. In a spectrum like this, it is challenging to measure the FSR. Even deciding which resonance is the fundamental one is difficult. The reasons for this complex spectrum are discussed in section 7.1. The different noise levels appear because two different measurements over different wavelength regions are combined together.

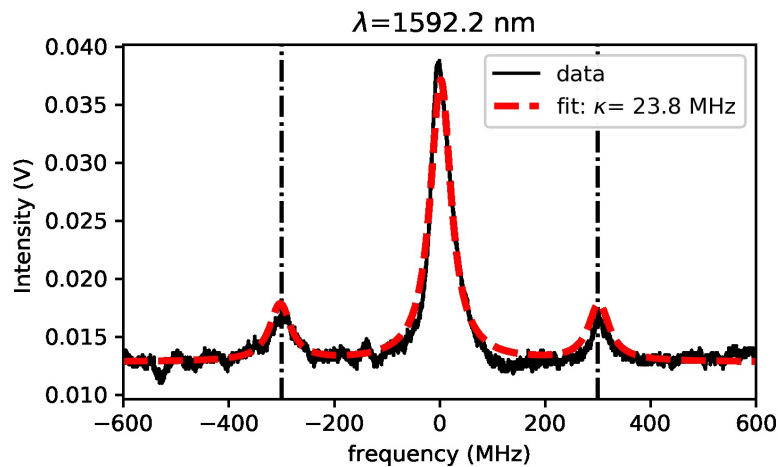


Figure 7.13: A sideband modulation measurement for the cavity row 4, column 5 on a 25 μm diamond with 100 μm air. The Q-factor can be evaluated as 4.02×10^6 . With a FSR of 0.8 THz calculated from the geometry a finesse of 16 800 can be given.

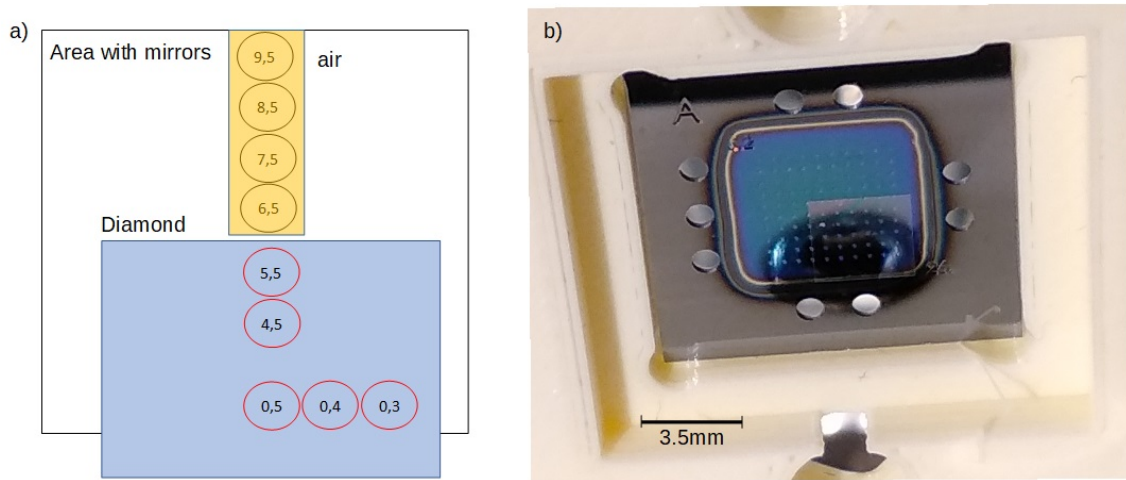


Figure 7.14: The figure a) indicates all measured cavities. The diamond chip one quarter of the mirror field so that it is possible to make measurements in air and with diamond on the same chip. This gives us a direct comparison of the two situations. Detailed measurement results can be found in table 7.1. b) shows a photo of the mirror chip inside the plastic mount with the diamond chip in the lower right corner. The diamond chip has a size of $3.5 \text{ mm} \times 3.5 \text{ mm}$ and the mirror chip a size of $13 \text{ mm} \times 13 \text{ mm}$.

In table 7.2 the results of the measurements are summarized. For an air cavity it is possible reach a very high finesse of up to 270 000. With a diamond inside it is more difficult. Our best cavity with diamond reaches 63 500 which is a promising sign that it should be possible to use this cavity design for coupling to NV centers [72].

Table 7.2: Finesse and Q-factor for the short cavities. Row and Column describe the position of the mirror on the chip.

type	Row	Column	Finesse	Q-factor
diamond	0	0	46 500	4.45×10^6
diamond	0	1	11 000	1.4×10^6
diamond	2	0	63 500	6.8×10^6
diamond	2	2	45 300	4.5×10^6
air	0	8	270 000	17×10^6
air	0	6	197 000	12×10^6

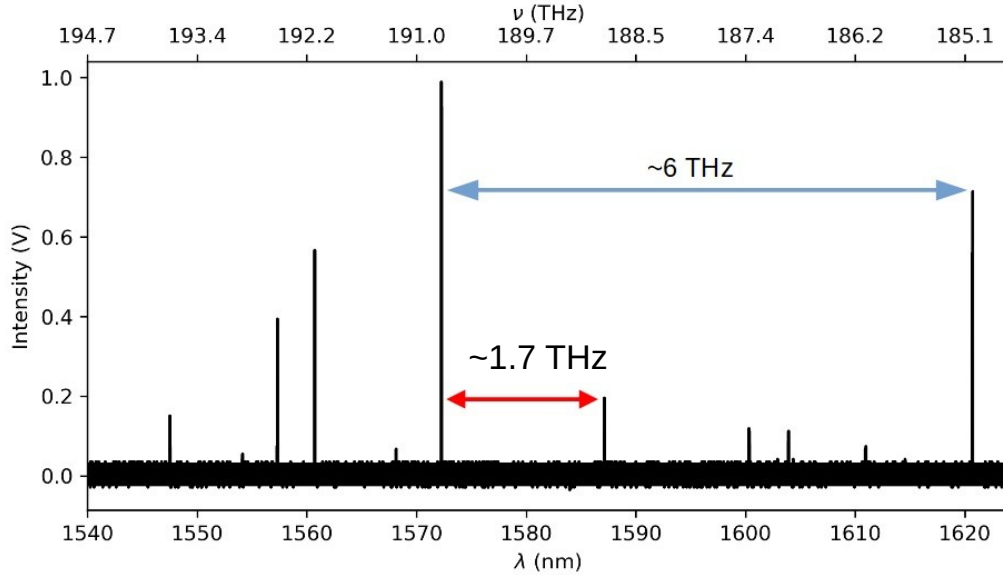


Figure 7.15: Spectrum of a cavity with 25 μm diamond and 25 μm air. The two most dominant resonances are 6 THz apart (blue arrow). The next smaller peak is 1.7 THz (red arrow) away from the highest. Detailed discussion in the main text.

7.4 Improvements for cavity enhanced quantum systems

After showing the performance of our cavities with a dielectric chip inside I will now compare our cavity system an other experiment from literature [76]. The paper use an optical cavity to enhance the fluorescence of the NV color center in diamond. The NV is an important system in quantum science [77], it can be seen as a quasi-atom trapped in a diamond lattice.

In general, to achieve a good coupling the waist has to be as small as possible. This can be achieved by reducing the ROC and the length of the cavity to a bare minimum. Also the losses inside the dielectric material have to be as small as possible.

The paper [76] describes a cavity with two SiO_2 mirror chips and a diamond membrane between them. One of the mirrors is curved to get a stable cavity. The diamond membrane contains the NVs, it is only 1 μm thin to reduce the mode volume and also the transmission losses. The membrane is manufactured by plasma etching to achieve a roughness of below 0.3 nm averaged over a $20 \mu\text{m} \times 20 \mu\text{m}$ area [78]. By scanning the SiO_2 mirror chip with the curved mirror over the diamond membrane, it is possible to find a single NV and couple it to the cavity.

The mirrors and cavities discussed in this chapter were initially intended for the nanoparticle experiment that I will describe in the following chapter. For this experiment, we want a rather long cavity to allow particles to enter. Also the beam

waist is kept not too small to increase the probability that a particle interacts with the field. If we would use these cavities without any design changes for a diamond NV experiment, we expect a Purcell factor on resonance of around 31.4. The cavity design can be optimized for this type of experiment, simply by making them significantly smaller. These new cavities are in production.

In table 7.3, the results of the two papers in comparison to our cavities is presented. The last column already shows the expected performance of the optimized version of our cavity design. With this it should be possible increase the Purcell factor over 170. Our cavities can achieve these high Purcell factors because their almost perfect shape and very low roughness make high quality factors in combination with a small mode volume possible. This could open a new regime of optical cavity enhanced quantum optics.

Table 7.3: Comparison of [76] with the expected performance of our microcavities. The last column shows the improved design. For the estimation of the Purcell factor we use $F_P = \frac{3}{4\pi^2} \frac{Q}{V} \left(\frac{\lambda}{n}\right)^3 \cdot \eta$. (η is 0.025 for the zero phonon line of the NV) The volume V and the waist w_0 are given by $V = \frac{1}{4}\pi w_0^2 L$ and $w_0 = \sqrt{\frac{\lambda}{n\pi} \cdot \sqrt{ROC \cdot L - L^2}}$.

	SiO ₂ cavity [76]	Cavities shown in chapter 7	future improved design
Finesse	5260	63 500	> 70 000
Quality factor (Q)	58 500	6.8×10^6	> 7×10^6
Cavity length (L)	contact to 3 μm	50 μm	< 7 μm
Diamond type	membrane	chip	membrane
thickness	1 μm	25 μm	around 1 μm
Waist w_0	1.4 μm	44 μm	< 2.7 μm
ROC	16 μm	175 μm	< 50 μm
Wavelength (λ)	637 nm	1550 nm	638 nm
Purcell factor (F_p^{ZPL}) measured	30	NaN ¹	NaN ¹
Purcell factor calculated	18.12	31.4	>170

7.5 Conclusion

Changing the dielectric inside a cavity changes the properties of the whole system. As we have seen in the theory part (section 7.2.3) of this chapter, the spectrum

¹ These experiments have not been performed until now, which means no measured data is available yet.

changes drastically. In section 7.3.2, such a spectrum is presented. A cleaner and more even spectrum is obtained by applying an anti-reflection coating on the internal interface, as shown in section 7.3.1. Another way to improve the cavity finesse is to make the cavity shorter, an example of which can be found in section 7.3.3. If the cavity is shorter the beam waist on the mirror is smaller, which improves the performance. The ideal results are expected for a thin diamond with anti-reflection coating.

To summarize, we are able to manufacture cavities containing dielectric layers, while maintaining good finesse values. The limiting factors are absorption inside the material and scattering at the interface. The comparison with other experiments in section 7.4 highlights the great potential of our silicon microcavities.



Die approbierte gedruckte Originalversion dieser Dissertation ist an der TU Wien Bibliothek verfügbar.
The approved original version of this doctoral thesis is available in print at TU Wien Bibliothek.

CHAPTER 8

Nano particle detection in cavities

In this chapter I will present a first experiment making use of the microcavities produced in the course of this project. The idea is to bring dielectric nanoparticles into a microcavity and create strong coupling between the field and the particle. This could pave the way towards optical cooling of massive particles, allowing experiments in the quantum regime with exceptionally heavy particles.

Why is it interesting to investigate the quantum properties of nanoparticles? In the past the quantum properties of many different objects were discussed and experimentally proven. One of the "most quantum" objects is the photon, it shows properties like single photon interference without much experimental effort. This can be shown with Young's famous double slit experiment. In this experiment the light goes through two slits and interferes afterwards. The interesting point is that the interference pattern also appears if the intensity of light is very small, even at the single-photon level. This is a clear indication that the photon behaves like a wave. This duality is called wave-particle duality. We know that the photon shows particle-like properties if the path information can be extracted. If this is impossible, it displays wave properties. It is also interesting that the choice of whether or not the path can be measured can be made after the particle has passed the double slit [79]. These experiments work well for photons, but what about other particles?

Similar experiments have been performed with a large variety of particles including: electrons [80], H₂ [81], neutrons [82] and also on atoms [83, 84] and big molecules like fullerenes C₆₀ [85]. The latest experiments show quantum interference patterns even with molecules with 10 000 atomic mass unit (AUM), equivalent to around 810 atoms [86].

All these experiments show that matter can display wave-like properties, depending on whether it is possible to measure the path information of the particle. To observe particle interference with a high mass (m) it is necessary to reduce the particle speed v . This can be seen from the definition of the de Broglie wavelength λ_{dB} :

$$\lambda_{dB} = \frac{h}{p} \propto \frac{1}{m \cdot v} \quad (8.1)$$

This equation connects the matter wavelength of a particle with its momentum

$p = m \cdot v$ and the Planck constant h . For interference experiments it is also necessary to have a very "monochromatic" source with a small Δv .

We therefore need to cool the mechanical motion of the nanoparticles in the cavity. If the incident laser light is red-shifted with respect to the cavity, the particle will lose energy with every photon scattered into the cavity mode. This cooling principle has been applied before to silicon nanoparticles and is explained in detail in [87]. There are also active cooling mechanisms, where the cavity field is modulated to create a damping force [88].

As the dielectric force is proportional to the intensity, our high-finesse microcavities are much better suited than the large optical cavities used before. With mirrors from the first production run we achieve beam waists as small as $12 \mu\text{m}$ and a finesse of 3.5×10^4 . With this it should be possible to cool particles as heavy as 1×10^9 AUM. This would be the biggest particles ever tried in a double-slit experiment.

A typical beam waist in a normal-sized cavity setup is around $68 \mu\text{m}$ and the finesse is 3×10^5 ([89]). That means the waist can be reduced by a factor of 5.6 since cooperativity defined in equation 1.2 is proportional to the square of the mode waist this means an improvement by a factor of 31 by using microcavities, even if the finesse is 10 times worse, a factor of 3 remains.

The main goal of these experiments is to answer the question of whether there is a boundary between the quantum and the classical worlds in terms of the mass of an object.

This idea sounds simple but is an experimental challenge. First particles of the right size have to be found or produced [90], then these particles have to be launched into the cavity in a controlled way. After bringing the particles into the cavity, they have to be cooled significantly in all directions. Only then we can start to think about matter-wave interference experiments.

Before such a complex experiment is performed, some preliminary work has to be done. For this purpose a much simpler experiment was built to test the ideas of the main experiment which will be built in the future. In this preliminary experiment, nanoparticles are detected and measured in a microcavity in vacuum, this work was inspired by the experiment described in [89] and performed together with our collaborators Markus Arndt and Stefan Kuhn. It is the first real world experiment for our microcavities and serves as a proof of principle for future work.

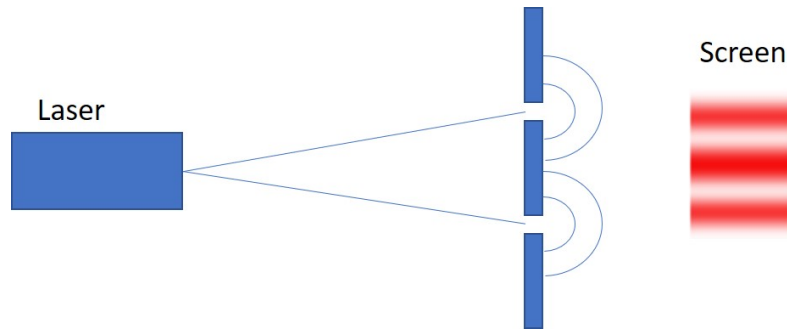


Figure 8.1: The concept of a double-slit experiment with light.

8.1 Experimental setup

The experiment uses a microcavity in the curved-curved configuration from the first production run. We use an open, L-shaped spacer to enable access to the cavities. The spacer thickness is $100\ \mu\text{m}$, the finesse is $34\,000 \pm 1500$, the mirrors have a radius of curvature of $(1.3 \pm 0.2)\ \text{mm}$ at a cavity length of $(130 \pm 3)\ \mu\text{m}$. The FSR is $(1.15 \pm 0.03)\ \text{THz}$. With the radius and length, a beam waist of $(12 \pm 1)\ \mu\text{m}$ is calculated. The mode volume is $3900\ \lambda^3$ (15 pl).

The cavity is mounted in a vacuum chamber with optical access from all sides, in-vacuum objectives are used to couple light in and out of the cavity. We use a Toptica CTL-1550 laser to pump the cavity with a power of 25 mW at a wavelength of 1547 nm. The laser frequency is locked to the cavity resonance through the intensity of the backreflected light. This yields an intracavity intensity at the beam waist of $2 \times 10^7\ \text{W cm}^{-2}$ and a cavity linewidth $\frac{\Delta\nu}{2} = (17.0 \pm 0.7)\ \text{MHz}$. We measure the transmission through the cavity with a photodiode.

Silica nanoparticles¹ with a size of $(150 \pm 20)\ \text{nm}$ are suspended in a solution. We put a drop of this suspension on a silicon chip and let it dry. The chip is placed in a steel mount, which hangs top-down in the vacuum chamber. The steel mount is held by a permanent magnet from outside. The particles are launched by Laser Induced Acoustic Desorption [91, 92]. We aim a short, high-power laser pulse at the back of the plate that the nanoparticles are placed on. In that way a thermal shockwave is sent through the plate and the particles are ejected from the surface.

A picture of the cavity in the vacuum chamber is shown in figure 8.2, the high-power laser pulse used for nanoparticle desorption enters through the big top window. The cavity itself is placed in the aluminum mount. A schematic of the cavity assembly is shown in figure 8.3.

¹ Bangs Laboratories

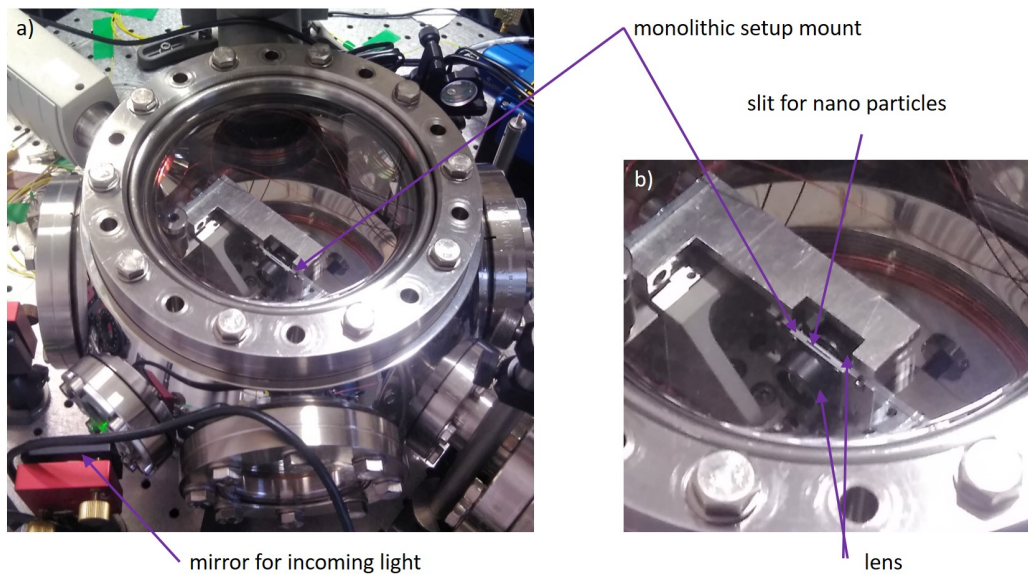


Figure 8.2: Vacuum chamber with the monolithic cavity setup. a) shows the full chamber, without nanoparticle source. In b), the top opening of the cavity assembly and the in-vacuum objectives for in and outcoupling of light are clearly visible.

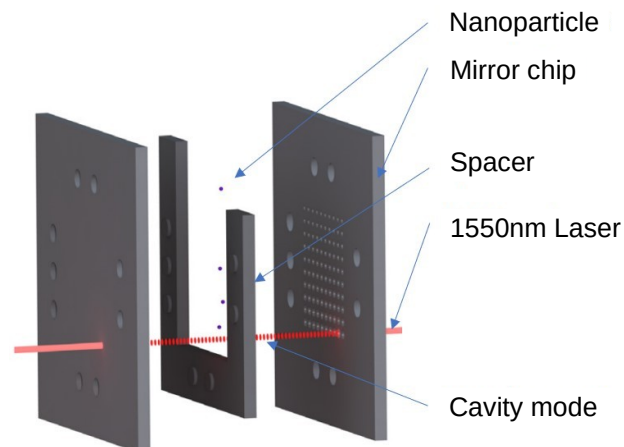


Figure 8.3: Explosion drawing of the nanoparticle setup. The nanoparticles are launched from the top and fly through the cavity arrangement, passing through the high-intensity cavity field.

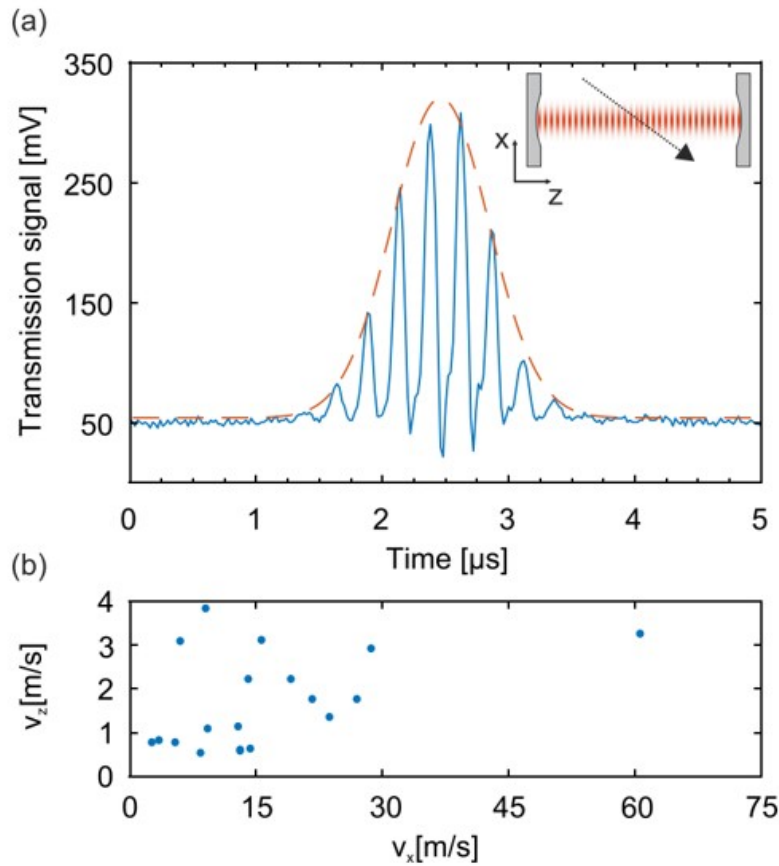


Figure 8.4: a) Transmission signal of a typical nanoparticle transit through our optical microcavity. The red dashed line indicates the particle passing through the Gaussian intensity profile of the cavity mode. The fast oscillations stem from the particle moving along the cavity axis. b) shows the velocities extracted from 19 different measurements. More details are given in the text.

8.2 Results, discussion and outlook

For the measurement, we detune the input laser from the cavity resonance by $\Delta = -2.3\frac{\Delta\nu}{2}$ and monitor the transmission. Short pulses of the high power laser are fired regularly to launch nanoparticles into the cavity. The data acquisition is triggered whenever the transmission signal changes. An exemplary particle transit is shown in figure 8.4.

If a dielectric particle enters the cavity mode volume, the effective optical path length increases and the cavity is therefore shifted towards resonance, leading to an increase in the transmission signal. The nanoparticle also scatters light out of the cavity which reduces the transmission. The scattering becomes negligible when the particle passes an anti-node of the cavity field and is maximum at the nodes.

A particle with a velocity v_z along the cavity axis leads to an approximately sinusoidal variation in the transmission signal. The Gaussian envelope of the signal is due to the particles motion v_x perpendicular to the cavity axis and reflects the transverse intensity profile of the cavity mode. We can therefore extract both v_z and v_x from a transit signal like in 8.4 a. A collection of 19 measured velocities is displayed in 8.4 b.

The signal-to-noise ratio in this measurement was about 35 for a particle radius of 150 nm. As the cavity shift is proportional to the volume of the particle, we should be able to detect particles as small as 50 nm with this setup.

The results of this preliminary experiment are published in [53]. We could show that microcavities work well for nanoparticle detection. For more advanced tasks, like cooling, it is necessary to build in better mirrors.

The cavities used in the nanoparticle experiment were from the first production run described in chapter 6.2. The mirrors from the second production run (chapter 6.3) should improve the cooperativity further. With the new cavity parameters ($F=350\,000$, $ROC=205\ \mu\text{m}$, $L=160\ \mu\text{m}$, $\lambda=1550\ \text{nm}$), we found a theoretical cooperativity of 3012, which should make these cavities suitable for more advanced experiments such as nanoparticle cooling. In [53] the potential of using the microcavities for cooling particles is discussed. The following criteria must be met: First, the cavity-particle interaction has to be in the strong regime, which means the dispersive frequency shift of the cavity resonance has to be larger than the cavity decay rate. Second the axial mechanical trapping frequency of the particle has to be larger than the cavity decay rate.

The dispersive shift U_0 is defined as:

$$U_0 = \frac{2\pi\omega_L r_p^3 \varepsilon - 1}{V_m \varepsilon + 1} \quad (8.2)$$

ω_L is the laser wavelength, r_p radius of particle, $V_m = \pi w_0^2 L/4$ the mode volume and ε the relative permittivity. The trapping frequency (ω_z) of the particle is given as:

$$\omega_z = \sqrt{\frac{24k^2 P_{cav} \varepsilon - 1}{\pi w_0^2 \rho c \varepsilon + 1}} \quad (8.3)$$

P_{cav} is the intra-cavity power and k the wave vector. The cavity decay rate (κ) is defined as

$$\kappa = \frac{c\pi}{2L\mathcal{F}} \quad (8.4)$$

The two criteria that need to be fulfilled for particle cooling are:

$$U_0 \geq \kappa \quad (8.5)$$

and

$$\omega_z \geq \kappa \quad (8.6)$$

This calculation is performed for spherical particles made from two different materials, silicon (Si) and silica (SiO₂). The goal is to find a size limit for these spheres, down to which the cooling criteria are met.

The results of the calculation can be found in table 8.1. Our cavities are able to cool particles down to a size of 1×10^8 amu. This is one hundred times smaller compared to the macroscopic cavity approach shown in [52]. With even smaller mirrors, having for example halve the ROC of the current generation, it should be possible to cool particles as light as 4.9×10^6 amu. Our new micro cavities therefore open a new field of small particle cooling.

Table 8.1: The input- and output values for different particle-cavity combinations. The upper half of the table contains the input parameters, the lower half the results of the calculation. Our new cavities reduce the mass limit of the particle by a factor of 100 to 1×10^8 amu. With a little smaller cavities, cooling should be possible for particles as light as 5×10^6 amu.

	Silicon particle, from [52]	Silicon, second generation mirrors	Silica, second generation mirrors	Silicon, future smaller mirrors
Finesse	300 000	500 000	500 000	500 000
Length	3 mm	160 μm	160 μm	20 μm
ROC	25 mm	205 μm	205 μm	45 μm
Laser wavelength	1560 nm	1550 nm	1550 nm	1550 nm
Intra-cavity power	300 W	100 W	100 W	100 W
Relative permittivity	11.68	11.68	3.9	11.68
Density	2330 kg m^{-3}	2330 kg m^{-3}	2633 kg m^{-3}	2633 kg m^{-3}
Waist	63 μm	6.5 μm	6.5 μm	3.3 μm
Cavity decay rate	166 kHz	1.8 MHz	1.8 MHz	15 MHz
Trapping frequency	1.6 MHz	18 MHz	14 MHz	28 MHz
Radius	119 nm	21 nm	25 nm	7.9 nm
Minimal mass	1.6×10^{10} amu	1.0×10^8 amu	1.6×10^8 amu	4.9×10^6 amu

CHAPTER 9

Summary and outlook

This thesis describes the design of silicon microcavities in detail. The manufacturing process is developed to a high level to reach ultra-high finesse. A key point is the improvement of the mirror fabrication in silicon by dry etching. These optimized processes make it possible to produce monolithic ultra high finesse cavities with high scalability. By using better mirror coating it should be possible to get even higher field intensities inside the cavities. The presented microcavity design can be operated in different configurations and forms a highly flexible platform for experiments.

As we began this project, we developed it around the idea to detect and cool nanoparticles. This guided us to the necessary values of finesse and the required stability. After the basic concept was born, we worked hard to get all necessary values into the right regime. After three and a half years and many different experiments, some more successful than others, we can present a record-breaking optical microcavity with a finesse of greater than 500 000.

High finesse microcavities can be used to enhance the light-matter interaction. In chapter 7 we show the effect of layer of dielectric material inside our microcavities. This analysis paves the way for future experiments that aim at coupling the cavity field to defects in crystals. In section 7.4 we compare our cavities with others and show that Purcell factors of 170 or more are possible. This highlights the great potential of this type of cavity.

In contrast to many other cavity types, most of which are mentioned in section 1.2, our approach is highly scalable. The density of micromirrors can be easily increased to fit the specific application, several hundred cavities per mm^2 are possible.

To get a large number of cavities working at the same time (and at the exact same resonance frequency), it is necessary to tune them. Our group has shown in the past that this is possible [41] by fabricating the micromirrors on the tips of cantilevers and individually deflecting these cantilevers electrically. In combination with Fiber Optic Bundles¹, we would have the ability to produce big arrays of multi purpose, fibre coupled, individually tunable cavities. Such a system would have numerous novel applications.

1 as an example: from SQS Vlaknova optika <http://www.sqs-fiberoptics.com>

A tunable microcavity array could also be used as an array of tunable lasers, if the volume between the mirrors is filled with a laser medium. Because everything is chip based, it should be straightforward to implement a phase shifter for each laser. If the frequency and the phase of an electro-magnetic field are well controlled, the whole light field can be tailored in an artificial way. An application of this system could be holographic screens.

Another possible future application of microcavities makes use of the fact that the cavity resonance is highly sensitive to any change in the cavity length. This allow any kind of length depending measurements, like pressure, temperature or vibrations. The cavities have, in contrast to electrical sensors, the advantage that they require no electrical power or communication. This can be an advantage in industrial environments with a lot of electromagnetic noise which can corrupt the communication, or in test chambers where any additional electric signal is undesirable.

As a last example for a system where the properties of our microcavities could be beneficial, I want to mention chemical sensors. One can imagine a spectrometer using a microcavity array, where each cavity is tuned to another reactant. In that way a live stream of a chemical reaction could be possible to produce. If the density of the cavities is high enough, even the spatial distribution of a reaction could be monitored.

In conclusion, this thesis presents the design, fabrication and testing of novel optical microcavities. The cavities are, to the best of our knowledge, unique in their specifications and promise versatile applications in both science and technology. Future developments will focus on maximizing the finesse and combine these high-performance mirrors with individual tuneability of each cavity like in [41]. Several fundamental research experiments as well as industrial applications are underway.

Bibliography

1. TRUPKE, M., HINDS, E. A., ERIKSSON, S., CURTIS, E., MOKTADIR, Z., KUKHARENKA, E., and KRAFT, M.: ‘Microfabricated high-finesse optical cavity with open access and small volume’. *Applied Physics Letters* (2005), vol. 87(21): p. 211106.
2. BIEDERMANN, G., BENITO, F., FORTIER, K., STICK, D., LOYD, T., SCHWINDT, P., NAKAKURA, C., JARECKI JR, R., and BLAIN, M.: ‘Ultrasooth microfabricated mirrors for quantum information’. *Applied Physics Letters* (2010), vol. 97(18): p. 181110.
3. HU, J.: ‘Ultra-sensitive chemical vapor detection using micro-cavity photothermal spectroscopy’. *Optics express* (2010), vol. 18(21): pp. 22174–22186.
4. ALQUAITY, A. B., ES-SEBBAR, E.-T., and FAROOQ, A.: ‘Sensitive and ultra-fast species detection using pulsed cavity ringdown spectroscopy’. *Optics Express* (2015), vol. 23(6): pp. 7217–7226.
5. ARMANI, D., KIPPENBERG, T., SPILLANE, S., and VAHALA, K.: ‘Ultra-high-Q toroid microcavity on a chip’. *Nature* (2003), vol. 421(6926): p. 925.
6. WIERSIG, J.: ‘Enhancing the sensitivity of frequency and energy splitting detection by using exceptional points: application to microcavity sensors for single-particle detection’. *Physical Review Letters* (2014), vol. 112(20): p. 203901.
7. REITHMAIER, J. Á., SEK, G., LÖFFLER, A., HOFMANN, C., KUHN, S., REITZENSTEIN, S., KELDYSH, L., KULAKOVSKII, V., REINECKE, T., and FORCHEL, A.: ‘Strong coupling in a single quantum dot–semiconductor microcavity system’. *Nature* (2004), vol. 432(7014): p. 197.
8. GERARD, J., SERMAGE, B., GAYRAL, B., LEGRAND, B., COSTARD, E., and THIERRY-MIEG, V.: ‘Enhanced spontaneous emission by quantum boxes in a monolithic optical microcavity’. *Physical review letters* (1998), vol. 81(5): p. 1110.
9. VUCKOVIC, J., PELTON, M., SCHERER, A., and YAMAMOTO, Y.: ‘Optimization of three-dimensional micropost microcavities for cavity quantum electrodynamics’. *Physical Review A* (2002), vol. 66(2): p. 023808.

10. REMPE, G., LALEZARI, R., THOMPSON, R., and KIMBLE, H.: ‘Measurement of ultralow losses in an optical interferometer’. *Optics letters* (1992), vol. 17(5): pp. 363–365.
11. VAHALA, K. J.: ‘Optical microcavities’. *nature* (2003), vol. 424(6950): p. 839.
12. BITARAFAN, M. and DECORBY, R.: ‘On-chip high-finesse fabry-perot microcavities for optical sensing and quantum information’. *Sensors* (2017), vol. 17(8): p. 1748.
13. MAIMAN, T. H., HOSKINS, R., D’HAENENS, I., ASAWA, C. K., and EVTUHOV, V.: ‘Stimulated optical emission in fluorescent solids. II. Spectroscopy and stimulated emission in ruby’. *Physical Review* (1961), vol. 123(4): p. 1151.
14. GOULD, R. G.: ‘The LASER, light amplification by stimulated emission of radiation’. *The Ann Arbor conference on optical pumping, the University of Michigan*. Vol. 15. 1959: p. 128.
15. COLLOT, L., LEFEVRE-SEGUIN, V., BRUNE, M., RAIMOND, J., and HAROCHE, S.: ‘Very high-Q whispering-gallery mode resonances observed on fused silica microspheres’. *EPL (Europhysics Letters)* (1993), vol. 23(5): p. 327.
16. KIPPENBERG, T., SPILLANE, S., ARMANI, D., and VAHALA, K.: ‘Fabrication and coupling to planar high-Q silica disk microcavities’. *Applied Physics Letters* (2003), vol. 83(4): pp. 797–799.
17. KIPPENBERG, T., SPILLANE, S., and VAHALA, K.: ‘Demonstration of ultra-high-Q small mode volume toroid microcavities on a chip’. *Applied Physics Letters* (2004), vol. 85(25): pp. 6113–6115.
18. KIPPENBERG, T. J., KALKMAN, J., POLMAN, A., and VAHALA, K. J.: ‘Demonstration of an erbium-doped microdisk laser on a silicon chip’. *Physical Review A* (2006), vol. 74(5): p. 051802.
19. MALAK, M., GABER, N., MARTY, F., PAVY, N., RICHALOT, E., and BOUROUINA, T.: ‘Analysis of Fabry-Perot optical micro-cavities based on coating-free all-Silicon cylindrical Bragg reflectors’. *Optics express* (2013), vol. 21(2): pp. 2378–2392.
20. SABRY, Y. M., SAADANY, B., KHALIL, D., and BOUROUINA, T.: ‘Silicon micromirrors with three-dimensional curvature enabling lensless efficient coupling of free-space light’. *Light: Science & Applications* (2013), vol. 2(8): e94.
21. SCHNEIDER, C., GOLD, P., REITZENSTEIN, S., HOEFLING, S., and KAMP, M.: ‘Quantum dot micropillar cavities with quality factors exceeding 250,000’. *Applied Physics B* (2016), vol. 122(1): p. 19.

22. HAUPT, F., OEMRAWSINGH, S. S., THON, S. M., KIM, H., KLECKNER, D., DING, D., SUNTRUP III, D. J., PETROFF, P. M., and BOUWMEESTER, D.: ‘Fiber-connectorized micropillar cavities’. *Applied physics letters* (2010), vol. 97(13): p. 131113.
23. LINDENMANN, N., BALTHASAR, G., HILLERKUSS, D., SCHMOGROW, R., JORDAN, M., LEUTHOLD, J., FREUDE, W., and KOOS, C.: ‘Photonic wire bonding: a novel concept for chip-scale interconnects’. *Optics express* (2012), vol. 20(16): pp. 17667–17677.
24. TOWE, E., LEHENY, R. F., and YANG, A.: ‘A historical perspective of the development of the vertical-cavity surface-emitting laser’. *IEEE Journal of Selected Topics in Quantum Electronics* (2000), vol. 6(6): pp. 1458–1464.
25. MOREAU, E., ROBERT, I., GERARD, J., ABRAM, I., MANIN, L., and THIERRY-MIEG, V.: ‘Single-mode solid-state single photon source based on isolated quantum dots in pillar microcavities’. *Applied Physics Letters* (2001), vol. 79(18): pp. 2865–2867.
26. STEINMETZ, T., COLOMBE, Y., HUNGER, D., HÄNSCH, T., BALOCCHI, A., WARBURTON, R., and REICHEL, J.: ‘Stable fiber-based Fabry-Pérot cavity’. *Applied Physics Letters* (2006), vol. 89(11): p. 111110.
27. MATHEW, J., SCHNELLER, O., POLYZOS, D., HAVERMANN, D., CARTER, R. M., MACPHERSON, W. N., HAND, D. P., and MAIER, R. R.: ‘In-fiber Fabry-Pérot cavity sensor for high-temperature applications’. *Journal of Light-wave Technology* (2015), vol. 33(12): pp. 2419–2425.
28. FLOWERS-JACOBS, N., HOCH, S., SANKEY, J., KASHKANOVA, A., JAYICH, A., DEUTSCH, C., REICHEL, J., and HARRIS, J.: ‘Fiber-cavity-based optomechanical device’. *Applied Physics Letters* (2012), vol. 101(22): p. 221109.
29. MULLER, A., FLAGG, E. B., LAWALL, J. R., and SOLOMON, G. S.: ‘Ultrahigh-finesse, low-mode-volume Fabry-Pérot microcavity’. *Optics letters* (2010), vol. 35(13): pp. 2293–2295.
30. TAKAHASHI, H., MORPHEW, J., ORUČEVIĆ, F., NOGUCHI, A., KASSA, E., and KELLER, M.: ‘Novel laser machining of optical fibers for long cavities with low birefringence’. *Optics express* (2014), vol. 22(25): pp. 31317–31328.
31. GARCIA, S., FERRI, F., OTT, K., REICHEL, J., and LONG, R.: ‘Dual-wavelength fiber Fabry-Pérot cavities with engineered birefringence’. *arXiv preprint arXiv:1805.04089* (2018), vol.
32. HUNGER, D., STEINMETZ, T., COLOMBE, Y., DEUTSCH, C., HÄNSCH, T. W., and REICHEL, J.: ‘A fiber Fabry-Pérot cavity with high finesse’. *New Journal of Physics* (2010), vol. 12(6): p. 065038.

33. UPHOFF, M., BREKENFELD, M., REMPE, G., and RITTER, S.: ‘Frequency splitting of polarization eigenmodes in microscopic Fabry–Perot cavities’. *New Journal of Physics* (2015), vol. 17(1): p. 013053.
34. PÖLLINGER, M., O’SHEA, D., WARKEN, F., and RAUSCHENBEUTEL, A.: ‘Ultrahigh-Q tunable whispering-gallery-mode microresonator’. *Physical review letters* (2009), vol. 103(5): p. 053901.
35. CAMPBELL, M., SHARP, D. N., HARRISON, M., DENNING, R., and TURBERFIELD, A.: ‘Fabrication of photonic crystals for the visible spectrum by holographic lithography’. *Nature* (2000), vol. 404(6773): p. 53.
36. JOANNOPOULOS, J. D., VILLENEUVE, P. R., and FAN, S.: ‘Photonic crystals: putting a new twist on light’. *Nature* (1997), vol. 386(6621): p. 143.
37. SIMBULA, A., SCHATZL, M., ZAGAGLIA, L., ALPEGGIANI, F., ANDREANI, L., SCHÄFFLER, F., FROMHERZ, T., GALLI, M., and GERACE, D.: ‘Realization of high-Q/V photonic crystal cavities defined by an effective Aubry-André-Harper bichromatic potential’. *APL Photonics* (2017), vol. 2(5): p. 056102.
38. HAPP, T., MARKARD, A., KAMP, M., FORCHEL, A., ANAND, S., GENTNER, J.-L., and BOUADMA, N.: ‘Nanofabrication of two-dimensional photonic crystal mirrors for 1.5 μm short cavity lasers’. *Journal of Vacuum Science & Technology B: Microelectronics and Nanometer Structures Processing, Measurement, and Phenomena* (2001), vol. 19(6): pp. 2775–2778.
39. XU, T., ZHU, N., XU, M. Y.-C., WOSINSKI, L., AITCHISON, J. S., and RUDA, H. E.: ‘A pillar-array based two-dimensional photonic crystal microcavity’. *Applied Physics Letters* (2009), vol. 94(24): p. 241110.
40. KNIGHT, J., BIRKS, T., RUSSELL, P. S. J., and ATKIN, D.: ‘All-silica single-mode optical fiber with photonic crystal cladding’. *Optics letters* (1996), vol. 21(19): pp. 1547–1549.
41. DERNTL, C., SCHNEIDER, M., SCHALKO, J., BITTNER, A., SCHMIEDMAYER, J., SCHMID, U., and TRUPKE, M.: ‘Arrays of open, independently tunable microcavities’. *Optics express* (2014), vol. 22(18): pp. 22111–22120.
42. PAUL, J. B., LAPSON, L., and ANDERSON, J. G.: ‘Ultrasensitive absorption spectroscopy with a high-finesse optical cavity and off-axis alignment’. *Applied optics* (2001), vol. 40(27): pp. 4904–4910.
43. ALBRECHT, R., BOMMER, A., DEUTSCH, C., REICHEL, J., and BECHER, C.: ‘Coupling of a single nitrogen-vacancy center in diamond to a fiber-based microcavity’. *Physical review letters* (2013), vol. 110(24): p. 243602.

44. ZHANG, X., LIU, L., and XU, L.: ‘Ultralow sensing limit in optofluidic micro-bottle resonator biosensor by self-referenced differential-mode detection scheme’. *Applied Physics Letters* (2014), vol. 104(3): p. 033703.
45. JANITZ, E., RUF, M., DIMOCK, M., BOURASSA, A., SANKEY, J., and CHIL-DRESS, L.: ‘Fabry-Perot microcavity for diamond-based photonics’. *Physical Review A* (2015), vol. 92(4): p. 043844.
46. VALLANCE, C., TRICHET, A. A., JAMES, D., DOLAN, P. R., and SMITH, J. M.: ‘Open-access microcavities for chemical sensing’. *Nanotechnology* (2016), vol. 27(27): p. 274003.
47. ST-GELAIS, R., MASSON, J., and PETER, Y.-A.: ‘All-silicon integrated Fabry–Pérot cavity for volume refractive index measurement in microfluidic systems’. *Applied physics letters* (2009), vol. 94(24): p. 243905.
48. KELKAR, H., WANG, D., MARTIN-CANO, D., HOFFMANN, B., CHRISTIANSEN, S., GÖTZINGER, S., and SANDOGHDAR, V.: ‘Sensing nanoparticles with a cantilever-based scannable optical cavity of low finesse and sub- λ 3 volume’. *Physical Review Applied* (2015), vol. 4(5): p. 054010.
49. SONG, W., ZHANG, X., LIU, A., LIM, C., YAP, P., and HOSSEINI, H. M. M.: ‘Refractive index measurement of single living cells using on-chip Fabry-Pérot cavity’. *Applied physics letters* (2006), vol. 89(20): p. 203901.
50. CHEN, Y., LEI, L., ZHANG, K., SHI, J., WANG, L., LI, H., ZHANG, X., WANG, Y., and CHAN, H. L.: ‘Optofluidic microcavities: Dye-lasers and biosensors’. *Biomicrofluidics* (2010), vol. 4(4): p. 043002.
51. PATEL, R. K., TRICHET, A. A. P., COLES, D. M., DOLAN, P. R., FAIR-CLOUGH, S. M., LEONTIADOU, M. A., TSANG, S. C. E., BINKS, D. J., JANG, E., JANG, H., TAYLOR, R. A., and SMITH, J. M.: ‘Gain Spectroscopy of Solution-Based Semiconductor Nanocrystals in Tunable Optical Microcavities’. *Advanced Optical Materials* (2016), vol. 4(2): pp. 285–290.
52. ASENBAUM, P., KUHN, S., NIMMRICHTER, S., SEZER, U., and ARNDT, M.: ‘Cavity cooling of free silicon nanoparticles in high vacuum’. *Nature communi-cations* (2013), vol. 4: p. 2743.
53. KUHN, S., WACHTER, G., WIESER, F.-F., MILLEN, J., SCHNEIDER, M., SCHALKO, J., SCHMID, U., TRUPKE, M., and ARNDT, M.: ‘Nanoparticle detection in an open-access silicon microcavity’. *Applied Physics Letters* (2017), vol. 111(25): p. 253107.
54. STECK, D. A.: ‘Classical and modern optics’. *Oregon Center for Optics and Department of Physics, University of Oregon* (2017), vol.

55. PURCELL, E. M., TORREY, H. C., and POUND, R. V.: ‘Resonance absorption by nuclear magnetic moments in a solid’. *Physical review* (1946), vol. 69(1-2): p. 37.
56. KRISTENSEN, P. T., VAN VLACK, C., and HUGHES, S.: ‘Generalized effective mode volume for leaky optical cavities’. *Optics letters* (2012), vol. 37(10): pp. 1649–1651.
57. GREIVENKAMP, J. E.: *Field guide to geometrical optics*. Vol. 1. SPIE Press Bellingham, WA, 2004.
58. IVES, H. E.: *An Introduction to the Theory of Optics*. 1925.
59. KOGELNIK, H. and LI, T.: ‘Laser beams and resonators’. *Proceedings of the IEEE* (1966), vol. 54(10): pp. 1312–1329.
60. KLECKNER, D., IRVINE, W. T., OEMRAWSINGH, S. S., and BOUWMEESTER, D.: ‘Diffraction-limited high-finesse optical cavities’. *Physical Review A* (2010), vol. 81(4): p. 043814.
61. BENEDIKTER, J., HÜMMER, T., MADER, M., SCHLEDERER, B., REICHEL, J., HÄNSCH, T. W., and HUNGER, D.: ‘Transverse-mode coupling and diffraction loss in tunable Fabry–Pérot microcavities’. *New Journal of Physics* (2015), vol. 17(5): p. 053051.
62. MERZIGER, G., MÜHLBACH, G., WILLE, D., and WIRTH, T.: *Formeln+ Hilfen zur höheren Mathematik*. Binomi, 2010.
63. KIEFER, J.: ‘Sequential minimax search for a maximum’. *Proceedings of the American mathematical society* (1953), vol. 4(3): pp. 502–506.
64. ROMBERG, W.: ‘Vereinfachte numerische integration’. *Det Kongelige Norske Videnskabers Selskab Forhandling* (1955), vol. 28(7): pp. 30–36.
65. LARSEN, K. P., RAVNKILDE, J. T., and HANSEN, O.: ‘Investigations of the isotropic etch of an ICP source for silicon microlens mold fabrication’. *Journal of Micromechanics and Microengineering* (2005), vol. 15(4): p. 873.
66. LAERMER, F. and SCHILP, A.: *Method of anisotropically etching silicon*. US Patent 5,501,893. 1996.
67. ASENBAUM, P. and ARNDT, M.: ‘Cavity stabilization using the weak intrinsic birefringence of dielectric mirrors’. *Optics letters* (2011), vol. 36(19): pp. 3720–3722.
68. SPRAGUE, R. A.: ‘Surface roughness measurement using white light speckle’. *Applied optics* (1972), vol. 11(12): pp. 2811–2816.
69. LAI, G. and YATAGAI, T.: ‘Generalized phase-shifting interferometry’. *JOSA A* (1991), vol. 8(5): pp. 822–827.

70. WACHTER, G., KUHN, S., MINNIBERGER, S., SALTER, C., ASENBAUM, P., MILLEN, J., SCHNEIDER, M., SCHALKO, J., SCHMID, U., FELGNER, A., et al.: ‘Silicon microcavity arrays with open access and a finesse of half a million’. *Light: Science & Applications* (2019), vol. 8(1): p. 37.
71. DEGALLAIX, J., FLAMINIO, R., FOREST, D., GRANATA, M., MICHEL, C., PINARD, L., BERTRAND, T., and CAGNOLI, G.: ‘Bulk optical absorption of high resistivity silicon at 1550 nm’. *Optics letters* (2013), vol. 38(12): pp. 2047–2049.
72. DOHERTY, M. W., MANSON, N. B., DELANEY, P., JELEZKO, F., WRACHTRUP, J., and HOLLENBERG, L. C.: ‘The nitrogen-vacancy colour centre in diamond’. *Physics Reports* (2013), vol. 528(1): pp. 1–45.
73. SCHRODER, D. K., THOMAS, R. N., and SWARTZ, J. C.: ‘Free carrier absorption in silicon’. *IEEE Journal of solid-state circuits* (1978), vol. 13(1): pp. 180–187.
74. KATSIDIS, C. C. and SIAPKAS, D. I.: ‘General transfer-matrix method for optical multilayer systems with coherent, partially coherent, and incoherent interference’. *Applied optics* (2002), vol. 41(19): pp. 3978–3987.
75. PEUMANS, P., YAKIMOV, A., and FORREST, S. R.: ‘Small molecular weight organic thin-film photodetectors and solar cells’. *Journal of Applied Physics* (2003), vol. 93(7): pp. 3693–3723.
76. RIEDEL, D., SÖLLNER, I., SHIELDS, B. J., STAROSIELEC, S., APPEL, P., NEU, E., MALETINSKY, P., and WARBURTON, R. J.: ‘Deterministic enhancement of coherent photon generation from a nitrogen-vacancy center in ultrapure diamond’. *Physical Review X* (2017), vol. 7(3): p. 031040.
77. JELEZKO, F. and WRACHTRUP, J.: ‘Single defect centres in diamond: A review’. *physica status solidi (a)* (2006), vol. 203(13): pp. 3207–3225.
78. APPEL, P., NEU, E., GANZHORN, M., BARFUSS, A., BATZER, M., GRATZ, M., TSCHÖPE, A., and MALETINSKY, P.: ‘Fabrication of all diamond scanning probes for nanoscale magnetometry’. *Review of Scientific Instruments* (2016), vol. 87(6): p. 063703.
79. KIM, Y.-H., YU, R., KULIK, S. P., SHIH, Y., and SCULLY, M. O.: ‘Delayed “choice” quantum eraser’. *Physical Review Letters* (2000), vol. 84(1): p. 1.
80. TONOMURA, A., ENDO, J., MATSUDA, T., KAWASAKI, T., and EZAWA, H.: ‘Demonstration of single-electron buildup of an interference pattern’. *Am. J. Phys* (1989), vol. 57(2): pp. 117–120.

81. AKOURY, D., KREIDI, K., JAHNKE, T., WEBER, T., STAUDTE, A., SCHÖFLER, M., NEUMANN, N., TITZE, J., SCHMIDT, L. P. H., CZASCH, A., et al.: 'The simplest double slit: interference and entanglement in double photoionization of H₂'. *Science* (2007), vol. 318(5852): pp. 949–952.
82. RAUCH, H., TREIMER, W., and BONSE, U.: 'Test of a single crystal neutron interferometer'. *Physics Letters A* (1974), vol. 47(5): pp. 369–371.
83. CARNAL, O. and MLYNEK, J.: 'Young's double-slit experiment with atoms: A simple atom interferometer'. *Physical review letters* (1991), vol. 66(21): p. 2689.
84. SHIMIZU, F., SHIMIZU, K., and TAKUMA, H.: 'Double-slit interference with ultracold metastable neon atoms'. *Physical Review A* (1992), vol. 46(1): R17.
85. ARNDT, M., NAIRZ, O., VOS-ANDREAE, J., KELLER, C., VAN DER ZOUW, G., and ZEILINGER, A.: 'Wave-particle duality of C₆₀ molecules'. *nature* (1999), vol. 401(6754): p. 680.
86. EIBENBERGER, S., GERLICH, S., ARNDT, M., MAYOR, M., and TÜXEN, J.: 'Matter-wave interference of particles selected from a molecular library with masses exceeding 10000 amu'. *Physical Chemistry Chemical Physics* (2013), vol. 15(35): pp. 14696–14700.
87. ASENBAUM, P., KUHN, S., SEZER, U., NIMMRICHTER, S., and ARNDT, M.: 'Cavity cooling of free nanoparticles in high vacuum'. *APS Meeting Abstracts*. 2014.
88. GIESELER, J., DEUTSCH, B., QUIDANT, R., and NOVOTNY, L.: 'Subkelvin parametric feedback cooling of a laser-trapped nanoparticle'. *Physical review letters* (2012), vol. 109(10): p. 103603.
89. KUHN, S., ASENBAUM, P., KOSLOFF, A., SCLAFANI, M., STICKLER, B. A., NIMMRICHTER, S., HORNBERGER, K., CHESHNOVSKY, O., PATOLSKY, F., and ARNDT, M.: 'Cavity-assisted manipulation of freely rotating silicon nanorods in high vacuum'. *Nano letters* (2015), vol. 15(8): pp. 5604–5608.
90. KOSLOFF, A., HEIFLER, O., GRANOT, E., and PATOLSKY, F.: 'Nanodicing Single Crystalline Silicon Nanowire Arrays'. *Nano letters* (2016), vol. 16(11): pp. 6960–6966.
91. ZINOVEV, A., VERYOVKIN, I., and PELLIN, M.: 'Molecular Desorption by Laser-Driven Acoustic Waves: Analytical Applications and Physical Mechanisms'. *Acoustic Waves-From Microdevices to Helioseismology*. InTech, 2011.
92. DOW, A. R., WITTRIG, A. M., and KENTTÄMAA, H. I.: 'Laser-induced acoustic desorption mass spectrometry'. *European Journal of Mass Spectrometry* (2012), vol. 18(2): pp. 77–92.

93. BECKMANN, P. and SPIZZICHINO, A.: 'The scattering of electromagnetic waves from rough surfaces'. *Norwood, MA, Artech House, Inc., 1987, 511 p.* (1987), vol.
94. HARVEY, J. E., CHOI, N., SCHROEDER, S., and DUPARRÉ, A.: 'Total integrated scatter from surfaces with arbitrary roughness, correlation widths, and incident angles'. *Optical Engineering* (2012), vol. 51(1): p. 013402.
95. REYNOLDS, J. L., NEUREUTHER, A. R., and OLDHAM, W. G.: 'Simulation of dry etched line edge profiles'. *Journal of Vacuum Science and Technology* (1979), vol. 16(6): pp. 1772–1775.



Die approbierte gedruckte Originalversion dieser Dissertation ist an der TU Wien Bibliothek verfügbar.
The approved original version of this doctoral thesis is available in print at TU Wien Bibliothek.

A Theory of etching mirrors in silicon

This chapter treats the etching and surface treatment of silicon from a theoretical standpoint. I will first discuss the intended etching process for mirror production and then introduce a numerical simulation of the first etch step. These simulations are not intended to provide a quantitative prediction of the production process, but they allow us to describe important features of the etching procedure. From the simulations, we can identify three regimes of etching. This is a very important result and will be discussed in the second section of this chapter.

A.1 Etching simulations

Numerical simulations are useful to get an idea how the mirror shape changes during the etch procedure and how to calculate or estimate the parameters for mirror production. The simulations are based on an idea which came up when dry etching was developed in the 1970s and is called String developed model [95].

The goal of the simulations is to calculate the time evolution of the chip surface. The more simple approach to simulate the plasma etching assumes the etch process to be isotropic. This assumption holds for big structures, where the free path of a

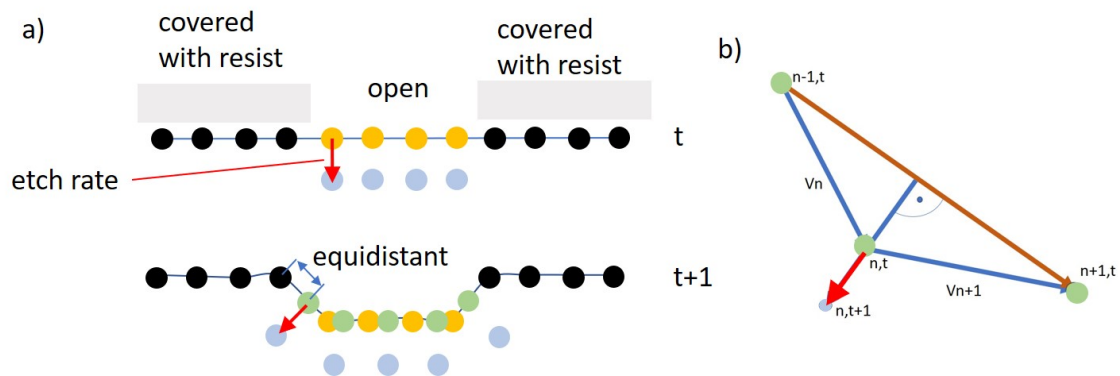


Figure A.1: Time evolution of the simulated points. In a), the black dots are covered with resist and are static. The yellow points are open and translated according to the etch rate (blue points at t). A spline is fit to all points and new, equidistant points (green) are placed on this curve. These are the starting points for the next etch step. In b), the general way to find the next point is shown. The green points represent the actual surface. To find the next point (blue) the vector between $n-1$ and $n+1$ is calculated and then the point n is translated in the perpendicular direction of this vector, determined by the etch rate.

reactive atom in the plasma is much smaller than the structure size. For experimental reasons it is desirable to use a very low density gas, which results in a long free path length. Therefore, the conditions for isotropic etching are only fulfilled for our larger structures. To get more realistic results, a non-isotropic etch rate is introduced. For this we need to estimate a distribution for the etch rates for different directions, as these rates can not be measured easily.

Since the problem is rotationally symmetric, a 2D simulation of the etching is sufficient. The algorithm works as follows: First, the chip surface is discretized as a chain of equidistant points. These points can either be open or covered with photoresist. Etching now shifts all open points in the direction perpendicular to the line connecting the previous and the next point. This is shown in figure A.1. Points located outside the substrate will be removed. In the next step, a spline is fit through the points. This operation produces a parametric function, the parameter is the position along the curve. Now, new equidistant points along the spline are calculated. The splining also results in a smooth and more realistic result.

The shift of each point is given by the etch rate, which depends on the open area of the wafer. This determines the loss of reactive atoms from the gas. For a wide-open wafer, a lot of reactive atoms are lost and the etch rate drops. If less silicon is exposed to the gas, the etch rate increases. When the features become very small, the etch rate drops due to shadowing effects. Because the size of the structures change during the etch process, the etch rate also becomes time dependent.

For the simulations we assume an average etch rate derived from a test run, we simply divide the depth of a medium-sized mirror by the etch time. We perform two kinds of simulations: the isotropic case and the more realistic anisotropic etching, where the former is just a special case of the latter.

The purpose of the simulations is to investigate at which point during the etch procedure the ideal mirror shape appears. The ideal shape is a parabola, and the effects of a deviation from this shape were discussed in chapter 3.

The problem with isotropic etch simulations is that the shape near to the edges does not match reality. A real mirror after the first etch does not look like a half sphere, more like an onion. To get to a more realistic result, an anisotropic etch simulation is required. The real etch process depends on many parameters and is difficult to model. For the simulation, it is necessary to assume a distribution for the etch rates, we restrict ourselves here to the easiest case. That means no time dependence, only the horizontal and the vertical etch rates differ. This can be written as:

$$Etchrate = r_g \cdot \begin{pmatrix} 1 - \gamma \\ 1 \end{pmatrix}. \quad (\text{A.1})$$

We are assuming a global etch rate r_g and an anisotropy parameter $\gamma \in [0,1]$. $\gamma = 1$ corresponds to a case with an etch rate only in z -direction and $\gamma = 0$ represents the isotropic case. The simulation is done unitless, which gives us the ability to choose the units later.

In figure A.2 the results of the simulations are summarized. The anisotropy parameter is changed over the whole range, in steps of 0.2, starting with a strictly vertical etch ($\gamma = 1$) straight into the substrate in the first line. This curve is not a rectangular slot because the spline fit smoothens the curve. The isotropic case with $\gamma = 0$ is shown in the last line.

The first column shows the ROC over etching time. How this value is calculated from the shape is explained in detail in section 3.1. In the second column the evolution of the simulated mirror surface is shown. The surfaces in the first four lines with $\gamma = 1 - 0.4$ represent realistic mirror shapes found in the experiment.

The simulated mirror surfaces are fit using a fourth order polynomial of the form $a_0 + a_2x^2 + a_4x^4$. For the fit, only the central part of the mirror with points between -1 and 1 are considered. This is justified because the mode of the cavity has a significant amplitude only in the center of the mirror. The coefficients for the quadratic and quartic terms are plot in the last column of the figure. The quadratic coefficient a_2 from the fit is used to calculate the ROC in the first column. The coefficient of the quartic term a_4 indicates how well the surface can be approximated by a parabola. As the parabola is the desired shape for a mirror, we want a small or vanishing quartic coefficient. In the third regime (refer to figure A.3), the quartic part vanishes for all $\gamma < 1$, which shows that we want to work in this regime.

The first and most important information we get from the simulations is that an anisotropic etching does not influence the mirror shape too much. For long enough etch times, it adds no higher order polynomial terms to the mirror shape. Second, anisotropic etching has only a slight influence on the mirror radius of curvature and can be easily corrected by adapting the etching time. To conclude, anisotropic etching changes the time evolution of the surfaces but does not add any additional dependencies to the problem, unless in extreme cases like in figure A.2 a.

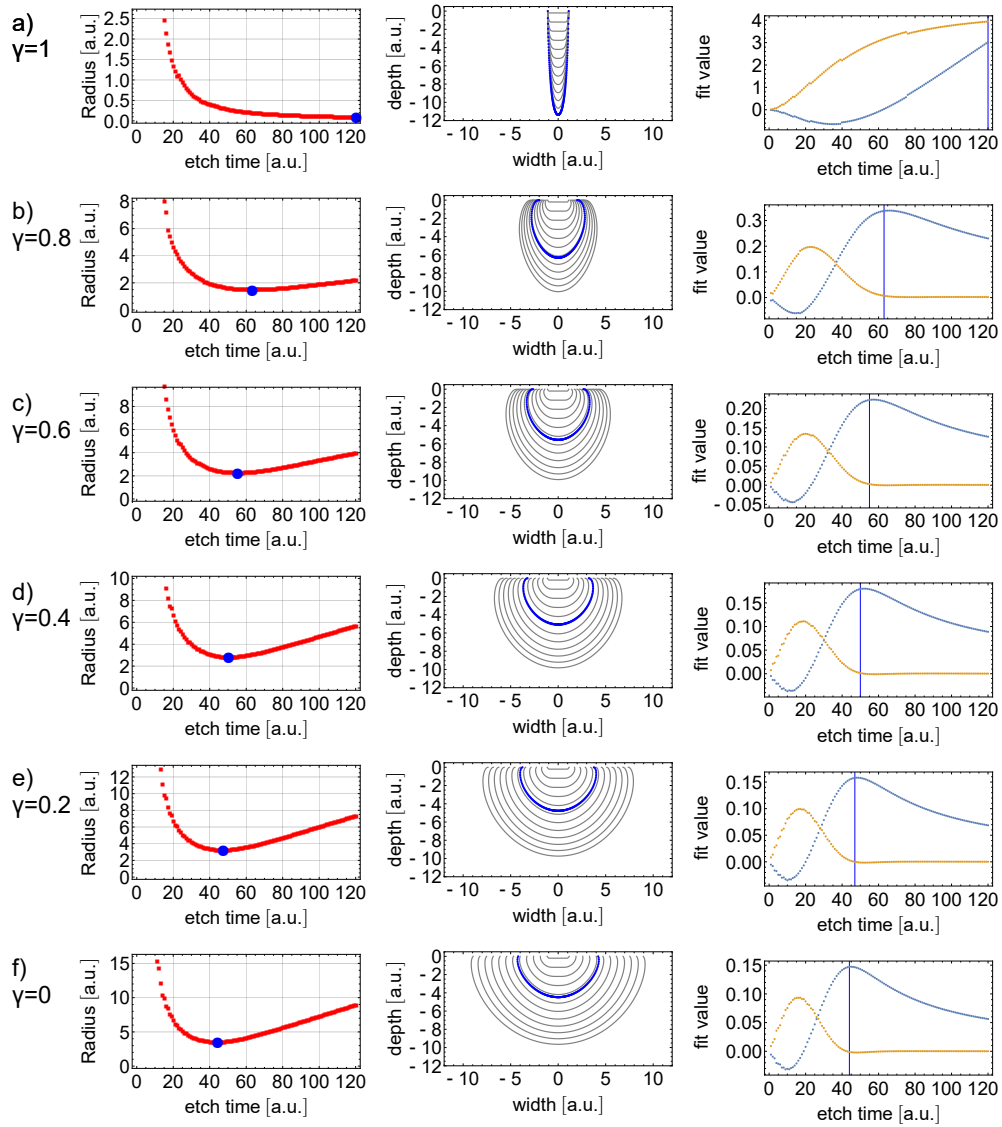


Figure A.2: The key results of the anisotropic etch simulations. Details are given in the text. γ is varied from 1 in line (a) to 0 in line (f). In the first column the radius over etch time is shown. In the second column the mirror shape is shown and in the last the fit parameters are plotted. The fit parameters are a_2 (blue) and a_4 (orange).

A.2 The three regimes of etching

The main conclusion of the simulation is that we can identify three regimes of etching. To illustrate this, we concentrate on the simulation results for the isotropic etch case, this equivalent to line f) in figure A.2 and displayed again in more detail in figure A.3.

The first regime is represented by the first curve (blue) in this figure. It shows what happens if the etch time is too short or the initial opening is too wide. The edge is sharp and bent to the top. The shape looks like a bowl or a drinking glass. This shape is a mirror with an infinite or very large radius with bent edges.

The best cavity from the first production run is exactly in this regime (cf. section 6.2). The three reasons for this behavior are: First, for mirrors with a ROC of 1 mm, the critical distance (for curved-curved configuration) is at 2 mm, as calculated in section 2.6.4. With a length of 130 μm the cavity is far away from any restriction by mode size on the mirror. Second, the position of the mirror is not so critical because of the large ROC. Small changes of the mode position on the mirror have no influence on the finesse. And third, deviations from the ideal shape do not affect the finesse for very short cavities as we calculated in chapter 3. So, every parameter is set to a non-critical regime. The drawback is that the field gradient is small as the waist is relatively big.

The second regime is between the orange and the brown curve in figure A.3, this is the region where the quartic part of the fit is considerable. Therefore the shape is far from the ideal case because the ROC in the middle differs from the edge. This varying ROC causes scattering losses into higher modes.

The last regime starts when the mirror reaches its smallest ROC. From that point onwards, the ROC increases as shown in figure A.3 b). For small mirrors this is the best regime. The radius is small and the shape is reasonably good. In this regime the shape, roughness, position and size are critical and if one parameter fails the finesse falls dramatically. To get working mirrors in this regime, the manufacturing process has to be highly optimized to achieve good results. The second mirror production run was deep in the third regime and resulted in many excellent microcavities, see section 6.3. The three regimes are also summarized in table A.1.

After the mirror shape is defined during the first etch step a second etch step is performed. This etch step is difficult to simulate. The sharp edges, where the photoresist was, produce huge artifacts for our simple algorithm.

Figure A.4 shows real mirror shapes. These mirrors are measured after the second etch step. Unfortunately no measurements after the first etch step exist, because the white light interferometer was bought 3 years after the production. The second etch step only opens and amplifies the shape, which means it is possible to identify the regimes of etching also in these shapes.

In figure A.5 a measurement of 100 mirrors are shown. The mirrors have different

opening diameters. Because the amount of etch gas inside an opening depends on the diameter, this situation has to be very similar to one opening diameter and a variation in etch time[65]. The curve which is found by fitting the radius inside these mirrors looks very similar to the curve which the theory predicts. Unfortunately it is very difficult get a reasonable prediction out of the theory because the etching depends strongly on the etch rates and their distribution.

Table A.1: Here the summary for the different regimes are shown.

	dominant part	features	mirror quality	critical numbers
regime I	flat middle, steep edges	mirrors with big ROC	ok	no
regime II	mixture between edge and middle part	bad shape	bad	
regime III	constant curvature over full mirror	small ROC, good shape, spot on mirror	good	all because of the big beam size on the mirror

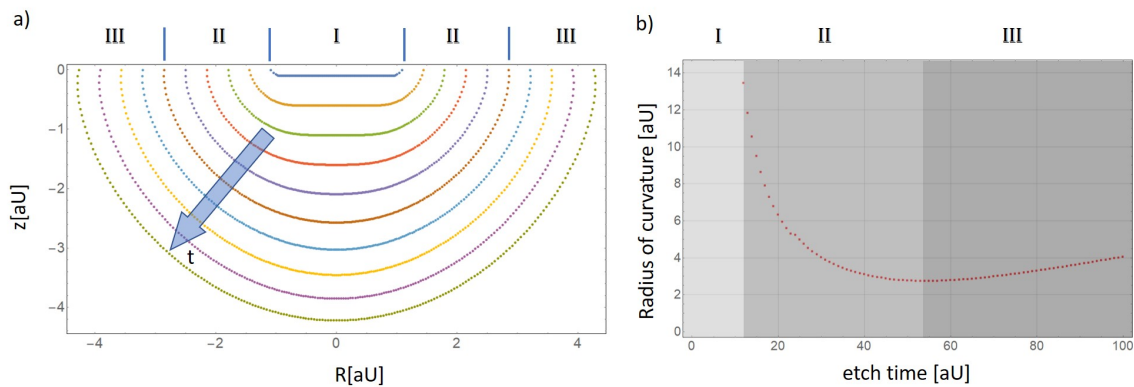


Figure A.3: Results of an isotropic etch simulation. Three regimes can be identified: Regime I for a flat mirror with a very large radius of curvature, which results in a very stable cavity. Regime II, where the radius at the edge differs from the radius in the middle of the mirror, has to be avoided because of scattering losses to higher modes (see text). The last regime features a uniform curvature across the full mirror and represents the preferred situation. In a) the simulated etch process is shown. The color codes the etch time, the blue curve represents the surface after the first and the green after the last etching step. b) shows the radius of curvature for the different etch times from a). For this purpose a parabola is fit into the center part of the curves from a) and the radius of curvature of the parabola is calculated (see section 3.3 for details).

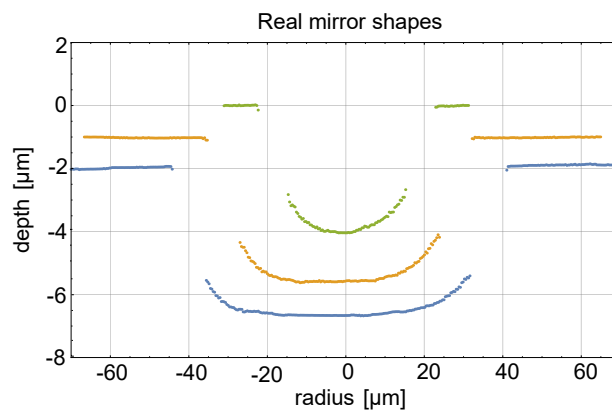


Figure A.4: Three different sized real mirrors. All of these mirrors are measured with a white light interferometer. They are etched with different opening diameters and the same etch time. In the simulation, this is equivalent to different etch times with the same opening diameter. These measurements are done after the second etch step. The second etch step only opens and amplifies the shape, without changing it. What we can see here is that the blue mirror was clearly in the first regime before the second etch. The orange mirror was near to the border between the first and the second regime. The green shape was obviously in the third regime.

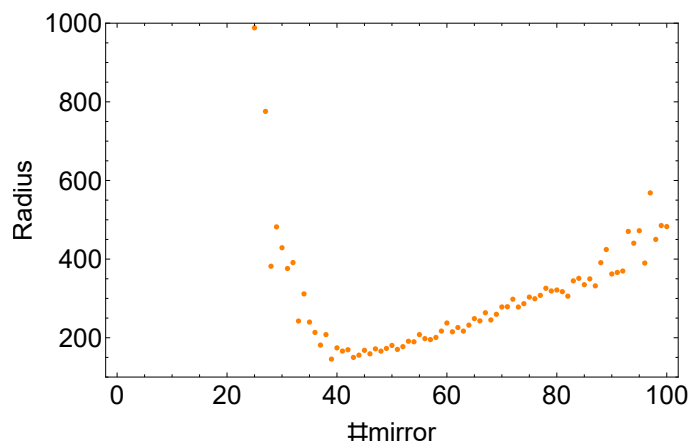


Figure A.5: A white-light interferometer measurement series. 100 mirrors with different mask opening diameter are measured. Because the opening defines the amount of etch gas we expect the same inverse behavior as for constant diameter and different etch times. The shape of the curve is very similar to the theory presented in this section.

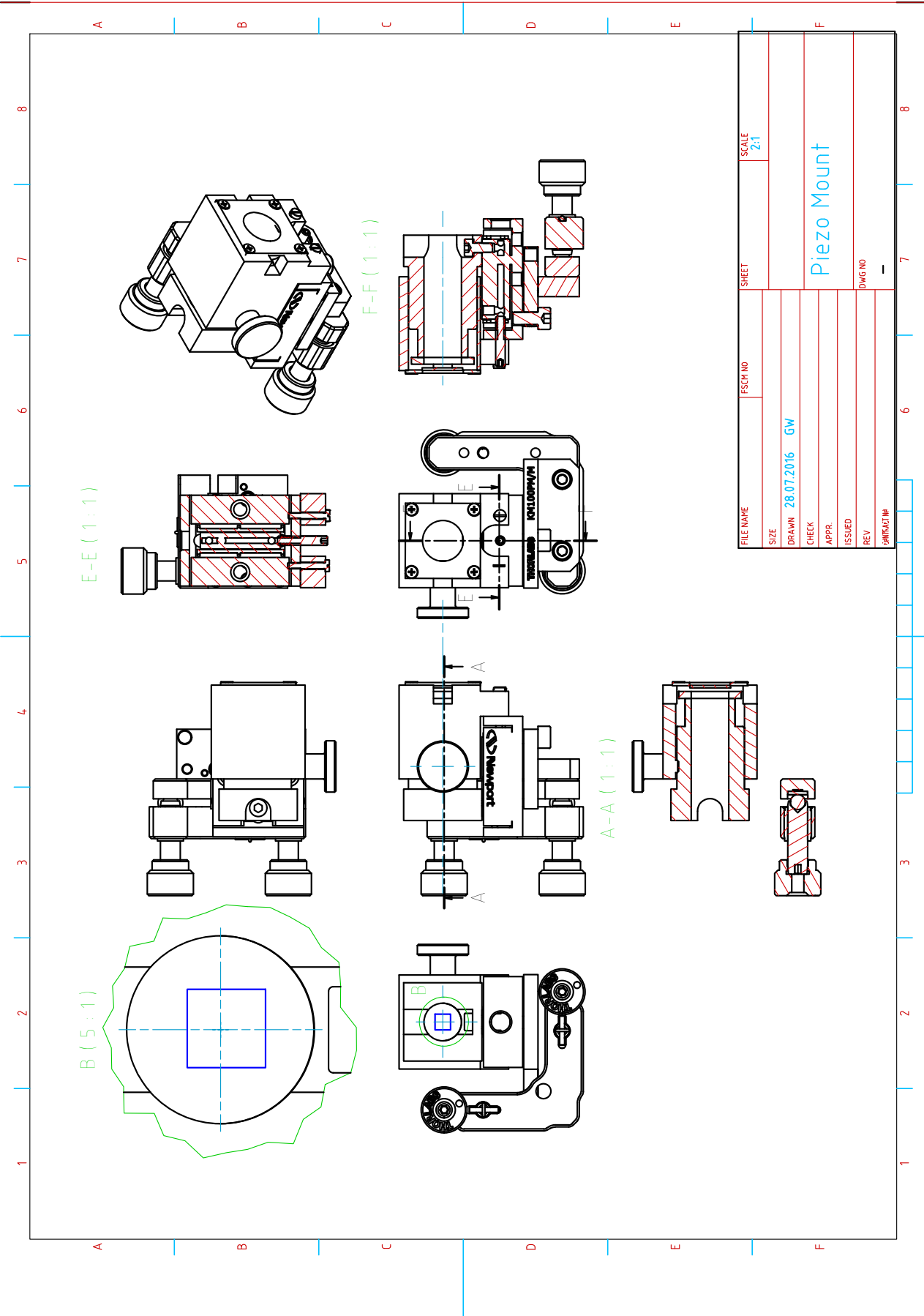
B Masks and schematics

B.1 piezo mount

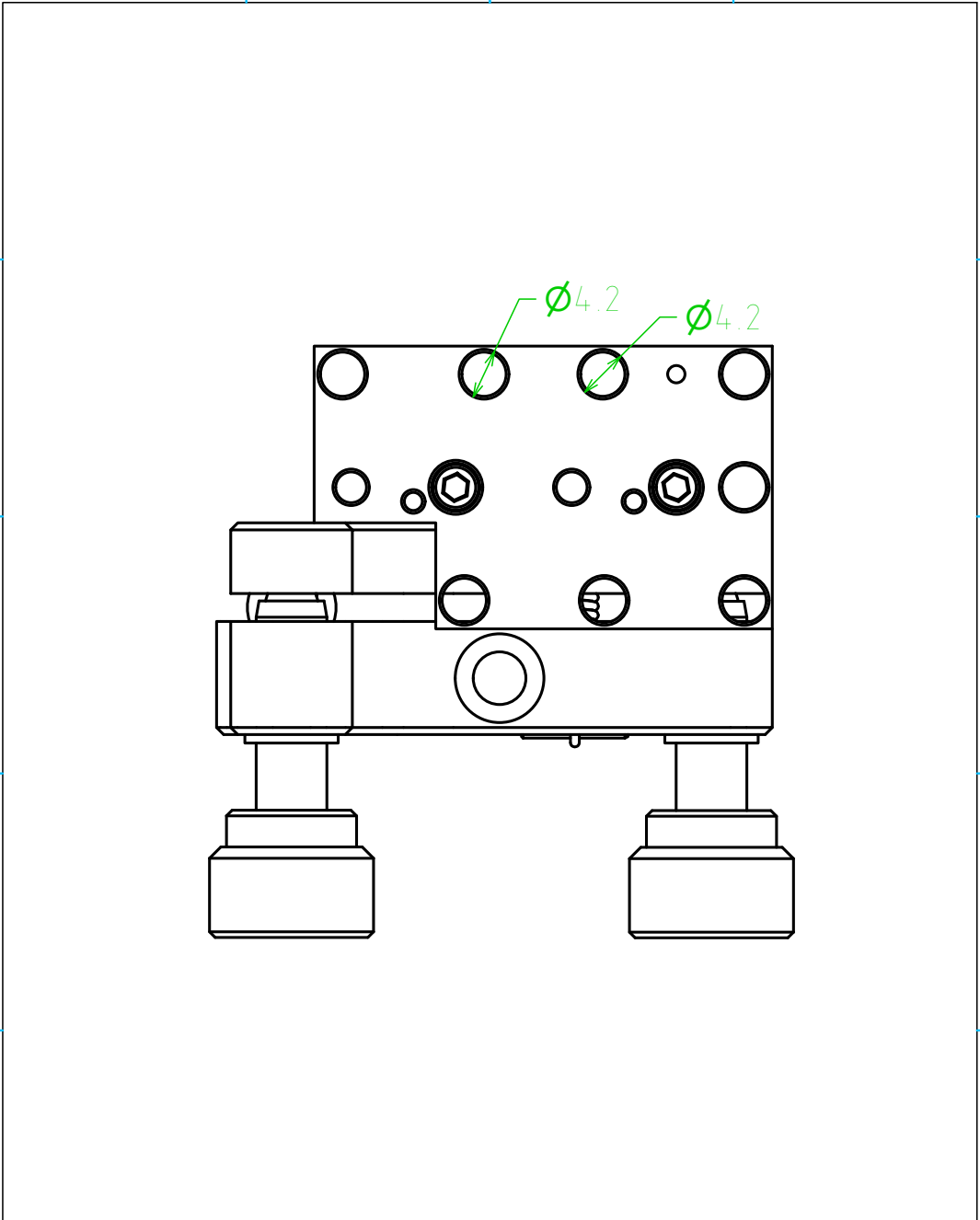
B.1.1 Mechanical drawings

Mechanical drawings for parts used in the piezo setup. The piezo ¹ makes it possible to tune the length between the mirrors.

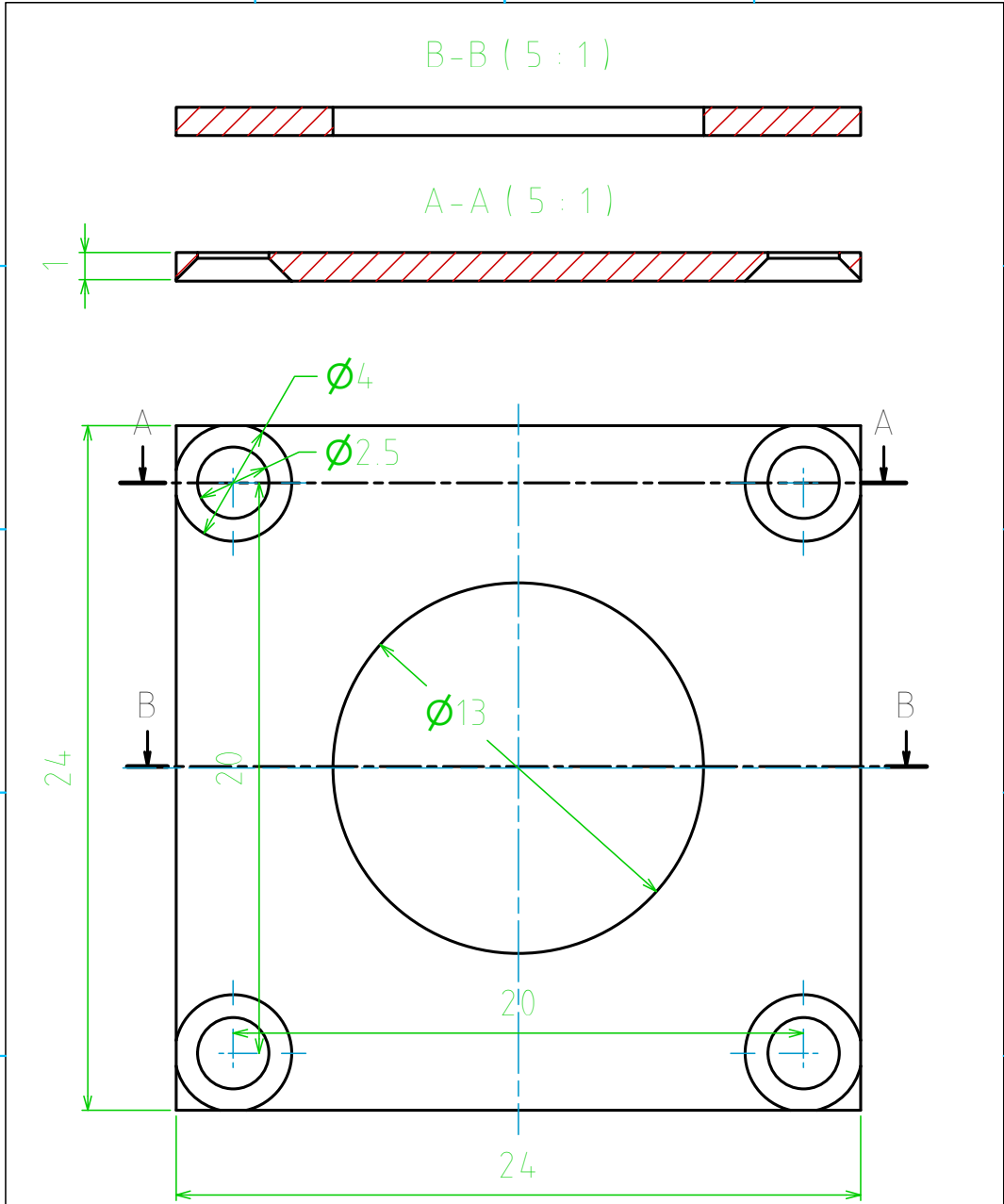
1 NAC2123 from Noliac



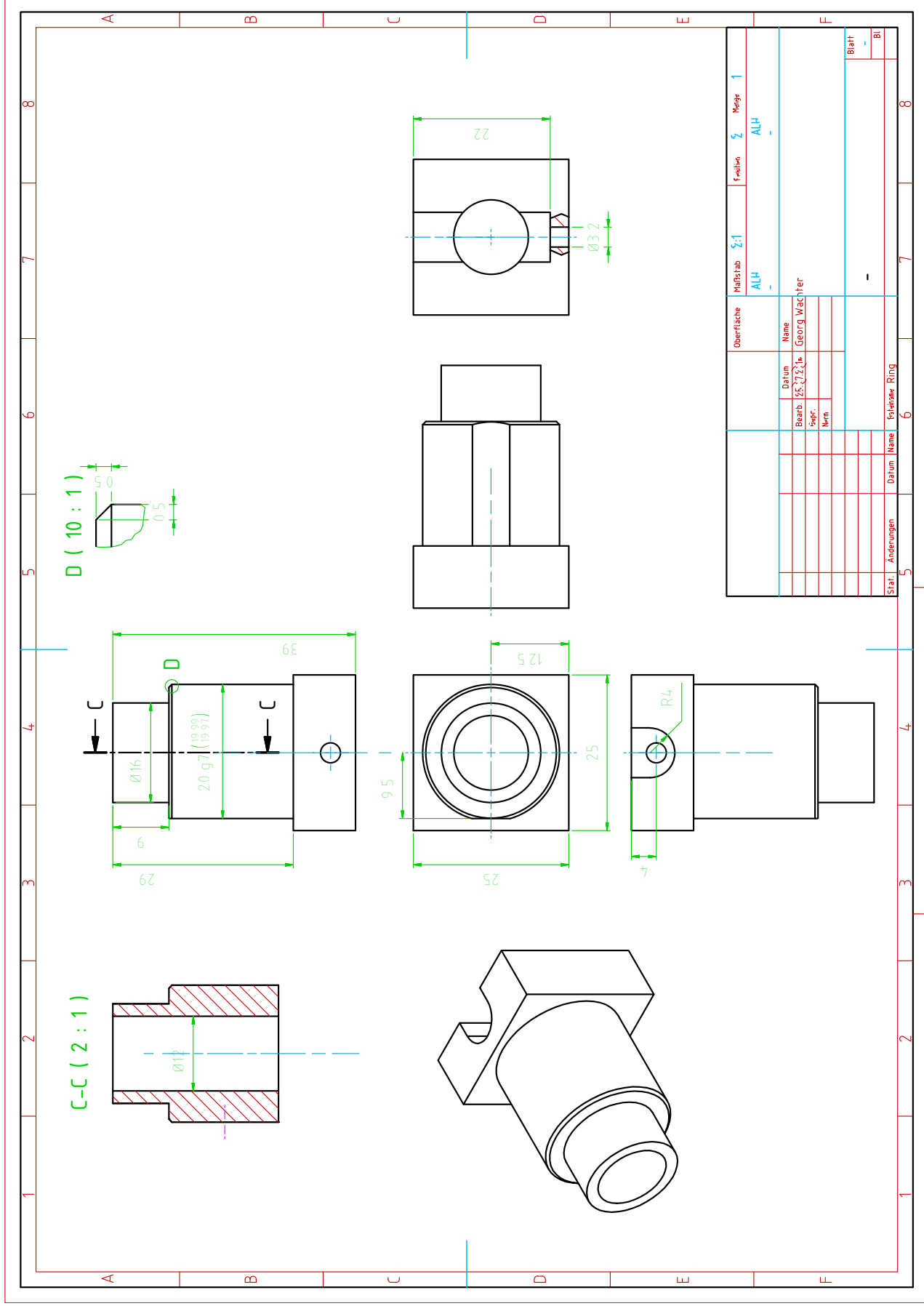
FILE NAME	FSC/NO	SHEET	SCALE
SIZE	DRAWN 28.07.2016 GW		2:1
CHECK			
APPR.			
ISSUED			
REV			
DWG NO			
DATE			
Piezo Mount			
DWG NO			
DATE			



		Oberfläche		Maßstab	Σ:1	Revision	Σ	Menge	1
				-		-			
			Datum	Name					
			Bearb.	25.7.2016	Georg Wächter				
			Gepr.						
			Norm						
								Blatt	
								-	
Stat.	Änderungen	Datum	Name	Erstkreislauf KM100PM-M-S				Bl	



		Oberfläche		Maßstab	5:1	Position	2	Menge	1
				ALH			ALH		
		Datum	Name						
		Bearb.	25.7.21	Georg Wachter					
		Geprf.							
		Norm							
Stat.	Änderungen	Datum	Name	Erstinsame mount				Blatt	
								-	
								Bl	



B.1.2 Electrical drawings

This electrical circuit is built to modulate a low ($< 1\text{ V}$) sinusoidal voltage signal with a frequency between 500 Hz and 1 kHz on a stable high voltage (max 200 V). This circuit is fully passive. It works as filter and a coupler. All files can be found under <https://circuitmaker.com/Projects/Details/Georg-Wachter/Piezo-AC-with-Biase>

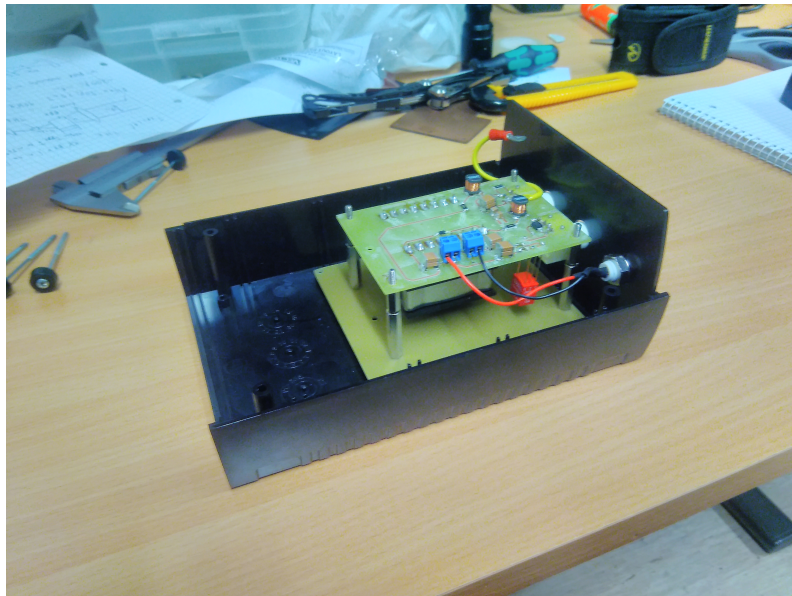


Figure B.1: Photo of the modulator.

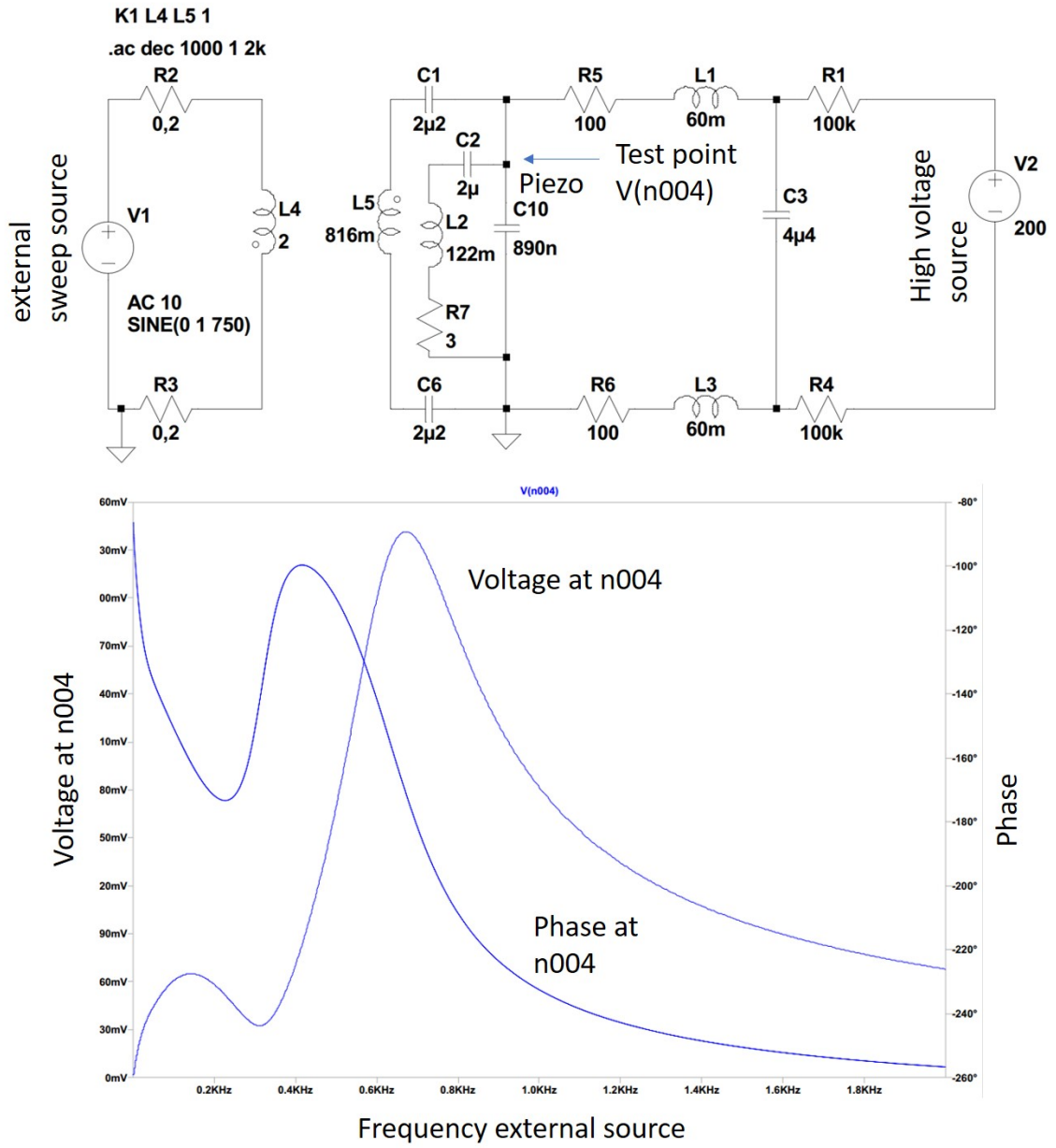
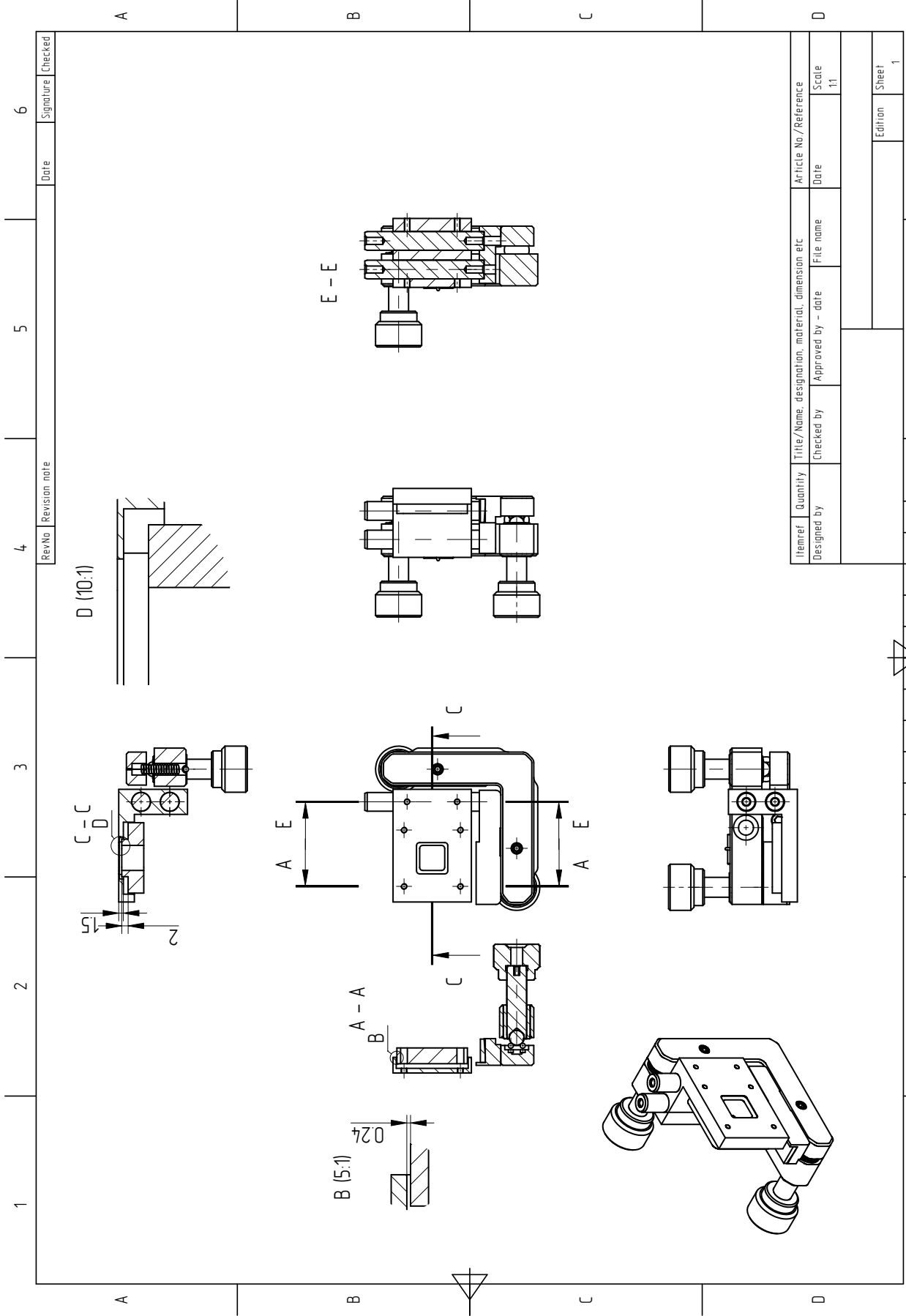


Figure B.2: Simulation of the circuit and Bode plot of signal which is applied to the piezo.

B.2 mount for monolithic cavities

Technical drawings for the mount designed for the monolithic cavities.

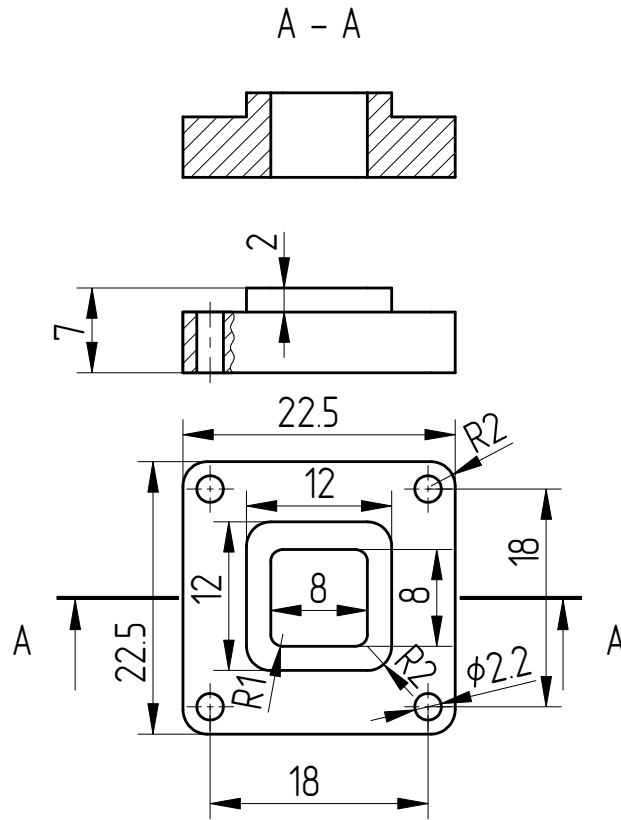


1	2	3	4	5	6		
RevNo				Revision note	Date	Signature	Checked

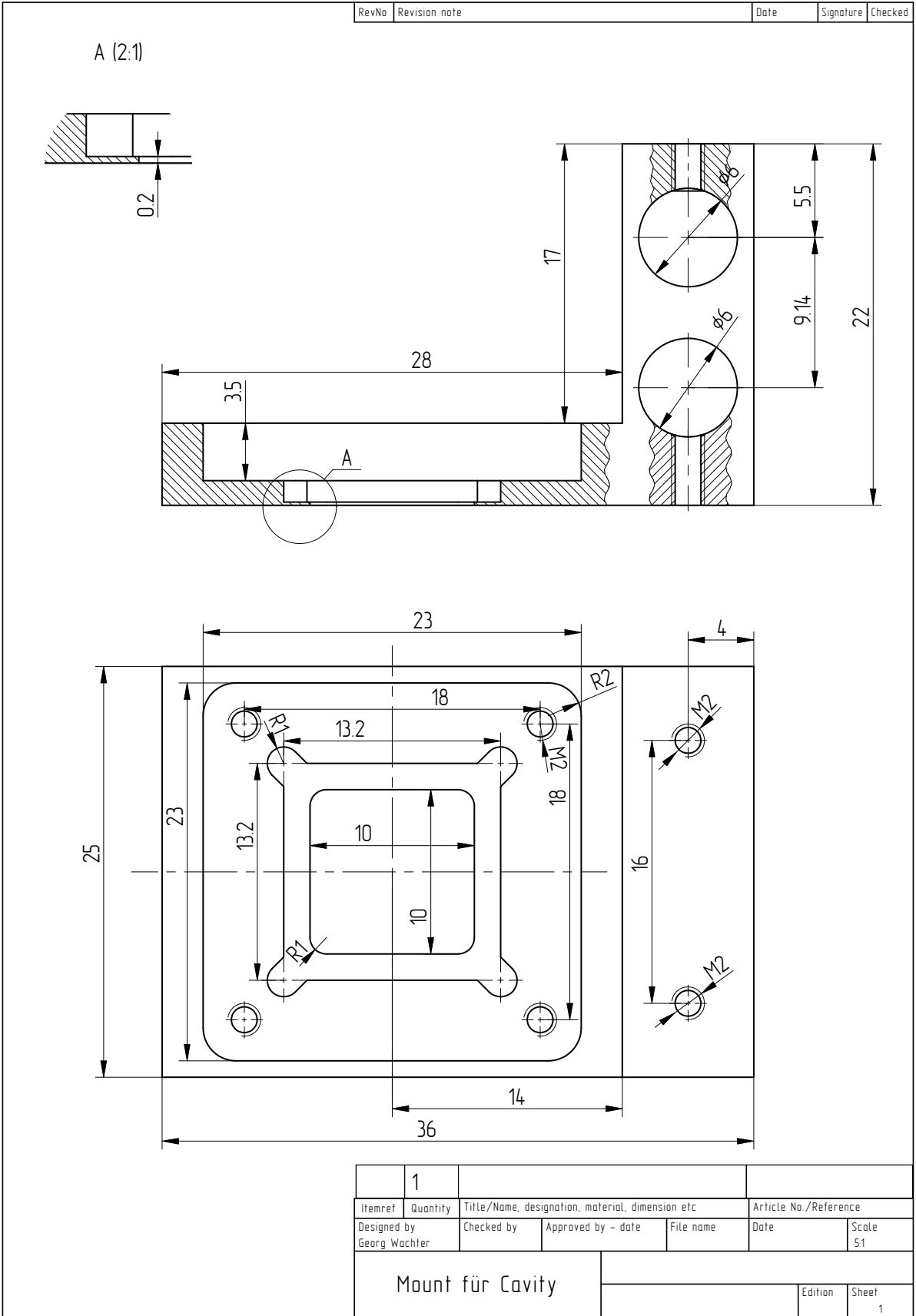
Itemref	Quantity	Title/Name, designation, material, dimension etc	Article No./Reference
Designed by	Checked by	Approved by - date	File name
			Date
			Scale
			1:1
			Edition
			Sheet
			1

1	2	3	4	5	6
				Edition	Sheet
				1	1

RevNo	Revision note	Date	Signature	Checked
-------	---------------	------	-----------	---------

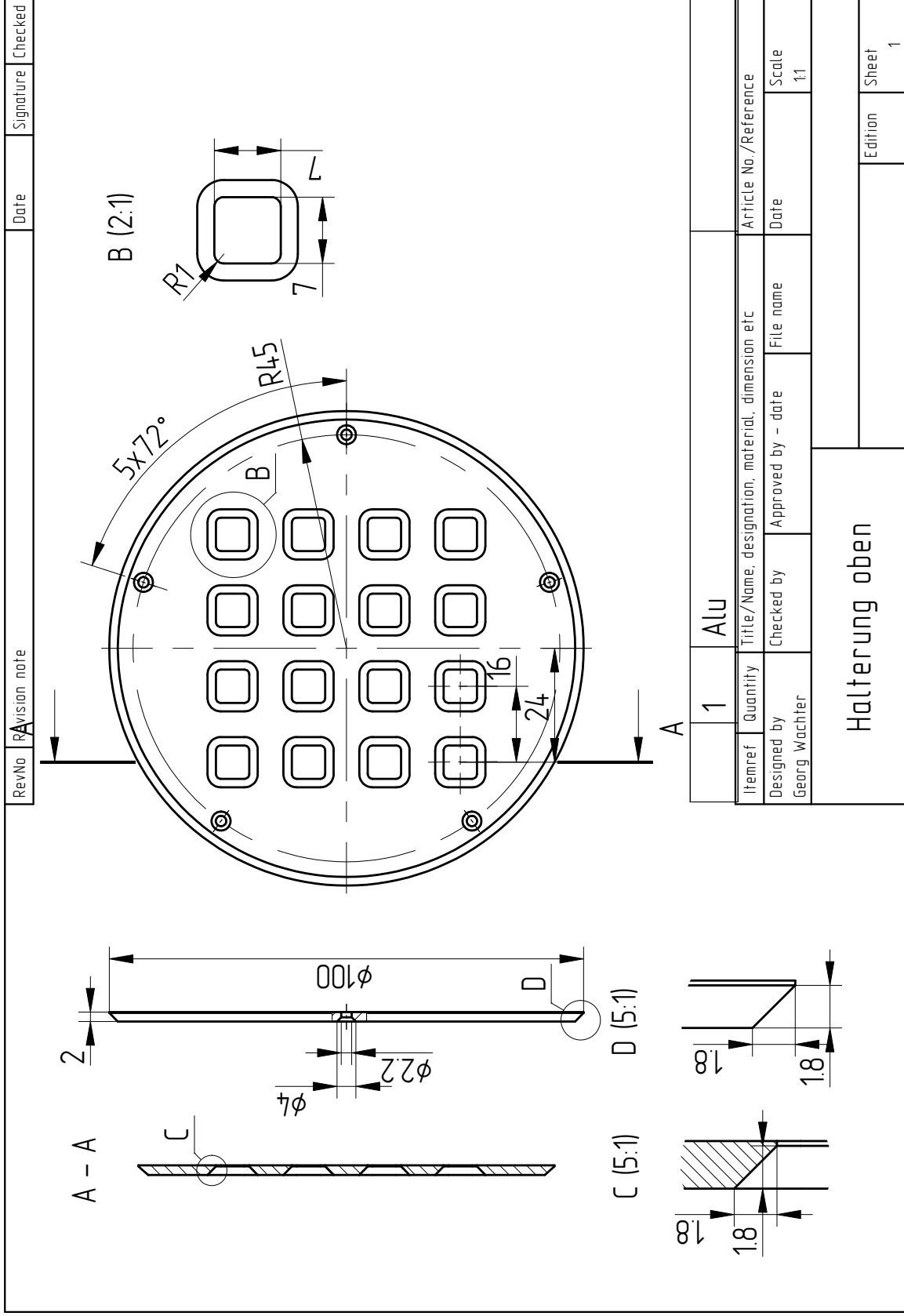


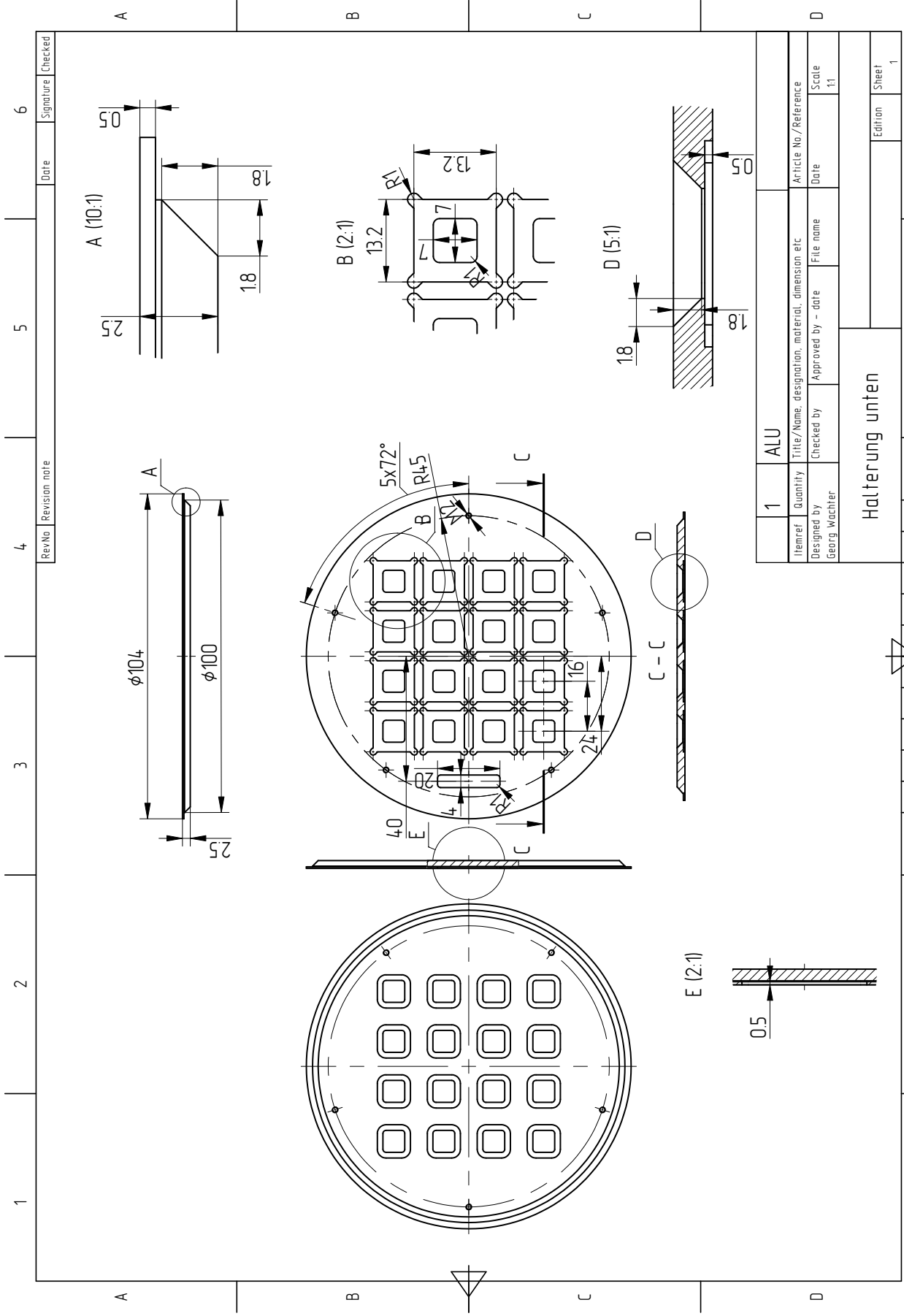
	1					
Itemref	Quantity	Title/Name, designation, material, dimension etc			Article No./Reference	
Designed by Georg Wachter		Checked by	Approved by - date	File name	Date	Scale 2:1
Cavity Mount						
				Edition	Sheet 1	



B.3 Coating mount

This mechanical drawings shows the mounts to hold the chips inside the coating device.





1	ALU			
Itemref	Quantity	Title/Name, designation, material, dimension etc	Article No./Reference	
Designed by Georg Wachter	Checked by	Approved by - date	File name	Scale
				1:1
Halterung unten			Edition	Sheet
				1

B.4 Mask set for mirrors

The whole set of masks used for mirror- and spacer production.

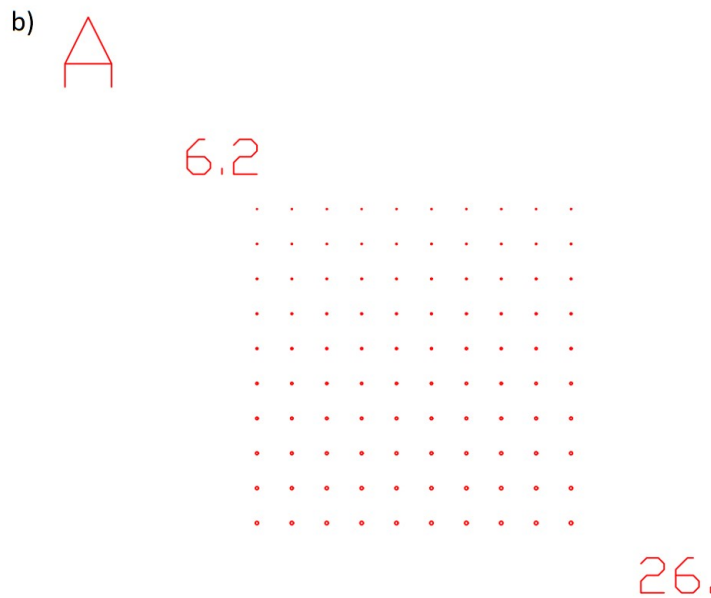
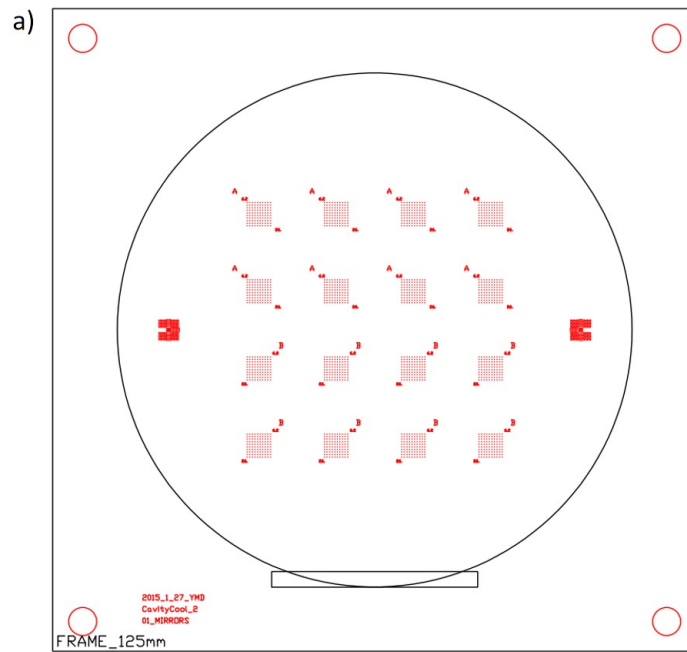


Figure B.3: Layer for the mirror masks. The holes are $12.4\ \mu\text{m}$ to $52\ \mu\text{m}$. a) is the full mask and b) a zoomed version on the chip.

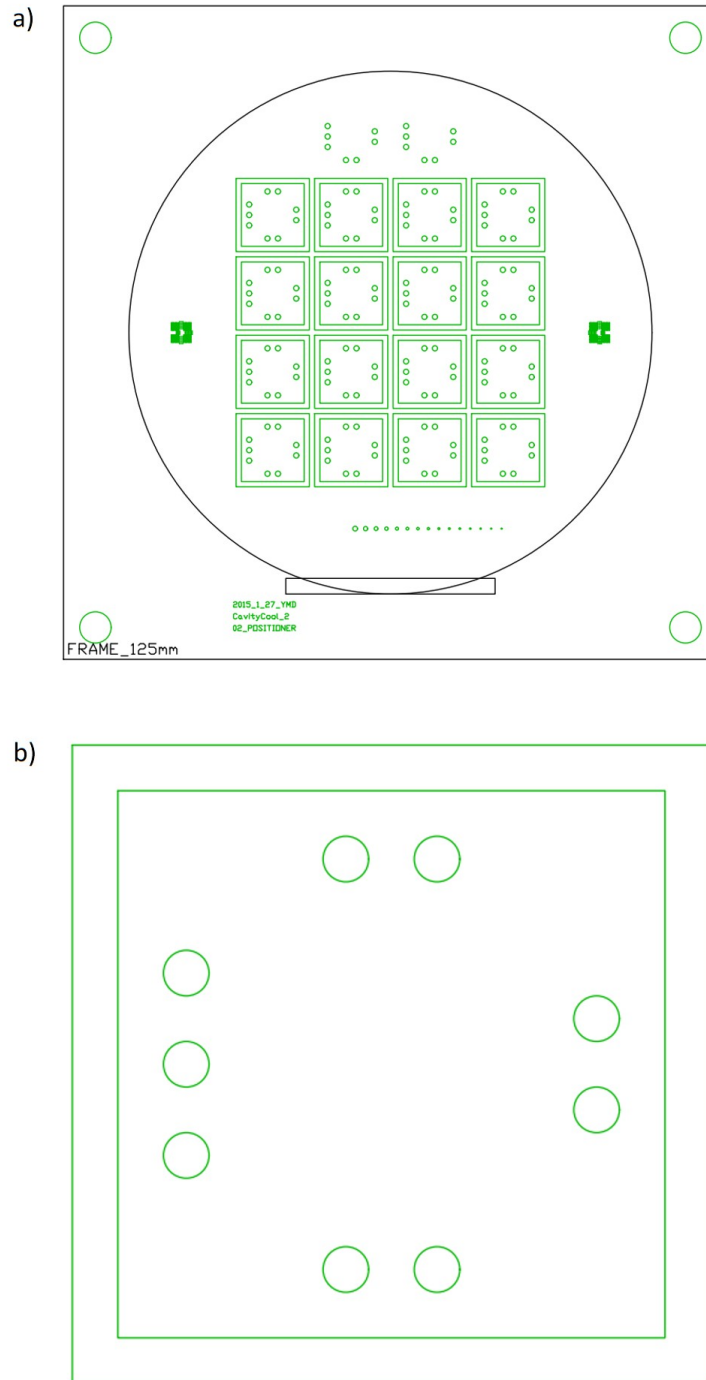


Figure B.4: Layer for the pillars. They have an diameter of 1 mm and are used to align the two mirrors chips. a) is the full mask and b) a zoomed version of the chip.

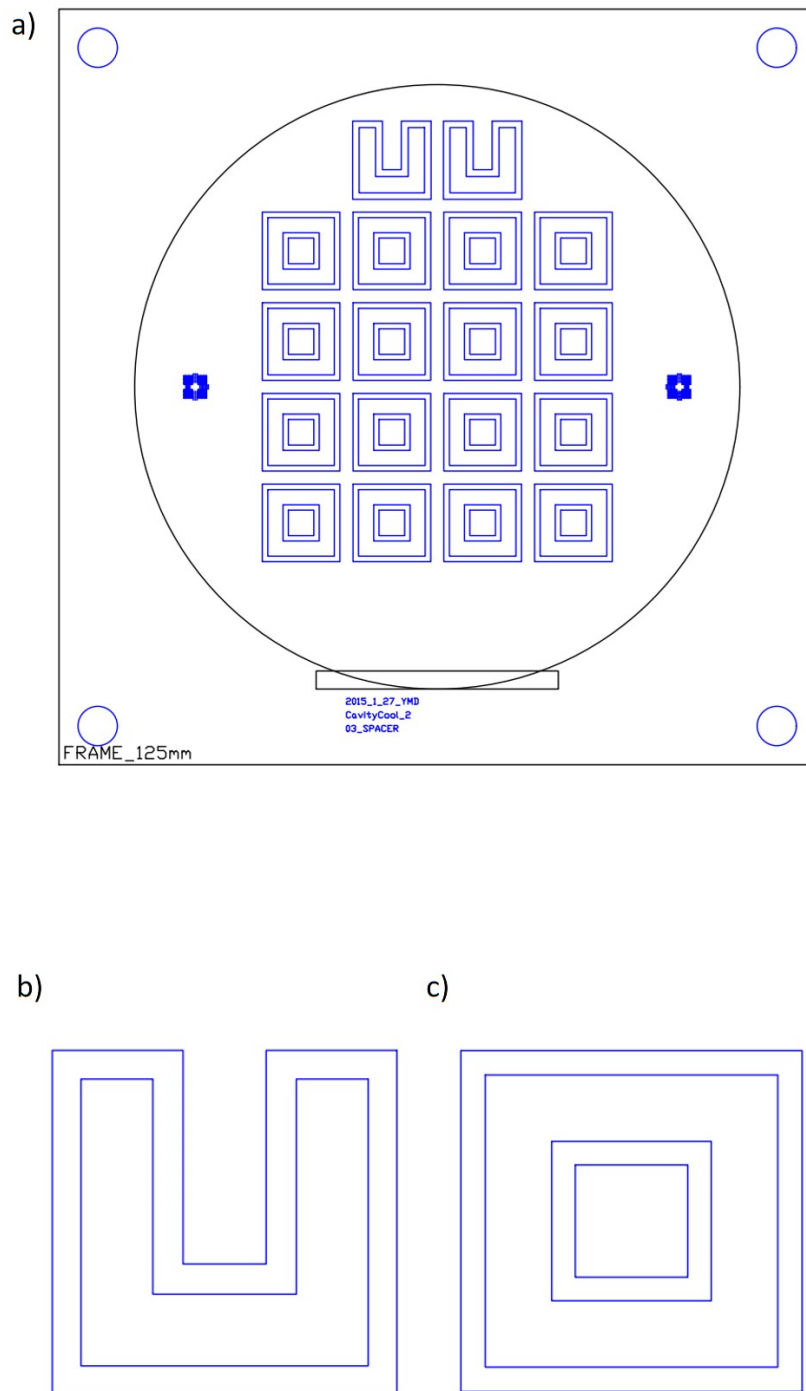


Figure B.5: This mask are used to etch the spacer chips out of the silicon. a) is the full mask and b) a zoomed version on the chip.

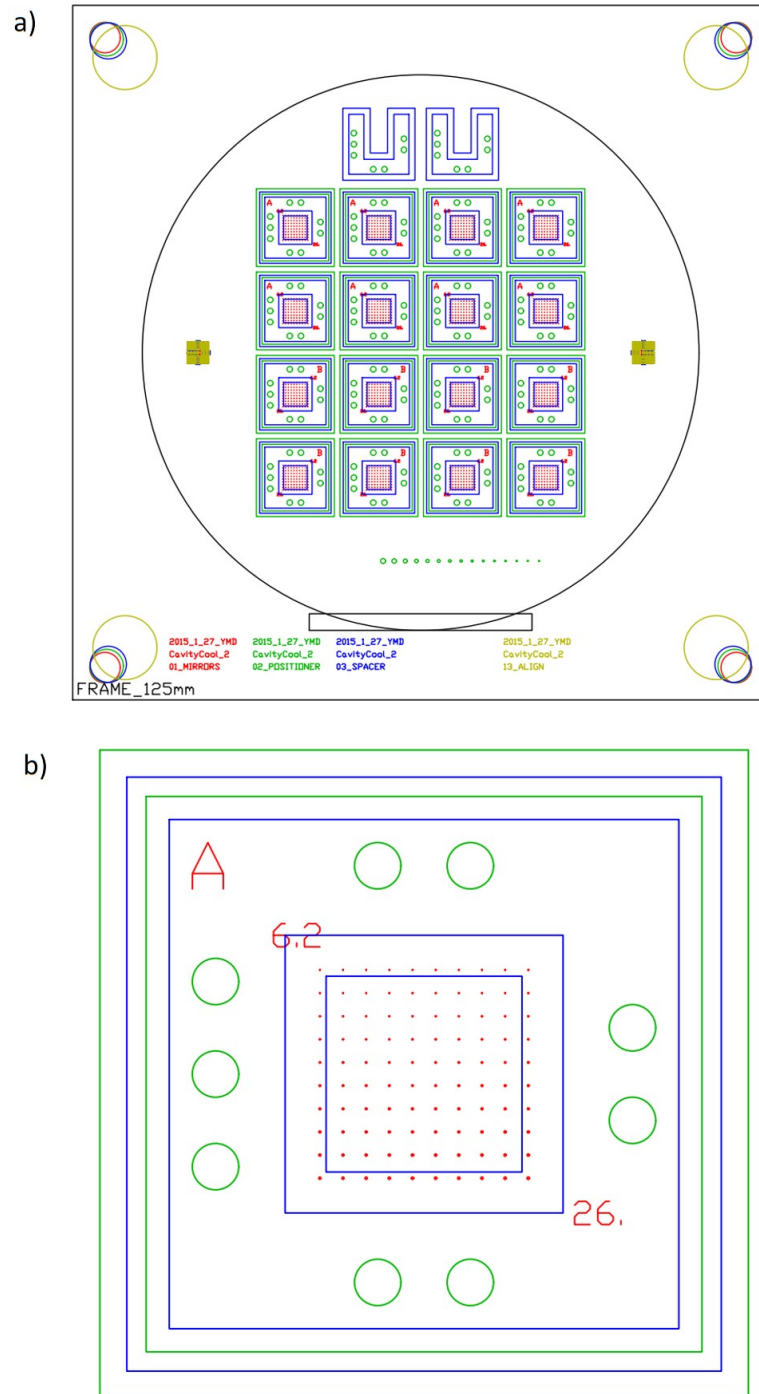


Figure B.6: This figure shows all masks together. a) is the full mask and b) a zoomed version on the chip.

Acknowledgments

The last lines of this text should be words of gratitude to all those who helped to make this thesis possible.

Firstly, I would like to express my sincere gratitude to my advisor Dr. Michael Trupke for the continuous support of my Ph.D study and related research, for his patience, motivation, and immense knowledge. His guidance helped me in all the time of research and writing of this thesis. I could not have imagined having a better advisor and mentor for my Ph.D study.

Also thanks to Prof. Schmiedmayer to give me the opportunity to write this PhD thesis and work on this challenging project. I am grateful to Prof. Ulrich Schmid for useful advice about the clean room processes. Prof. Markus Arndt for the opportunity to use his labs for the nano particle experiments and Prof. Philip Walther for give the micro cavity setup a new home at the university of Vienna.

I am thankful to my fellow labmates Rui, Cameron, Stefan P., Sara and Daniel for the stimulating discussions, their help in many situations and for all the fun we have had in the last four years. So thanks to the group which I am working in.

In particular I thanks Stefan Minniberger for the proofreading and a lot of discussion about this thesis.

My sincere thanks also goes to Michael Schneider which show me how an atomic force microscope works and how I can measure the mirror shape with it.

My gratitude goes to Johannes Schalko. He explain my all detail about mask for semiconductors gave my his guidance in my first steps into the clean room. Later he was always a great help if somewhere a problem appears.

I also thanks Michael Buchholtz which has done a lot of work as a clean room technician for me. He operates all the highly advanced devices which are necessary to produce the mirrors.

I thank in particular Stefan Kuhn, who made it possible to detect nano particles inside our cavity. His great knowledge and experience make it possible that we have seen together the first cavity resonance in the micro cavities in a dark lab in the basement of the Atomic Institute.

I also thank the electronic workshop and mechanical workshop at the TU and the University of Vienna for many parts and components crucial to the success of this

thesis. They have build the mount for the cavity in several different forms, coating holders and many more. I have never found an error or aberration in all of these parts.

I would thank all the nameless people which write the open software which is used to write this thesis (TeXstudio) or analysis AFM figures (Gwyddion)...

Last but not the least, I would like to thank my family: my parents, grandparents and my brother for supporting me spiritually throughout writing this thesis and my my life in general.



Georg Wachter, MSc

Curriculum Vitae

Education

- since 2014 **PhD student**, *TU Vienna*, Atomic Physics and Quantum Optics group of Prof. Schmiedmayer.
- since 2014 **Meber of Solids4fun**, *TU Vienna*.
- 2011-2014 **Master of Science**, *TU vienna*, technical physics.
- 2006 **Obligatory military duty**.
- 2005-2011 **Bachelor of Science**, *TU vienna*, technical physics.
- 2000-2005 **HTL Mechatronic**, *Mödling*.

Masters Thesis

- Title Electron dynamics and practical magnetometry using Nitrogen-Vacancy defects in diamond
- Supervisors Univ. Prof. Dr. techn Hannes Jörg Schmiedmayer, Univ. Ass. Dr. phil Michael Trupke
- Description This thesis explored the application of nitrogen vacancy centers as magnetometer and their optical dynamics.

Poster and Talks at Conference

- 2017 **Summer School and Poster**, *CoQus*, vienna.
Scaleable Silicon Microcavities with finesse $>10^5$
- 2015 **Poster**, *QuPoN*, vienna.
Hight sensitivity magnetometry using nitrogen-vacancy centers
- 2015 **Summer School and Poster**, *QUICC Summer School 2015*, warwick UK.
High-performance silicon microcavities for quantum science
- 2013 **Talk and Poster**, *Greenhorn Meeting*, Innsbruck.
Optical dynamics of the nitrogen-vacancy centrer in diamonds

Stranzenberggasse 5/2/3 – 1130 vienna
☎ 0676/9358584 • ✉ ge.wachter@gmail.com

1/2

Computer and programming skills

Basic Assembler

Intermediate Verilog, VHDL, \LaTeX , OpenOffice, PCB Programmes (EAGLE, Altium)

Advanced C, Labview, Mathematica, CAD Programms (Solid works, T-Flex, Autocad Inventor)

Electronic Skills

Basic RF circuits, antenna design

Intermediate Programming FPGAs, digital and analog electronics

Advanced Microcontroller (Atmel and Pics)

Lab Skills

Basic Cleanrooms: Lithographs, Mask design, Bosch etch, Atomic force microscopy

Intermediate Optics; Lasers, Fibre, Acousto-optic modulator, Electro-optic modulator

Advanced Control of Experiments

Languages

German **Mother tongue**

English **Intermediate**

Con conversationally fluent

List of papers

- [1] **Wachter, G.**, Kuhn, S., Minniberger, S., Salter, C., Asenbaum, P., Millen, J., Schneider, M., Schalko, J., Schmid, U., Felgner, A., "Silicon microcavity arrays with open access and a finesse of half a million". In: *Light: Science & Applications* 8.1 (2019), p. 37.
- [2] Kuhn, S., **Wachter, G.**, Wieser, F.-F., Millen, J., Schneider, M., Schalko, J., Schmid, U., Trupke, M., Arndt, M., "Nanoparticle detection in an open-access silicon microcavity". In: *Applied Physics Letters* 111.25 (2017), p. 253107.
- [3] Bourgeois, E., Londero, E., Buczak, K., Hruby, J., Gulka, M., Balasubramaniam, Y., **Wachter, G.**, Stursa, J., Dobes, K., Aumayr, F., "Enhanced photoelectric detection of NV magnetic resonances in diamond under dual-beam excitation". In: *Physical Review B* 95.4 (2017), p. 041402.
- [4] Gulka, M., Bourgeois, E., Hruby, J., Siyushev, P., **Wachter, G.**, Aumayr, F., Hemmer, P. R., Gali, A., Jelezko, F., Trupke, M., "Pulsed Photoelectric Coherent Manipulation and Detection of N- V Center Spins in Diamond". In: *Physical Review Applied* 7.4 (2017), p. 044032.